NASA/TM—1998-208823

IN-07
432215
290P

Improved Modeling of Finite–Rate Turbulent Combustion Processes in Research Combustors

Thomas J. VanOverbeke
Lewis Research Center, Cleveland, Ohio

November 1998

The NASA STI Program Office . . . in Profile

Since its founding, NASA has been dedicated to the advancement of aeronautics and space science. The NASA Scientific and Technical Information (STI) Program Office plays a key part in helping NASA maintain this important role.

The NASA STI Program Office is operated by Langley Research Center, the Lead Center for NASA's scientific and technical information. The NASA STI Program Office provides access to the NASA STI Database, the largest collection of aeronautical and space science STI in the world. The Program Office is also NASA's institutional mechanism for disseminating the results of its research and development activities. These results are published by NASA in the NASA STI Report Series, which includes the following report types:

- TECHNICAL PUBLICATION. Reports of completed research or a major significant phase of research that present the results of NASA programs and include extensive data or theoretical analysis. Includes compilations of significant scientific and technical data and information deemed to be of continuing reference value. NASA's counterpart of peer-reviewed formal professional papers but has less stringent limitations on manuscript length and extent of graphic presentations.
- TECHNICAL MEMORANDUM. Scientific and technical findings that are preliminary or of specialized interest, e.g., quick release reports, working papers, and bibliographies that contain minimal annotation. Does not contain extensive analysis.
- CONTRACTOR REPORT. Scientific and technical findings by NASA-sponsored contractors and grantees.
- CONFERENCE PUBLICATION. Collected papers from scientific and technical conferences, symposia, seminars, or other meetings sponsored or cosponsored by NASA.
- SPECIAL PUBLICATION. Scientific, technical, or historical information from NASA programs, projects, and missions, often concerned with subjects having substantial public interest.
- TECHNICAL TRANSLATION. English-language translations of foreign scientific and technical material pertinent to NASA's mission.

Specialized services that complement the STI Program Office's diverse offerings include creating custom thesauri, building customized data bases, organizing and publishing research results . . . even providing videos.

For more information about the NASA STI Program Office, see the following:

- Access the NASA STI Program Home Page at ***http://www.sti.nasa.gov***
- E-mail your question via the Internet to help@sti.nasa.gov
- Fax your question to the NASA Access Help Desk at (301) 621-0134
- Telephone the NASA Access Help Desk at (301) 621-0390
- Write to:
  NASA Access Help Desk
  NASA Center for AeroSpace Information
  7121 Standard Drive
  Hanover, MD 21076

NASA/TM—1998-208823

Improved Modeling of Finite–Rate Turbulent Combustion Processes in Research Combustors

Thomas J. VanOverbeke
Lewis Research Center, Cleveland, Ohio

National Aeronautics and
Space Administration

Lewis Research Center

November 1998

Available from

NASA Center for Aerospace Information
7121 Standard Drive
Hanover, MD 21076
Price Code: A13

National Technical Information Service
5285 Port Royal Road
Springfield, VA 22100
Price Code: A13

Abstract

The objective of this thesis is to further develop and test a stochastic model of turbulent combustion in recirculating flows. There is a requirement to increase the accuracy of multi-dimensional combustion predictions. As turbulence affects reaction rates, this interaction must be more accurately evaluated. In this work a more physically correct way of handling the interaction of turbulence on combustion is further developed and tested. As turbulence involves randomness, stochastic modeling is used. Averaged values such as temperature and species concentration are found by integrating the probability density function (pdf) over the range of the scalar. The model in this work does not assume the pdf type, but solves for the evolution of the pdf using the Monte Carlo solution technique. The model is further developed by including a more robust reaction solver, by using accurate thermodynamics and by more accurate transport of elements. The stochastic method is used with Semi-Implicit Method for Pressure-Linked Equations. The SIMPLE method is used to solve for velocity, pressure, turbulent kinetic energy and dissipation. The pdf solver solves for temperature and species concentration. Thus, the method is partially familiar to combustor engineers. The method is compared to benchmark experimental data and baseline calculations. The baseline method was tested on isothermal flows, evaporating

sprays and combusting sprays. Pdf and baseline predictions were performed for three diffusion flames and one premixed flame. The pdf method predicted lower combustion rates than the baseline method in agreement with the data, except for the premixed flame. The baseline and stochastic predictions bounded the experimental data for the premixed flame. The use of a continuous mixing model or relax to mean mixing model had little effect on the prediction of average temperature. Two grids were used in a hydrogen diffusion flame simulation. Grid density didn't affect the predictions except for peak temperature and tangential velocity. The hybrid pdf method did take longer and required more memory, but has a theoretical basis to extend to many reaction steps which cannot be said of current turbulent combustion models.

TABLE OF CONTENTS

Chapter 1

INTRODUCTION

1.1 Motivation for the thesis

Improving the numerical simulation of combustor flows is a never-ending endeavor. There is a continuing demand to increase gas turbine performance and decrease emissions. These demands do not complement each other. The demand for increased performance is typically met by increasing cycle pressure and final temperature. This is allowed by continual advances in metallurgy. However, increasing pressure and temperature usually increases emissions. Thus, combustor designs are being evaluated to test for increased performance with lower emissions. One method to help in designing gas turbine combustors is Computational Fluid Dynamics and combustor models. These models are benchmarked or validated using existing engine or test data. CFD combustor model predictions are accurate or calibrated within similar engine designs. Thus, new concepts cannot be totally evaluated by current CFD models. The number of prototypes in an engine development program may be reduced by using CFD combustor model predictions. Initial computational designs must be tested on engine stands. CFD can be also be used to correct design deficiencies found in prototypes. Commercial gas turbines are very difficult and costly to instrument and test. The use of CFD models provides data at all locations in a combustor field. Thus, the nature of CFD complements engine test programs.

Newer engine designs are going to higher peak temperature and pressure to improve both fuel economy and thrust to weight ratio. Severe reductions in emissions are being required by governments. Some European countries are considering instituting fees based upon the total amount of pollutants emitted by aircraft flying through their airspace. Older aircraft producing more pollution would be more heavily taxed. The evaluation of proposed engine designs is causing a demand for increased accuracy in CFD combustor models as well as a wider range of validity in those models. Engine designers are tolerating more complex combustor models in a desire for more accurate CFD predictions. Computer resources to allow more accurate modeling is becoming more affordable with time. Combustion simulations were once entirely done on mainframe computers or supercomputers. Running many combustion simulations on supercomputers can cost thousands of dollars. Workstations have been developed to the point that taking into account the amount of time jobs are in queues, the total turn-around time is comparable for high-end workstations and supercomputers. The cost of doing calculations on workstation is significantly less than running on supercomputers. To further reduce turn-around time of workstations, computers may be clustered together to give performance similar to dedicated super-computers. Many workstations see relatively little use at off hours. With suitable networking, these under-utilized workstations may be used to perform complex 3-D predictions at small additional cost.

1.2 - Progress in the Simulation of Combustion

Much of the model improvement in the last decade has been in the area of gridding. Curved boundaries and round dilution jets are modeled without stair-stepping the geometry. Unfortunately, generating grids for complex combustors can take up most of the time to perform the calculation. One way around this is to overlap simpler grids. This technique essentially allows imbedding grid for a flow feature into another simpler grid which poorly defines the flow feature. A good example is a cylindrical grid for a rod imbedded into a cartesian grid for a rectangular duct. Another technique being developed is the use of unstructured grid solvers. In unstructured grids, the grid is generated by breaking the flow geometry into many smaller general elements. If more refinement is needed, the elements are further divided. The data storage for fluid elements is quite different than for structured grid solvers. The unstructured grid method incurs additional work to keep track of neighboring grid cells. This technique is only in its infancy. It is unknown which solution method will prove best for combustor design.

Over the past twenty years, most elliptic flow calculations have been done using variants of the Semi-Implicit-Method for Pressure-Linked-Equations developed by Patankar[1]. The usual implementation is to assume low Mach number flow. In this flow regime, pressure is largely a relative variable, that is, pressure is fairly constant. Changes in density are due to changes in molecular weight and temperature. This solution technique is referred to as pressure based method. Industry regards the solution method as robust, but, as rather dissipative. If flow is at an angle to the grid, calculated flow quantities may be dissipated. A great deal of effort was expended in the eighties to develop improved differencing methods to improve accuracy of pressure based schemes. Skew differencing was developed to take into account the angle of the flow to the grid. Quadratic upwind interpolation and second-order upwind differencing were also developed. Theoretically these schemes are more accurate, but, the schemes are not as robust as first-order upwind differencing schemes. Convergence is much more difficult for improved schemes. Some of these schemes blend in varying amounts of upwind differencing to improve robustness.

Density based solvers are thought by some individuals to be less dissipative than the pressure based solvers. However, these solvers must include artificial dissipation terms for robustness. Density based solvers are efficient in the solution of higher Mach number or compressible flows.

The convergence of the solver greatly deteriorates with decreasing Mach number as the flow becomes incompressible. Solution techniques using density based solvers for low speed flows are being developed, such as NASA Lewis Research Center's ALLSPD[2] code. The ALLSPD code uses preconditioning, gauge pressure and pseudo-time stepping to maintain good convergence rates at low Mach number flows. This solution technique is in the development phase.

Another technique to improve convergence rates is to use multi-grid solvers. Joshi and Vanka[3] performed multi-grid calculations for gas-turbine type geometries. The method was also demonstrated for 3-D geometries for studying hot gas ingestion for short take off and vertical landing aircraft[4]. Multi-grid was also used in a numerical ramjet study by Vanka and Krazinski[5]. A four-step combustion mechanism with combination eddy-breakup and arrhenius reaction rate submodel was used in the study. A single grid system was used in the solution of species concentration due to the strong influence of the source terms in the chemical kinetic equations.

The overall chemistry or reaction kinetics of fuels can be very complicated. Also, combustion in practical gas turbine combustors is highly turbulent. Improved turbulence models for variable density flows are the least developed of all turbulence models, and typically have been calibrated for isothermal incompressible flows. Turbulence is usually ignored by researchers who study fundamental combustion processes the most, the experts in chemical reaction kinetics. These experts predict reaction rates accurately over the range of combustor temperature, pressure and species concentration. Unfortunately, this is accomplished by employing dozens of chemical reactions with widely varying time characteristics. These kinetic reaction systems must be solved by specialized solvers using small time steps, predictor-corrector steps, etc. Many reactions involve species the engineer isn't concerned with. Not enough effort is being spent on producing reduced chemical reaction mechanisms that will give acceptable engineering predictions. Laminar combustion experts have yet to develop simpler kinetic reaction schemes which they feel are accurate enough to predict exhaust emissions for different engine concepts. Typical combustor models employ five to ten species and as few chemical reactions as possible. The chemical kineticists typically insist on twenty or more reactions for hydrocarbons and would like to see as many as fifty reactions. The time steps needed to accurately solve species concentrations for these kinetic mechanisms can be extremely small, much shorter than the pseudo time step taken in typical combustor calculations. A good time step for the LSENS[6] general kinetics and sensitivity solver is of the order of ten micro-seconds. The code employs variable time steps to improve solution speed. The solution efficiency has been substantially improved from the original solver. This code is one of the most highly developed and efficient chemical kinetics solver existing today. However, it is still too computationally expensive to use for solving complex multi-dimensional combustor flows. Techniques used to accurately solve laminar one dimensional combustion are too complex and costly at the present time to use for the solution of multi-dimensional turbulent recirculating flows. Typical design models use a very small number of reaction steps to predict performance. Engine emissions are usually predicted by post-processing, adjusting constants or employing empirical corrections.

1.3 - Turbulent Combustion

The prediction of combustion is greatly affected by turbulence. The length of current gas turbine combustors is fairly short. Fuel and oxidant must be thoroughly mixed within a short distance at fairly high velocities. Combustor velocities are greater than laminar flame velocities. Combustor exit velocities in the newer gas turbine engines are getting into the high subsonic realm. The overall mixing of fuel and oxidants in a combustor is greatly augmented by turbulence.

Turbulence causes changes in the instantaneous values of velocity, species and temperature. Reaction rates are nonlinear functions of concentration and temperature. Thus, the averaged reaction rate isn't the same as the reaction rate of averaged species concentration and temperature. Previous modeling has employed many ad-hoc corrections to account for the interaction of turbulence on combustion. One such correction is to include a factor to convert laminar reaction rates into turbulent reaction rates. Turbulence produces eddies or modules with varying concentrations of fuel and oxidant. These eddies go through a breakup or decay process before the eddies completely mix. As turbulence continually generates new eddies in the flows, this is an ongoing process. Thus, turbulence causes incomplete mixing which causes an overlap of fuel and oxidant species concentration particularly near stoichiometric conditions where there is the greatest chemical reactivity. The overlap in average reactant specie concentration makes turbulent combustion resemble finite rate combustion. Current turbulent combustion methods do a good job of predicting combustor exit temperature patterns and major species concentrations. Minor species and intermediates, especially carbon monoxide, are not well predicted. Unfortunately, minor species can cause significant pollution levels. The level of engine emissions is being monitored and future emissions have been regulated due to serious environmental considerations. The development of an American supersonic transport was canceled in the seventies due to concerns of immense nitrous oxide production at high altitudes. Lakes and forests are being adversely affected by current fossil fuel combustion. The combustion process must be better predicted to aid in the design of lower emissions combustors.

1.4 - Stochastic Turbulent Combustion Models

A more physically correct model of the turbulence-chemistry interaction is to treat combustion as a stochastic process. This is the idea behind current assumed shape probability density function models. These models assume certain shapes for the probability of a conserved scalar. The probability density function may be inferred by solving modeled equations for the means and variances of variables. The major assumption in presumed shape pdf modeling is that reaction rates are fast in these models. This can be partially relaxed by including another independent variable, typically for reactedness. The additional variable is usually assumed to be uncorrelated to the conserved scalar. Unfortunately, the additional variable is usually correlated. Including more species and chemical reactions adds complexity and increases the number of assumptions. Even allowing for incomplete or partial combustion in assumed shape pdf models causes predictions of high reaction completeness as the simplified combustion mechanisms employed typically used are only valid at high temperatures.

Another stochastic method involves solving for the evolution of probability density function. This modeling eliminates the chemical reaction rate closure problem inherent in traditional combustion modeling. Stochastic treatments of species transport are said to exactly include the chemical reaction rate term. This has been known for quite some time, but, the capability to perform stochastic calculations of practical combustor flowfields is being developed at the experimental or research level. Actual engine combustor design predictions have to be done in a short period of time to be effective in the combustor design process. Also, industrial predictions have to be cost effective. Stochastic modeling demands large expensive computer resources. As computer power continues to increase and the cost of doing combustion simulations becomes more acceptable, the use of stochastic combustion models will increase.

1.5 - Contribution of the Present Work

Assumed shape pdf models have been used for over a decade and development of these models has largely stagnated. The next step in pdf modeling is the composition pdf, which requires roughly an order of magnitude increase in memory and computer time. Pdf modeling allows a substantially more robust and accurate method of calculating minor species for turbulent combustion, albeit at substantially increased cost.

Newly developed hybrid pdf models have predicted excellent agreement with experimental data for parabolic or one-way combustor flow. The method is called hybrid as stochastic methods are used to solve for average species composition, density and temperature, while traditional CFD techniques are used to solve for other flow quantities. Full stochastic simulations of all flow quantities is beyond current capabilities. The hybrid method retains the traditional CFD techniques which engineers are used to, while it treats turbulent chemistry interactions in a much more physically correct manner.

The purpose of my work is to incorporate and further develop a composition and enthalpy pdf model into a computational fluid dynamics model. The hybrid pdf model uses individual species particles to solve for the evolution of composition and temperature pdfs. The hybrid pdf model consists of consecutively solving for velocity, pressure, turbulence length and time scales, species transport and chemical reaction. A Monte Carlo solution technique is used to predict species transport, mixing and species reactions. Many improvements to the original pdf model were made in the work. The pdf model was improved to more properly calculate species transport. The original model used an incorrectly coded upwind differencing scheme to calculate species transport. A more accurate scheme was implemented. The original model had major thermodynamic simplifications. This was corrected to better predict actual combustor data. The original model had an extremely simple combustion solver. This solver worked with the original reaction rate constants, but, didn't for the reaction models in this work. An improved species solver was implemented. Pdf results are properly compared against good CFD results. Some pdf predictions are performed against CFD predictions done years ago, and claiming the improved results are due solely to pdf modeling. This ignores many improvements which have been made to CFD models over the years. Pdf predictions have also been compared to initial or other poorly refined predictions. The hybrid pdf model will be tested against a proven baseline turbulent combustion model and experimental data for various research combustor flowfields. The baseline model uses the pressure based method to solve for velocity, pressure, mean species, species fluctuation and turbulence scales in elliptic flow fields. The k-ε turbulence model is used. A fuller description of the model development in this work is covered in chapter 4.

Chapter 2

BASELINE SOLUTION METHOD FOR CONVECTION-DIFFUSION PROBLEMS

The Semi-Implicit Method for Pressure Linked Equations or SIMPLE method of Patankar is used in conjunction with the hybrid composition pdf method in this thesis. The SIMPLE algorithm method is used for solving momentum, overall mass conservation, turbulent kinetic energy and dissipation rate of turbulent kinetic energy. The pdf method used here solves turbulent combustion and species transport. This chapter covers a rather short discussion on the SIMPLE method, boundary conditions used and source terms for combustion species.

2.1 - Governing Equations

The gas phase equations can be put in the following general form for cartesian geometries:

$$\frac{\partial}{\partial t}(\rho\phi) + \frac{\partial}{\partial x}\left[\rho U\phi - \Gamma_\phi \frac{\partial \phi}{\partial x}\right] + \frac{\partial}{\partial y}\left[\rho V\phi - \Gamma_\phi \frac{\partial \phi}{\partial y}\right] = S_\phi \tag{2.1}$$

where ρ is the density, U is the axial velocity, V is the radial velocity, Γ_ϕ is the appropriate diffusion coefficient and S_ϕ is the source term for the variable ϕ. For example, the diffusion coefficient for the laminar momentum equations would be μ_l, the laminar viscosity. Turbulence introduces additional complexity into the transport equation. The way this is traditionally done for incompressible flow is to perform a Reynolds decomposition of velocity into a mean and fluctuating components:

$$U = \overline{U} + u' \tag{2.2}$$

where,

$$\overline{U} = \lim_{t_0 \to \infty} \frac{1}{t_0} \int_{t_0}^{t_0+dt} U dt \tag{2.3}$$

Substituting in the Reynolds decomposition of axial and radial velocity into the momentum equation and time averaging results in terms such as:

$$\rho\overline{u'u'},\ \rho\overline{v'v'}, and\ \rho\overline{u'v'},\ etc$$

which are known as Reynolds stresses. The first two terms are normal stresses. These can be incorporated into the pressure term. If density varies, the dilatation or divergence of velocity isn't zero. The dilatation can also be included in the pressure term:

$$P \equiv p + \frac{2}{3}\mu_t\left(\frac{\partial U_k}{\partial x_k}\right) + \frac{2}{3}\rho k \tag{2.4}$$

where μ_t is the turbulent coefficient of viscosity. The Reynolds stresses are unknown. The Reynolds stresses must involve modeling at some point due to problems with closure. Lower level modeling involves simple correlations for the stresses. Higher level or second moment modeling involves solving modeled equations for the transport of Reynolds stresses. These equations are formed by a sequence of multiplication of the momentum equations, Reynolds decomposition and time averaging. These equations have unknown triple correlation terms, which must then be modeled. Lower level turbulence modeling has proved suitable for prediction of turbulent combustion. The non-normal Reynolds stresses are modeled using a generalization of Boussinesq's eddy viscosity concept or the gradient model assumption:

$$\tau_{ij} = -\mu_t\left(\frac{d\overline{U_i}}{dx_j} + \frac{d\overline{U_j}}{dx_i}\right), \qquad i \neq j \tag{2.5}$$

Following the Prandtl-Kolmogorov definition of eddy viscosity, the viscosity coefficient is composed of length and velocity scales. The preferred method of supplying these scales is the two equation k-ε turbulence model. The k-ε model was developed by Jones and Launder[7]. The term k is known as the turbulent kinetic energy:

$$k = \frac{1}{2}\left(\overline{u'u'} + \overline{v'v'} + \overline{w'w'}\right) \tag{2.6}$$

The term ε is known as the turbulent kinetic dissipation rate. If the characteristic length is defined as $k^{3/2}/\varepsilon$ and velocity as $k^{1/2}$, the turbulent diffusion coefficient can be defined as:

$$\mu_t = C_\mu \rho \frac{k^2}{\varepsilon} \tag{2.7}$$

Equations can be formed for k and ε. However, these equations have been modified to better predict turbulence. The modeled equations are:

$$\frac{\partial}{\partial t}(\rho k) + \frac{\partial}{\partial x}\left[\rho Uk - \Gamma_k \frac{\partial k}{\partial x}\right] + \frac{\partial}{\partial y}\left[\rho Vk - \Gamma_k \frac{\partial k}{\partial y}\right] = \mu_t G - \rho\varepsilon \qquad (2.8)$$

and

$$\frac{\partial}{\partial t}(\rho\varepsilon) + \frac{\partial}{\partial x}\left[\rho U\varepsilon - \Gamma_\varepsilon \frac{\partial \varepsilon}{\partial x}\right] + \frac{\partial}{\partial y}\left[\rho V\varepsilon - \Gamma_\varepsilon \frac{\partial \varepsilon}{\partial y}\right] = C_1 C_\mu G\varepsilon/k - C_2\rho\varepsilon^2/k \qquad (2.9)$$

where G is the turbulence generation term:

$$G = \frac{\partial u_i}{\partial x_j}\tau_{ij} \qquad (2.10)$$

The k-ε model allows for the variability of length and velocity scales with history effects. That is, the viscosity isn't just a function of local gradients or scales.

Some of the non-normal turbulent stresses can be incorporated into diffusion terms in the general equation by defining a effective diffusion coefficient which is the sum of the laminar and turbulent diffusion coefficients.

$$\mu_{eff} = \mu_l + \mu_t \qquad (2.11)$$

The left over turbulent terms are put into source terms for the momentum equations. For example, the axial momentum source term for Cartesian flows is:

$$S_u = \frac{\partial}{\partial x}\left(\mu_t \frac{\partial U}{\partial x}\right) + \frac{\partial}{\partial y}\left(\mu_t \frac{\partial V}{\partial x}\right) \qquad (2.12)$$

2.2 - Discretization of the general equation

Except for simplified problems, the general equations do not have an analytic solutions. The equations must be solved numerically. The equation is discretized by using the control volume approach. The general transport equation is integrated over the dashed control volume for the node P shown in figure 2.1. The values at the faces of the control volume are presumed to preside over the whole face. This gives:

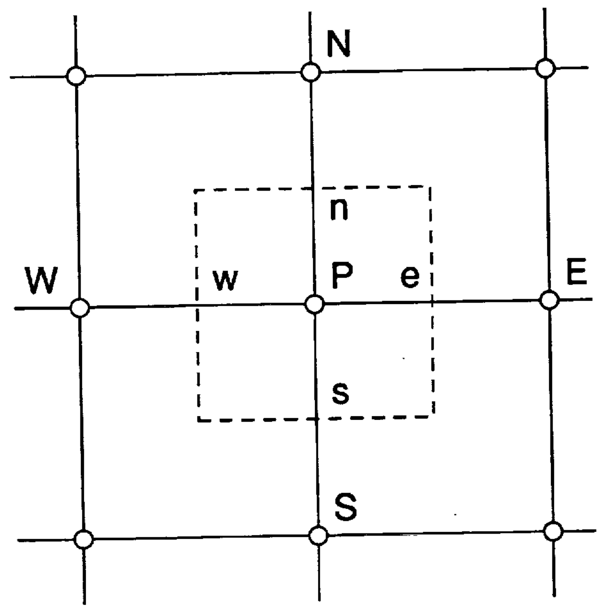

figure 2.1 Control Volume

$$\frac{(\rho_P\phi_P-\rho_P^0)\,\Delta x\Delta y}{\Delta t}+F_e\phi_e-D_E(\phi_E-\phi_P)-F_w\phi_w+D_W(\phi_W-\phi_P)+F_n\phi_n-D_N(\phi_N-\phi_P)-F_s\phi_s+D_S(\phi_P-\phi_S)=(S_C+S_P\phi_P)\,\Delta x\Delta y \tag{2-13}$$

where the source term has been linearized and the convection coefficients at the control volume faces are given by:

$$F_e = (\rho U)_e\Delta y, \tag{2.14a}$$

$$F_n = (\rho U)_w\Delta y, \tag{2.14b}$$

$$F_n = (\rho V)_n\Delta x, \tag{2.14c}$$

$$F_s = (\rho V)_s \Delta x, \tag{2.14d}$$

where Δx and Δy are the width and height of the control volume. The diffusion coefficients are given by:

$$D_E = \left(\frac{\Gamma_\phi}{\Delta x}\right)_e \Delta y, \tag{2.15a}$$

$$D_N = \left(\frac{\Gamma_\phi}{\Delta y}\right)_n \Delta x \tag{2.15b}$$

$$D_W = \left(\frac{\Gamma_\phi}{\Delta x}\right)_w \Delta y, \tag{2.15c}$$

$$D_S = \left(\frac{\Gamma_\phi}{\Delta y}\right)_s \Delta x, \tag{2.15d}$$

where the term $(\Delta x)_e$ is the distance between the points P and E, etc.

The equation is further developed by manipulation of the continuity equation. Integrating the continuity equation over the same volume gives:

$$\frac{(\rho_P - \rho_P^0)\,\Delta x \Delta y}{\Delta t} + F_e - F_w + F_n - F_s = 0 \tag{2.16}$$

If the integrated continuity equation is multiplied by ϕ_P and subtracted from the integrated general equation, the following equation is obtained:

$$(\phi_P-\phi_P^0)\frac{\rho P^0 \Delta x \Delta y}{\Delta t} +F_e(\phi_e-\phi_P) -D_E(\phi_E-\phi_P) -F_w(\phi_w-\phi_P) +D_W(\phi_P-\phi_W) +F_n(\phi_n-\phi_P) -D_N(\phi_N-\phi_P) -F_s(\phi_s-\phi_P) +D_S(\phi_P-\phi_S) = (S_C+S_P\phi_P)\Delta x \Delta y \tag{2.17}$$

This equation involves intermediate values at the cell faces. The goal is to discretize the above equation into an equation involving ϕ_P and its neighboring nodes:

$$a^P\phi_P = a_E\phi_E + a_W\phi_W + a_N\phi_N + a_S\phi_S + b \tag{2.18}$$

This may be done by forming interpolations involving the adjoining nodes for the intermediate values at the cell faces. However, if any of the above coefficients is allowed to become negative, the answers may become non-physical. To ensure physically realistic results the hybrid differencing scheme is used in this work. The hybrid differencing scheme is a combination of central differencing and upwind differencing. Hybrid differencing uses more accurate central differencing when the absolute value of the ratio of the convective flux to the diffusive flux (or Peclet number) is less than two. When the Peclet number is greater than two, the upwind differencing scheme coefficients are used, which is physically realistic at high convection rates. The use of hybrid differencing is illustrated with the following expression for fluxes on the east side of the control volume:

$$F_e(\phi_e - \phi_P) - D_E(\phi_E - \phi_P) = a_E(\phi_P - \phi_E) \tag{2.19}$$

If the absolute value of the Peclet number is less than two, central differencing is used for the term ϕ_e, thus:

$$F_e\left(\left(\frac{\phi_E + \phi_P}{2}\right) - \phi_P\right) - D_e(\phi_E - \phi_P) = a_E(\phi_P - \phi_E) \tag{2.20}$$

which gives:

$$a_E = D_e - \frac{F_e}{2}, \qquad for \quad |Pe| \le 2 \tag{2.21}$$

If the Peclet number is greater than two, the convective flux from node P overwhelms the diffusive flux. The diffusive flux is ignored and ϕ_e is taken as ϕ_P, and:

$$F_e(\phi_P - \phi_P) = a_E(\phi_P - \phi_E) \tag{2.22}$$

which gives:

$$a_E = 0, \qquad for \quad Pe > 2 \tag{2.23}$$

If Pe is less than -2, then the convective flux from node E is much larger than the diffusive flux, which is ignored. Thus:

$$F_e(\phi_E - \phi_P) = a_E(\phi_P - \phi_E) \tag{2.24}$$

which gives:

$$a_E = -F_e, \qquad for \quad Pe < -2. \tag{2.25}$$

The general value for a_E has been worked out to be:

$$a_E = \left[\!\left[-F_e, D_e - \frac{F_e}{2}, \ 0 \right]\!\right] \tag{2.26}$$

where the symbols $[\![\ ]\!]$ stands for the largest of the quantities within it. The formula for a_W is:

$$A_W = \left[\!\!\left[F_w, D_w + \frac{F_w}{2}, 0 \right]\!\!\right] \tag{2.27}$$

The formulas for a_N and a_S are similar. The formula for the rest of the coefficients are:

$$a_p = a_E + a_W + a_N + a_S + a_P^0 - S_P \Delta x \Delta y, \tag{2.28a}$$

$$a_P^0 = \frac{\rho_P^0 \Delta x \Delta y}{\Delta t}, \tag{2.28b}$$

$$b = S_C \Delta x \Delta y + a_P^0 \phi_P^0 \tag{2.28c}$$

2.3 - Solution for Pressure

An offset or staggered grid is used to solve the momentum equations. The nodes for axial velocity occur on the east and west faces of the scalar control volume. Thus, the control volume for axial momentum is offset from the scalar control volume. Thus the discretization equation for axial velocity is:

$$a_e U_e = \sum a_{nb} U_{nb} + b + (P_P - P_E) A_e \tag{2.29}$$

where the change in pressure with axial distance has been pulled out of the source terms. A_e is the area term on which the pressure is acting. A shorthand expression is used for neighbor coefficients and velocities. A very similar discretization equation for radial velocity can be formed.

In the pressure solution process, the solutions of velocity and pressure is divided into two components. The current velocity and pressure solutions are denoted U^*, V^* and P^*. Due to an inexact solution there is a pressure correction P' which causes corresponding velocity corrections U', V'.

$$U = U^* + U', \tag{2.30a}$$

$$V = V^* + V', \tag{2.30b}$$

$$P = P^* + P' \tag{2.30c}$$

A velocity correction equation may be formed by plugging in U^* and V^* into the discretized momentum equations. Subtracting the equation for U^* from the equation for U gives a velocity correction equation:

$$a_e U_e' = \sum a_{nb} U_{nb}' + (P_P' - P_E') A_e \tag{2.31}$$

The first term is unknown, but, disappears at convergence, so is ignored. This gives:

$$U_e' = \frac{A_e}{a_e} (P_P' - P_E') \tag{2.32}$$

Plugging this in the equation for U gives the velocity correction equation:

$$U_e = U_e^* + \frac{A_e}{a_e} (p_P' - P_E') \tag{2.33}$$

The continuity equation is integrated over the control volume for node P. The resulting equation involves velocities at the faces of the control volume. The equations for velocity correction are then substituted into this equation. A discretized for P' equation is formed by rearranging the terms:

$$a_P p_P' = a_E p_E' + a_W p_W' + A_N p_N' + a_S p_S' + b, \tag{2.34}$$

where b includes the mass imbalance due to U^* and V^* and the change in density with time.

This procedure for the solution of convection-diffusion problems is a very brief description of the Semi-Implicit Method for Pressure Linked Equations. The SIMPLE algorithm and its variants are the most used solution methods for low Mach number combustor flows. A much more general and thorough development of the SIMPLE method is given in Patankar [1].

Computational models using the SIMPLE algorithm and hybrid differencing have been widely used and have proven robust for combustor flows. The accuracy of the hybrid differencing scheme is believed to deteriorate when the flow does not align with the grid. Correa and Shyy et al.[8] have studied second order upwind differencing and the QUICK differencing scheme of Leonard[9]. Using simple simulations, it was demonstrated that one scheme was not generally superior for all cases. Higher order schemes are generally thought to have problems with robustness. However, Correa and Shyy stated that convergence rates of the more accurate numerical schemes were comparable to the hybrid scheme in the context of curvilinear coordinates. It was also found that with an appropriate grid distribution, the difference between finite difference operators could be quite small.

2.4 - Grid System and Axisymmetric Equations

The grid system used in this work is orthogonal. The grid setup is Practice B cited by Patankar [1]. Practice B first sets up the control volumes and then places the scalar gridpoints in the center of the control volume. The method used in this work uses plain averages rather than the more exact geometric interpolations or harmonic averages for physical quantities such as viscosity, etc. at cell faces. The boundary control volumes are of infinitesimal thickness, which eliminates half control volumes for scalar values. Axisymmetric geometries are solved in this thesis. The equations are slightly different than for Cartesian geometries. The general equation for orthogonal axisymmetric geometries is:

$$\frac{\partial}{\partial t}(\rho\phi) + \frac{\partial}{\partial x}\left[\rho U\phi - \Gamma_\phi \frac{\partial\phi}{\partial x}\right] + \frac{1}{y}\frac{\partial}{\partial y}\left[y\rho V\phi - y\Gamma_\phi\frac{\partial\phi}{\partial y}\right] = S \tag{2.35}$$

The source terms and diffusion coefficients for the various momentum and scalar equations are given in Appendix 1.

2.5 - Boundary conditions

Inlet conditions are read in and set the main program. Initial values are set in subroutine INIT. A restart capability is also in the main program. Each variable has its own calculation subroutine and entry point in the boundary condition subroutine. The Boundary conditions are implemented in subroutine MODPRO. The program must be modified for different geometries.

2.5.1 - Inlet conditions

All inlet conditions are specified. A large portion of this work is to validate computational algorithms. This requires that inlet conditions be as well specified as possible, so that quality of numerical predictions can be judged. Inlet velocities, temperatures, species mass fractions, and turbulence kinetic energies are specified based on actual measurements, if possible. If there are multiple inlets, the inlet pressure is set to be the same for both.

2.5.2 - Axis of Symmetry

Radial velocity is zero at the axis of symmetry. The radial gradient of all variables, except radial velocity is zero at the axis of symmetry. Mathematically:

$$\left(\frac{\Delta\Phi}{\Delta r}\right)_{r=0} = 0 \tag{2.36}$$

The axis of symmetry is located on the *j=1* gridline. The axisymmetric boundary condition produces the result:

$$\Phi_{i,j=1} = \Phi_{i,j=2}, \quad \textit{except for velocity V} \tag{2.37}$$

This boundary contribution is implemented each iteration. During the iteration process the neighbor coefficient for the axis of symmetry is zero as the area term is zero.

2.5.3 - Outlet

At the exit of the combustor the axial gradient of all variables except for axial velocity is assumed to vanish. Thus, the neighbor coefficient a_E is set to zero at the exit. Thus, exit variables, except axial velocity, need not be specified.

For axial velocity, an exit velocity correction due to mass conservation is applied every iteration. Generally, this greatly helps the rate of convergence.

2.5.4 - Solid walls

The law of the wall is used for velocities parallel to solid walls. The laminar sublayer extends to y^+ of 11.63. The value of y^+ is calculated by using the density, laminar viscosity, turbulent kinetic energy and appropriate length for the grid cell adjacent to the wall. Thus for axial velocity:

$$y^+ = \left(\frac{\rho C_\mu^{1/4}\sqrt{k}\,\Delta y/2}{\mu_l}\right) \tag{2.38}$$

If y^+ is less than 11.63, the shear stress is laminar and is given by:

$$\tau_w = \left(2\mu_l \frac{U}{\Delta y}\right) \tag{2.39}$$

Otherwise the cell is in the turbulent flow regime and shear stress is calculated using the law of the wall:

where κ is taken as 0.4187. Shear stresses are included in

$$\tau_w = \left[\frac{\kappa\rho C_\mu^{1/4}\sqrt{k}U}{\ln(9y^+)}\right] \tag{2.40}$$

the momentum equations as source terms.

For turbulent kinetic energy, the neighbor coefficient corresponding to the wall is set to zero and the source term is:

$$S_k = \mu_t G - \left[2C_\mu^{3/4}\rho k^{3/2} y^+/\Delta y\right], \qquad y^+ < 11.63 \tag{2.41a}$$

$$S_k = \mu_t G - \left[2C_\mu^{3/4}\rho k^{3/4}\ln(9y^+)/(\kappa\Delta y)\right], \quad y^+ \geq 11.63 \tag{2.41b}$$

The turbulent dissipation rate next to the wall is calculated by assuming that the rates of generation of turbulent kinetic energy and dissipation are equal so that the value of ε is:

$$\varepsilon = \left(\frac{2C_\mu^{3/4}k^3/2}{\kappa\Delta y}\right), \quad \textit{next to the wall} \tag{2.42}$$

The value of ε next to walls is fixed by the forcing the source term coefficients to overwhelm all other neighbor contributions:

$$S_P = -1.0\times 10^{30}, \tag{2.43a}$$

$$S_C = 1.0\times 10^{30}\varepsilon \tag{2.43b}$$

Walls are treated as adiabatic. Thus, the neighbor coefficients for wall influences for heat transfer and diffusion of species is set to zero.

2.6 - Spray Combustion Modeling

Spray modeling has been under development for about three decades. Many review type papers on spray combustion modeling have been written. These include, Faeth's paper in 1977[10], and Law's paper in 1982[11], which cites improvements to original droplet evaporation modeling. The sophistication of spray models being used for combustor calculations is increasing. The earliest spray models treated spray vaporization as a single droplet in quiescent flow. The difference in velocity between the droplet or fluid phase and the gas phase velocity was ignored. In a 1983[12] paper, Faeth cites models which include consideration of the difference between the droplet velocity and gas phase velocity. In Sirignano's paper in 1983[13], fluid flow within the droplet itself was incorporated in a spray model.

One of the earliest studies of spray combustion was performed by Onuma and Ogasawara[14]. Some conclusions were that for the spray burner used, the region where the droplets exist is limited to a small area above the burner nozzle, and that it was reasonable that droplets do not burn individually, but, that the vapor cloud formed by the vaporization of the droplets burns like a diffusion flame. Many past calculations have successfully ignored spray vaporization or the fluid phase. Fuel was treated as being completely in the gaseous phase. However, as the demand for more efficient and lower emissions combustors has increased along with the needed computer resources, spray modeling is being developed and implemented in the prediction of gas turbine combustors.

According to Law, the basic droplet combustion model was formulated by various people, including Spaulding[15]. This model has since been termed the d^2-Law because the model predicts a linear relationship between the square of droplet diameter and time. Many improvements have been made to the d^2-Law. These include modeling of droplet heating, variable specific heat in the gas phase, and the multi-component fuels.

Actual sprays consists of a fairly continuous distribution of droplet size and droplet number density. Spray modeling employs discrete droplets in the prediction of spray combustion. Onuma and Ogasawara [14] thought that modeling a single characteristic droplet would be sufficient to accurately calculate spray combustion. The characteristic droplet is determined by some sort of averaging process regarding initial droplet size, position and velocity. The effect of multiple droplets or groups is found by taking multiples of the characteristic droplet effects. Most gas turbine spray modeling assumes that droplets do not interact, that the spray is dilute. Thus, the calculation of spray vaporization is treated as a function of individual droplet characteristics and the surrounding gas phase. Current models track numerous droplet groups. A range of different size, position and velocities may be used to approximate a droplet distribution. The most computationally expensive droplet models even model turbulent droplet dispersion. This is done by incorporating the effect that a random turbulent eddy would have on the droplet. Enough droplets must be computed to accurately predict overall spray.

Consideration is being given to modeling non-dilute or dense sprays, which exist in fuel atomizers. Faeth's paper in 1987[16] includes a section on the modeling of droplet to droplet interactions or dense sprays. Tsai and Sterling[17], show that the interaction between droplets increases as the distance between droplets decreases. There is difficulty in measuring dense spray properties. Non-intrusive optical methods are usually used. When multiple droplets are detected in a measurement volume, the measurement is typically invalidated.

The fuel break up process is non-uniform. In a section on the design and development of gas turbine combustors, A.H. Lefebre[18] writes that the fuel atomization is normally accomplished by spreading the fuel into a thin sheet and then increasing its surface area until it becomes unstable and disintegrates into threads or ligaments. These threads then break up into rows of droplets. The ligaments and droplets are highly nonuniform. The droplets are of various sizes and shapes and are not generally spherical. Droplet vaporization modeling assumes perfectly spherical droplets. It simply is too difficult to calculate non-spherical droplets in combustors or measure them for that matter. The break up of fuel stream into droplets is generally handled by empirical functions, rather than any physical modeling.

2.7 - Spray Solution Method

A spray combustion model including most of the above mentioned characteristics was modified. Simplified internal droplet fluid flow and temperature distribution is handled by the simplified vortex model of Tong and Sirignano[19]. The spray model is a simplification of the multicomponent spray modeling done by Raju and Sirignano[20]. The model assumes a dilute spray. Constant properties are assumed within the droplets. The droplet trajectories are solved using discretized Lagrangian equations. The turbulent dispersion of droplets isn't considered, as it would add at least an order of magnitude time to spray computations.

Sprays consist of many thousands of droplet particles each having their own velocity, drag forces, position, droplet diameter, and distributions of temperature and vortex strength. Due to limited numerical capabilities, a limited number of droplets are calculated. Each characteristic droplet has its own axial position x_k, and axial velocity U_k, which is a function of time. The subscript k refers to the kth droplet group. The change in droplet position with time is given by:

$$\frac{\partial x_k}{\partial t} = U_k, \tag{2.44}$$

$$\frac{\partial y_k}{\partial t} = V_k, \tag{2.45}$$

$$\frac{\partial z_k}{\partial t} = W_k \tag{2.46}$$

The droplet velocities are affected by drag effects caused by differences in velocity with the surrounding gas phase:

$$\frac{\partial U_k}{\partial t} = \frac{3}{16}\frac{C_D \mu_g Re_k}{\rho_k r_k^2}(\overline{U_g}-U_k)\,, \tag{2.47}$$

$$\frac{\partial V_k}{\partial t} = \frac{3}{16}\frac{C_D \mu_g Re_k}{\rho_k r_k^2}(\overline{V_g}-V_k)\,, \tag{2.48}$$

$$\frac{\partial W_k}{\partial t} = \frac{3}{16}\frac{C_D \mu_g Re_k}{\rho_k r_k^2}(\overline{W_g}-W_k) \tag{2.49}$$

Where the subscript g denotes the gas phase, r_k denotes the radius of the k^{th} droplet and Re_k is the droplet Reynolds number taken with respect to the difference in velocity with the surrounding gas phase:

$$Re_k = 2\frac{r_k \rho_g}{\mu_g}\left[(\overline{U_g}-U_k)^2 + (\overline{V_g}-V_k)^2 + (\overline{W_g}-W_k)^2\right]^{1/2} \tag{2.50}$$

The coefficient of drag is a function of droplet Reynolds number:

$$C_D = \frac{24}{Re_k}\left(1 + \frac{Re_k^{2/3}}{6}\right) \tag{2.51}$$

Molecular viscosity is evaluated by Sutherlands's equation:

$$\mu_g(T) = 1.4637x10^{-6}\frac{T^{3/2}}{T+120} \tag{2.52}$$

A reference temperature is used for calculation of viscosity in the vicinity of the droplet:

$$T_{ref} = \frac{1}{3}T_g + \frac{2}{3}T_{ks} \tag{2.53}$$

where the subscript s refers to the droplet surface.

The droplet regression rate is a composite function of droplet Reynolds number, Re_k. Three ranges are used to approximate the function:

$$\frac{d(r^2)}{dt} = -2\frac{\mu_l}{\rho_k}\left[\frac{2}{\pi}Re_k\right]^{1/2} f(B_k)\,, \qquad Re_k>20 \tag{2.54a}$$

$$\frac{d(r^2)}{dt} = \frac{\mu_l}{\rho_k}\left[1+(1+Re_k)^{1/3}\right]Re_k^{.077}\ln(1+B_k)\,, \qquad 1<Re_k<1 \tag{2.54b}$$

$$\frac{d(r^2)}{dt} = \frac{\mu_l}{\rho_k}\left[1+(1+Re_k)^{1/3}\right]\ln(1+B_k)\,, \qquad Re_k<1 \tag{2.54c}$$

where B_k is the Spaulding transfer number. The function

$f(B_k)$ is obtained from the solution of Emmon's problem.

The internal droplet temperature is calculated from:

$$\frac{\partial T_k}{\partial t} = 17\frac{k_l}{C_{pl}\rho_l r_k^2}\left[\alpha\frac{\partial^2 T_k}{\partial \alpha^2} + (1+C(t)\alpha)\frac{\partial T_k}{\partial \alpha}\right] \tag{2.55}$$

where k_l refers to thermal conductivity in the droplet or liquid phase, and $C(t)$ is given by:

$$C(t) = \frac{3}{17}\left[\frac{C_{pl}\rho_l}{k_l}\right] r_k \frac{dr_k}{dt} \tag{2.56}$$

α represents the streamline of a Hill's Vortex in the droplet. The boundary conditions for the droplet temperature are:

$$\frac{\partial T_k}{\partial \alpha} = \frac{1}{17}\left[\frac{C_{pl}\rho_l}{k_l}\right] r_k^2 \frac{\partial T_K}{\partial t} \qquad \alpha=0 \tag{2.57a}$$

$$\frac{\partial T_k}{\partial \alpha} = -\frac{3}{32}\frac{\rho_k}{k_l}\left[\frac{C_p(T_g-T_{ks})}{B_k} - l_k\right]\frac{d(r^2)}{dt} \qquad \alpha=1 \tag{2.57b}$$

where l_k is the latent heat of vaporization of the fuel. The initial droplet temperature is set to the droplet injection temperature. The Spaulding transfer number is:

$$B_k = \frac{C_p(T_g-T_{ks})}{l_{k,eff}} = \frac{(Y_{fs}-Y_f)}{(1-Y_{fs})} \tag{2.58}$$

$l_{k,eff}$ is the effective latent heat of vaporization modified for heat loss to the droplet interior:

$$l_{k,eff} = l_k + 4\pi \frac{k_l r_k^2}{m_k}\left(\frac{\partial T_k}{\partial r}\right)_s \qquad (2.59)$$

where m_k is the droplet vaporization rate. The fuel mass fraction at the droplet surface is given by:

$$Y_{fs} = \left(1 + \frac{W_a}{W_f}\left(\chi_{fs}^{-1} - 1\right)\right)^{-1} \qquad (2.60)$$

where W_a is the molecular weight of the gas excluding the fuel and χ is the mole fraction which is found by assuming phase equilibrium at the droplet surface, and using the Clausius-Clapeyron relation:

$$\chi_{fs} = \frac{P_n}{P}\exp\left[\frac{l_a}{R_u}\left(\frac{1}{T_b} - \frac{1}{T_{ks}}\right)\right] \qquad (2.61)$$

where P_n is the normal atmospheric pressure, P is the prevailing pressure, l_a is a constant and T_b is the boiling temperature for the droplet. More accurate expressions than the Clausius-Clapeyron relation involving additional parameters can be found in Reid et al.[21]

The spray provides a mass source term in the continuity equation. The droplets also affect the momentum equations through drag forces. Thus, appropriate source terms must be included in the gas-phase equations. The source terms are listed in Appendix 2.

Chapter 3

NUMERICAL SIMULATION OF COMBUSTION

The field of combustion demands knowledge in computational fluid dynamics, turbulence modeling, chemical kinetics modeling of combustion, real gas effects, combustor concepts and turbulent-chemistry effects. A variety of combustion models exist. Combustion models cannot be implemented as easily as changing damping coefficients for a turbulence model. Many of these turbulent combustion models are application specific, that is, the combustion model was developed for a specific combustion regime. The combustion regime is decided by the length scale of combustion, which is dependent on the rates of mixing and the rates of chemical reactions. Much combustion model development of late has involved combustion for jet flames where the combustion scale is of the order of the smallest scales of turbulence. The chemical reaction rate is very fast compared to the mixing rate. Unfortunately, combustion is distributed in practical combustors due to the use of slower reacting, more complex fuels and high turbulence levels.

The expertise in computational combustion is divided into two main groups. One group very closely models thermodynamic and transport properties. Turbulence is generally ignored by this group. If there is transport, it is laminar, and species diffusive velocities, viscosities, etc. are precisely modeled. Equilibrium, partial equilibrium, or complete system of chemical reactions may be solved. Equilibrium assumes infinite time for chemical reaction. Species concentrations do not change after reaching equilibrium. Reactions are still proceeding, but, forward reactions are perfectly balanced by reverse reactions. The final chemical species for equilibrium combustion calculations are found by minimizing the Helmholtz or Gibb's free energy depending on whether it is a constant-volume or constant-pressure process. Finite rate combustion involves time stepping through a large number of ordinary differential equations, which are usually stiff. Small time steps must be used to retain numerical stability. The combustion process is viewed as a collection of a number of elementary reactions involving likely combinations of reacting species. Each of these elementary reaction steps has its own constants for activation energy, pre-exponential constant, the species concentration dependence and possibly some extra temperature dependence. Many of these elementary reactions are reversible and many of the species are in numerous competing chemical reactions. Some reaction rate constants may be calibrated using shock tube experiments. Other reactions are currently unknown, so combustion rates are inferred. When the kinetic scheme duplicates shock-tube data over a range of conditions the scheme is said to be accurate or validated. Not too surprisingly, there are multiple schemes which have been semi-validated for the combustion of simple fuels. Improving the accuracy of the model is done by adding more reactions, which increases the applicability of the kinetic combustion model over wider temperature, pressure and species concentration ranges. There are multiple competing paths in which fuel and oxidant are burned. The influence of these competing reaction paths is highly affected by temperature. At different temperature ranges, different reaction paths can take precedence. Including multiple reaction paths extends the validity of the kinetic model. The current state of chemical kinetic modeling is that the combustion of hydrogen and some of the lower hydrocarbons is quite accurate. Laminar flame speed and heat release are well predicted for the very simple fuels. The kinetic combustion modeling of heavier fuels used in practical combustors, such as kerosene, is still in a development stage. Kinetic modelers will not advocate combustion schemes for heavier fuels until the combustion models for the lighter fuels are sufficiently validated, as the heavier fuels break down into lighter fuels and other intermediate species during the combustion process.

The fine degree of kinetics combustion modeling does not lend itself to calculation of multi-dimensional turbulent combustion flow. They are simply too computationally expensive. Thus, the implementation of kinetic reaction submodels into multi-dimensional CFD models has only involved hydrogen or methane with no turbulent-chemistry interaction. That is, mean quantities are used in the reaction rates, there is no turbulence correction. Currently, the solution of species transport for recirculating flows using CFD is such that the calculation of individual species without chemical reaction is inaccurate. That is, the transport of one species can easily be off by over ten percent, a level of accuracy CFD calculations should meet to have predictive validity in the design of low-emission combustors. Designers would like to be able to predict within a few percent. Various combustion models have been implemented to predict combustor flows in a reasonable time.

3.1 - Infinite Rate Combustion Models

The simplest CFD combustion model is the fast or infinite rate reaction model. This type of scheme does a good job of predicting the exit temperature profiles of combustors. In this scheme, once the fuel and oxidant are mixed, the reaction rate is such that the reactants are immediately converted to products. The reactants are consumed in strict proportions. A simple example is the stoichiometric burning of methane. The reaction is referred to as stoichiometric as it assumes stoichiometric burning of

$$CH_4 + 2\ O_2 \rightarrow CO_2 + 2\ H_2O$$

the fuel and oxidant. One molecule of methane is consumed with two oxygen molecules to produce one molecule of carbon dioxide and two of water. In units of mass 16 Kg of fuel react with 64 Kg of oxygen. Four Kg of oxygen react with each Kg of methane. The reaction rate source terms are related.

$$R_{fu} = R_{ox}/4 \tag{3.1}$$

Using the general transport equation for species, equations may be written for the mass fractions of oxygen and fuel. Subtracting a constant specific portion of the transport equation of oxidant to that of fuel eliminates the chemical reaction source term, leaving a conserved scalar. Using a conserved scalar eliminates calculating troublesome reaction rates. In the previous example, if we form a variable composed of the fuel mass fraction minus one quarter of mass fraction of oxygen the troublesome reaction rate term is eliminated. The general equation for this conserved scalar is:

$$f = Y_F - (F/O)_{st} Y_O \tag{3.2}$$

The term $(F/O)_{st}$ is the fuel to oxidant molecular weight ratio for stoichiometric burning process. Other conserved variables could be formed. Another popular conserved variable is the sum of all fuel fractions, both unreacted and reacted. This conserved variable is often referred to as the mixture fraction. The solution of the conserved variable defined in (3.2) gives the fuel and oxidant mass fractions. If the conserved variable is positive, the fuel mass fraction is the same as the conserved variable, and the mass fraction of oxygen is zero. If the conserved variable is negative, the fuel mass fraction is zero and the mass fraction of oxygen is 4 times the negative of the mixture fraction. The sum of the mass fractions of all species is one so the mass fraction of products is simply:

$$Y_{pr} = 1.0 - Y_F - Y_O \tag{3.3}$$

An atom balance is done to figure the individual product species fractions. If the oxidant is air, the above equations must be slightly modified to include nitrogen. In this infinite rate combustion model, the width of the reaction zone is zero. Combustion occurs in a flame sheet. There is no overlap of oxidant and fuel. Fuel exists on one side of the combustion sheet, and oxygen on the other.

An enthalpy equation is solved from which temperature can be found from the various mass fractions. Radiation is typically ignored as research combustors are usually operated at lower temperatures and pressures. The equation of state is used to solve for density:

$$\rho = PM/R_u T \tag{3.4}$$

The equation uses the universal gas constant and the mixture molecular weight (inverse of sum of number of moles of each species divided by each species molecular weight). The mixture molecular weight in terms of mass fractions is:

$$M = \left(\frac{m_{ox}}{M_{ox}} + \frac{m_{fu}}{M_{fu}} + \frac{m_{pr}}{M_{pr}} \right)^{-1} \tag{3.5}$$

Various improvements can be included, such as allowing for variable specific heat with temperature. As specific heat increases with temperature, this change alone can improve the prediction of temperature by a couple of hundred degrees. The use of infinite reaction rates is known to give good predictions of exit combustor temperature profiles, and major species concentrations. Partially reacted species or nitrous oxides are not predicted by infinite rate combustion models. Rather than assume complete chemical reaction, equilibrium combustion can be modeled. At equilibrium the species concentrations are fixed, but, the rate of forward chemical reaction is just balanced by the rate of back or reverse chemical reaction. Equilibrium modeling allows for the presence of minor chemical species, allows reactant species to overlap and a broadening of the reaction zone width. Carbon monoxide is usually overpredicted with rich fuel mixtures. Equilibrium combustion models significantly overpredict chemical reaction and product species at low temperature. Formation of some species such as nitrous oxide is a function of time. The equilibrium model does a very poor job of predicting nitrous oxides.

One model that allows for overlap of reactant species at low temperature is the finite rate combustion model.

3.2 - Finite Rate Combustion Models

Finite rate combustion means that fuel and oxidant can co-existing at the same time. A conserved scalar is still conserved in finite rate combustion modeling, but, the concentration of fuel or oxidant cannot be solely obtained from the conserved variable as before. An additional equation must be solved for that includes a finite rate reaction source term. The calculation of the finite rate reaction term is usually based on arrhenius reaction rates. Arrhenius was the first to include the Boltzmann factor into chemical reaction rates. At room temperature oxygen and hydrogen can co-exist with no reaction. Energy must be supplied to begin the combustion process. Arrhenius postulated that collisions between fuel and oxidant do not automatically produce combustion. The collision between molecules must be strong enough that an energy barrier is overcome. The Boltzmann factor takes this into account. The equation:

$$k = \exp\left(-\frac{E_a}{R_u T}\right) \tag{3.6}$$

is called Arrhenius law. A typical Arrhenius reaction rate may look like

$$\frac{dC_{fu}}{dt} = -A\left(C_{fu}\right)^a \left(C_{ox}\right)^b \exp\left(\frac{-E_a}{R_u T}\right) \tag{3.7}$$

where C is the molar concentration. By employing the perfect gas law, the expression may be algebraically manipulated to use mass fractions which is more commonly used in CFD. A is the frequency number to take into account the collisions between molecules. Sometimes a dependency on temperature to some power is also included. For fundamental or elementary chemical reactions, the exponents *a* and *b* are whole numbers from the molar coefficients in the chemical reaction equation. Fundamental chemical equations are reactions that actually occur. The combustion of hydrogen with oxygen is globally represented by:

$$H_2 + 1/2\ O_2 \rightarrow H_2O$$

The actual combustion process occurs as a series of reactions of which only a few are:

$$OH + H_2 \rightarrow H_2O + H$$

$$H + O_2 \rightarrow OH + O$$

$$O + H_2 \rightarrow OH + H$$

$$OH + OH + M \rightarrow O + H_2O$$

$$OH + HO_2 \rightarrow O_2 + H_2O$$

$$H + O_2 + M \rightarrow M + HO_2$$

There are numerous elementary reactions to get the final product, H_2O. In the process there are many reaction radicals which are also in many elementary competing reactions. To further complicate things, the intermediate species, H_2O_2, is also important. R.J. Kumar[22], and S. W. Kim[23] have successfully used a set of 24 elementary reactions involving 9 species to predict hydrogen-oxygen combustion. This set of elementary reactions was reduced from a set of 48. At different temperature ranges different reaction paths take dominance. There is wide disparity in the reaction rates which causes great difficulty in their solution. Some kinetic reaction schemes are validated by duplicating calculated flame structure, laminar flame speeds, and chemical composition using large numbers of fundamental reactions. Computational models used to do this are one-dimensional, include modeling of individual species laminar diffusion velocities and use very small time steps.

In multi-dimensional recirculating flow global reaction models are typically used. The global reaction models are only calibrated over limited temperature, species concentration and pressure ranges. In a 1972 paper, Dryer and Glassman[24] used a temperature range of 1030 to 1230 K for oxidation of carbon monoxide and methane. The most often cited global reaction schemes are from Westbrook and Dryer[25]. The reaction schemes were designed to capture rich and lean flammability limits, information on flame temperature and burned gas composition and flame speed. They do not accurately describe the chemical structure of the flame. Different models can produce different results with the same reaction numbers. Coffee[26] recommends higher frequency numbers as his results were slightly different than Westbrook and Dryer's, unless he adjusted the reaction numbers. There is further controversy in regards as to what phenomena should have primary importance in modeling. Coffee[27], in another report, states that heat release should be used to calibrate reaction numbers, not the criteria used by Westbrook and Dryer. The frequency number given in this paper is orders of magnitude higher.

If one wants to calculate intermediate species such as carbon monoxide, at least one additional equation must be solved. Nikjooy et al.[28] gives an example with the variables and source terms. A four step scheme has been used by Srivatsa[29]. This scheme is from Hautman et al.[30] and allows for additional species of Hydrogen and ethylene. This scheme includes product concentration in the reaction rates. The scheme was validated over 960 to 1540 K for propane.

An early study of global reaction schemes was done by Abdalla et al.[31] One conclusion was that "inaccuracies could arise from the unrealistic simplification of chemical kinetics and the variable effects of turbulence". Duterque et al.[32] also came up with a global scheme for methane, propane, benzene and isoctane validated for a well-stirred reactor model. The authors stated that the model could be used in the predictions of burners and combustors.

In a more recent paper, Westbrook and Dryer[33] discuss detailed kinetic modeling for various hydrocarbon fuels along with a short section on global modeling. They note that using a single reaction scheme leads to overprediction of products and temperature. In 1986, Paczko et al.[34] gave a four-step reaction mechanism for methane and a five step reaction mechanism for propane. The propane mechanism includes two reactions for the initial break up of propane. A three-step mechanism is recommended by Seshadri and Peters[35] for stoichiometric methane-air flames. The mechanism was tested for a counterflow diffusion flame. In 1987, Kiehne et al.[36] discuss an improved eight-step mechanism for propane. The model is based on the original work of Hautman et al. The model better predicts ignition delay and combustion at higher pressures. In 1988, Jones and Lindstedt[37] proposed a four-step global mechanism for the combustion of alkane hydrocarbons up to butane. The scheme was tested on methane and propane flames, along with diffusion flame data for a methane-air flame. Good agreement was predicted for flame speed, flame thickness, and species profiles. Bilger and Starner[38] constructed a four-step mechanism from a set of 58 elementary reactions. The model uses steady-state approximation for the oxygen atom rather than a partial-equilibrium approximation. The mechanism was used to predict flame structure for the counterflow diffusion flame. Good predictions were obtained for minor species over a range of flame stretch.

Some of these schemes involve the implementation of source terms for calculating product species. This researcher found problems when calculating product species for multi-dimensional recirculating flows. The frequency numbers used in arrhenius rates are fairly large. At higher temperatures, arrhenius reaction rates can predict rapid reaction even though reactant concentrations are quite low. The arrhenius reaction rate is only accurate for an extremely short time step, not the typical time steps used in implicit calculations. Thus, product concentrations can be overpredicted at high temperatures. Most often, overpredicted concentrations are simply overwritten during the iteration process.

3.3 - Turbulent Combustion

All practical gas turbine combustors operate in the turbulent regime. Thorough mixing and burning must occur within rather short axial distances in current gas turbine combustors. Turbulence for chemical species means that there is variation with time in the chemical species and temperature. A consequence of this is that even with infinite reaction rates, fuel and oxidant can exist at the same location, but, not at the same time. Where this occurs, the time averaged concentration of fuel and oxidant will not be zero. Many different turbulent combustion models have been worked on in the last two and a half decades. Many of these models do well within the range of their assumptions.

3.3.1 - Eddy Break Up Combustion Models

One of the earliest turbulent combustion models is the eddy-breakup model proposed by Spaulding[39]. The original application for the model was for premixed combustion. It was observed that changes in velocity and fuel to air ratio had little affect on combustion in premixed combustors. The use of so-called laminar arrhenius reaction rate combustion models didn't predict this. The controlling mechanism wasn't temperature related, but, was controlled by mixing rates. In the eddy-breakup model combustion is viewed as a mixture of burned and unburned eddies. The combustion process is controlled by the mixing and exchange of energy from burned eddies to neighboring unburned eddies. The eddies are stretched and folded around each other until local gradients are strong enough that mixing occurs. This is very similar to the cascade of turbulent kinetic energy from large eddies to smallest eddies where the energy is finally dissipated. It was further proposed that combustion was also proportional to reactant concentration. If oxygen concentration was low, as if most of the oxygen were already consumed, the reaction rate should be lower. The initial combustion model did a good job of qualitatively predicting the correct hydrodynamic phenomena for premixed combustors. The eddy-breakup model was modified over the next few years.

In another paper[40], it was proposed that reaction rates should be proportional to the concentration fluctuation not the reactant concentration. An equation for concentration fluctuation was proposed and successfully tested for a turbulent jet. In another paper, Mason and Spaulding[41] tested the combustion model. From a later review[42], it was reported that the improved more physically realistic model predictions were worse than previous modeling. In 1976, Magnussen and Hjertager[43] proposed an another eddy-breakup model where the reaction term was proportional to the minimum of related constants times appropriate fuel, oxidant, or product concentration. The model performed well results, but, the constants had to be increased for a different case. Isothermal turbulence modeling was also developing. The k-ε turbulence model was developed and has proven successful. Using the k-ε turbulence model, the form of Spaulding's eddy-breakup model is:

$$\overline{S_p} = C_{EBU}\frac{\varepsilon}{k}\sqrt{\overline{Y_F'^2}} \tag{3.8}$$

A measure of the rate of eddy breakdown is the reciprocal of eddy lifetime. A measure of eddy-lifetime is the ratio of turbulent energy, k, over the dissipation rate, ε.

The eddy-breakup rate was developed for premixed combustors but has been applied to other combustors. In work at Garrett research[44] the eddy-breakup model was combined with an Arrhenius type reaction rate. The reaction rate was taken as the minimum of the Arrhenius rate or the eddy-breakup rate. Multiple step chemical reactions were also implemented. The combination of eddy-breakup model and arrhenius model is easy to implement. The model was superior to earlier models.

3.3.2 - Probability Density Function Models

The eddy-breakup model has been long regarded as a semi-empirical combustion model, even though it has proven successful. In turbulence modeling, the current thought is to include as much of the physical process as possible to improve the models. Thus, there has been great effort to model various turbulent terms in the averaged Naviar Stokes equations for chemical species. One method is to incorporate a correction factor for turbulence which can be applied to the laminar Arrhenius reaction rate. Employing Reynolds decomposition and the perfect gas law, a typical turbulent reaction rate may look like:

$$\omega_{fu} = \frac{-BP^2}{R_u^2(\overline{T}+T')^2}(\overline{Y}_{fu}+Y'_{fu})(\overline{Y}_{ox}+Y'_{ox})\exp\left(\frac{-E_a}{R_u(\overline{T}+T')}\right) \tag{3.9}$$

Using $T_a = E_a/R_u$ and some algebraic manipulation, the exponential part of the above expression is:

$$\exp\left(\frac{-T_a}{\overline{T}+T'}\right) = \exp\left(\frac{-T_a}{\overline{T}}\right)\exp\left(\frac{T_a}{\overline{T}}\frac{T'/\overline{T}}{1+T'/\overline{T}}\right) \tag{3.10}$$

The second exponential may be expanded in an infinite series. This infinite series is only convergent if T_a is not large compared to the averaged temperature and if the variation in temperature is not large compared to the averaged temperature. This is not probable in practical combustors. An additional problem with this method is modeling the correlation term $Y'_{fu}Y'_{ox}$. One way around the reaction rate closure problem is to treat turbulent reacting flow as a stochastic process[45]. That is, the solution of average scalar quantities involves the weighting of the scalar with the probability of the scalar.

$$1 = \int_0^1 P(f)\,df \tag{3.11}$$

$$\overline{Y_i} = \int_0^1 Y_i(f)\,P(f)\,df \tag{3.12}$$

Here it is implicitly understood that the probability density function is also a function of time and position. The first stochastic methods used in multi-dimensional turbulent combustor flow involved the use of two-parameter probability density functions. The pdf is completely specified by two parameters, the mean and variance of a conserved scalar. These are referred to as the first and second moments.

One of the basic assumptions of this model is that the reaction is very fast or near equilibrium. This allows the use of a single variable, mixture fraction, to specify the mixture. Physically, the fast reaction assumption means there is little or no overlap of reactant species at any instance in time. The incorporation of stochastic modeling of turbulence allows the overlap of reactant species over time. Much like the eddy-breakup model, reactants occur in separate parcels. Over time these parcels move around so that the time average of reactant concentrations overlap. This occurs with mixtures near stoichiometric conditions causing a broadening of the reaction zone. As actual gas turbine combustion zones are distributed, this modeling better portrays actual combustion.

Typical two parameter probability density functions are rectangular or battlement pdf, Gaussian pdf, clipped Gaussian pdf and Beta pdf. Initially, rectangular or battlement probability density functions were used due to their simplicity. Gaussian pdf's are more appropriate in highly turbulent flows, but, are more complicated to calculate. Gaussian pdf's are determined by their mode or most probable value and standard deviation, not the mean and variance which is found by solving their CFD transport equations. There is no direct way of solving for the Gaussian pdf from the scalar mean and variance. The pdf must be specified so that other scalar averages, such as temperature and density can be solved. The most efficient way of solving for the Gaussian pdf is to construct a table lookup of mode and standard deviation versus mean and variance. Thus, when the mean and variance of conserved scalar are found during the iterative process, an interpolation of the table is done to find mode and standard deviation which specifies the gaussian pdf.

One problem with Gaussian pdf's is the tails which extend to infinity. These tails can correspond to physically impossible states. The clipped gaussian was developed to take care of this. Delta functions are added to take the place of clipped tails. The solution of clipped gaussian pdf's is slightly more difficult. A pdf which resembles the gaussian pdf is the Beta pdf, which was proposed by Richardson[46]. The Beta pdf has been successfully used by a number of researchers[47]. Unlike the Gaussian pdf, the Beta pdf can be directly calculated from the mean and variance.

The conserved variable or mixture fraction is typically non-dimensionalized for calculations. The mixture fractions at the fuel and oxidant inlet streams represent the range of mixture fraction in the combustor.

$$\theta = \frac{[Y_F - (F/O)_{st}Y_O]_M - [Y_F - (F/O)_{st}Y_O]_A}{[Y_F - (F/O)_{st}Y_O]_F - [Y_F - (F/O)_{st}Y_O]_A} \qquad (3.13)$$

The mean mixture fraction is found by solving the averaged equation for the mixture fraction. The variance of mixture fraction is often referred to as g:

$$g = \widetilde{\theta''^2} = \int_0^1 (\theta-\tilde{\theta})^2 Pr(\theta)\, d\theta \tag{3.14}$$

where the overbar refers to Favre or density averaging rather than the normal time averaging. A modeled transport equation is solved for the local variance. The formula for beta pdf is:

$$F(x) = \frac{\Gamma(a+b)}{\Gamma(a)\Gamma(b)} x^{a-1}(1-x)^{b-1} \quad \begin{array}{l} where\ 0 \le x \le 1, \\ and\ a>0,\ b>0 \end{array} \tag{3.15}$$

the formulas to find a and b from mean and variance are:

$$a = \bar{\theta}\left[\frac{\bar{\theta}(1-\bar{\theta})}{g} - 1\right], \tag{3.16}$$

$$b = \frac{a(1-\theta)}{\theta} \tag{3.17}$$

The major limitation of this method is that computed mixtures are close to equilibrium. Equilibrium assumptions tend to overpredict CO concentrations. Another choice in combustion models is the laminar flamelet model. In reviewing experimental work done by Tsuji and Yamoka[48], Bilger[49] noticed that measurements of temperature and species concentration, including CO appeared to be functions of mixture fraction for laminar diffusion flames despite differing shear rates and positions. That is, there exists a state relationship to the mixture fraction. Thus, a table of species concentration and temperature versus mixture fraction can be constructed from the experimental data. This is very useful in computations as the table can be used to find thermodynamic quantities during the iteration process. This eliminates calculating reaction rates and enthalpy. Instead of assuming infinite rate or chemical equilibrium, actual experimental data is incorporated into numerical predictions. Jeng[50] used this in his thesis to perform buoyant free jet combustion calculations using the GENMIX[51] computer program. Jeng also modified an equilibrium program to check the experimental concentration data. The program was modified for rich combustion. Very high carbon monoxide concentrations were predicted, characteristic of high equivalence ratio equilibrium combustion calculations.

This thermochemical alternative to chemical equilibrium was further developed into the flamelet model by Liew et al.[52] In this model, reaction rates are very high compared to the mixing rate. An instantaneous snapshot of the combustion process would show a flame with finite thickness or a flame sheet. The interaction of turbulence with this flame surface involves movement and wrinkling of the flame surface. In a geometrically similar type combustor, laminar diffusion flame data is measured. These data are then used to provide unique thermochemical relationships solely as a function of mixture fraction. These relationships are then coupled with an assumed shape pdf to account for turbulence interaction with combustion. The actual flame is viewed as an ensemble of laminar diffusion flames. This method has produced substantial improvements in prediction in fuel-rich regions of an open combustor, particularly in CO concentration.

The laminar diffusion flamelet idea was further developed by Liew and Bray[53] for highly stretched combustion. It was found that if flames were substantially stretched, the state relationship between thermochemical values and conserved scalar was affected. As the flame is stretched or instantaneous scalar dissipation is substantially increased, it was noticed that temperature decreased. Also, the mixture fraction at which maximum temperature occurs, increases with increasing stretch. The region surrounding this maximum temperature is the region of greatest chemical reaction. Beyond a certain level of flame stretch, the imbalance between local heat loss, local active species loss, and smaller heat production due to flame stretch leads to flame quenching or blowoff. The thermochemical or state relationships now involve two variables, mixture fraction and flame stretch or average instantaneous scalar dissipation. Conceptually, a library of flames is measured or calculated as a function of two variables. Turbulence effects are still handled by an assumed shape pdf. However, the pdf is now a function of two variables, it is a joint pdf. The shape of joint probability density functions are much more difficult to deduce. The simplest joint pdf is to assume that the two variables are completely independent. That is, the joint pdf is a product of pdf for mixture fraction and another pdf for scalar dissipation. Liew and Bray used a Beta pdf for mixture fraction. They assumed that the pdf for scalar dissipation was log-normally distributed at high Reynolds number. Equations are then formed for the Favre average scalar dissipation and other quantities needed to specify the pdf for scalar dissipation. This model allows the prediction of oxygen penetration into fuel jets where there is large strain. The chemistry is laminar and can be calculated very accurately. Drake and Blint[54] found that finite rate kinetics have an important effect on flame structure. The use of partial equilibrium modeling for carbon monoxide concentration in low temperature fuel-rich flames was shown to be inadequate. The local effects of flame stretching correspond to a turbulent ensemble to average the flamelet characteristics.

Flamelet models are based on a one-dimensional approximation of the flame. The curvatures of the various flamelets are neglected. Coherent vortices which are present in many mixing layers are neglected. Borghi[55], in his review of turbulent combustion modeling, states that flamelet modeling should be confined to cases where the chemistry is very fast and the Reynolds number is not too large. Peters[56] did a review of the laminar flamelet approach which describes the method more fully. The method is an attractive way of treating the prediction of minor species in turbulent flow calculations at reasonable computer costs.

Janika and Kollman[57] used a two-variable pdf scheme in their studies of turbulent H_2-air flames. The two pdf variables are mixture fraction and reaction completeness. This method assumes partial equilibrium for its H_2/air chemistry. The kinetic mechanism selected consists of fast shuffle reactions which are considered to be in partial equilibrium:

$$H + O_2 \rightleftharpoons OH + O \tag{R1}$$

$$O + H_2 \rightleftharpoons OH + H \tag{R2}$$

$$H_2 + OH \rightleftharpoons H_2O + H \tag{R3}$$

$$2OH \rightleftharpoons H_2O + O \tag{R4}$$

and slow three-body recombination reactions.

$$H + OH + M \rightarrow H_2O + M \tag{R5}$$

$$H + O + M \rightarrow OH + M \tag{R6}$$

$$H + H + M \rightarrow H_2 + M \tag{R7}$$

The authors stated that the partial equilibrium scheme was not good below 1200 K. To reduce the number of variables, combined variables are used. This was proposed by Dixon-Lewis et al.[58]. The combined variable for hydrogen is:

$$C_{H_2}^{*} = C_{H_2} + \frac{1}{2}\frac{M_{H_2}}{M_{OH}}C_{OH} + \frac{M_{H_2}}{M_O}C_O + \frac{3}{2}\frac{M_{H_2}}{M_H}C_H \tag{3.18}$$

The reaction rate for the combined variable is independent of the fast shuffle reactions (R1-R4). The source terms for the hydrogen combined variable are:

$$\omega_{H_2}^{*} = -M_{H_2}(2\omega_5 + 2\omega_6 + 2\omega_7) \tag{3.19}$$

The combined variable varies between its unburned and equilibrium values. Thus, a nondimensional reaction progress variable is:

$$\eta \equiv \frac{C_{H_2}^{*} - C_{H_2}^{*^u}}{C_{H_2}^{*^{eq}} - C_{H_2}^{*^u}} \tag{3.20}$$

Transport equations are used to solve for mixture fraction and reaction progress variable. The solution of enthalpy, mixture fraction, and reaction progress variable, coupled with partial equilibrium relations completely specifies the instantaneous thermochemical state. Turbulence is handled by a combination of assumed shape probability density functions. The mixture fraction and combined variable are assumed uncorrelated so that the joint pdf is the product of the pdf of mixture fraction and another pdf for the reaction progress variable. Transport equations for the mean and variance of the mixture fraction and progress variable are solved. The transport equation for mean reaction progress variable must include a reaction term for the recombination reactions. A beta pdf can be used for the mixture fraction. Three dirac delta functions can be used for the pdf progress variable pdf corresponding to unburned, equilibrium and mean of the reaction progress variable:

$$P(\eta) = c_1\delta(\eta) + c_2\delta(\eta-\overline{\eta}) + c_3\delta(\eta-1) \tag{3.21}$$

The coefficients of the dirac delta terms are determined from simple functions of the mean and variance of the progress variable. From Janika and Kollman's[59] 1982 paper:

$$c_1 = \frac{\overline{\eta''^2}}{\overline{\eta}}; \tag{3.22a}$$

$$c_2 = 1 - \frac{\overline{\eta''^2}}{\overline{\eta}(1-\overline{\eta})}; \tag{3.22b}$$

$$c_3 = \frac{\overline{\eta''^2}}{1 - \overline{\eta}} \tag{3.22c}$$

where favre averaging is actually used.

The scheme was used to calculate the jet diffusion flame of Kent and Bilger[60]. The reaction progress variable varied between 0.88 and 1.0 across the calculation at x/D of 20. The progress values increased further downstream. Janika and Kollman state that the more elaborate modeling used in the calculation didn't significantly improve prediction of stable components and temperature. However, the modeling did considerably help in the prediction of monatomic oxygen and reasonable NO concentrations.

Correa et al.[61] include a couple of CO reactions in the above scheme for calculation of CO/H_2/-air turbulent diffusion jet flame. The calculation method successfully predicted experimental measurements of superequilibrium concentrations of OH. A year later, Correa[62] published another paper where a progress variable was added for CO concentration. The partial equilibrium equations used in the above models are only valid above at least 1200 K. The correlation assumptions made about joint probability density functions is questionable. Pope and Correa[63] found that joint pdf of velocity, conserved scalar and reaction progress variable were correlated. The kinetics models for higher molecular weight fuels are much more complicated. Including additional variables into the joint pdf for breakup of the heavier fuels into lighter components is even more questionable and untested. Borghi in his 1988 review paper generates partial pdf shapes for some situations. At best, these shapes only qualitatively resemble Gaussian like profiles. The next step in turbulent combustion calculations is to actually remove some of the assumptions.

Some recent papers were written about the current status of Combustion modeling. This include Hukam Mongia's paper[64] which covers some of the calculations done at the

Allison Gas Turbine Division of General Motors Corp. Correa and Shyy [8] covers the combustion modeling effort done at General Electric's Corporate Research and Development Center. Much of this effort was to develop their CONCERT code. There are also quite a few texts on combustion which include: Kuo's[65] text on the principles of combustion, Williams'[66] reference on combustion theory, Bartok and Sarofim's[67] book on fossil fuel combustion, Chigier's[68] reference on energy, combustion and environment, and Oran and Boris'[69] reference on CFD simulation of reactive flow.

Chapter 4

HYBRID COMPOSITION PDF SOLVER

Many assumptions have been made in developing the previous assumed shape pdf models. Implicit in those assumptions was that chemistry is very fast. Even correcting this by using partial equilibrium solutions for jet flames is only valid at higher temperatures and thus, a high degree of reactedness. Another assumption was the shape of the pdf. The focus of this work will be to further develop and test a pdf method which does not make these assumptions.

For this work, the pdf is initially assumed to be a function of time, position, temperature or enthalpy, and multiple species concentration. This is referred to a composition joint pdf. The pdf is called joint because the pdf is a function of more than one variable. The hybrid composition pdf uses traditional CFD techniques to obtain solutions of velocity, pressure, turbulence kinetic energy and dissipation. The composition pdf handles the solution of species concentration and temperature. The hybrid composition pdf solution is thus a combination of traditional CFD methods and stochastic modeling. If the pdf is assumed to be also a function of velocity, the solution method is vastly different from traditional CFD techniques. Thus, the composition pdf represents a good intermediate step to complete pdf modeling, which is in its infancy. In

1989 Anand et al.[70] used the joint velocity pdf method to calculate the turbulent flow behind a backward facing step. In this calculation only the pressure field was needed from another solver. Preliminary work is being done to calculate all quantities, including pressure in the pdf solver. In 1993, Anand, Pope and Mongia presented predictions for a swirling flow. The method did not incorporate a radial dependence for pressure, although an externally imposed pressure gradient could be incorporated into the equations. The mean swirl number for the flow was reported to be 0.09.

As it has been shown that turbulent combustion models are rather simplistic and full stochastic methods are not developed, the hybrid pdf represents an excellent testbed for testing predictions of turbulence effects on combustion.

Various pdf transport equations can be written. One form for the composition pdf is:

$$\bar{\rho}\partial_t\tilde{P} + \bar{\rho}\tilde{U}_\alpha\partial_\alpha\tilde{P} + \bar{\rho}\sum_{i=1}^{N}\partial_{\psi_i}[\omega_i(\psi_1,\ldots,\psi_N)\tilde{P}] = \tag{4.1}$$

$$- \partial_\alpha(\bar{\rho}\langle u''_\alpha|\phi_k(x)=\psi_k\rangle\tilde{P}) - \bar{\rho}\sum_{i=1}^{N}\sum_{j=1}^{N}\partial^2_{\psi_i\psi_j}(\langle\epsilon_{ij}|\phi_k(x)=\psi_k\rangle\tilde{P})$$

The terms represent the time rate of change, mean convection, chemical reaction, turbulent convection, and a mixing term, respectively. The symbol over P denotes Favre averaging.

$$\tilde{P} = \rho P/\overline{\rho} \tag{4.2}$$

$\varepsilon_{i,j}$ is the scalar dissipation:

$$\varepsilon_{i,j} = D\partial_\alpha \phi_i \partial_\alpha \phi_j \tag{4.3}$$

where D is the diffusion coefficient. The use of favre or density weighing eliminates some terms in the averaged equation. The notation $\langle x|y\rangle$ denotes the mathematical expectation of a random function x conditioned on y.

Terms on the left side of the pdf evolution equation do not need modeling. That is to say, they don't have additional unknown variables which demand assumptions or relations to produce closure models. The time rate of change and mean convection are seen in traditional CFD modeling. The last term on the left side is the evolution of the pdf in transform space due to chemical reaction. This term does not employ modeling assumptions about various turbulence quantities such as Y_i' and T'. The pdf method can use the laminar kinetic reaction rate modeling. As was mentioned previously, using regular moment methods to solve for chemical reaction produces correlations that have to be calculated or modeled. These correlations correct the laminar chemical reaction rate for turbulence. All of these correlations involve modeling assumptions. The pdf method does not include these assumptions. This is why pdf modeling is promoted as exactly modeling chemical reaction.

The terms on the right side of the pdf evolution equation must be modeled. The turbulent convection term is modeled by gradient diffusion:

$$-\langle v''_\alpha | \psi_k \rangle \tilde{P} = D_t \partial_\alpha \tilde{P}, \tag{4.4}$$

where D_t is the turbulent diffusion coefficient, which is related to the eddy viscosity by the turbulent Schmidt number. The next term that needs modeling is the molecular mixing term. A proper molecular mixing model causes the scalar variance to decrease with time while the mean remains constant. Some molecular mixing models are: the coalescence/dispersion model attributed to Curl[71], modified Curl model of Janicka et al.[72], and the quasi-Gaussian model of Dopazo[73]. The general form of the coalescence/dispersion model is:

$$\bar{\rho}\sum_{i=1}^{n}\sum_{j=1}^{n}\partial^2_{\psi_i\psi_j}(\langle\epsilon_{ij}|\psi_k\rangle\tilde{P}) = \frac{C_D}{\tau}\iint\tilde{P}(\psi')\,\tilde{P}(\psi'')\,T(\psi',\psi''|\psi)\,d\psi' d\psi'' - \hat{P}$$
$$\equiv M(\tilde{P}) \tag{4.5}$$

where T is the probability that particles will undergo a transition in concentration between one particle with concentration of ψ' and another particle with concentration ψ'' to produce two particles with concentrations ψ and $\psi'+\psi''-\psi$ respectively. In Janicka et al.'s paper, a general equation for transition probability is developed using the concentration mixing equations developed by Curl for droplet mixing. Using the simplest approximation, the transition probability is:

$$T(\psi', \psi''|\psi_i) = \begin{cases} \dfrac{1}{(\psi_i'' - \psi_i')} & \text{for} \, \psi_i' \le \psi_i \le \psi_i'' \text{ or } \psi_i'' \le \psi_i \le \psi_i'; \\ 0 & \text{otherwise}, \end{cases} \tag{4.6}$$

This approximation assigns equal transition probabilities for each point in the range ψ' to ψ''. The time scale τ for this process is taken as the integral time scale, $\tau = k/\varepsilon$.

Traditional finite difference techniques are not feasible for solving this pdf evolution equation as the pdf is a function of a large number of variables (five species plus temperature or enthalpy). Instead, a Monte Carlo method will be used to solve for the pdf evolution.

4.1 - The Monte Carlo Solution Method

The Monte Carlo method is easy to implement, even if the number of variables is large. The evolution of the pdf entails the movement of particles in physical space as well as the scalar space (ψ space). The movement of the particles is governed by the pdf evolution equation. The solution to the pdf evolution equation is a finite set of particles or events for each grid cell. The actual pdf is a continuous function. Increasing the number of particles does not result in a continuous solution. Another problem with Monte Carlo is the level of solution accuracy. The ensemble average a solution particle property (species concentration, temperature, enthalpy or density) for a grid cell is an estimate of the true mean since the expected value of the ensemble average is the mean. It can be shown that the solution accuracy is proportional to the square root of the number of particles. Thus to get an order of magnitude increase in accuracy the number of particles must be increased by two orders of magnitude.

Mathematically, the particles for the Monte Carlo pdf are represented by a set of delta functions. The distribution function is the integral of the probability density function. The Monte Carlo distribution function is a sum of heavy-side functions. An example from Pope's 1985 paper[74] is shown in figure 4.1. A Gaussian pdf and a set of 20 normally-distributed random numbers are compared. The mean is 0.5 and the standard deviation is 0.01 for both probability density functions. It can be seen that the Monte Carlo distribution function approximates the continuous distribution function in a step-wise manner. The delta functions are represented by finite spikes. The actual height of the spikes is infinite and the integral of each spike is 1/20.

Using fractional time-steps, the pdf solution is divided into 3 phases. The time derivative is first discretized as:

$$\partial_t \tilde{P} = (\tilde{P}^{n+1} - \tilde{P}^{n})/\Delta t \tag{4.7}$$

then the pdf evolution equation can be written as:

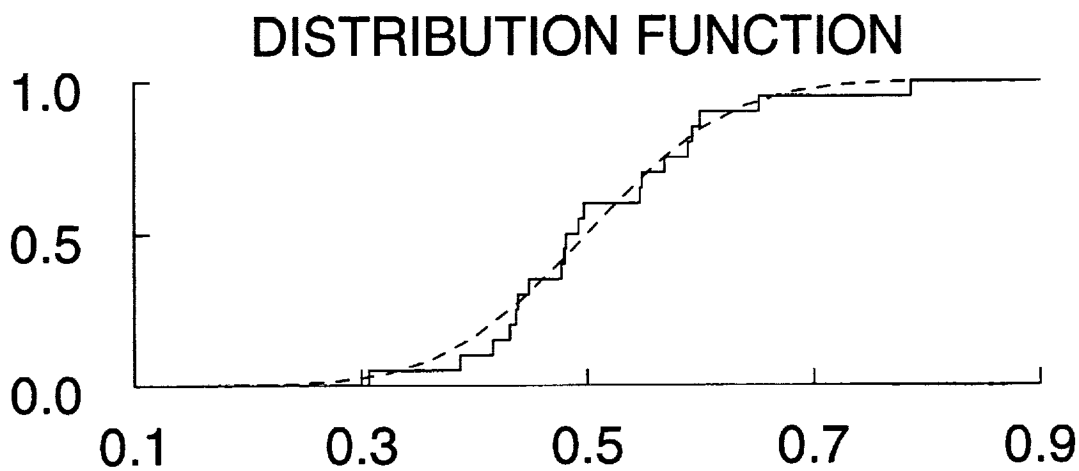

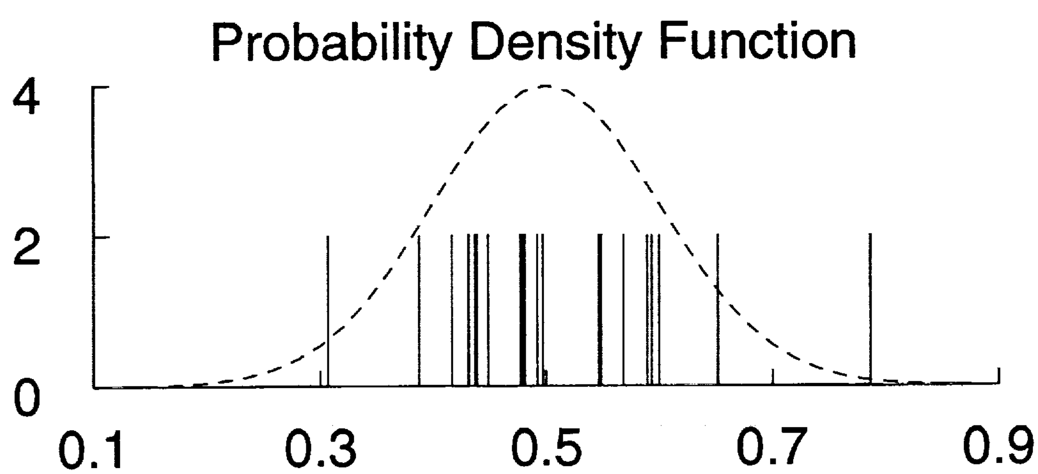

Figure 4.1 Comparison of continuous and discrete pdf's and distribution functions

$$\tilde{P}^{n+1} = [1 - \Delta t\overline{\rho}\tilde{v}_\alpha\partial_\alpha - \Delta t\sum_{i=1}^{m}\partial_{\omega_i}(\psi_1, \ldots, \psi_m) + \Delta t\partial_\alpha D_t\partial_\alpha + \Delta tM]\,\tilde{P}^n \tag{4.8}$$

Using approximate factorization, the above equation is recast as

$$\tilde{P}^{n+1} \cong (1-\Delta t\sum_{i=1}^{m}\partial_{\psi_i}\omega_i(\psi_1, \ldots, \psi_m))\,(1+\Delta tM)\,(1-\Delta t\overline{\rho}\tilde{v}\partial_\alpha+\Delta t\partial_\alpha D_t\partial_\alpha)\,\tilde{P}^n$$

$$\cong (1+\Delta tC)\,(1+\Delta tM)\,(1+\Delta tR)\,\tilde{P}^n \tag{4.9}$$

where C denotes the convection/diffusion operator, M is the molecular mixing, and R is the chemical reactions. Using the above expression the different processes may be performed consecutively:

(1) convection/diffusion between grid cells:

$$\tilde{P}^{*} = (1+\Delta tC)\,\tilde{P}^n, \tag{4.10}$$

(2) molecular mixing within each grid cell:

$$\tilde{P}^{**} = (1+\Delta tM)\,\tilde{P}^{*}, \tag{4.11}$$

(3) chemical reaction in each grid cell:

$$\tilde{P}^{n+1} = (1+\Delta tR)\,\tilde{P}^{**}. \tag{4.12}$$

In the Monte Carlo pdf calculation, each particle has its own species mass fraction and temperature-enthalpy. Each particles has the same mass. Particle position within gridcells is not modeled. In the Monte Carlo simulation a continuous pdf is replaced by N x m delta functions,

$$P^*(\psi_1, \psi_2, \ldots, \psi_m) = \frac{1}{N}\sum_{n=1}^{N} \delta(\psi_1 - \phi_1^{(n)}) \times \delta(\phi_2 - \phi_2^{(n)}) \cdots \delta(\psi_m - \phi_m^{(n)}) \tag{4.13}$$

each product of the m delta functions representing one event of an ensemble of N sample events. The pdf is a function of position and time.

The Monte Carlo pdf formulation/solution is initialized with a SIMPLE method solution. The pdf solution technique could be started with an unconverged flowfield, but, the time needed to get a converged solution would be much higher. Each of the initial particles in a grid cell have identical properties. Inlet particle properties are set to the inlet boundary conditions. The first step in the iteration technique for the pdf solution is calculating the exchange of particles between grid cells by convection and diffusion.

4.1.1 - Convection/Diffusion phase

Replacing the continuous pdf with the Monte Carlo pdf, the convection/diffusion step of the evolution equation can be written as:

$$\bar{\rho}\partial_t P^* + \bar{\rho}\tilde{v}\partial_\alpha P^* = \partial_j (D_t \partial_\alpha P^*) \tag{4.14}$$

re-writing this for the x-y coordinate system:

$$\frac{\partial \rho P^*}{\partial t} + \frac{\partial}{\partial x}\left[\rho U P^* - \Gamma_P \frac{\partial P^*}{\partial x}\right] + \frac{1}{y}\frac{\partial}{\partial y}\left[y\rho V P^* - y\Gamma_P \frac{\partial P^*}{\partial y}\right] = 0 \tag{4.15}$$

The convection/diffusion step does not have any source terms. The SIMPLE scheme solves the transport of species semi-implicitly. That is, very large time steps can be taken. Solution information travels very quickly in this system. The Monte Carlo pdf scheme uses the evolution of particles to calculate scalar properties such as concentration, temperature and density by ensemble averaging. The Monte Carlo scheme does not implicitly calculate particles or particle properties. Particle properties are calculated from existing neighbor particles in time and space. Thus, it is incorrect to use implicit differencing in Monte Carlo simulations. Explicit differencing must be used, which limits the time step that may be taken. It should be obvious that the time step must small enough that any particle does not travel further than one grid cell in any direction. In the SIMPLE scheme the weighing of neighboring grid cell properties is based on coefficients calculated from the convection and diffusion using an implicit formulation. The coefficients used in the Monte Carlo solver must be figured using explicit formulas as the exchange of particles is explicit. For example, assuming 1-D diffusive heat transfer we have as a general formula:

$$a_P T_P = a_E [f T_E + (1-f) T_E^0] + a_W [f T_W + (1-f) T_W^0] + [a_P^0 - (1-f) a_E - (1-f) a_W] T_P^0 \tag{4.16}$$

where

$$a_P = fa_E + fa_W + a_P^0 \tag{4.17}$$

and a_E and a_W are calculated as before. The letter *f* is the weight of implicit differencing. Generalizing this for 2-dimensional convection and diffusion with *f=0* for explicit differencing:

$$a_P\phi_P = a_E\phi_E^0 + a_W\phi_W^0 + a_N\phi_N^0 + a_S\phi_S^0 + [a_P^0 - a_E - a_W - a_N - a_S]\,\phi_P^0 \tag{4.18}$$

where

$$a_P = a_P^0 = \frac{\rho c\,\Delta x\,\Delta y}{\Delta t} \tag{4.19}$$

thus, the time step must be small enough so that the weighing for the previous time step is non-negative (which introduces non-physical solutions). A maximum step is calculated for each iteration by finding the cell with the smallest allowable time step and using that value.

Dividing the above equation by a_p and using the Monte Carlo pdf with *i,j* notation, the convection/diffusion step is:

$$P_{i,j}^{\star} = \alpha P_{i+1,j+1}^0 + \beta P_{i-1,j-1}^0 + \gamma P_{i,j+1}^0 + \delta P_{i,j-1}^0 + \epsilon P_{i,j}^0 \tag{4.20}$$

In this step the new Monte Carlo pdf is made of a fixed number of particles. This is a combination of particles from neighboring cells and the particles from the same cell (particles from the previous time step). The particles from each cell are randomly chosen. Only whole numbers of particles are exchanged. In the conversion from a floating point number into an integer number some fraction is lost. The coding is such that the remainder is added in at random iterations so that the exchange process is more accurate. If the remainder were not randomly added in, it is thought that the iteration process may become cyclic, at least with a small number of particles per cell. The time step is reduced so that the possibility of extra convection or diffusion exchange particles does not cause the number of particles at the previous time to go non-negative (ie. exchange more particles than you actually have). Of course, using high numbers of particles per cell cuts down on the truncation error. The Monte Carlo scheme does not keep track of where the particles are within each cell. The solution quantities to a SIMPLE method calculation (as most CFD solutions) represent the means and sometimes the modeled variance for individual cells. The variance represents the degree of mixing within a grid cell.

4.1.2 - Molecular Mixing Models

In the second fractional time step, molecular mixing is performed using the continuous mixing model of Hsu. The modified Curl model has non-gaussian higher moments. Curl's model assumes complete mixing between chosen mixing pairs. In the modified method of Curl, the Monte Carlo simulation randomly chooses N_{mx} pairs of particles based on the following formula:

$$N_{mx} = 0.5\frac{\delta t}{C\tau}N = 0.5\frac{\delta t\varepsilon}{Ck}N, \tag{4.21}$$

where C is 6.0. The pairs are allowed to mix as:

$$\psi_n(t+\delta t) = A\psi_m(t) + (1-A)\psi_n(t) \tag{4.22a}$$

$$\psi_m(t+\delta t) = A\psi_n(t) + (1-A)\psi_m(t) \tag{4.22b}$$

where A = 0.5ξ, with ξ a random variable uniformly distributed on the interval [0,1]. The remaining N - $2N_{mx}$ particles remain unchanged:

$$\psi_n(t+\delta t) = \psi_n(t) \tag{4.22c}$$

A plot of the mixing process in composition space is shown in figure 4.2. The value of A used in this plot is 1/6. This model is discontinuous as the sample particles change properties abruptly regardless of how small the time interval is made. Reducing the time interval reduces the number of particle pairs chosen for mixing, but, does not affect the total property change for the chosen particles. A. Hsu and J.Y. Chen[75] modified this process to become continuous. In this model all particles are chosen to undergo mixing and the time interval is incorporated into the mixing level term A. Thus, the jump in physical properties mixing pair particles undergo decreases with the time step, and thus, the process becomes continuous. There are $N/2$ particle mixing pairs for each cell. A is now

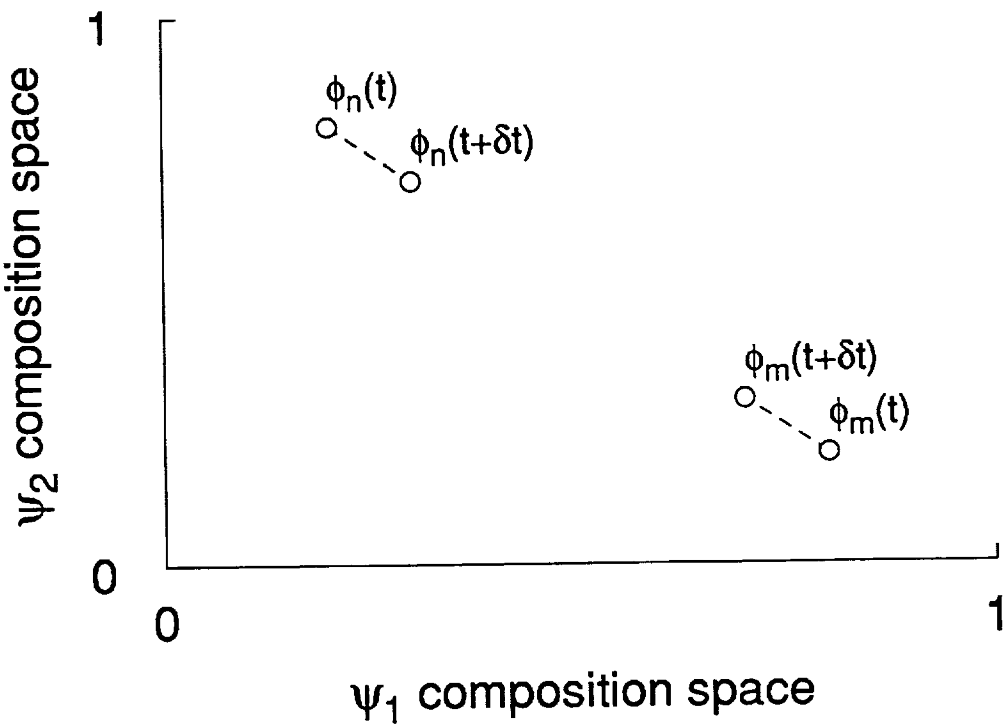

Figure 4.2 Plot of Monte Carlo Mixing process

defined as:

$$A = C'\xi\frac{\delta t\,\varepsilon}{k}, \tag{4.23}$$

where $C' = 2.0$. Hsu showed that this method resulted in more appropriate higher order moments, specifically flatness and superskewness in his calculations. In a 1990 paper, Chen and Kollman[76], use the modified Curl method for a two-step hydrogen combustor calculation and conclude that the model did predict cross correlation properties reasonably well for turbulent shear flows, despite the problems with non-Gaussian character in the higher moments.

Other mixing models have been suggested and employed. Pope[77] suggested that the sampling probability of particles should be biased in regards to the elapsed time since the last mixing event. This entails an additional scalar for the elapsed time since the last mixing event for each particle and the use of an appropriate weighing function for age. Another mixing model is the relax-to-mean model. In this model, the cell mean is calculated, then each individual particle's variance from the mean is reduced exponentially depending on turbulent mixing and time step. The formula for this is:

$$\psi_n(t+\delta t)=\bar{\psi}+(\psi_n(t)-\bar{\psi})*\exp(-0.5C'\tau\delta t) \qquad (4.24)$$

This mixing model was used in A. Norris and A. Hsu's[78] Monte Carlo pdf calculation of Masri et al[79] $CH_4/CO/H_2/N_2$-air pilot stabilized jet flame. A somewhat similar model which uses a linear relaxation is the IEM model developed by Villermaux,[80] and by Yamazaki and Ichigawa[81]. The formula for this is:

$$\frac{\partial Y_i}{\partial t}+u_j\frac{\partial Y_i}{\partial x_j}=\frac{\tilde{Y}_i-Y_i}{\tau_{IEM}}+\omega_i \qquad (4.25)$$

The model name comes from exchanges by Interaction with the Mean Value. The term τ_{IEM} is an exchange time. This model treats combustion simultaneously with mixing. This model has been used by Correa and Braaten[82] to test reduced chemistry mechanisms against full chemistry mechanisms for methane-air combustion in a Partially Stirred Reactor (PaSR) model. This model was chosen in preference to pair exchange models because it is easier to employ on parallel computers. The simulations take many hours to perform on a single processor. Doing calculations in parallel, that is, dividing the numerical work between multiple machines will result in greatly improved turn-around time. The PaSR represents a step into pdf modeling which can use full laminar chemistry for a single grid cell or reactor.

The PaSR pdf calculation admits a fixed number of inlet particles per mixing step. At the same time, the same number of particles is taken from the PaSR. The PaSR has two other simpler reactor models as mixing limits. With no mixing the reactor is simple plug flow. The other limit is infinite mixing which corresponds to a fully stirred reactor. Actual multi-dimensional flowfield calculations can be thought of as a collections of Partially stirred reactors. The exchange of particles between grid cells amounts to exchange of particles between neighboring reactors. The mixing frequency inside each reactor is governed by local turbulence mixing. The results of Correa and Braaten's PaSR calculations varied with the frequency of mixing. Specifying low mixing frequencies resulted in blowoff for a reactor with separate fuel and oxidant inlets. Even with steady-state combustion, concentrations, particularly NO and CO, varied with mixing frequency even using full-up chemistry. As reducing CO and NO emissions is of prime concern in engine design, this is somewhat troubling. Taking individual gas samples amounts to measuring an average. This also disturbs the flow, which affects accuracy. Laser Raman Spectroscopy can take nearly instantaneous concentration measurements without disturbing the flow, but, the measurements must undergo substantial corrections. Thus, it may be some time before data are calibrated well enough to fully validate the pdf method.

In a later paper, Sanjay Correa[83] compared the IEM mixing model with Curl's model and the modified Curl's model for premixed CO/H_2 combustion in a PaSR. At a frequency of 316 Hz, the results were similar. From figures 4-6 of his paper, the difference in temperature between IEM and the pair exchange models was on the order of 50 degrees. The difference in predicted CO and OH concentrations was close to a factor of two. Oxygen predictions were not affected by the mixing model at this frequency. At a frequency of 1000 Hz, the pair exchange models and the IEM model produced nearly identical results. As Correa and Braaten predicted in-flame mixing frequencies of 1000 Hz and larger, Correa stated that the choice of mixing models was not critical in the distributed reaction regime of lean premixed combustion, as long as the turbulent mixing frequencies were above 1000 Hz. This thesis will employ benchmark data from research combustors. These combustors operate at lower temperatures and less intense combustion than practical combustors. Thus, the IEM model is probably not appropriate to use for this work. Research combustor data is used in this work as experimental data from practical combustors is sparse.

Combustion was also effected in a Coalescence-Dispersion Model used for infinite reaction cited by J.Y. Chen and W. Kollman[84]. If chemistry is very fast compared to mixing, as in the flamelet combustion modeling, combustion occurs within a very limited mixture range close to stoichiometric. If combustion isn't treated simultaneously with molecular mixing, combustion can be vastly under predicted. In scalar space, if only the final mixing concentration is examined, particles can pass through a combustible mixture during the mixing phase without reacting. This problem does not occur with distributed combustion which is considered for this thesis.

4.1.3 - Combustion phase

Combustion is proceeds after the exchange and mixing of particles. The pdf method does not have to employ corrections to reaction rates due to turbulence. The unmodified laminar reaction rate is used in the pdf evolution term. Each particle has its own species concentration and enthalpy. Each particle then undergoes chemical reaction without having to worry about modeled turbulence correlations, turbulent flame speed or other ad-hoc turbulent combustion rate. The laminar reaction rate is the actual reaction rate. However, as mentioned previously, there is much controversy about true reaction rates. Even laminar combustion involves tens of reactions with diverse time constants. Including "exact" kinetics into a pdf scheme would result in 100,000 "exact" solutions per iteration for a rough grid of 50 by 80 with 250 particles per grid cell. Semi-implicit turbulent combustion calculations take thousands of iterations to converge a few orders of magnitude. Explicit pdf calculations require at least ten thousand iterations for elliptic flows. The current use of pdf methods must inherently include simplification combustion modeling to give realistic calculation times. Some of these approximations have been already mentioned. If the number of scalars is kept low it is possible to construct thermodynamic state tables. The table is then interpolated to find thermodynamic data during the iteration process. For instance, J. Y. Chen et al.[85] have constructed state tables for methane combustion using 4 and 5 scalar reaction mechanisms and two time increments. Reaction submodels incorporated in the Lewis pdf model have included infinite reaction rate, a two step global reaction model for hydrogen by Chinitz, an Intrinsic Low-Dimensional Manifold (ILDM) method of Maas and Pope[86]. The ILDM method uses dynamical systems approach to reduce the number of degrees of freedom to simplify the chemical kinetics system and construct a state look-up table. The method was successful in the calculation of Norris and Hsu [78]. The ILDM method for heavier, more complex fuels more difficult and is currently being worked on. Also, the table look-up method for higher molecular weight, more complex fuels requires more reaction steps. This is beyond current computer memory limits. A single finite-rate reaction submodel is used in this work.

In 1990, Chen and Kollman[87] compared simplified chemical reaction models for hydrogen-air combustion. At conditions near equilibrium, the chemistry models all produced similar results. Only one of the models was reported to be able to predict flame blowout, but, the blowout velocity was incorrect. They concluded that further improvements in the turbulent mixing model and the numerical scheme were required to obtain quantitatively correct predictions. Also needed are data from simultaneous measurements of radical species and mixture fraction.

4.2 - Further Development of Composite PDF Method

One contribution of this work is further development of the composition pdf and testing the model for finite-rate combustion in recirculating flows. The composition pdf has been primarily used for parabolic or one-way flows with modifications of equilibrium type combustion models. Equilibrium or fast kinetics combustion models should be used where the rate of mixing is much smaller than the combustion rate. These models are valid for low molecular weight fuels as hydrogen and methane at high temperatures. Practical combustors use higher molecular weight fuels. Burning is distributed in practical combustors. There is significant overlap in reacting species, particularly at low temperature.

The SIMPLE method of Patankar and its variants is the most widely used solution method for practical combustor flows. The composition pdf method is combined with the SIMPLE method. Momentum, overall mass conservation, turbulent kinetic energy and dissipation are solved using the SIMPLE method. The composition pdf model used in this work was initially developed by Hsu and co-workers at NASA Lewis Research Center. The first release of this composition pdf model was with the Lewis RPLUS 2-D combustor code[88]. RPLUS is used to predict high speed combustor flows. As Mach number is lowered the solution convergence rate deteriorates. It is an extension of the Lower-Upper Symmetric Solver used by Yoon and Jameson[89] to predict species composition. The first dissemination of the development model was at a workshop in 1993. The model released at the workshop was set up to solve the flow configuration of Burrows and Kurkov's supersonic hydrogen combustor[90]. The model was set up to use a global five species, two step reaction submodel originally proposed by Rogers and Chinitz[91] for hydrogen-oxygen combustion.

Many changes were made to the original composite pdf model. The implementation of the finite rate combustion model didn't calculate steady state combustion using suggested reaction numbers for methane. A different species composition solver was implemented. The species concentration solver uses the Newton-Raphson technique. In the original coding, an incorrect implementation of upwind differencing was used to calculate the number of particles to exchange between cells. Pure upwinding is regarded as highly diffusive in CFD. So as to fairly compare the predictive capability of the combination pdf model against the baseline combustion model, hybrid differencing was implemented in the composition pdf for the calculation of exchange coefficients. The thermodynamics of the base pdf model were highly simplified. Constant C_p was assumed. C_p changes markedly over the range of combustor temperatures. Predictions of exit temperature were adjusted in development model by adjusting C_p. The baseline combustion model used in this work has variable C_p. Variable C_p was also incorporated into the thermodynamics of the composition pdf model. This necessitated the use of enthalpy rather than temperature as one of the pdf variables. The development combination pdf model used a combination of temperature solver in Monte Carlo solver and enthalpy solver in RPLUS code to solve for temperature. The model implemented here properly solves for temperature completely in the pdf solver.

Trial calculations are done using the SIMPLE method as it is more economical than the hybrid pdf method. The best solution is used to begin hybrid pdf solution and is also used to compare predictions and measurements.

Chapter 5

COMBUSTOR MODEL VALIDATION

Experimental data used to evaluate modeling should be selected based on the quality and quantity of experimental data, especially initial or boundary condition data. Experimental data should include measurement of multiple chemical species, velocity, temperature and turbulence quantities. If comparison is performed with limited data, the quality of a CFD solution may not be adequately evaluated. CFD solutions are usually repeated changing initial conditions, gridding, turbulence modeling, etc. until an optimum comparison is given. With limited data, an optimum solution may be found for the wrong reason. A good prediction of one species does not necessarily mean that all other species are equally well predicted. Similarly, a good prediction of one velocity profile does not mean that other velocities profiles are equally as good. Good predictions at one station in a combustor does not mean that all stations are of the same quality.

Suitable and accurate data must be used to ascertain the appropriateness and accuracy of numerical predictions. Past measurement techniques have used hot wires and pressure probes to determine velocities. Over the past decade, optical measurements of velocity have become standard. Measurements require some kind of access. Probes can be handled by access from the rear of the combustor. Lasers demand optical access through the combustor. This is usually handled by installing heat resistant windows in the combustor. The windows degrade faster with increasing temperature, heat transfer and pressure. Thus, almost all benchmark quality data for combustors have assembled using research-type combustors. These combustors incorporate the major features of practical commercial gas turbine combustors, but, their designs are vastly simplified. Running an actual combustor is very expensive and very difficult to instrument. Most research type combustors are axisymmetric, except for the possible addition of dilution jets. The dilution jets are required to cool the combustion liner and lower the overall equivalence ratio of the combustor. The solution of combustors with dilution jets requires 3-D models. Combustors flows undergo substantial change in density. The flow through a combustor without the flow expansion caused by combustion can be substantially different than with combustion. Measurements of some cold combustor flows have shown reverse flow at the exit of the combustors. Most CFD models assume one-way flow at the solution exit plane. One way exit flow may be enforced by installing flow restrictions at the combustor exit.

5.1 - Combustor Model Validation Data

In 1985 an evaluation of data for parabolic turbulent reacting flows was published. The editors were Strahle and Lekoudis[92]. The work was sponsored by the Air Force Office of Scientific Research. The purpose was to conduct a program similar to that run at Stanford in 1968[93], except on turbulent reacting flow as opposed to turbulent boundary layers. A committee was set up to help in the evaluation of the data. At the final committee meeting it was recommended that a computational effort not be initiated at the time. One reason was that most combustion theories are application specific and cannot be readily used for flows of different character or chemistry from those for which they were developed. Some problems noted in the data were: lack of completeness, incomplete specification of initial and boundary conditions and excessive experimental uncertainty. This work did not include data for complex reacting turbulent recirculating flows.

One of the major problems with early combustion data is the limited number of experimental quantities measured. Many of the experiments were performed to characterize only parametric variations of a combustor type, not to validate CFD models. In a paper by Baker et al.[94], only velocities and stresses are reported. In another paper by Lockwood et al.[95], only flame length and mixture fraction were reported. McDannel, Peterson and Samuelson[96] gave species and temperature measurements for a premixed flow. The flame was stabilized by a recirculation zone formed by a high velocity jet opposed to the direction of bulk flow. Velocities were varied in a the study. El Banhawy, Sivasegaram and Whitelaw[97] took measurements of temperature, velocity and species concentration for a premixed combustor in 1983. The measurements are presented in contour form. In premixed combustors the fuel and oxidant are combined upstream of the combustor inlet. In this configuration, combustion is anchored by a hot recirculation zone caused by a sudden area increase. This geometry is known as a step combustor. Two different step sizes were studied. Premixed combustors aren't used in practical gas turbine engines, due to stability problems. The concept has been under study for quite some time because the concept reduces engine emissions. Smith, Giel and Catalano[98] measured hydrogen-air combustion in an axisymmetric recirculating combustor flow. A lean mixture was used. Due to its low molecular weight, hydrogen diffuses much more rapidly than oxygen or water. Preferential diffusivity wasn't included in the numerical model, so this flow was not calculated. There is a wide disparity in the inlet velocities, which causes the recirculation zone. The hydrogen has a bulk velocity of .914 m/s, while the air inlet velocity was 102 m/s. Temperature and species concentration for the reacting case was measured by laser raman spectroscopy. However, not enough measurements were taken at each location for high confidence levels. The temperature profiles are quite rough for the first three measurement stations.

Lightman et al.[99] performed measurements on a bluff-body combustor at Wright-Patterson Aero Propulsion Laboratory. Measurements were for combusting and non-combusting flows. They reported that most of the features of the cold flowfield also were present in the combusting flow. However, in a later paper[100], high speed pictures of the combustor flow revealed the existence of large scale structures. By examining laser Doppler anemometer measurements and measurements of luminosity it was concluded that the flow is comprised of non-luminous regions and flame turbules. The combusting flow was unsteady. Schefer et al.[101] also saw coherent structures in their study of another combustor flow stabilized by a bluff body. The flow was characterized by large scale entrainment of air into the recirculation zone. Pdf's of Velocity and velocity correlation were measured. Bimodal pdf's were observed in regions of high shear in the recirculating zone boundaries and in the downstream stagnation region. This bimodality was associated with the alternate passage of large-scale turbulent structures consisting of unmixed fuel and air through the measurement volume. In 1987, Sivasegaram and Whitelaw[102] published a paper studying oscillations in axisymmetric dump combustors. Another study was published in 1989 by Sivasegaram et al.[103] Some unsteady combustion predictions have been done, but, the practicality of the work is somewhat controversial.

Samuelson and his students have produced a number of papers regarding the design and experimental measurements of axisymmetric combustors. The most complete 2-D database is an University of California , Irvine, Combustion Laboratory paper by R. Charles[104]. A parametric series of measurements were made by modifying the combustor inlet conditions including the fuel nozzle. Unfortunately, only axial and tangential velocity measurements are reported. The radial velocity is unknown, although it may be inferred from continuity for non-combusting flows. In general, the number measurements taken in the radial direction number around ten. This number is too small to accurately validate or benchmark combustor models. Axial velocities measured 1 cm from the inlet show considerable backflow. Azimuthal velocity generally shows a peak near the outside wall at this axial location. Peak azimuthal velocity at other axial locations is much closer to the combustor centerline. Inlet data from this configuration would have to be set up based on flow geometry, bulk flow and experience of the combustion modeler.

J.C. Pan[105] did a parametric study of turbulent confined premixed flames. The flame was stabilized by conical bluff bodies. In the study, the size and angle of the conical bluff bodies, the equivalence ratio, the inlet velocity and turbulence were varied. The data given in the reference were not in tabular form. Velocity and temperature pdf's were given, velocity vector diagrams, contours of velocity and reynolds stresses and centerline profiles of velocity and temperature. Some cases used very lean mixtures close to the blow-out limit. The data may be good for validating flamelet combustion models.

Some three dimensional combustor flows have also been measured. Heitor and Whitelaw[106] measured velocity, temperature and species in a combustor having dilution jet holes. The combustor exit is constricted to one side. The fuel was gaseous propane. The scalar field was dominated by the presence of the dilution jets. Air to fuel ratio was varied. Combustion efficiency was low for some of the runs. In a 1990 paper, Bicen, Tse, and Whitelaw[107] reported up to 98 % combustion efficiency for a similar can-type combustor. The primary zone of the combustor was fuel rich.

5.2 - Spray Model Validation

The baseline combustion model was tested in various stages to benchmark its predictive capability. The first stage was predicting an isothermal open combustor flow. The spray vaporization model was then tested. Finally, calculations of spray combustion were performed.

5.2.1 Isothermal Swirling Flow

The isothermal swirling combustor flow of D. Bulzan[108] was used to validate the baseline combustor model. This combustor is part of an on-going effort to provide experimental data to validate spray combustion models. The experimental configuration is a Parker Hanifin research simplex air-assist atomizer surrounded by a co-flowing air stream. The configuration used here is unconfined, that is, it does not have an outer wall. This was done to simplify taking experimental measurements. A schematic drawing of the combustor is shown in fig. 5.1. Most unconfined or free-jet combustors are notorious for poor mixing, and require significant axial distances for complete mixing. The atomizer and the co-flow air had 45 degree swirl in the same direction. This swirl causes the formation of a large recirculation zone which promotes rapid mixing and stabilizes the flame for the reacting case. The recirculation bubble is longer than the laser measurement system can traverse. The model was able to handle this negative outflow condition by suitable treatment of the exit boundary conditions as suggested by P. George Huang. Normally, exit boundary conditions assume zero-gradient or one-way flow where the flow is not significantly changing with axial distance. The exit velocity is unknown, but, is needed in the calculation of pressure. The solution is part of the iterative process. The exit velocity is set to the last calculated upstream velocity plus a velocity correction due to mass conservation. Thus pressure for the exit computation cell can be calculated. In the process of calculating the upstream velocity, the downstream contribution to the exit computational cell is set to zero without adding any significant error, since the downstream contribution is either zero or very small. For the case where the exit velocity is negative for a computational cell, the exit neighbor coefficient is the upstream coefficient and the contribution is very significant and cannot be

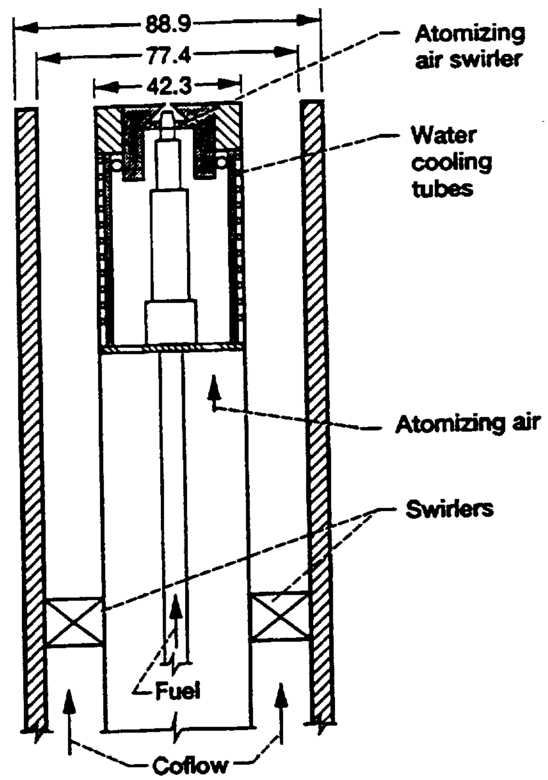

Figure 5.1 Schematic drawing of the combustor. Dimensions in mm.

ignored. This is actually an unspecified inlet condition, which must be calculated. This is handled in the iteration process by setting the boundary cell velocity equal to the velocity of the downstream adjacent cell, which is calculated. Then the upstream or boundary neighbor coefficient is added to the non-constant part of the source term. Then the neighbor coefficient is set to zero (the boundary coefficient isn't included in the sum of neighbor coefficients). To summarize, first neighbor coefficients are calculated in the normal way. Then the (negative) exit velocity coefficient is added to the non-constant part of the source term. Then the exit velocity is treated as if it were zero in the difference equation. Pressure is still calculated the same as before. The mass correction at the exit boundary is only made where the exit velocity is positive.

The flowfield in the inlet region is quite complicated. The combination of the blunt body atomizer with the highly swirling co-annular flow produces two recirculation zones. The first has already been mentioned. The second is a small toroidal vortex adjacent to the blunt atomizer between the outward swirling flow and the reverse flow along the center-line. The unconfined combustor entrains surrounding ambient air. A velocity-vector diagram from a calculation is shown in figure 5.2. The centerline is on the right side of the figure. The flow is from bottom to top. The small vortex near the bottom center-line is somewhat larger than what was

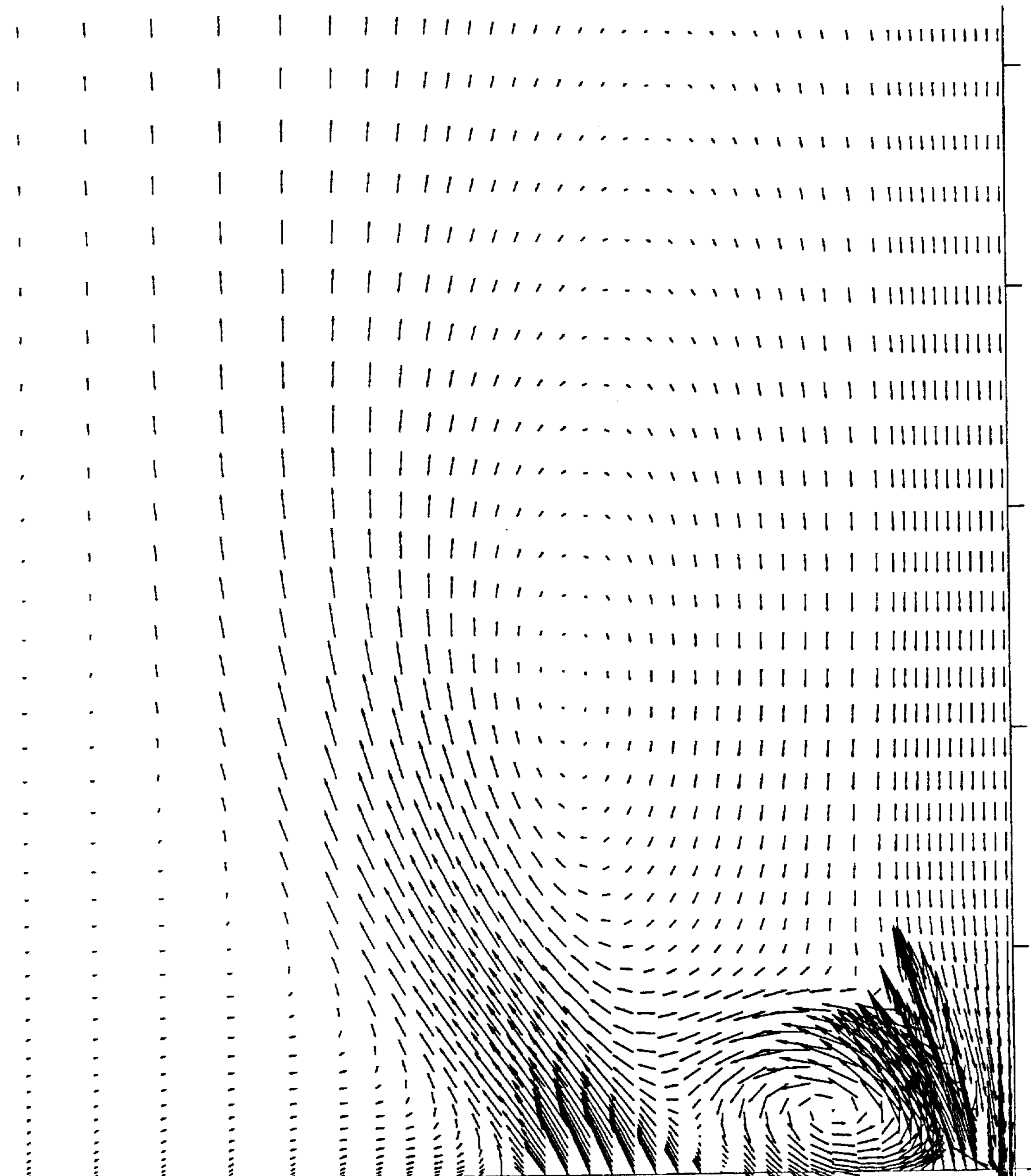

Figure 5.2 Velocity vector diagram for isothermal calculation

experimentally measured. Calculation of the flow-field is difficult. One problem is reverse flow at the first measurement location. The current model can handle moderate amounts of reverse flow at the combustor inlet, as it uses a pressure based algorithm. Another problem is that the initial flow is rapidly expanding into an open environment. Entraining flow is difficult to accurately predict using pressure based algorithms. The strong swirling flow, which produces the very large recirculation bubble, could not be contained by boundary conditions intended for entraining free-jet flow. Using wall-type boundary conditions did contain the flow, but, the size of the calculated recirculation zone depended on placement of the non-physical wall. Using a larger radial calculation domain produced a larger recirculation bubble, with most of the positive axial flow occurring close to the wall. The experimental measurements show an axial velocity peak which gradually moves outward. A solution to this was to specify velocities on the outer radial boundary. Dr. Bulzan measured some velocities at radial distances of 143 mm and 168 mm from the combustor centerline. This data was obtained directly from Dr. Bulzan. The measurements at 143 mm were used for this calculation. At this radius, flow was entrained to an axial distance of about 130 mm. Measured values of velocity at 5 mm downstream of the atomizer were used as initial conditions for the calculation. Predicted flow fields varied greatly by using different initial values of turbulent kinetic energy and dissipation. Normally, the k-ε turbulence model is believed to produce only small change due to rather large change in initial turbulence quantities. Typically, the use of poor initial turbulence quantities is overcome within a few gridpoints. Thus, the k-ε model is perceived as a good model to use as predictions are not unusually dependent on initial dissipation or length scale, which are usually unknown. Unfortunately, the initial structure of the flow-field is quite complicated, is unconfined, and involves very high shear. The atomizer causes large velocity gradients. This causes a huge generation of kinetic energy and rapid dissipation. Using the full measured turbulence energy and a length scale of 30 % of the diameter of the atomizer and co-flowing air passage smeared out the small secondary vortex and blocked the reverse flow along the centerline. Also, the predicted central recirculation zone was over a factor of two wider than measured at the calculation exit.

Another calculation was done using peak turbulent kinetic energy around an order of magnitude smaller than measured and specifying a length scale of 30 % of the width of the total calculation domain. This resulted in very good predictions of the velocity field. Evidently, the low initial values allowed lower initial dissipation and which later built up enough to predict the correct amount of spreading.

Due to convergence problems, initial swirl was slowly ramped up to the full value. The total number of iterations was 6000. Calculated versus measured axial velocities are shown in figure 5.3. The comparisons are done at axial distances of 20, 50, and 100 mm. The axial velocity predictions show quite good agreement with the measurements. The velocity peaks are slightly underpredicted. Figure 5.4 shows comparisons of radial velocity. Radial velocities are underpredicted.

Figure 5.5 shows comparisons of tangential velocity. Similar to axial velocity profiles, the calculated tangential velocity profiles are very good. Peak velocities are only slightly underpredicted. Plots of turbulent kinetic energy are shown in figure 5.6. The comparison is poor for the lower half of the profile at 20 mm, where the turbulent kinetic energy is vastly underpredicted. This part of the flow represents shear between the second vortex and the backflow along the centerline from the large recirculation zone. The local axial velocity peak is also underpredicted in this shear region.

Predicted profiles at other locations are very good. These calculations show that juggling initial turbulence values has a significant effect on computational results for this flow. As reducing initial turbulence values reduced mixing and produced good computational results, a modification to the turbulence model was considered. The k-ε model assumes isotropic turbulence and is not regarded as optimal where swirl, body forces, or curvature exist. In the past, some researchers have resorted to a curvature corrections to improve predictions for strongly swirling flows[109].

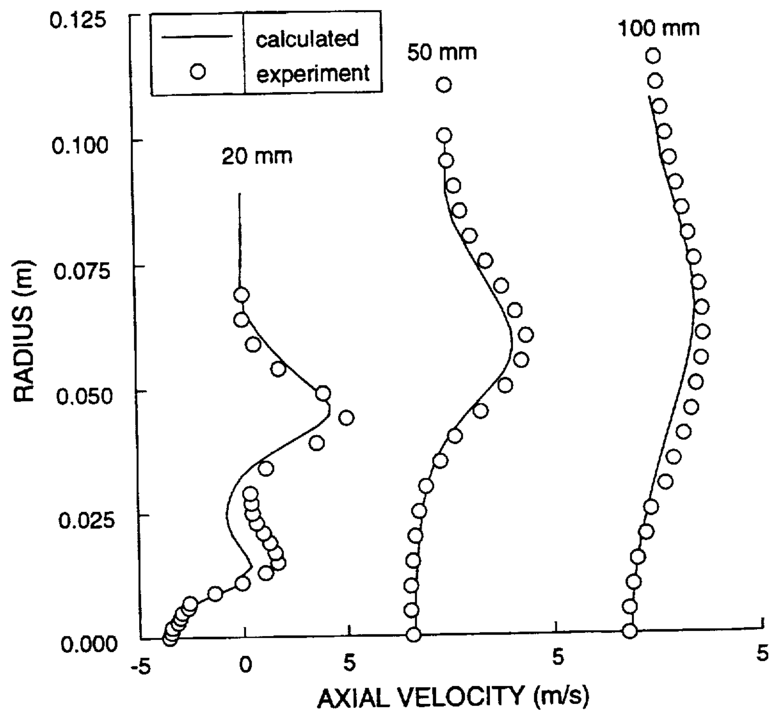

Figure 5.3 Calculated and experimental axial velocity at 20, 50, and 100 mm.

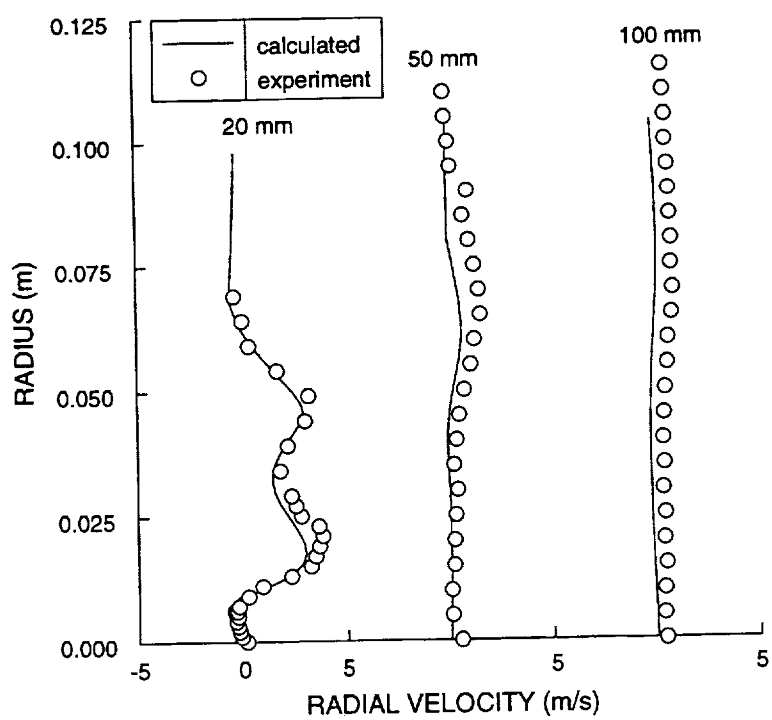

Figure 5.4 Comparisons of radial velocity at 20, 50, and 100 mm.

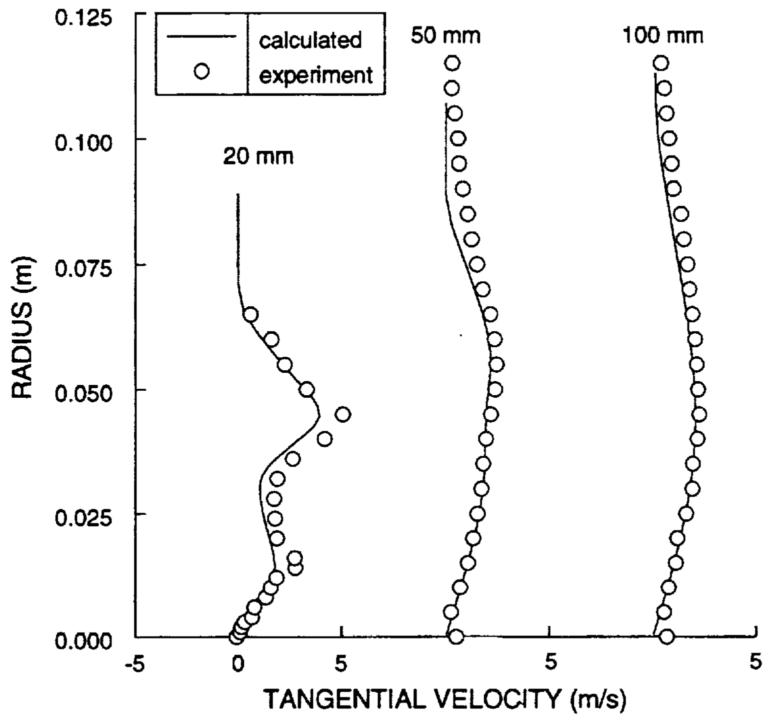

Figure 5.5 Comparisons of tangential velocity at 20, 50 and 100 mm.

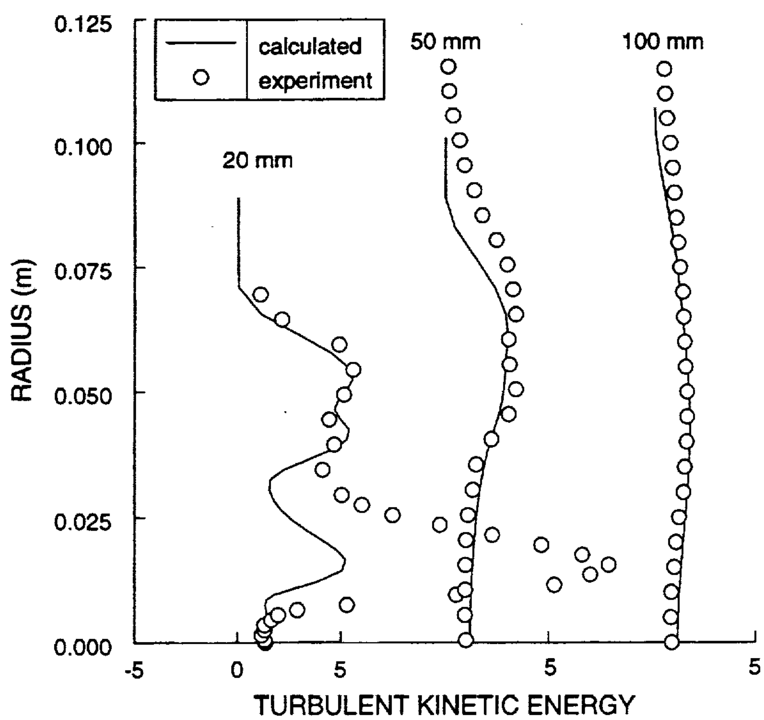

Figure 5.6 Calculated and experimental turbulent kinetic energy.

Several modifications were tested by Sloan et. al.[110] for thirteen cases. Unfortunately, the lack of initial conditions prevented drawing absolute conclusions about the improvements. This work does not employ curvature or Richardson number corrections. Instead, a simpler method of changing the turbulent viscosity coefficient based on shear was tried. Recently, a modification for high shear was proposed and tested by Shih et. al.[111]. This development is based on invariant theory in continuum mechanics. The modification is done so that negative normal stresses are not calculated in any situation of rapid distortion. This involves damping of the coefficient for turbulent viscosity, which is normally treated as a constant. The equations used are:

$$\nu_t = C_\mu \frac{k^2}{\varepsilon} \tag{5.1}$$

$$C_\mu = \frac{2/3}{A_1+\eta} \tag{5.2}$$

$$\eta = Sk/\varepsilon \tag{5.3}$$

$$S = \sqrt{2S_{ij}S_{ij}} \tag{5.4}$$

$$S_{ij} = (U_{i,j}+U_{j,i})/2 \tag{5.5}$$

The predicted viscosity coefficient ranges from a high of 0.121 to a low of 0.0178 at the edge of the co-flowing air.

The results of this calculation are shown in figures 5.7-10. The axial velocity profile at 20 mm is similar to the results with the regular k-ε model, but, the 50 and 100 mm profiles do not show as much radial spreading. The radial velocity profiles are slightly reduced which accounts for the lower spreading rate. This is also reflected in the tangential velocity profiles. The peak turbulent kinetic energy for the 20 mm axial location is improved, but, at all other locations predictions are worse with much less radial spreading. It appears that modification of the turbulence can be made to improve predictions in one area, but, unfortunately reduce accuracy in other areas.

These calculations were done with hybrid differencing which is known to be overly diffusive, especially for calculation of round free jets. Higher order differencing should be used before judgements about the validity of various turbulence modeling improvements.

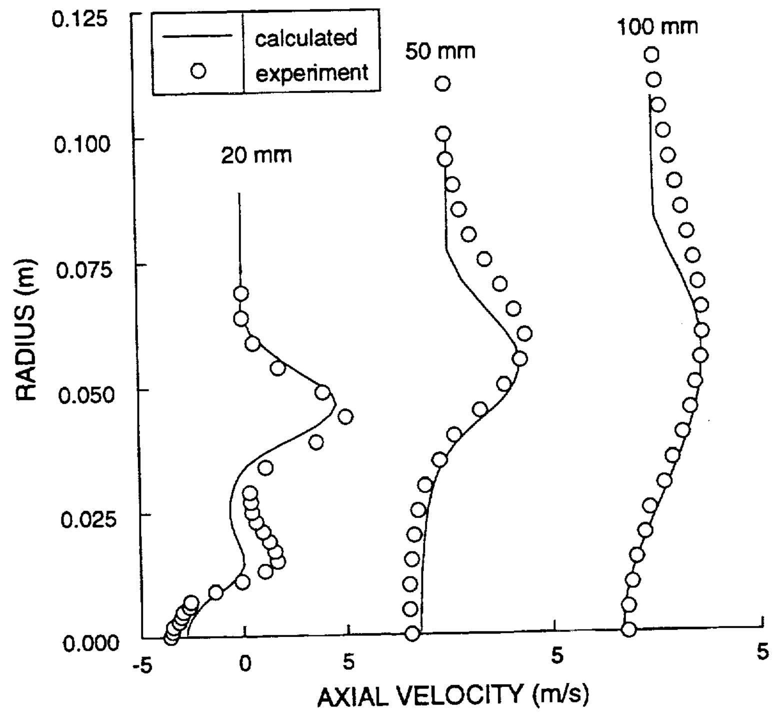

Figure 5.7 Axial velocity profiles at 20, 50, and 100 mm with modified turbulence model

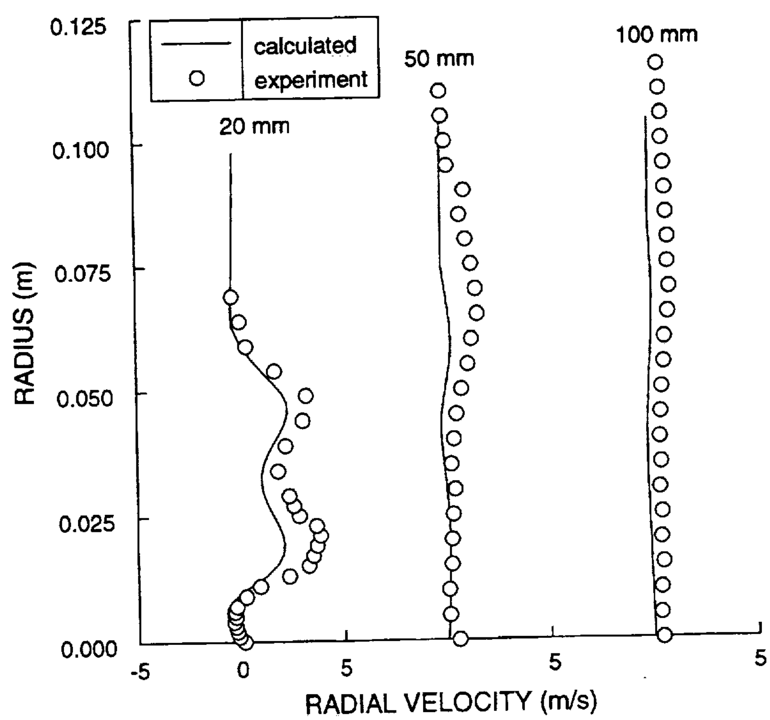

Figure 5.8 Radial velocity profiles at 20, 50, and 100 mm.

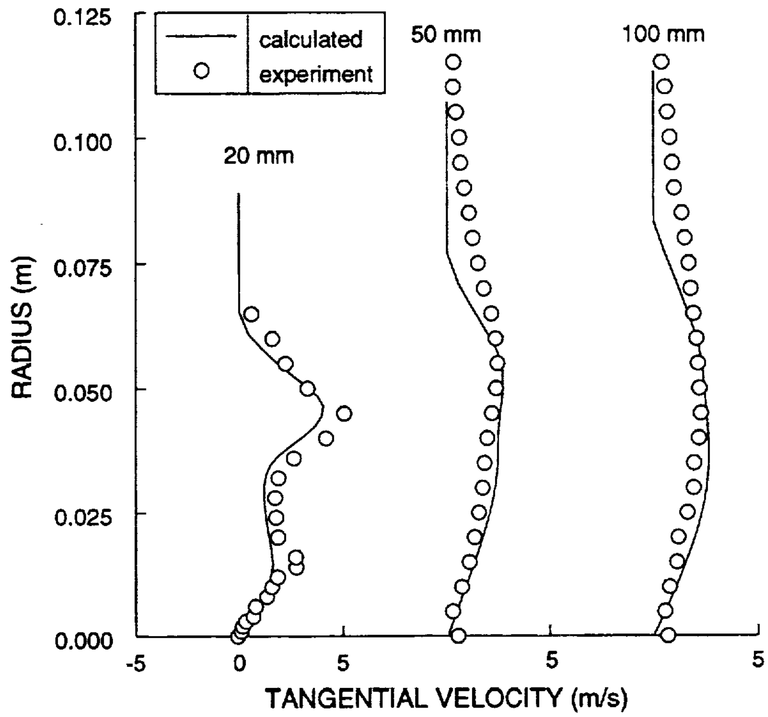

Figure 5.9 Tangential velocity profiles at 20, 50, and 100 mm with modified turbulence model

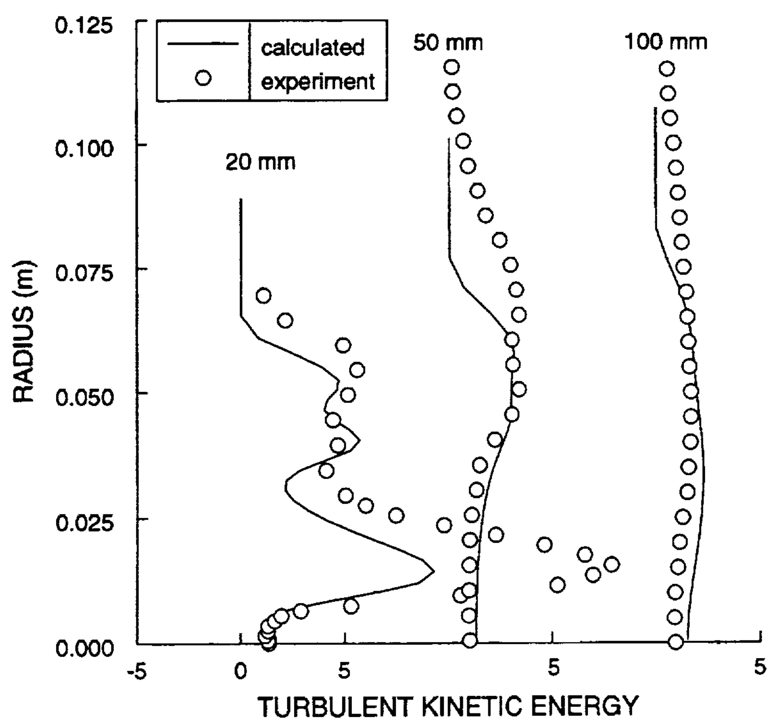

Figure 5.10 Turbulent kinetic energy at 20, 50 and 100 mm with modified turbulence model

5.2.2 Evaporating Spray Model Validation

The methanol vaporization data of McDonell et. al.[112] was used to validate the spray model. McDonell's data were specifically taken to validate spray models. The experimental apparatus consists of a research atomizer injecting methanol spray downward into a 457 mm square duct with co-flowing air stream at an approximate bulk velocity of 1.0 m/s. Measurements were made of axial and radial gas-phase and droplet velocities, methanol vapor concentration, and droplet fluxes. No reverse flow was measured in this non-combusting case. The droplet data were measured by Phase Doppler Interferometry (PDI). The spray droplet data were partitioned into 10 different size groups due to limitations of the instrument. Data at an axial distance of 7.5 mm were used as initial conditions for the calculation. Gas phase velocities were measured to a radial distance of 88.0 mm. Initial gas phase velocities beyond this distance were ramped to the bulk velocity of 1.0 m/s. Spray droplet data were specified at radial distances out to 13.0 mm in 1 mm increments. The total number of droplet groups measured at this axial location was 102 as the large droplets were not found near the center line.

According to McDonell, the error in vapor concentration measurement was about 10 %. The error in droplet measurements is higher, especially in the initially dense spray. The sum of the measured methanol vapor and droplet fluxes only accounted for 23 % of the known methanol flow at the first axial measurement location. The fraction of the measured methanol flux goes up to 85 % at the last measurement location. The PDI measures the number of fringes crossed and does not accurately measure flows in very dense sprays. Droplets are going through the measurement zone at various angles, velocities, shapes, and sizes. The measurements are invalidated if there are multiple droplets detected in the measurement zone. As a rough approximation, the corrected droplet count rate is usually taken as the sampling rate. The error in measuring small droplets in dense sprays is larger as there exists a higher probability that multiple droplets are in the measurement zone. The ratio of the sample rate to the validated rate is around 5 for the smallest droplets at the first axial measurement location. This ratio drops to 1.1 for the largest droplets in the outer less dense region of the spray.

Four sets of spray droplet input data were used in the predictions. For the first calculation the droplet data rate was incremented at each radial location so that the McDonell's flux rate at that radial location was achieved. Then, an overall final correction was done for the flux rates so that the total methanol flow rate was correct. This droplet rate correction seemed to bias the numbers towards the larger droplets. Larger droplets evaporate more slowly than smaller droplets as the surface to volume ratio is smaller for the large droplets. The calculated methanol vapor flux was lower than that measured by McDonell for the last two stations, as shown in figure 5.11. In the second prediction, the sampling rate was simply multiplied by an overall value to give the total methanol flux. This slightly increased the vaporization rate. For the third prediction, the actual probe area values were obtained from McDonell. These probe volumes changed from location to location. This information allowed for a more accurate measurement of droplet flux. The calculated vaporization was similar to that obtained in previous predictions. In the fourth prediction, the overall mass correction was weighed for each droplet size according to the ratio of the sampling rate to the validated measurement rate. This calculation had the largest number of small droplets and predicted the highest vaporization rate. It was hoped in using different initial spray distributions that the velocity field predictions would improve. As shown by figures 5.12-15 this did not happen. The use of different droplet data did not drastically change the axial velocity profiles. Thus, the error in predictions does not appear to be caused by the initial spray distribution, or the spray model. Some of the error may be due to the initial radial gas phase velocities. McDonell's data for these velocities is sparse. Near the atomizer, measurements were taken only very 4 mm. In a

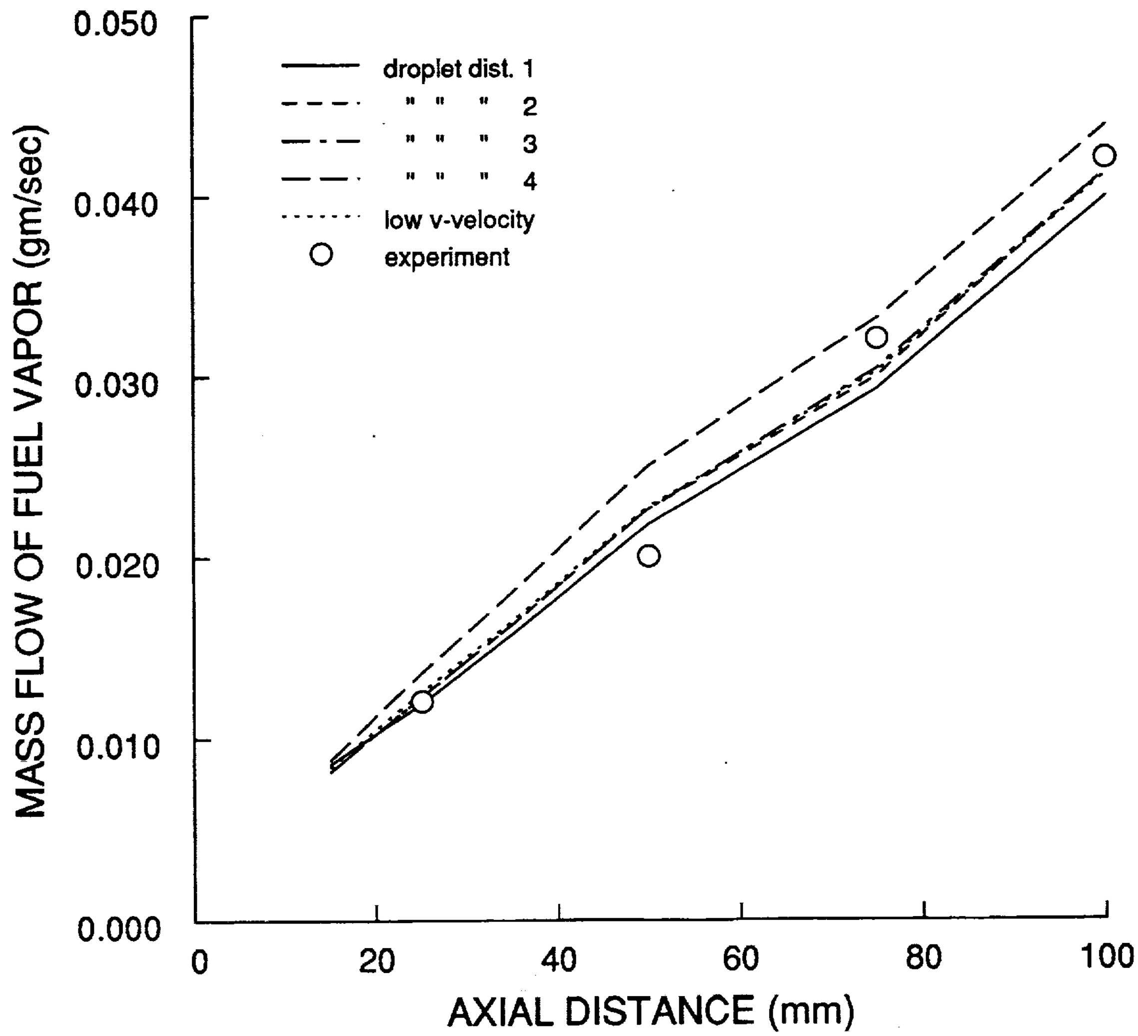

Figure 5.11 Mass flow rate of vaporized Methanol

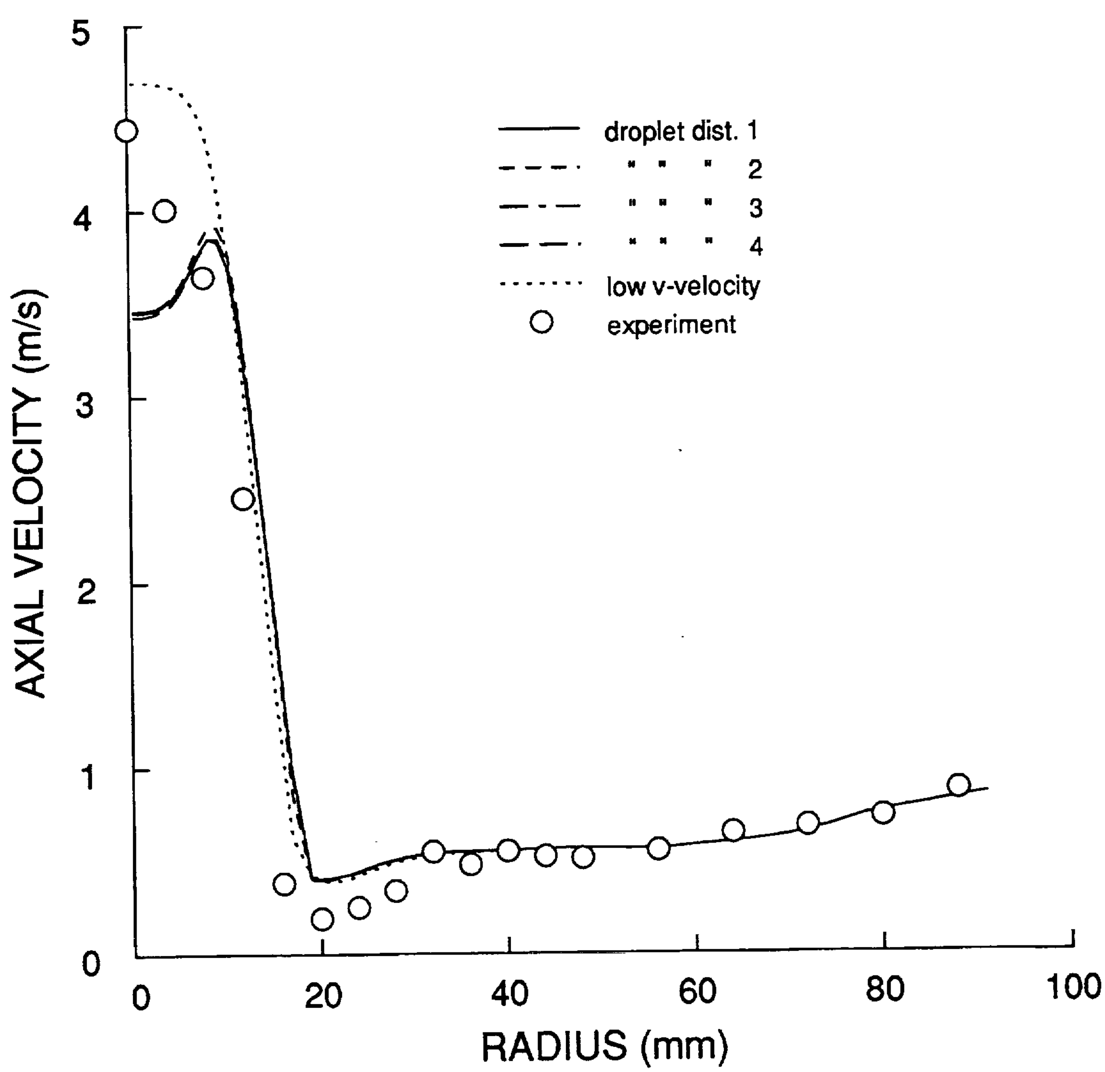

Figure 5.12 Axial Velocity at 15 mm

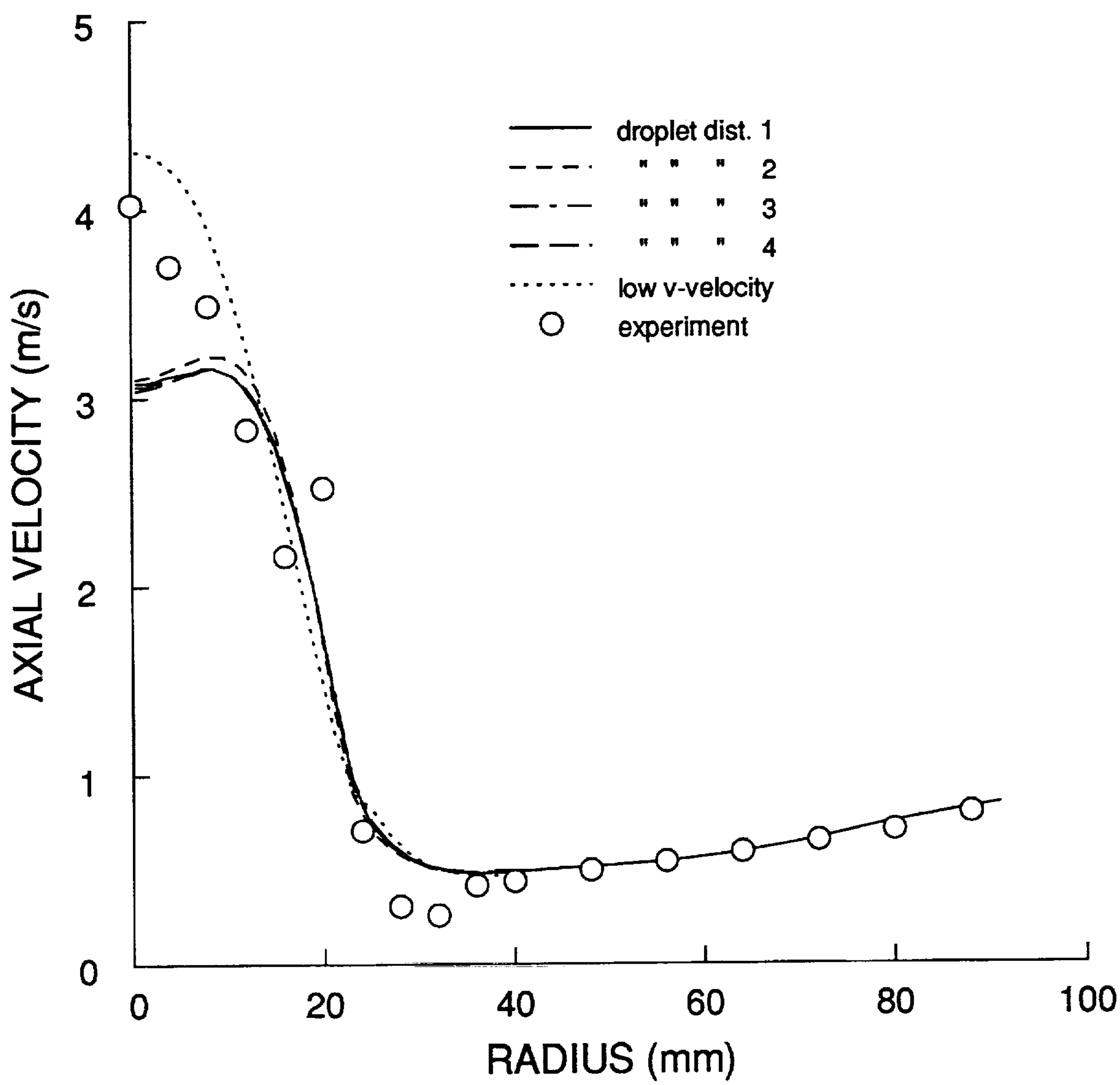

Figure 5.13 Axial Velocity at 25 mm

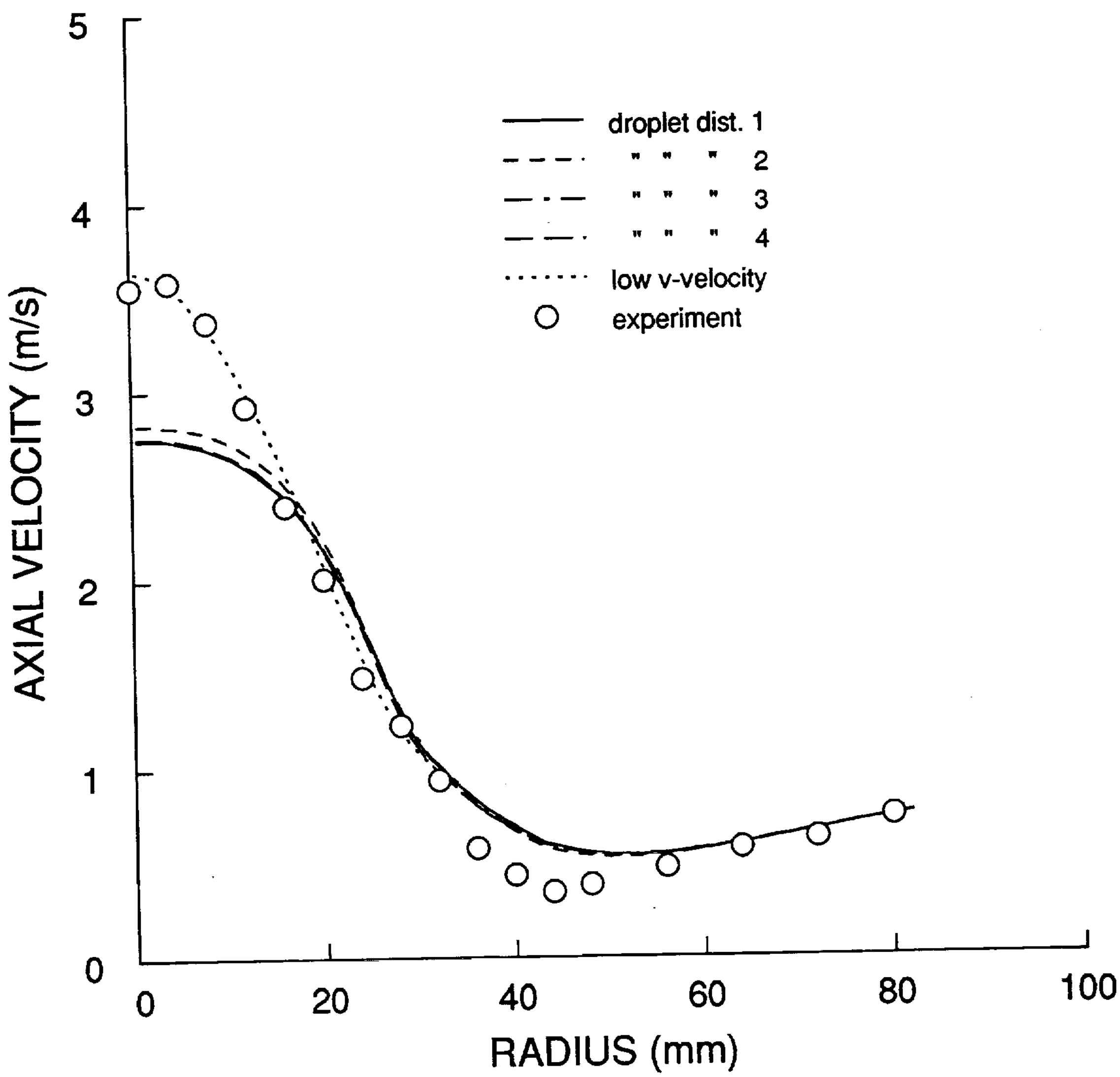

Figure 5.14 Axial velocity at 50 mm

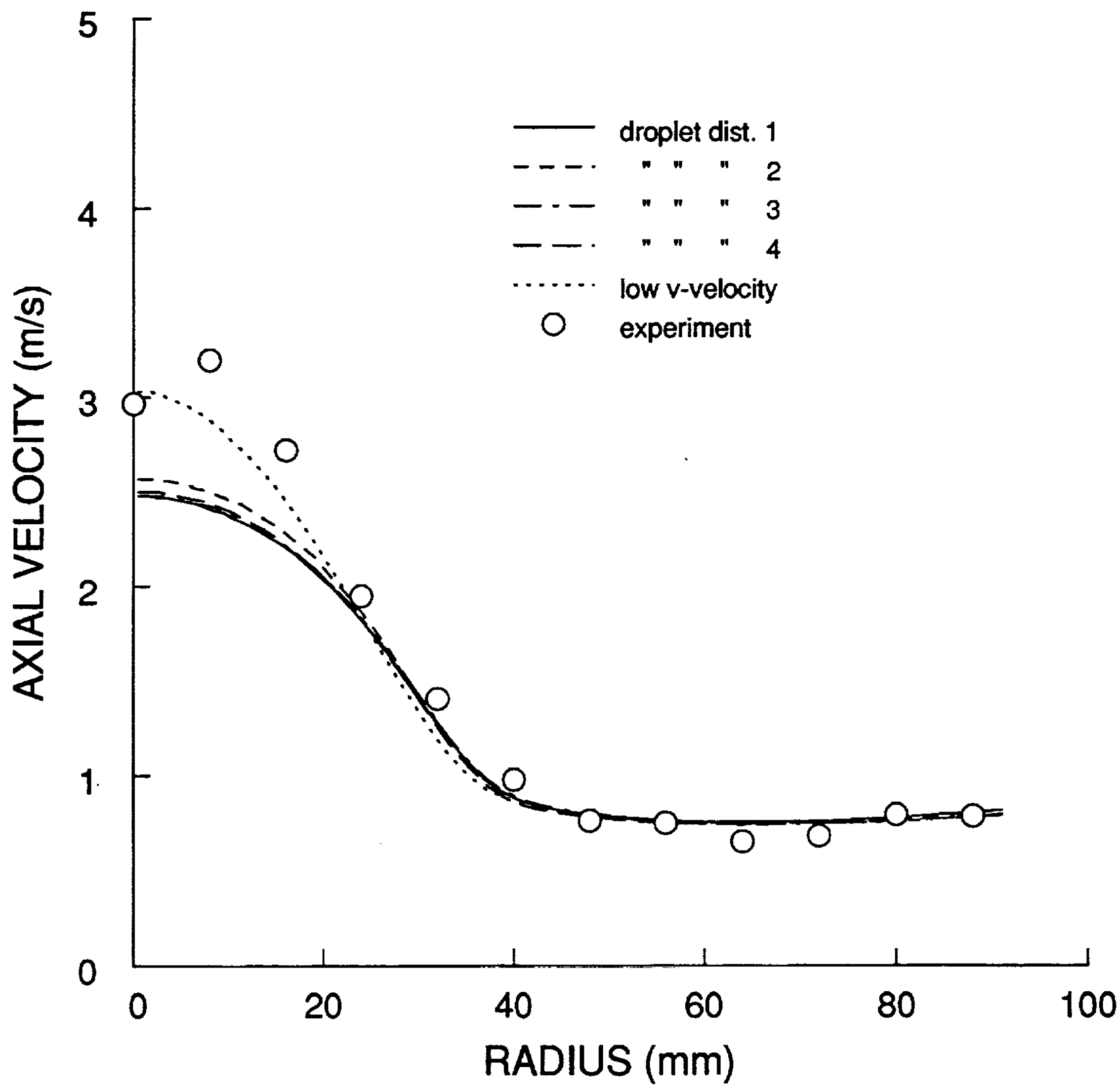

Figure 5.15 Axial velocity at 100 mm

distance of 12 mm, the reported radial velocity increases to over 3.2 m/s and then decreases to -1.547 m/s. The turbulence is extremely high. Axial velocities vary as much as 5% between the axial-radial and the axial-azimuthal velocity sweep measurements. In the predictions, the initial high radial velocity components caused a rapid decay in radial and axial velocity components. To check the radial velocity components, another calculation was done with much smaller radial velocity component near the atomizer. This produced axial velocity profiles with higher peaks. Also, the peaks occurred along the centerline, as is shown by most of the measured velocity profiles. With the reduction in radial velocity, the predicted velocity profile almost perfectly matches the measured velocity profile at 50 mm, but, at 100 mm the predicted profile is flatter. The predictions appear to be suffering from too much diffusion. Various curvature effects can be applied to coefficients in the turbulence model, but, with the rather small amount of curvature in this flow, these corrections would do relatively little to improve predictions.

Predicted methanol vapor concentration is shown in figure 5.16 for an axial distance of 15 mm. The contours are remarkably similar for all of the predictions at this axial location. Experimental measurements were not given at this location. A comparison of experimental and predicted contours at 25, 50 and 100 mm is given in figures 5.17-19.

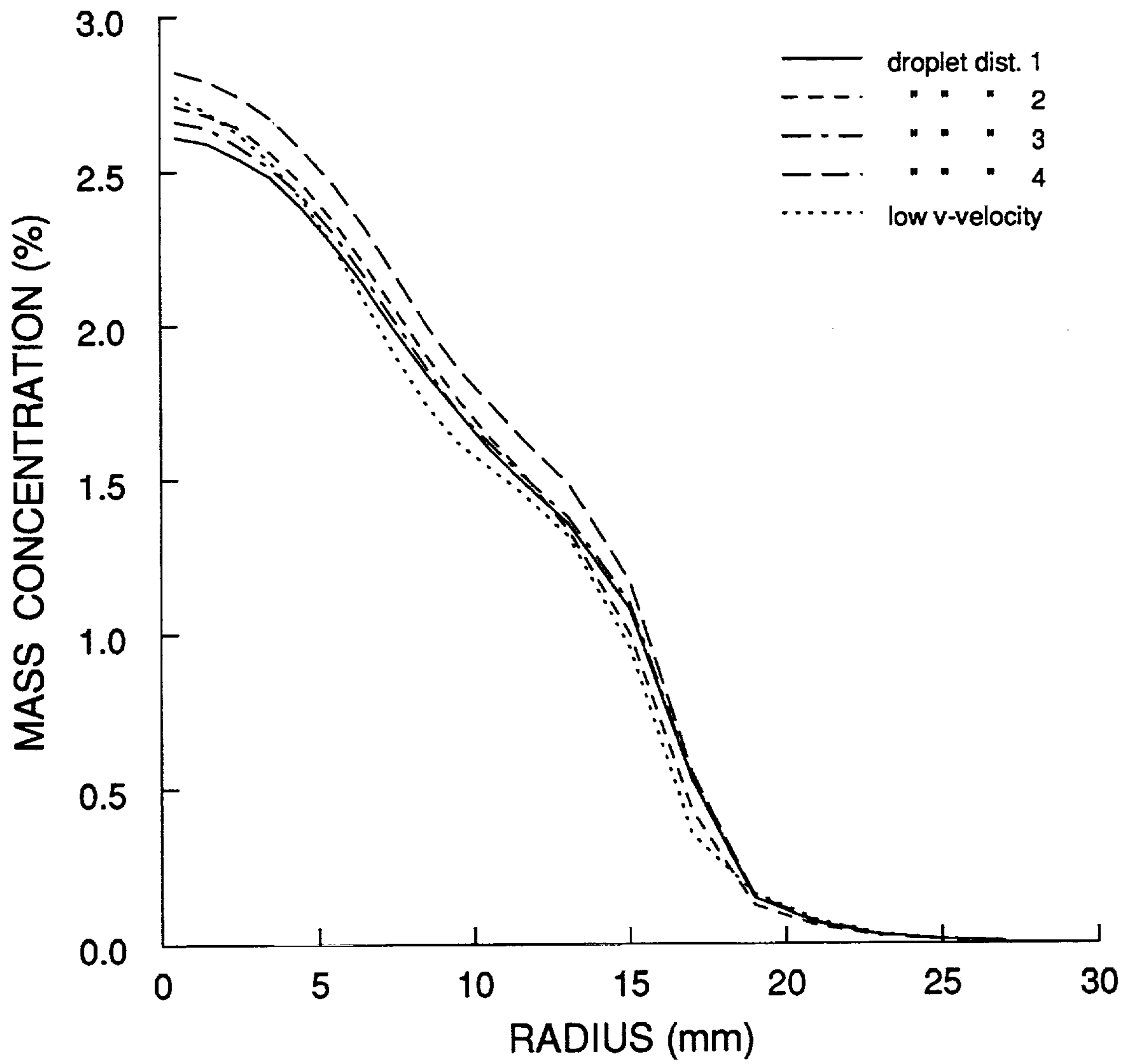

Figure 5.16 Methanol concentrations at 15 mm

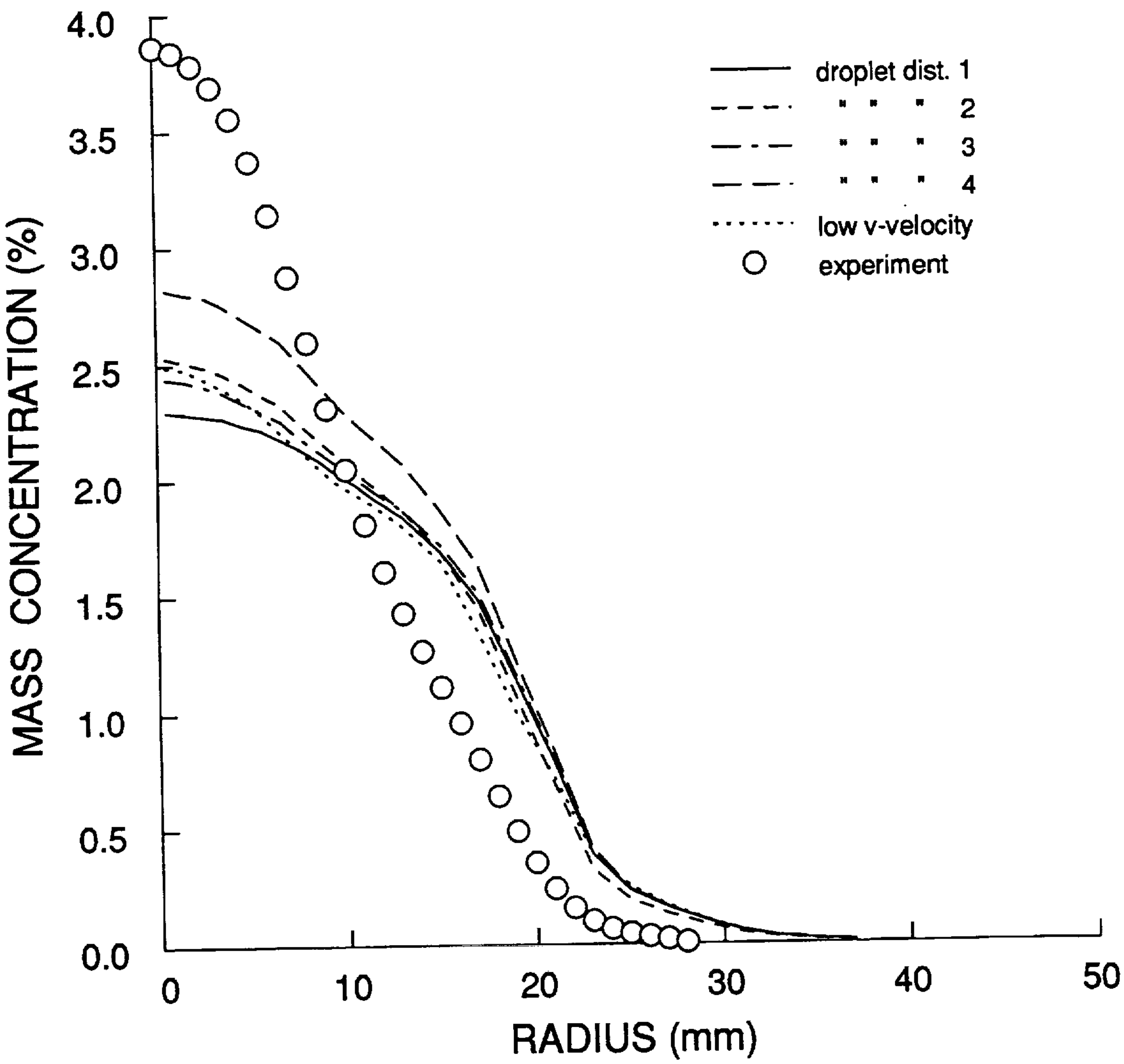

Figure 5.17 Methanol concentration at 25 mm

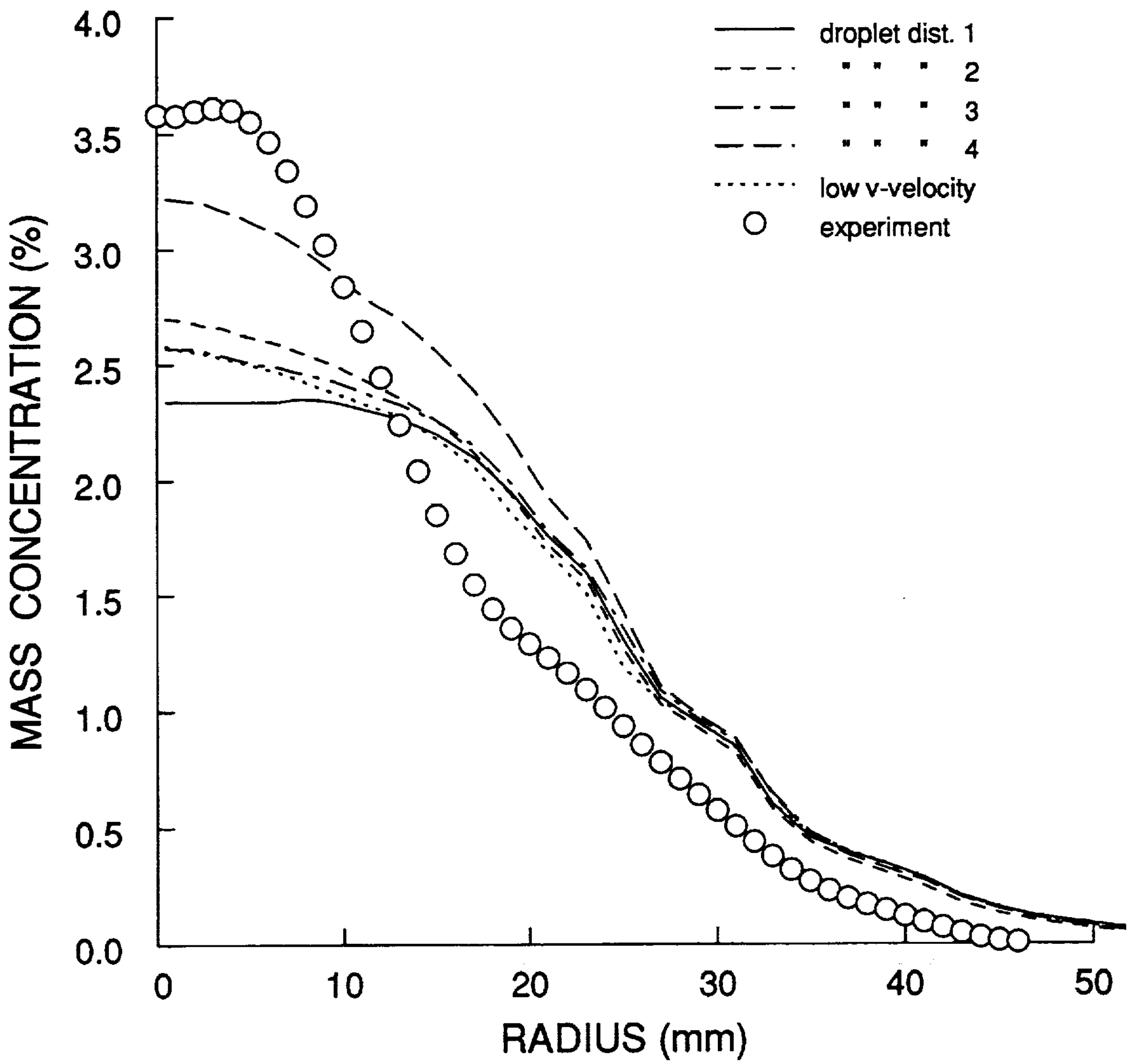

Figure 5.18 Methanol concentration at 50 mm

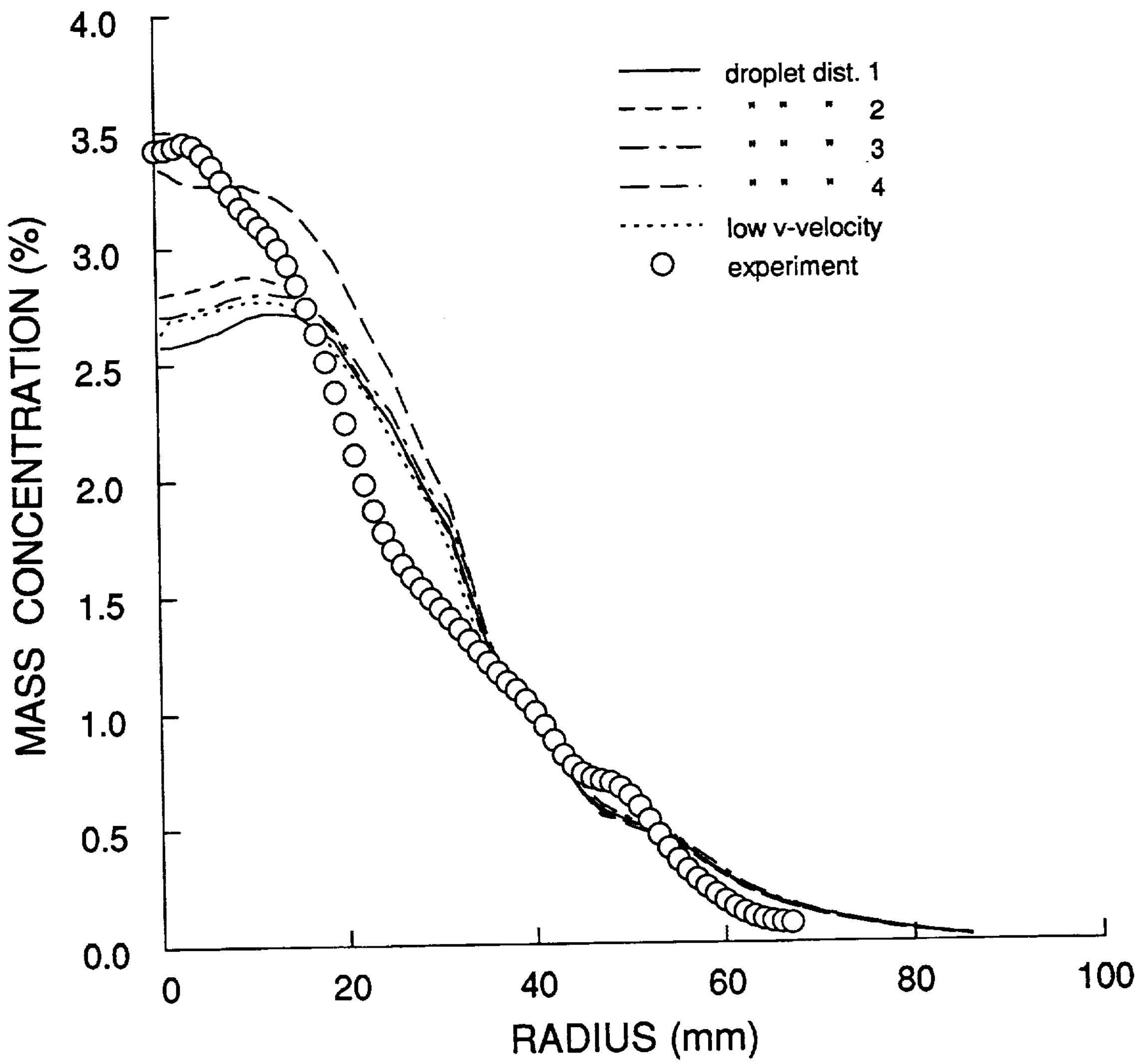

Figure 5.19 Methanol concentration at 100 mm

All of the predicted profiles are flatter and wider than the measured profiles, with the highest peak shown by droplet distribution number 4 which has the largest number of small droplets. The predicted methanol contours are diffusive, suggesting a deficiency in the numerical differencing model. Correcting this deficiency is beyond the scope of this work. The outer portions of all of the predicted contours are similar. McDonell states that some of the methanol concentration measurements are at a saturation state along the center-line. Predicted methanol concentration initially drops along the centerline. The maximum calculated concentration is never as high as the peak experimental measurements. This suggests that the spray model may be somewhat deficient in regards to the saturation concentration. An off-center peak is shown by all of the predicted contours at 100 mm while the measurements show off-center peaks at 50 and 100 mm. In the predictions, an axial location is eventually predicted in the flowfield where all droplet groups are continually spreading outward. Even if a droplet group is started with a negative radial velocity, the calculated droplet trajectory will eventually cross the centerline, be reflected in the calculation and become positive. Thus, the calculation should predict an off-center methanol concentration peak as the evaporating methanol droplets move further from the center-line. Some predicted and measured droplet axial velocities at axial distances of 15, 25, 50, and

75 mm are shown in figures 5.20-23, respectively, for the third prediction (probe area taken into account, no individual weighing of error measurement). The data for the other predictions should be almost identical, as the largest difference should be the gas-phase velocities which was shown to be almost identical for all the changes in spray input. The predicted velocities are shown as curves while the measurements are shown as symbols. The predictions were done with initial droplet sizes of 7.4, 15.5, 25.5, 35.5, 45.5, 55.5, 68.0, 83.0, 98.0, and 120.0 μm in diameter to correspond to the ten size ranges used in the measurements. The profiles at 15 mm are very good and remarkably smooth. This tends to verify the initial conditions used for the calculation. The predictions for the large droplets at the next axial measurement location are also very good. The prediction for the 31 to 40 μm droplet groups show some oscillation. Some of the droplet groups are crossing each other. One group with lower axial velocity is crossing the path of a droplet group with higher axial velocity, resulting in a discontinuous profile when plotting the velocities of the droplet groups. The further downstream, the more opportunity for the predicted droplet groups to cross paths. However, all of the droplet groups do approach the gas phase velocity as a function of their size and speed. This tends to smooth the velocity profiles, canceling the first effect. Also, this effect should not have much of an effect on the

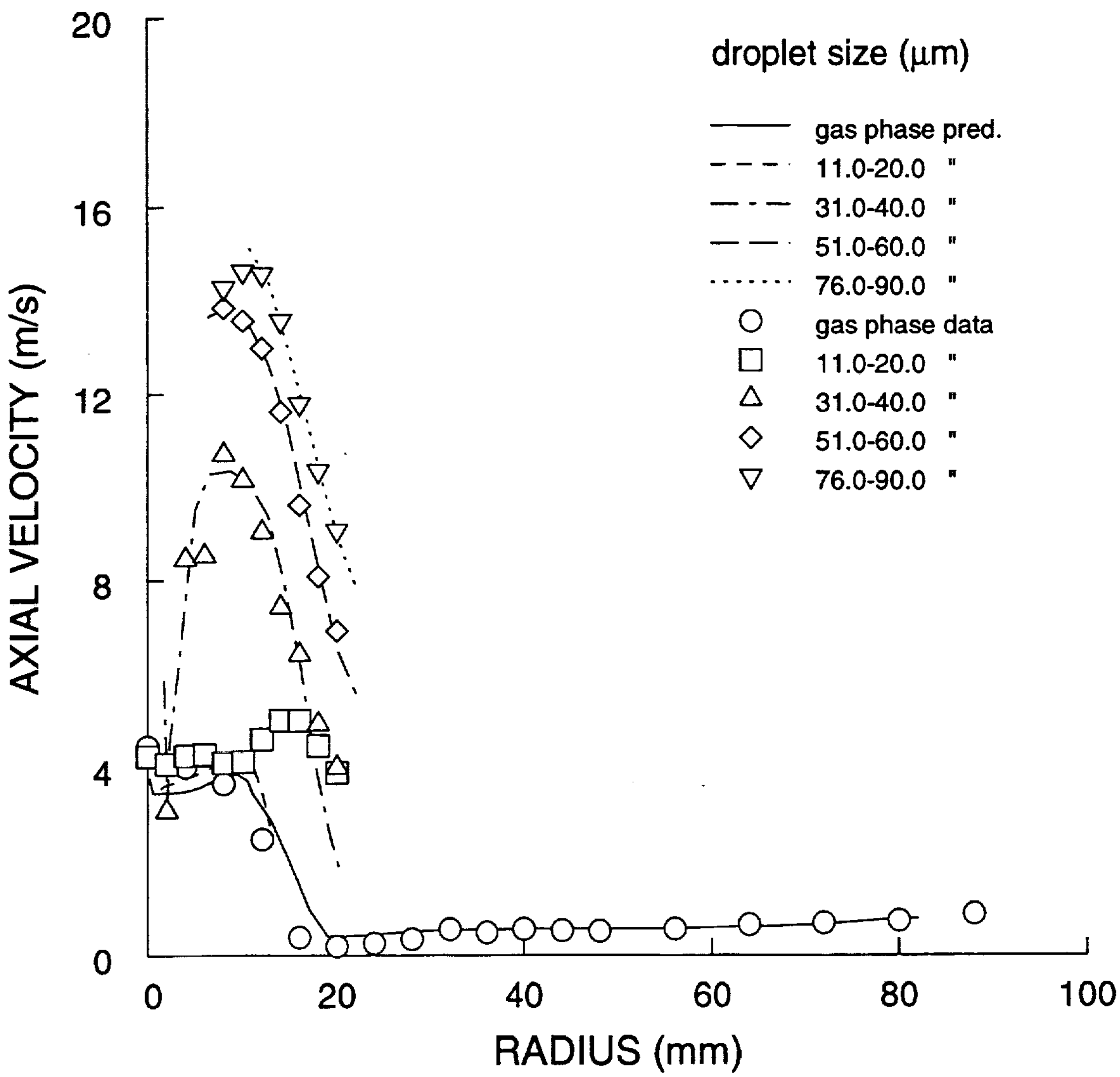

Figure 5.20 Droplet and gas-phase axial velocity at 15 mm

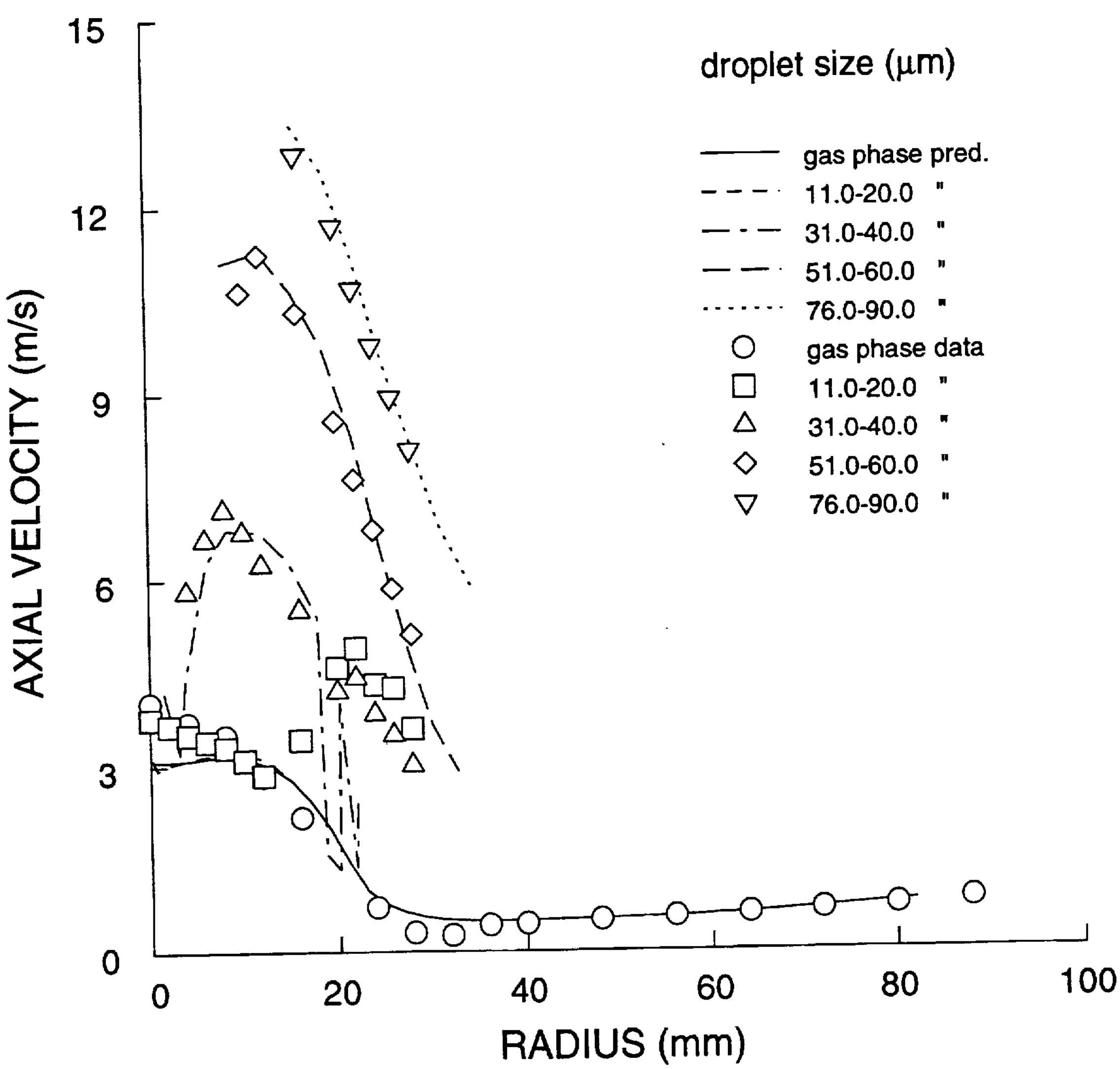

Figure 5.21 Droplet and gas-phase axial velocity at 25 mm

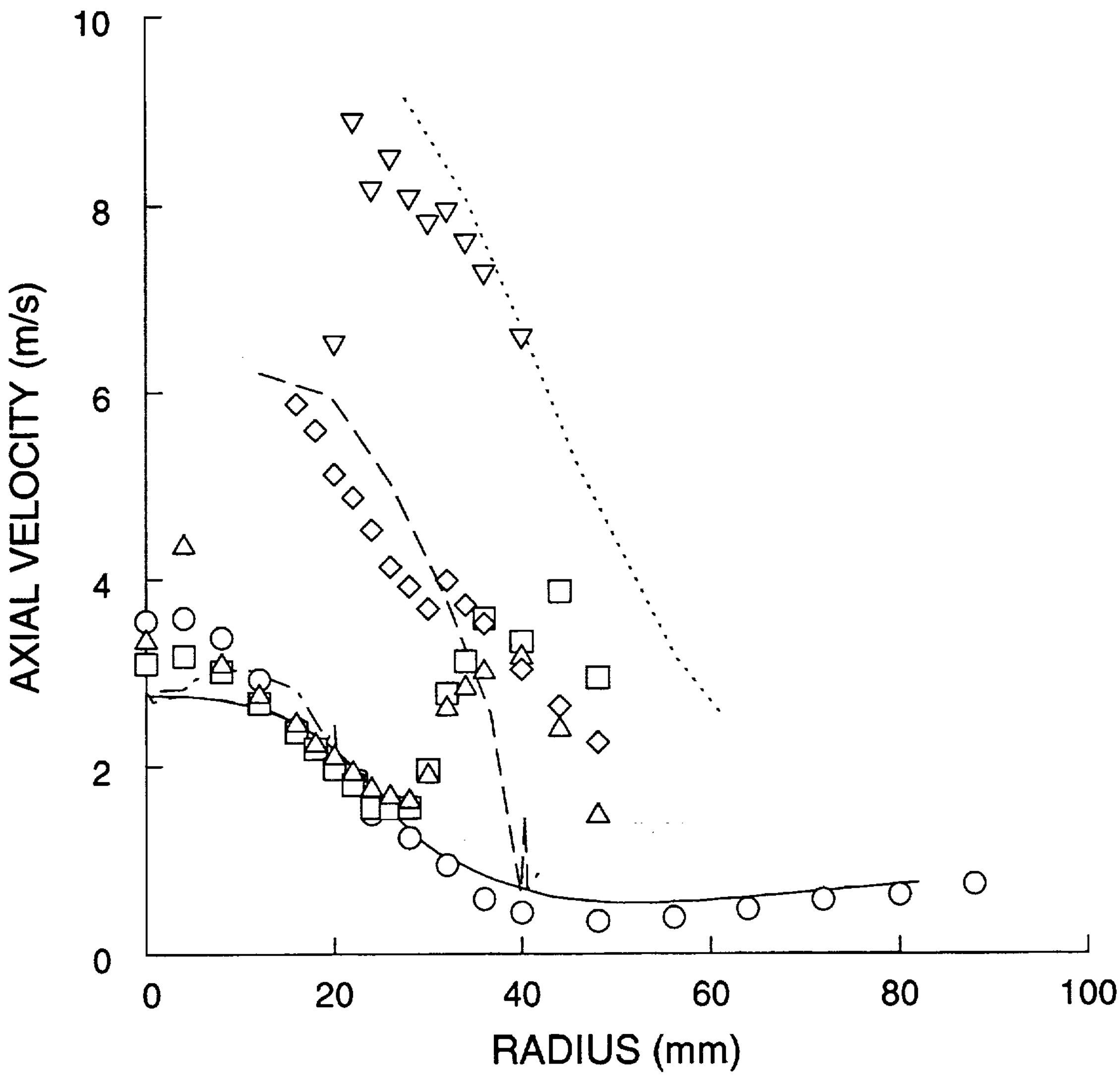

Figure 5.22 Droplet and gas-phase velocity at 50 mm

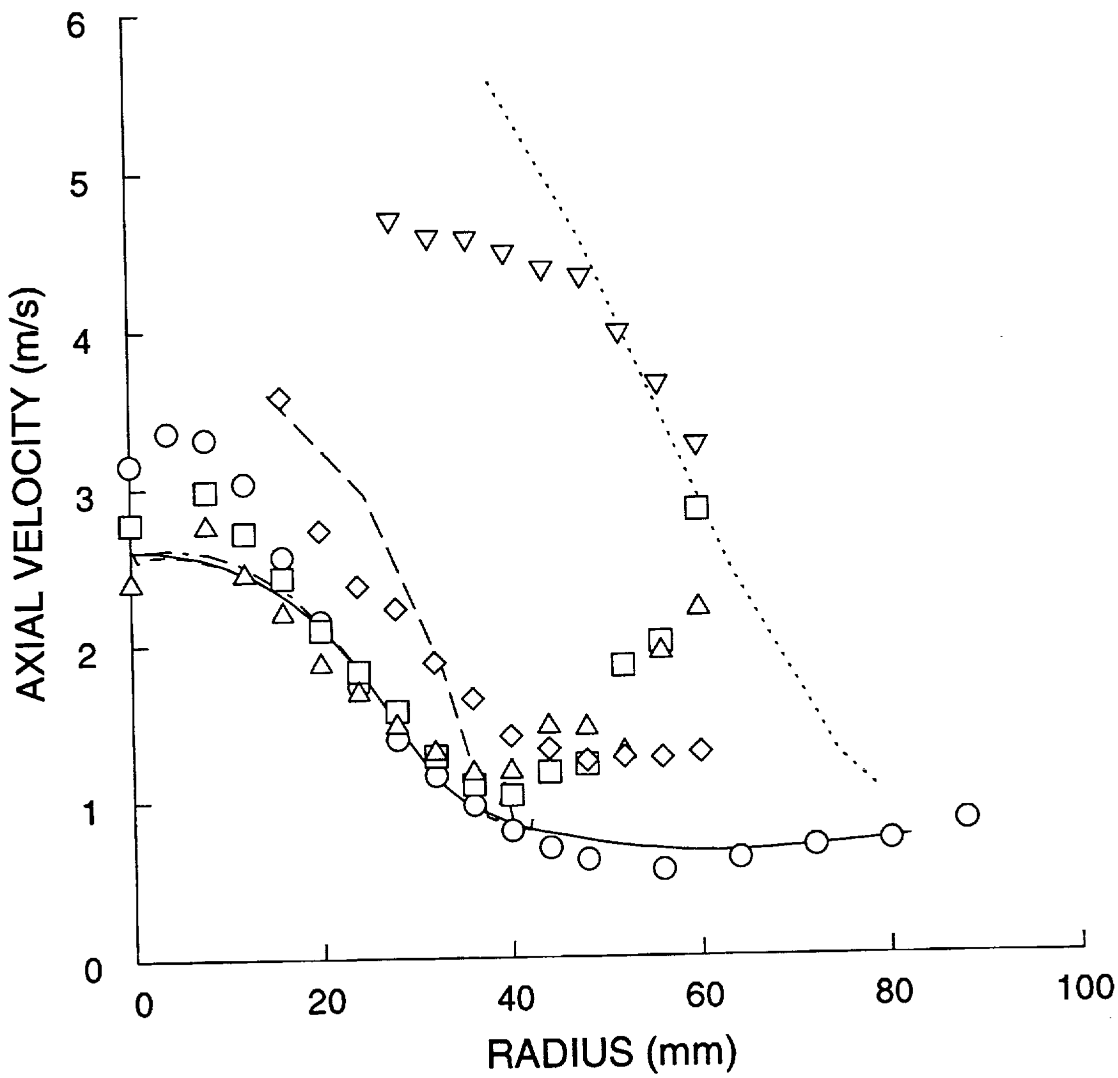

Figure 5.23 Droplet and gas-phase axial velocity at 75 mm

concentration prediction, which is more important than the prediction of each droplet group's velocity. At an axial distance of 50 mm the predicted velocities for the two smallest groups shown are nearly the same as the gas-phase velocities while the measured profile shows the same behavior at less than 28 mm radius but shows a second outer peak with nearly the same velocities as measured for the 31-40 and 51-60 SMD droplet group measurements. In checking the predictions more closely, it was found that no droplets in this size range were found beyond a radius of 18.5 mm at this axial location. The initial measurements at 7.5 mm do not show a secondary peak. There is no gas-phase fluid dynamic structure or effect that would cause this. The only possibility is droplets from another droplet group. In the predictions, only the smallest droplets significantly evaporate, while the larger droplets only lose a small fraction of their size. The smallest droplets eventually are treated as totally evaporated when they reach a certain size. This is done because the fixed droplet time step could produce non-physical results. The use of smaller droplet time-steps would allow tracking the droplets longer but this would increase the number of computations and memory needed dramatically. The predictions do not show any droplets losing enough mass to be included in a lower size droplet group within the first 100 mm. The predictions show that some of the original 15.5 μm droplets are reduced to

10.5 μm in size when they pass the last measurement location of 100 mm. Larger diameter droplet groups are reduced in diameter even less. The largest droplets only lose about 2 μm in diameter in 100 mm. The predictions are started using 10 different droplet sizes. Each inlet droplet represents an average of a very large number of droplets spanning at least 10 μm in diameter. Conceptually, a group of droplets near the smaller end of a droplet bin size range would drop into the next size measurement bin at a downstream location. The secondary peaks measured later in the flowfield are most likely part of a group of droplets having larger diameter and velocity near the injector. This effect could be duplicated in a calculation by increasing the number of initial sizes. The smaller size would evaporate enough to drop into the next size range during the simulation, providing data for the smaller-diameter group at that location. However, the prediction of these velocities is not a requirement for accurate calculation of methanol concentration. The predicted droplet is still there, producing vapor, and other effects. It's just that the spray model works with a discrete size and the measurements deal with a range of sizes. The production of methanol vapor is largely unaffected if additional droplet groups are added with the appropriate averaging for the diameters. More droplet groups would help along the calculation axis of symmetry where calculated droplet trajectories eventually all diverge. The spray model interpolates between droplet sources for individual grid cell source terms. With no or few source terms near the axis of symmetry, the predicted methanol concentration can be depressed.

There is another difference between predictions and measurements. The predictions show large droplets up to and beyond a radial distance of 60 mm at an axial distance of 50 mm. The measurements were stopped at an radial distance of 48 mm. The measurements at this location show a fairly high droplet rate. From these numbers, it may be deduced that there are many droplets beyond 48 mm. This same defect is also seen at an axial distance of 75 mm, where the calculation shows droplets up to 80 mm radius and the measurements are cut off at 60 mm. This defect shows up also in bar graphs of the droplet flux.

In the measurements, the number of droplets crossing the probe area are counted. A radial profile of these numbers is somewhat Gaussian. In the predictions, the droplet flux must be converted into a number of droplets entering the calculation domain in a certain time-step. The number of droplets crossing an area must be converted into a set of droplet groups with specified numbers, sizes and velocities. The Lagrangian predicted radial location of droplet groups changes as the groups move downstream. The predicted radial location does not vary uniformly as does the experimental measurements which are taken at specific locations. Also, in the predictions, the number of droplets in a group does not change, unless that group evaporates (is taken out of the calculation). Thus, the measurements of density and the predictions of droplet location cannot be directly compared. In this case, the predicted data will be processed to resemble a normalized droplet density to compare to the measured droplet fluxes. This was done by dividing by a pseudo-area for the droplet group and then non-dimensionalizing this by the total number of droplets in that size range. A minimum area was specified so that a unrealistically large number would be calculated at small radii. Also, if more than one group was calculated at nearly the same radius, the groups were sometimes combined in the plots. The measured data are also normalized. That is, the sum of all normalized droplet densities adds up to 1.0. Accordingly, the data obtained are a somewhat graphical representation of the calculated position of the droplet groups and the fraction in each group. The droplet distributions at 15, 25, and 75 mm are shown in figures 5.24-31. Both the measured and predicted droplet densities are somewhat Gaussian and show spreading. The numerical predictions generally keep the same shape through the calculation until droplet trajectories cross each other. At this point, the predicted bar graphs become somewhat ambiguous. Droplet group fractions should probably be combined in some of plots. In the predictions, the effect of an increase in

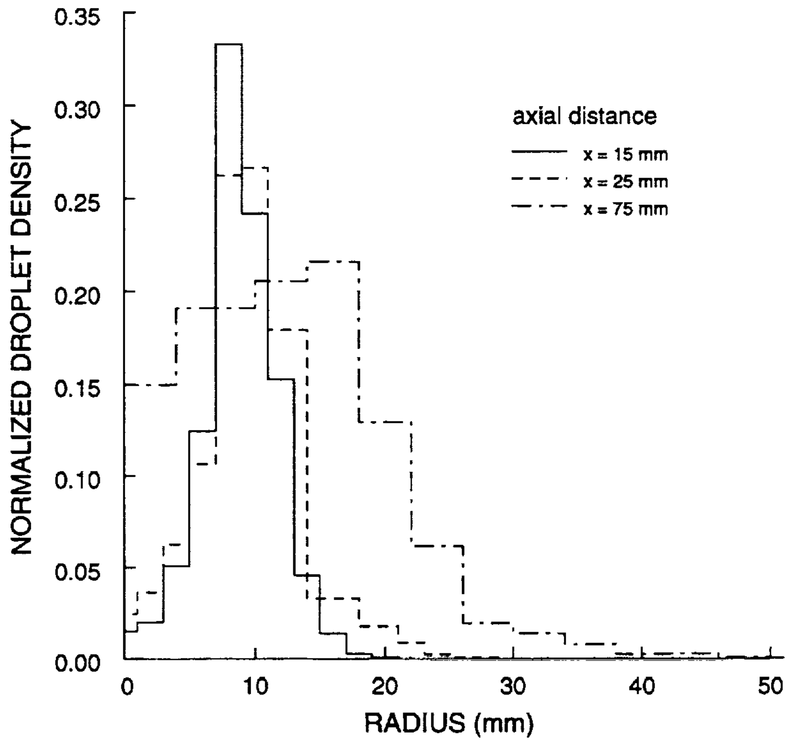

Figure 5.24 Measured droplet density data for 11 - 20 micro-meter droplets

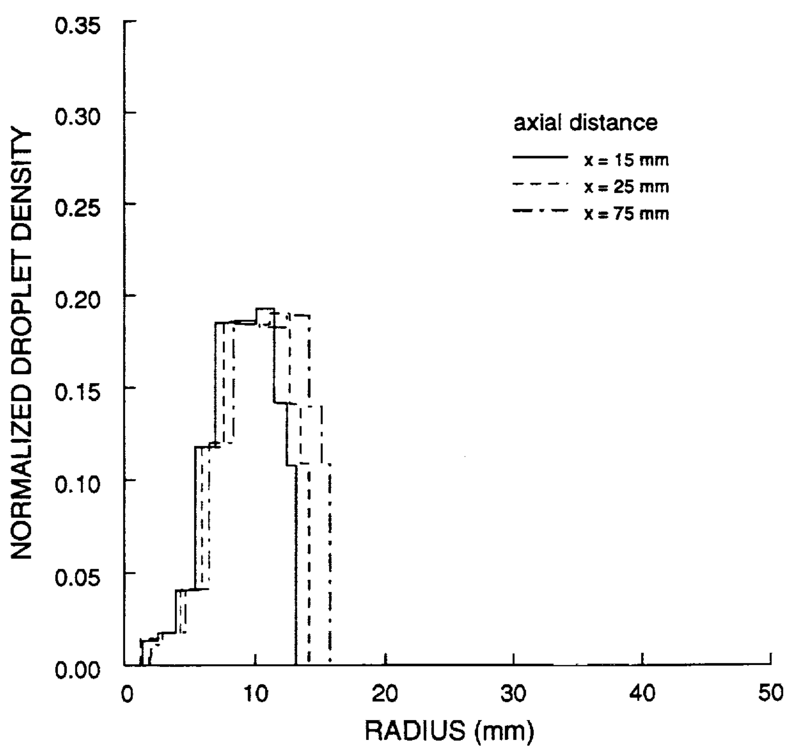

Figure 5.25 Calculated Droplet density for 10.5 - 20.5 micro-meter droplets

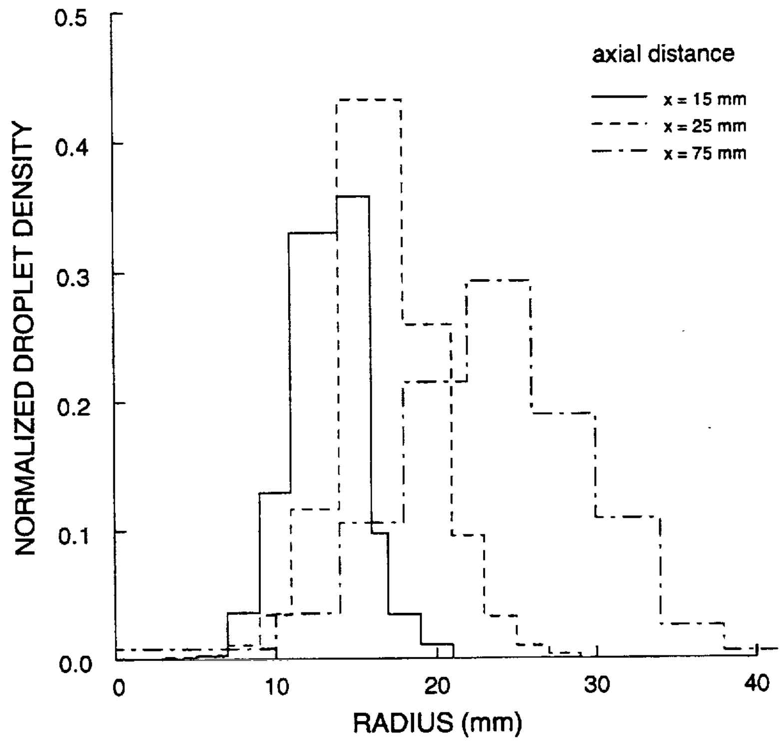

Figure 5.26 Measured droplet density for 31 - 40 micro-meter droplets

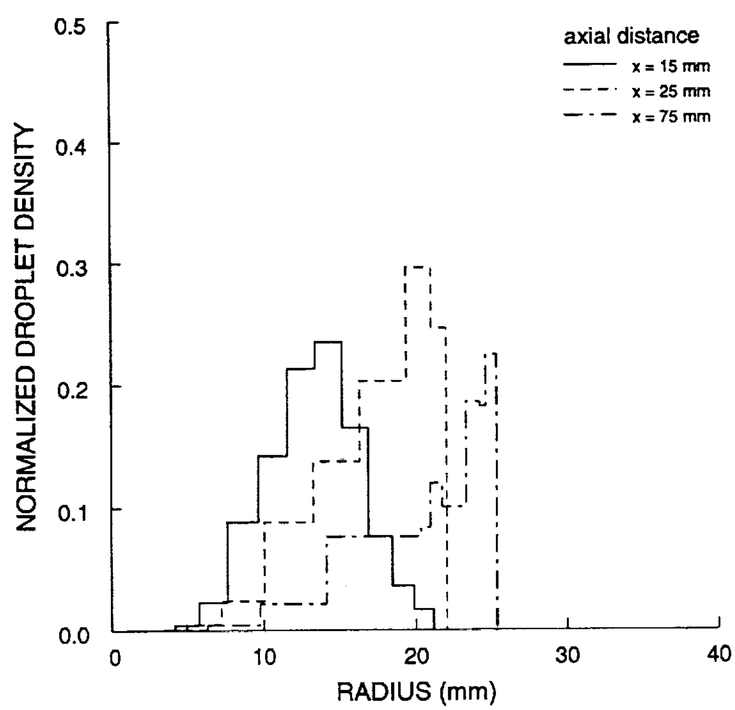

Figure 5.27 Predicted droplet density for 30.5 - 40.5 micro-meter droplets

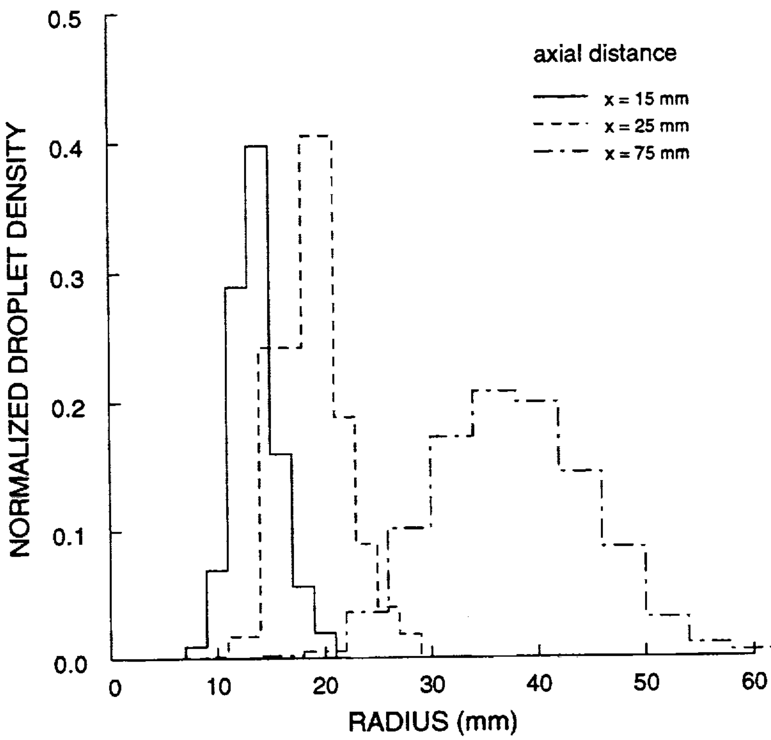

Figure 5.28 Measured droplet density for 51 - 60 μm droplets

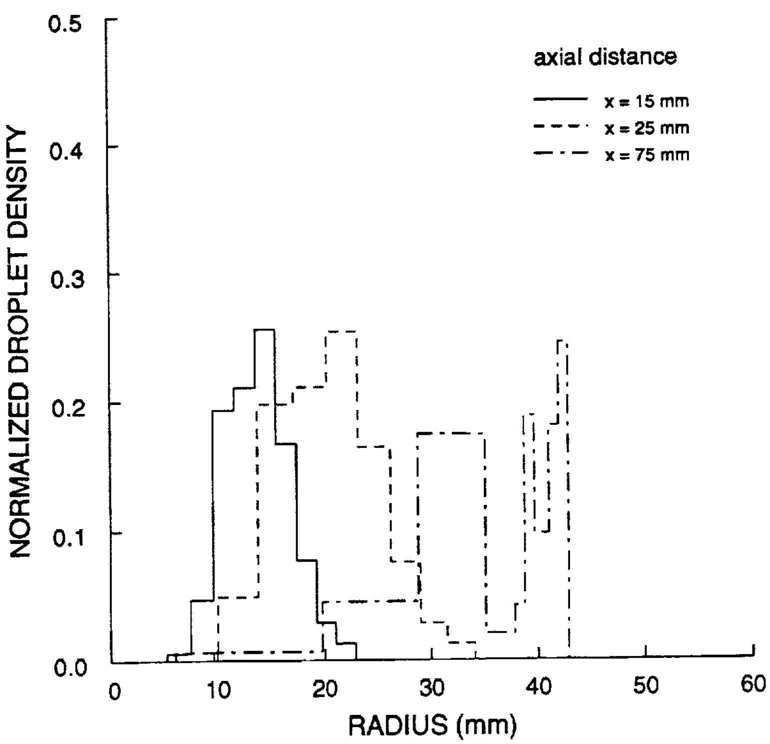

Figure 5.29 Predicted droplet density for 50.5 - 60.5 μm droplets

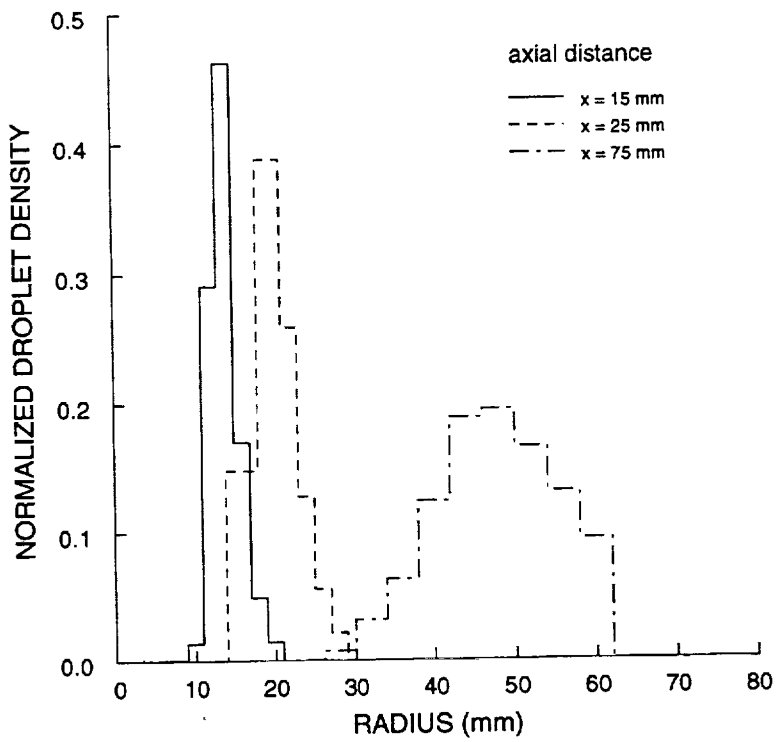

Figure 5.30 Measured droplet density for 76 - 90 μm droplets

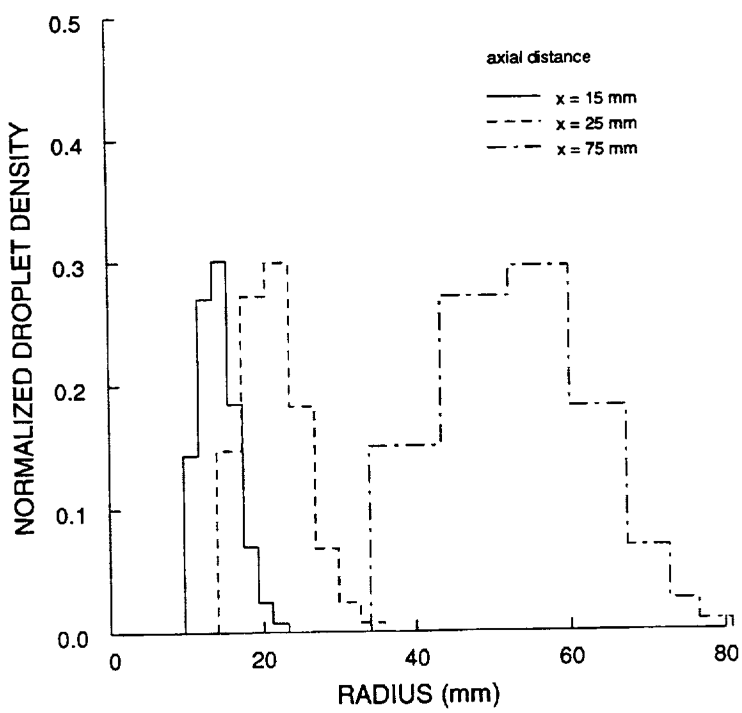

Figure 5.31 Predicted droplet density for 75.5 - 90.5 μm droplets

droplet density is seen as a decrease in distance between droplet groups, not as an increase in the number of droplets. An increase in droplet density is intuitively contradictory for this flowfield, and numerical predictions of such effects most likely represent slightly incorrect initial velocities. However, the somewhat inaccurate calculation of numerous droplet densities does not have a large effect on the prediction of methanol vapor concentration. It would be computationally impossible to model each droplet. The numerical predictions do not show as much spreading as do the measured droplet densities, except for the largest diameter droplets. The spray prediction model does not take into account interaction between turbulent eddies and droplet groups. Droplet turbulent dispersion models take this effect into account. In this model, droplet interactions with the turbulent eddies are modeled by varying the instantaneous gas phase velocity surrounding the droplet by using statistical fractions of the turbulent fluctuation velocity calculated from local turbulence quantities. This would tend to increase the droplet spreading. However, to do this the number of droplet groups must be increased by at an order of magnitude in order to maintain meaningful results. This would increase calculation time also by an order of magnitude. This is impractical for this work as testing turbulent combustion models will also substantially increase calculation time.

The largest diameter droplet density graphs show similar spreading for both experimental and numerical predictions. The larger droplets are affected less by gas-phase drag, having a lower surface to volume ratio. Thus, the larger droplets tend to spread further. The full extent of large droplet spreading was not found since the measurements were terminated too early.

The current droplet spray model produces good results for methanol concentration. Droplet velocities can be surprising well predicted. There is an error in the amount of droplet spreading. However, there isn't a large enough variance from experimental measurements to justify a turbulent dispersion spray model, with its substantially increased computational costs.

5.2.3 - Spray Combustion Calculations

Both spray modeling and spray measurement capabilities have markedly improved in the last 15 years. In a 1980 paper, El Banhawy and Whitelaw[113] assumed two spray distributions. Also, the droplet vaporization model used in the calculations did not take into account the effect of combustion. The capability now exists to measure droplet spray distributions for size, number flux, and velocity. Spray combustion data is being assembled from simplified research-type combustors. Gaseous data is also needed to validate or benchmark spray combustion models, as the gas phase must be accurately predicted in conjunction with the liquid phase. Thus, measurements of gaseous velocity, species concentration and temperature must also be taken. There is some progress at measuring species and temperature using non-intrusive optical methods, but, this is a developing and specialized discipline. Measurements of temperature and species can have substantial error. Spray measurements at the inlet of the combustor have the greatest impact on numerical predictions. These measurements are also the most difficult. The flow is optically dense close to the spray nozzle. Thus, the more accurate spray measurements are at substantial distances from the spray nozzle. The accuracy of inlet conditions for spray combustion leaves room for improvement. The gaseous species concentrations may have to be inferred from the difference of liquid fuel delivered to the combustor and measurements of fuel spray flux.

A partial database for spray model validation is given in Edwards and Rudoff[114]. An optically dense zone of roughly 25 mm diameter and 25 mm long is shown in one of the figures. Spray data are given at an axial station of 50 mm. Velocity vector diagrams for the gas phase and spray show that the reverse flow along the combustor centerline reaches no closer than 25 mm from the spray nozzle. Droplet data at the first two measurement locations are marked as biased. A central recirculation zone is caused by swirling inlet flow. The flow is not contained. Maximum velocities within the burning flow are of the order of 15 m/s. The rest of the flow appears quiescent. This type of open, recirculating flow is particularly difficult to accurately predict. Phase Doppler Particle Analyzer or PDPA is used in the measurements. In a 1988 paper[115], the PDPA measurement method was compared to another method. It was found to agree within 15%. In a 1993 paper[116], a correction scheme is demonstrated. It was concluded that this correction scheme was difficult to employ in swirling 3-D flows. A new correction scheme is being worked on.

In another 1993 paper, Presser et. al.[117] present some non-burning and burning data for swirl numbers of 0.0, and 0.53. Laser sheet pictures are shown for swirl numbers of 0.0, 0.39, 0.53, and 0.76. The gas phase flow velocities of the open combustor are low, giving a moderate sized central recirculation zone. The maximum axial velocity is about 3 m/s. Maximum axial spray velocity is over 15 m/s. Droplet axial velocities seem to be all positive for a swirl number of 0.53. Increasing swirl increases the radial displacement of the spray. Temperature and species concentration measurements are not given.

In another 1993 paper, Ghaffarpour and Chehroudi[118] present temperature and droplet data for a hollow cone kerosene spray. Droplet characteristics were reported for mean velocity and mean droplet diameter. Negative mean axial droplet velocities are shown along the combustor centerline at distances of 40, 55, and 70 mm for the non-burning case. The first measurement location was 15 mm from the injector. Mean axial droplet velocities at this station were all positive, although the velocities were lower for the burning case. The burning case shows considerably more radial spreading of the fuel spray. The only gas phase velocities reported were from the non-burning case, which indicated a central recirculation region. Measurements of burning and non-burning droplet flux are nearly identical, indicating negligible droplet vaporization and/or burning. Conversely, temperatures within the hollow cone area were fairly high, about 500 degrees C at 15 mm and 600 degrees at 25 mm. The authors infer that this is due to a downward movement of the central recirculation zone for the burning case, but this flow needs to be properly seeded to measure velocities in this region. Before this case can be used for spray model development, the gas phase velocities must be accurately measured and droplet statistics should be specified for various droplet size groups, not just for mean diameters. Using mean quantities limits the number of droplet groups at the 15 mm location to about sixteen.

The combustion case of Bulzan [108] was used to benchmark the combustion spray model. The flow configuration is identical to the isothermal case studied earlier, except that the injector was supplied with liquid heptane fuel. Temperature, gaseous and liquid velocities were measured. Data were meticulously taken and repeated to minimize experimental error. Great pain was taken to eliminate 3-Dimensional effects, such as locating the swirler for the co-flowing air-stream 140 mm upstream of the injector face. The combustion experiment does not have combustor walls. This makes it simpler to get optical measurements, but makes it difficult for the combustion modeler, as the flow entrains ambient air. Runs were made with entraining boundary conditions, but this modeler found it best to specify boundary conditions at measured radial locations. The average radial velocities are rather low but show large variation. This modeler was not able to duplicate such high turbulence with low velocity. Initial calculations were performed using 70 axial gridpoints and 55 gridpoints in the radial direction. Measurements taken 2.5 mm from the face of the spray injector were used as initial conditions. These data are much closer to the combustor spray nozzle than reported by others. The droplet groups are differentiated by droplet size ranges and location. Close to the injector, droplet measurements were taken at 1 mm intervals out to a radius of about 13 mm, where the data rate became negligible. The droplet data were separated into 10 size ranges or bins. These bins are then characterized by average diameters. The average group diameter range is from 6.893 to 122.65 micrometers. These data were reduced to 79 droplet groups as some velocity data were unreliable due to the scarcity of data, or the amount of fuel spray in the group was judged as insignificant. Obviously, the computer time needed to calculate the spray and its influence on the gas phase will roughly scale with the number of groups. Data were taken as a number flux at specified radius. For calculation purposes, the flux data were multiplied by an appropriate area to get the total number of drops in a group. The total spray mass was calculated and this was significantly different than the measured fuel flow rate to the injector, which was originally taken as 0.38 g/sec. The difference was input as a combination of fuel and combustion products. Originally, it was planned to take probe samples for discerning gaseous species concentrations. Bulzan now feels that sample probes would distort the flowfield producing inaccurate results. Measured values of temperature are low in the dense spray due to droplet impingement on the probe. Gas sample probes would also be greatly affected by the spray. The only data with which to infer gaseous mass fractions are the total rate of fuel flow and temperature measurements. The temperatures in this area were inferred from neighboring temperatures not exhibiting droplet cooling. To come up with appropriate inlet mass fractions, a sub-program was used to calculate temperature as a function of increasing fuel mass fraction. A fixed final ratio of unburned to burned fuel was used while keeping the total enthalpy constant. The numbers were iterated/modified upon to get the total overall fuel rate. As initial rough grid calculations produced higher than measured temperatures, the heating value of the fuel was dropped by 10 % for better agreement. Initial calculations were done assuming no correction to droplet number flux. In McDonnel's thesis, it was concluded that most of the droplets were not measured in the area of dense spray close to the injector. If multiple drops are detected within the measurement zone, the data are discarded. The measurement of mass fractions were determined to be more accurate than that of droplet flux, so the droplet flux was corrected. The droplet flux closest to the injector was off by a factor of almost 4. Bulzan didn't report species concentrations which would have enabled correcting inlet droplet number flux. Also, the data are further complicated by combustion, widely varying temperature, and very rapid evaporation. Several 70 by 55 grid calculations were made with different spray flux corrections. It was found that the best agreement was found by assuming that about 35% of the fuel and fuel in combustion products were gaseous. Temperature was significantly overpredicted. Since the rougher grid calculations were made, it was found that the total fuel flow rate was actually 20% lower. Succeeding calculations used a finer grid and a corrected overall fuel flow rate. The finer grid essentially doubled the number of radial gridpoints in the fuel injector zone. A velocity vector diagram of a portion of the flowfield is shown in figure 5.32. The flowfield structure is simpler than for the isothermal case. In the combusting case, the recirculation bubble is closed within the confines of experimental measurement limits. Axial velocities are all positive 200 mm from the combustor injector. In the isothermal case, reverse flow existed out beyond the last measurement station, and modeling proved to be rather difficult. In addition, the small toroidal recirculation bubble seen near the fuel injector and co-flowing air stream in the isothermal case isn't measured or predicted for the combusting flow case. Calculation of entrainment is still a problem for the combusting case.

Measured centerline axial velocity next to the fuel injector is negative. This reverse flow is part of a large central recirculation bubble caused by high inlet swirl.

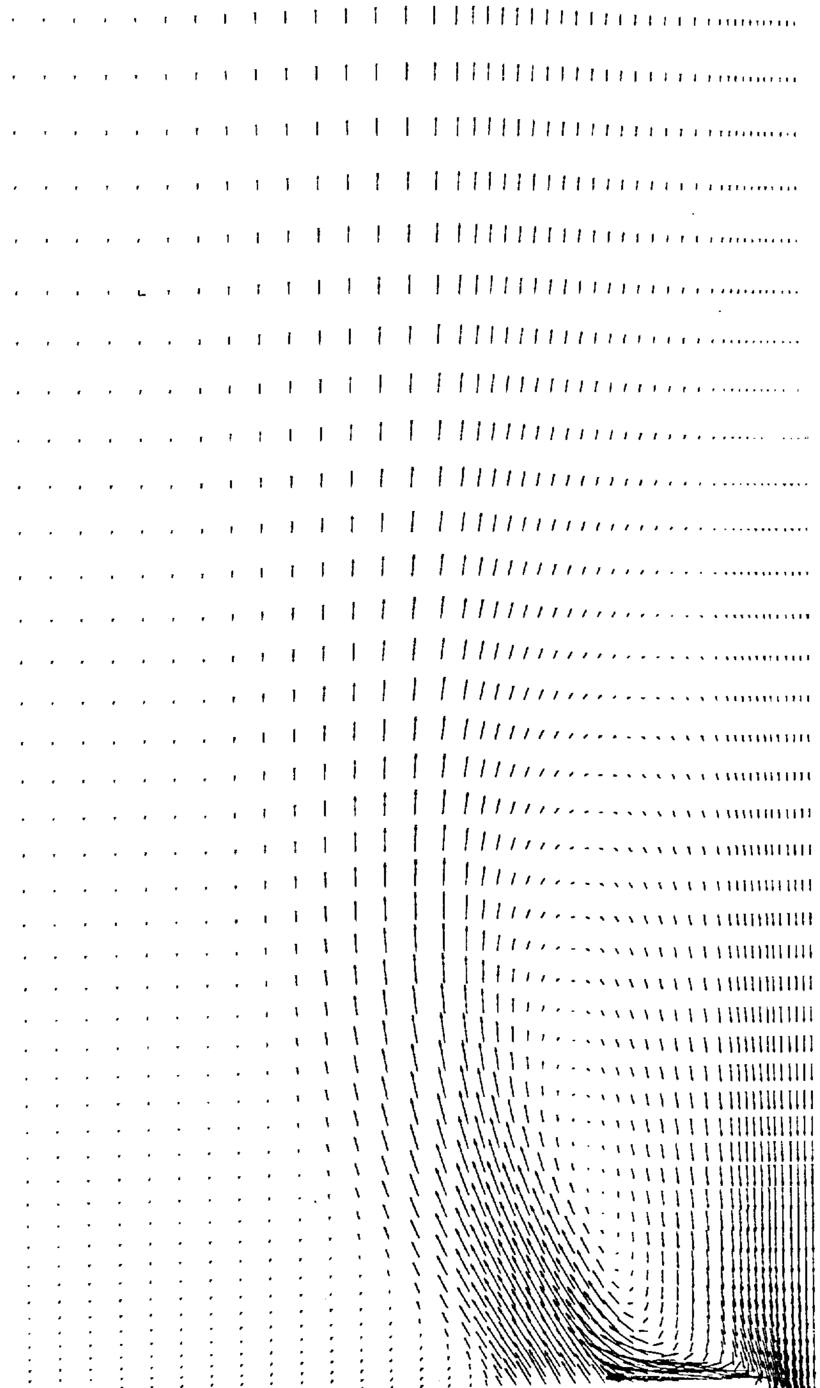

Figure 5.32 Velocity Vector Diagram

Theoretically, the reverse flow should end very close to the fuel injector. The closest Dr. Bulzan was able to perform measurements was 1.0 mm from the injector. At this location, the axial velocity was non-negative, but the spray measurement data were in question. It may be possible to perform calculations starting from the injector face, but the fuel stream breakup would then have to be modeled, which cannot be done at the present time. In this work it was desired to see how good the spray model was, without coupling it to additional modeling to develop or back calculate suitable droplet distributions. It was decided to start with the best possible measured droplet distribution and see how well the combustion spray model predicted successive axial spray distributions.

The numerical simulations started 2.5 mm from the injector face. Plots of the experimental and numerically predicted axial velocities are shown in figure 5.33-38 corresponding to axial distances of 5.0, 10.0, 20.0, 50.0, 100.0, and 200 mm from the fuel injector. In taking the experimental measurements a complete traverse was taken across the combustor. The measurements on one side of the combustor are plotted with negative radii. Numerical predictions were 2-D axisymmetric, thus, the numerical results are simply reflected for comparison purposes. The axial velocity predictions are quite good beyond the region of fuel injector flow. Surprisingly, there is little

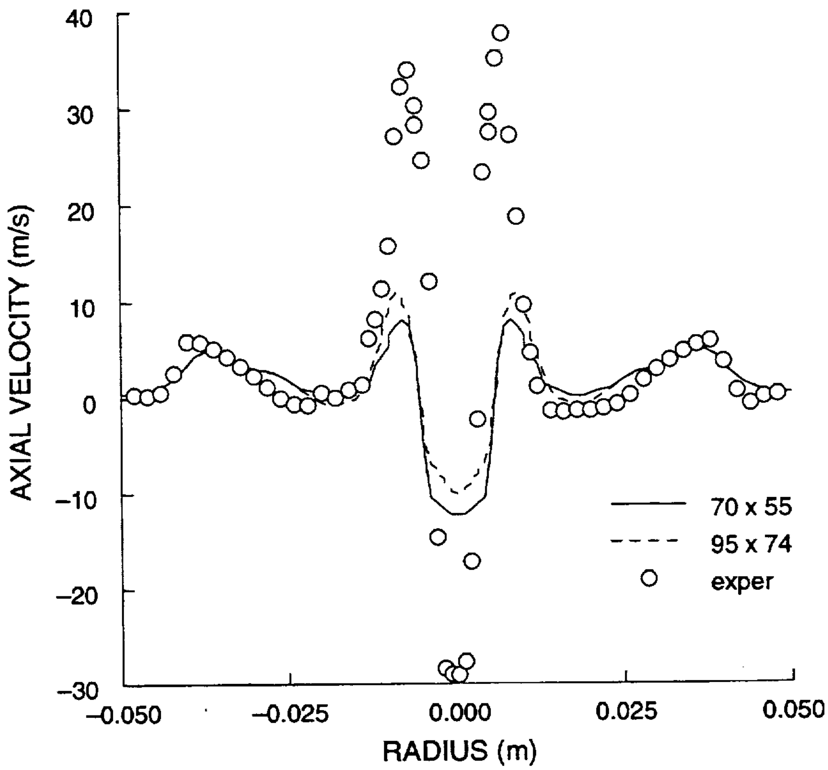

Figure 5.33 Axial Velocity at 5.0 mm.

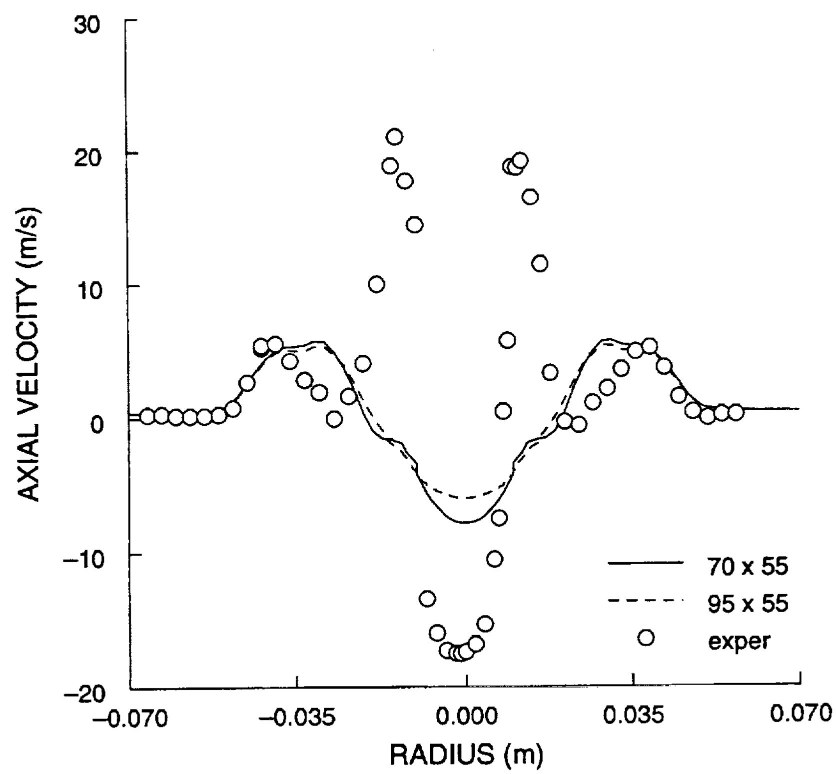

Figure 5.34 Axial Velocity at 10.0 mm

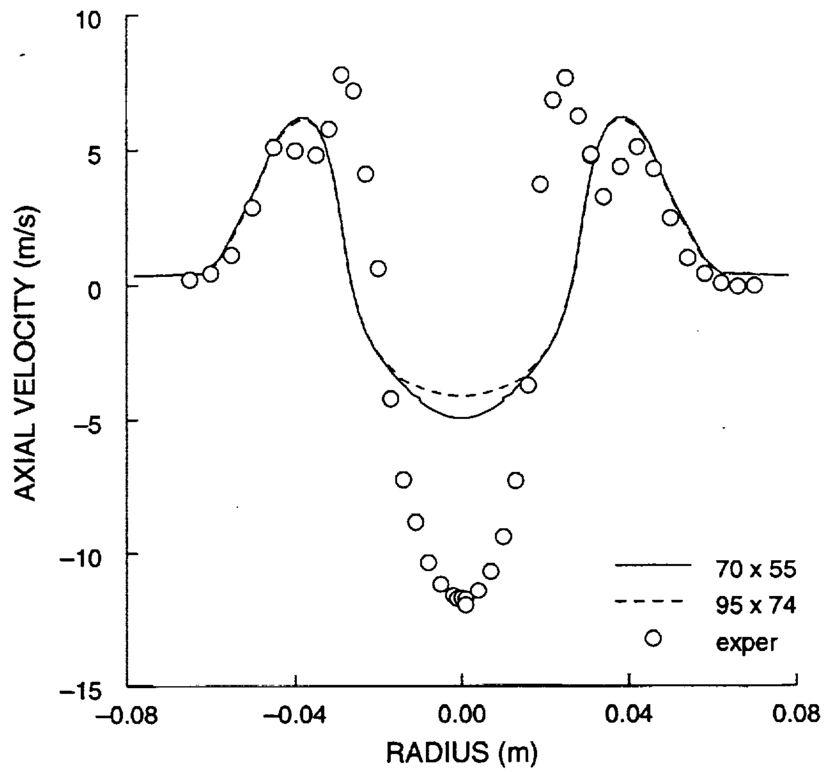

Figure 5.35 Axial Velocity at 20.0 mm.

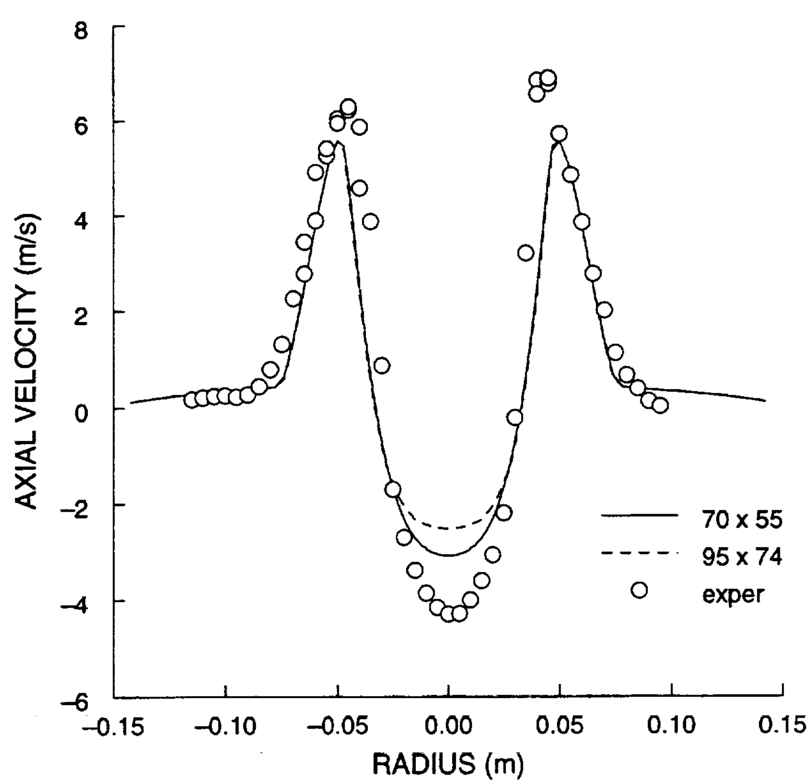

Figure 5.36 Axial Velocity at 50.0 mm.

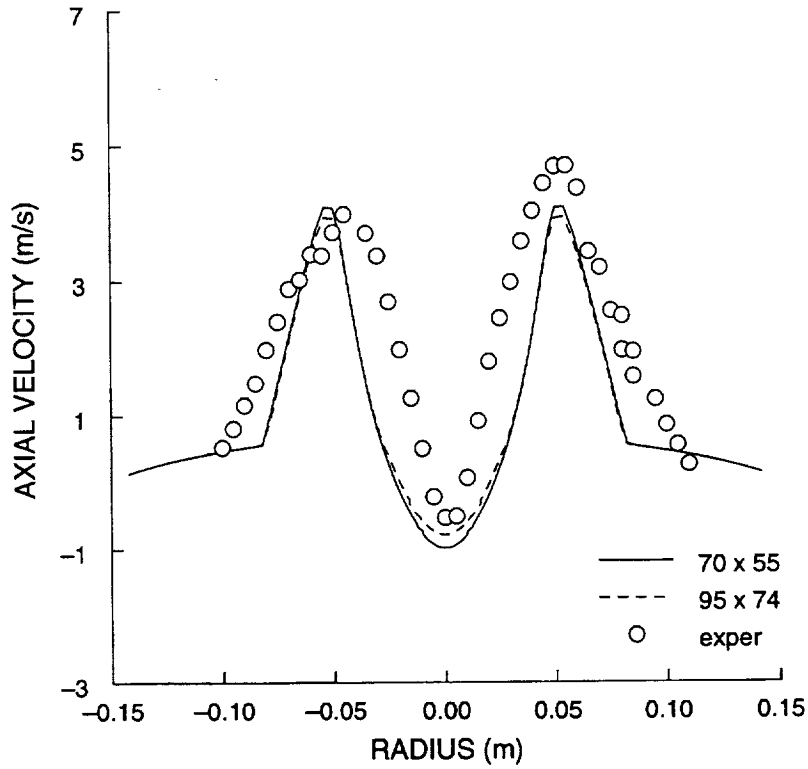

Figure 5.37 Axial Velocity at 100.0 mm.

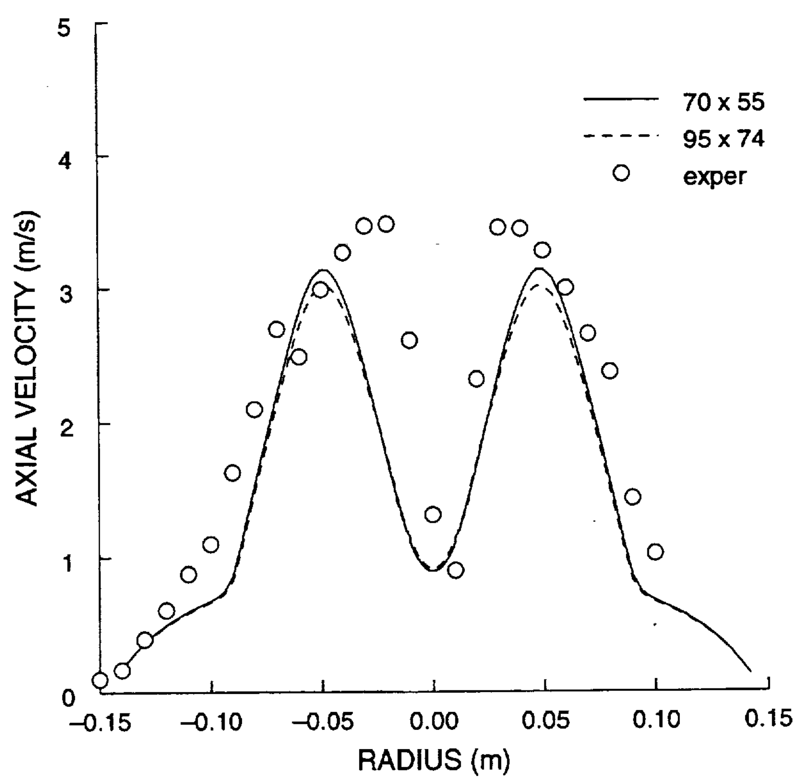

Figure 5.38 Axial Velocity at 200.0 mm.

difference between numerical predictions despite the modeling changes.

The inlet reverse flow velocity specified next to the centerline was about -23.0 m/s. The predicted centerline velocity at an axial distance of 5 mm is about 10 m/s, while the measured centerline velocity is about -30.0 m/s. Experimental centerline axial velocity increases while the simulations predict a decrease in centerline velocity. This poor prediction pattern is also seen for peak axial velocity. The numerical simulations predict peak axial velocity of approximately 10 m/s at an axial distance of 5 mm, while measured peak axial velocity is almost identical to the inlet peak velocity of 35 m/s. The numerical simulations are poorly predicting a critical zone of the combustor. This area of the flow contains the highest concentration of fuel spray. The gaseous velocities should be correctly predicted in order that spray predictions are also correctly predicted. Many additional calculations were done modifying turbulent inlet conditions and modifying the turbulence model in an attempt to better predict reverse flow along the combustor centerline and peak axial velocity. These simulations did not appreciably improve the prediction of axial velocity close to the injector, but mostly shifted the axial velocity peak in the radial direction.

Experimental and predicted peak axial flow velocities at an axial distance of 10 mm are smaller than at the 5.0 mm station. Predicted peak axial velocities are roughly one-third of the measured velocities. The simulations predict almost complete merging of the air-assist fuel injector flow with the surrounding co-flowing air-stream. The simulations predict a larger radial displacement of the fuel-air injector flow than measured. Predicted reverse flow centerline velocities are less than half of measured velocities.

The experimental data taken at an axial distance of 20 mm shows distinct peaks due to the fuel-air injector flow. The simulations are nearly identical except in the central recirculation zone. The simulations predict a single velocity peak. Qualitatively, predicted axial velocities are fairly good, except in the central reverse flow region. Predicted reverse flow velocities are about half of the measured velocities.

At 50 mm, the axial velocity predictions seem to improve. Single velocity peaks are shown for predictions and measurements. The simulations slightly underpredict peak velocity. The quality of the axial velocity predictions in the central recirculation zone are much improved from previous axial stations. The finest grid shows the lowest centerline velocity.

Peak velocity is well predicted at an axial distance of 100 mm. There is little difference between the two numerical simulations. The width of the predicted axial velocity profiles are noticeably thinner than the measured profiles.

This implies the simulations may be incorrectly predicting the total mass flow in the axial direction. This is probably due to the complexity of calculating an open recirculating flow which is entraining ambient fluid.

At 200 mm, the simulations predict nearly identical profiles. Centerline axial velocities are all positive. The recirculation zone closed somewhere between 100 and 200 mm downstream of the fuel spray nozzle. Axial velocity is well predicted from a radius of 5 cm to 15 cm. The simulations predict parabolic-type axial velocity profiles that are symmetric about the peaks. The experimental profile is noticeably non-symmetric around the peak. Large axial velocity gradients are measured about the combustor centerline. The simulations predict a much lower gradient. Qualitatively, the large velocity deficit at the combustor centerline is well predicted. The velocity deficit along the centerline will disappear much more quickly in the experimental profile than in the predicted profiles. The local minimum experimental axial velocity isn't located exactly at the combustor centerline. The experimental axial velocity profile is slightly shifted to the right. This is probably due to a slight asymmetry in the flow.

The radial velocities are shown in figures 5.39-44. The peak radial velocity is underpredicted by both simulations. However, the radial velocity peak is better predicted than the axial velocity peak. The fuel-air flow

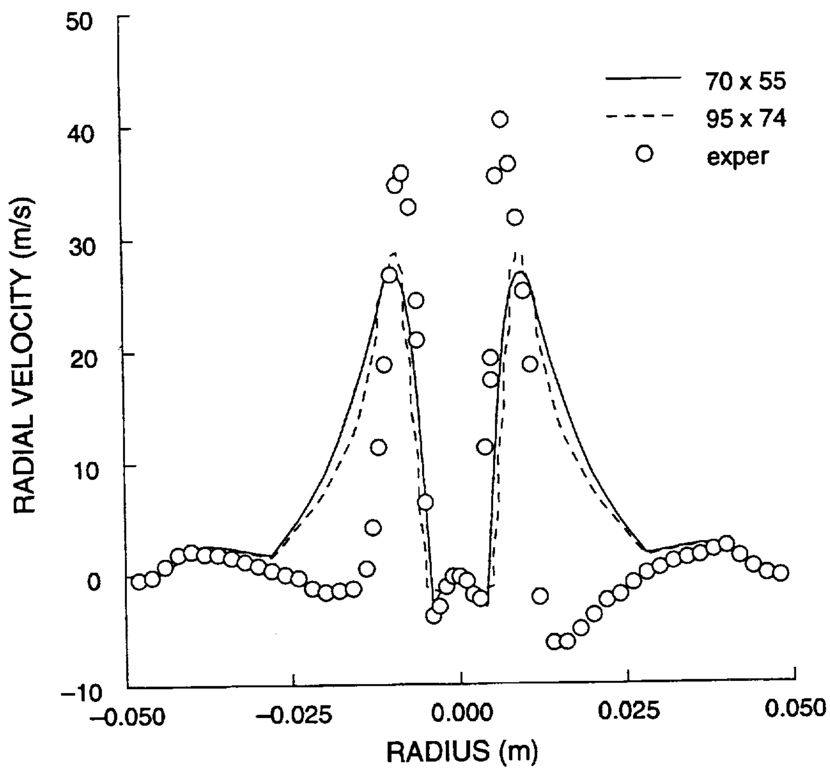

Figure 5.39 Radial Velocity at 5.0 mm.

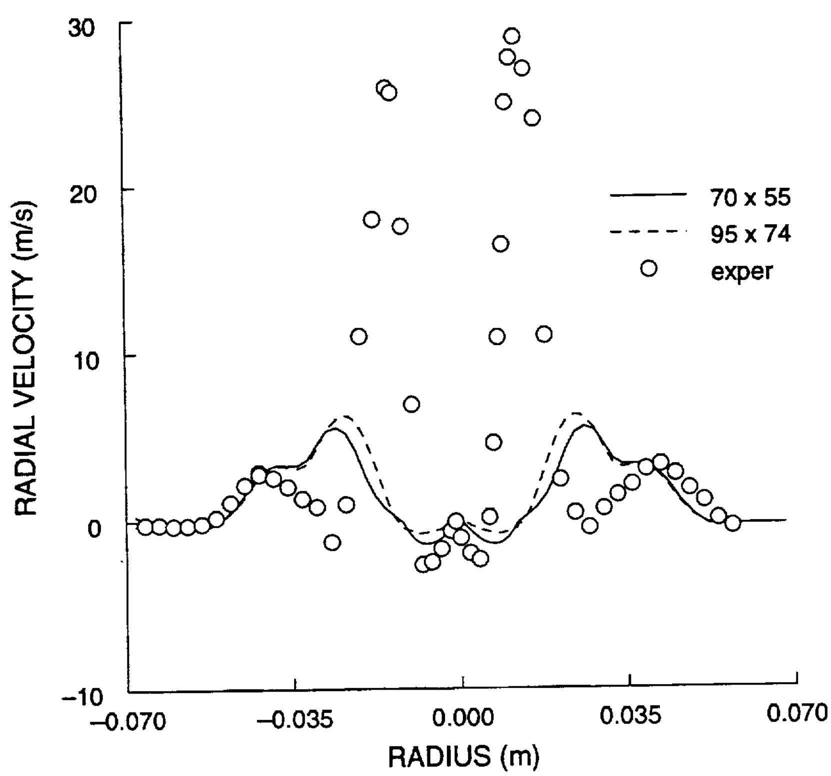

Figure 5.40 Radial Velocity at 10.0 mm.

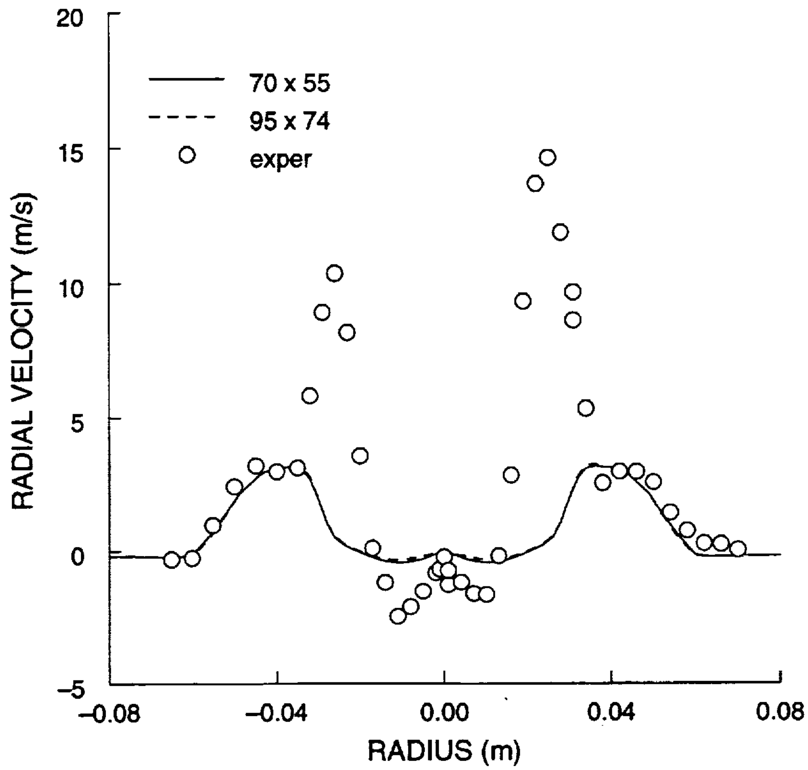

Figure 5.41 Radial Velocity at 20.0 mm.

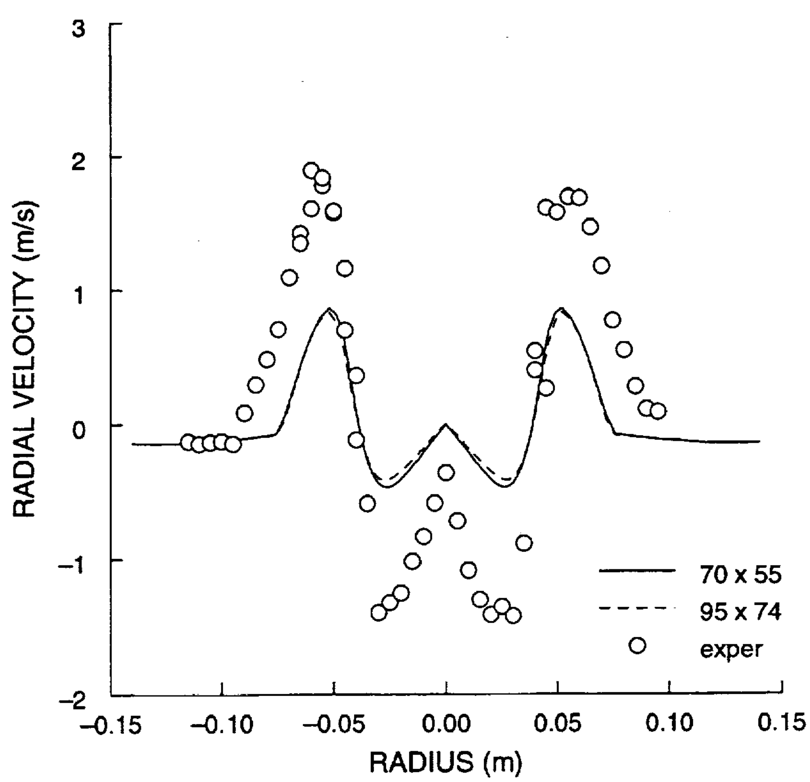

Figure 5.42 Radial Velocity at 50.0 mm.

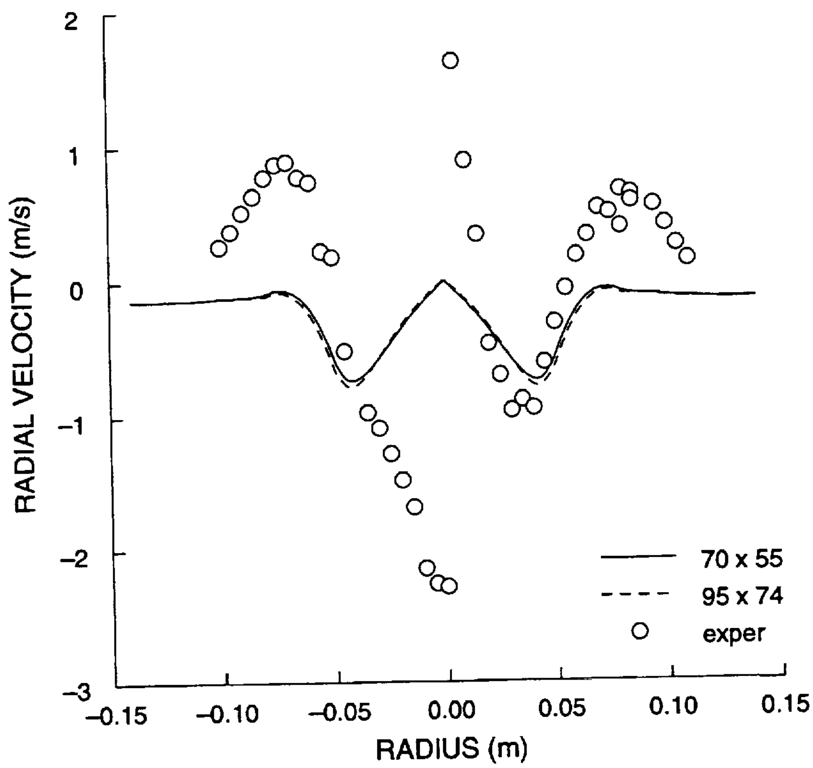

Figure 5.43 Radial Velocity at 100.0 mm.

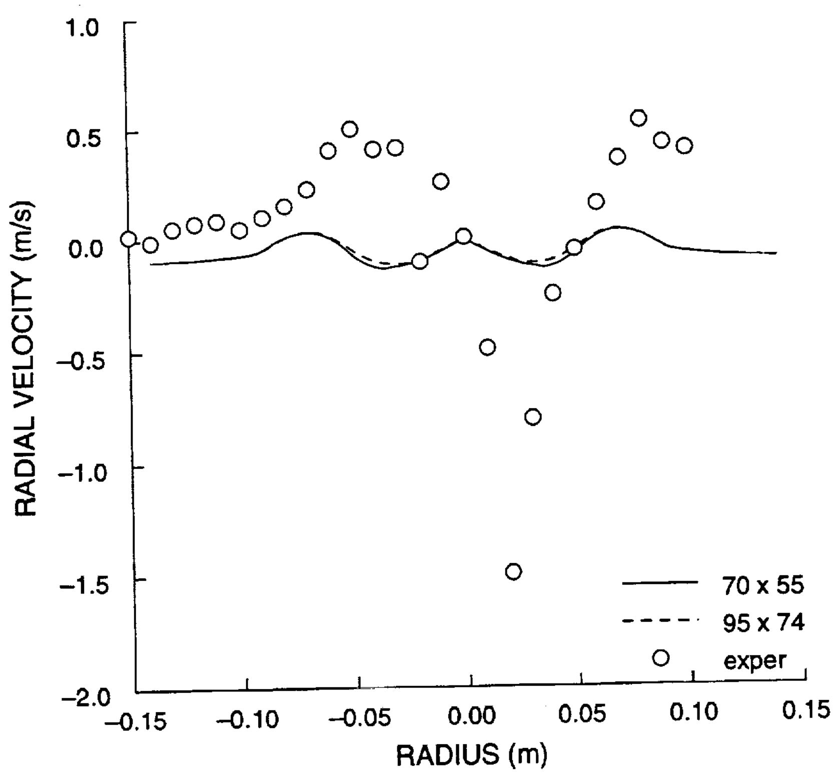

Figure 5.44 Radial Velocity at 200.0 mm

expansion due to combustion seems to occur more in the radial direction. The simulations predict a larger radial expansion of the fuel-air injector flow than measured. The predicted width of the fuel-air injector flow is nearly twice as wide as measured. The predicted radial over-expansion destroys the large radial velocity peak at successive axial locations. At 10.0 mm, the predicted radial velocity peaks are about twice as far from the centerline as the experimental peaks. The predicted peak radial velocity is less than one-fifth of the experimental peaks. Radial velocities beyond a radius of 4 cm are well predicted.

At 20.0 mm, both the numerical simulations predict a single radial velocity peak. The flow from the fuel-air injector has completely merged with the co-flowing stream in the simulations at this axial location. The experimental data shows separate velocity peaks. The experimental velocity peaks are about four times higher than predicted peaks. Radial velocity in the co-flowing stream is well predicted.

The experimental data shows a single radial velocity peak at the 50.0 mm station. Flow originating from the fuel-air injector and the co-flowing air-stream have combined. Qualitatively the simulations correctly predict the radial velocity at this station. The simulations underpredict the velocity peak by about 50 percent. The radial velocity in the central recirculation zone is off by at least a factor of four. The negative velocities near the combustor centerline indicate the recirculation zone is starting to close.

The radial velocity profiles for the entraining flow and outer co-flow are well predicted for the 5.0, 10.0, and 20.0 mm stations. However, the portion of the outer profile that is in agreement, grows progressively smaller with axial distance. At 50.0 mm, the agreement in the outer flow is the smallest. The width of the predicted profile is under-predicted. There is the thought that the initial radial velocities may be over-specified, causing an over-rapid broadening of the injector flow. This researcher did a calculation specifying reduced radial velocities for the injector flow. This modification remarkably improved the calculation of the peak velocity flow from the injector. However, there is little evidence to support such a change in radial velocities, other than it works. Another possibility of error is the flow direction to the computational grid. The injector flow is roughly 45 degrees to the grid lines, which is known to cause accuracy problems. It would be interesting to implement an improved or higher order numerical differencing scheme in the model.

At 100 mm, the numerical radial velocity predictions are all negative. That is, there is inflow across the whole combustor, no expansion. The experimental data shows some expansion at larger radii. At the 200 location, the predicted radial velocities are very close to zero. The measured velocities at this station are generally larger. There is significant non-symmetry for the 100.0 and 200.0 experimental data near the centerline. The velocity should go to zero near the centerline but doesn't. Part of the problem is the sign of the radial velocity. It is believed that the flow is slightly off to one side, which causes problems in interpreting the sign of the radial velocity component. The experimental axial velocity profile exhibited sharp gradients near the centerline for the 100.0 and 200.0 stations, thus, there should be significant radial velocity in this area.

The plots of tangential velocity are shown in figure 5.45-50. As in previous figures, the part of the flow agreeing least with the experimental data is the injector flow. The numerical predictions at 5.0, 10.0, and 20 mm show a large drop in tangential velocity for the injector flow. The inner profile is worst predicted at the 10.0 mm station, where it is a quarter of what it should be. The predicted inner profile actually gains some strength at the 20.0 mm station. The experimental data for the injector flow exhibits quite a bit of variability and asymmetry. Between the 5.0 and 10.0 station, the experimental velocity peak changes sides! The difference in injector flow velocities from one side to the other is of the order of 25%.

The outer velocity profiles are well predicted at the 5.0, 10.0, and 20.0 locations. Then the width of the

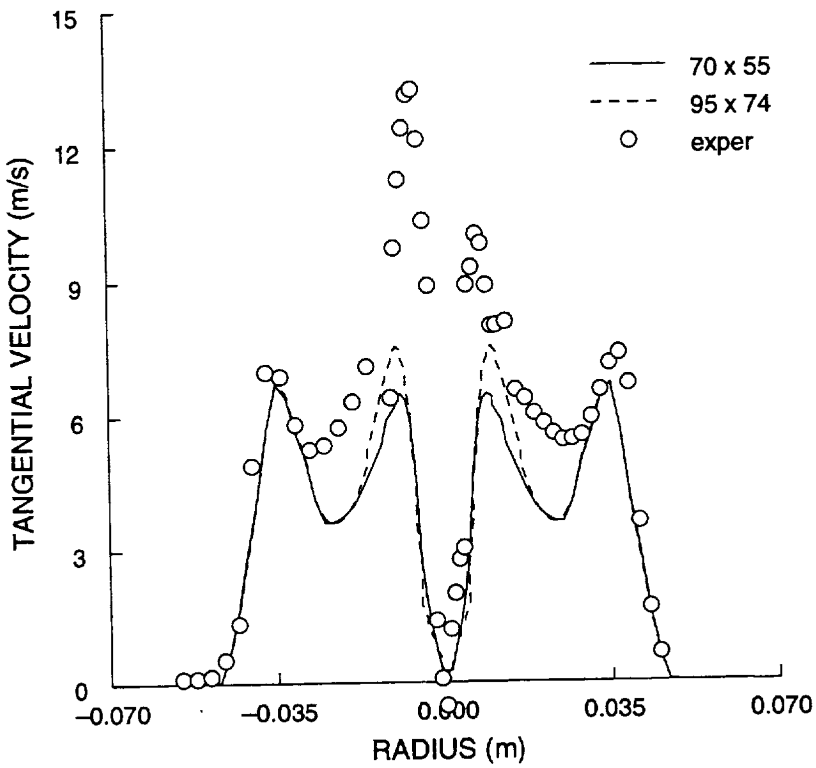

Figure 5.45 Tangential Velocity at 5.0 mm

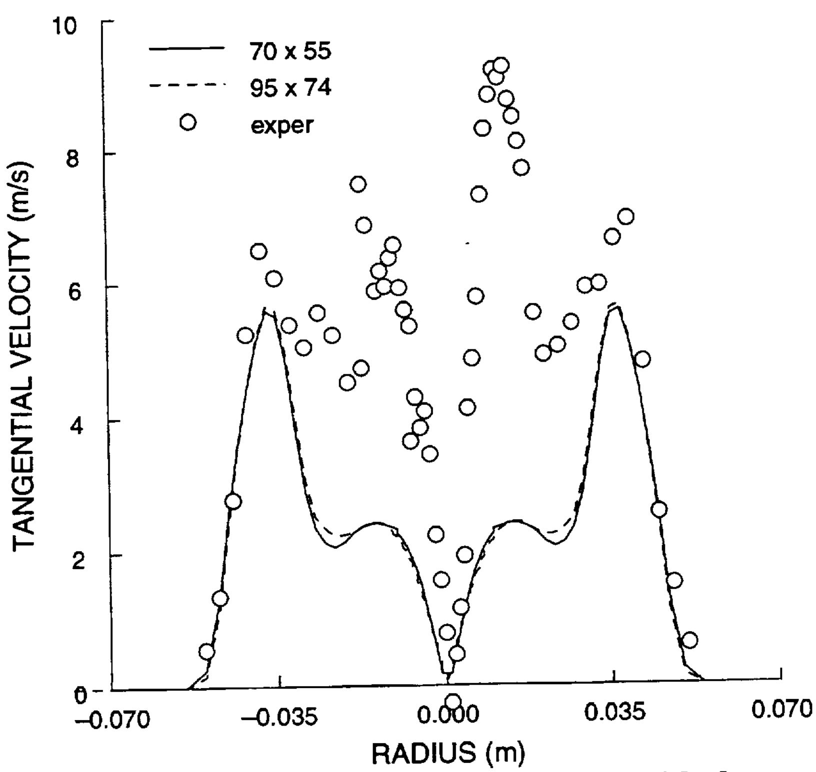

Figure 5.46 Tangential Velocity at 10.0 mm

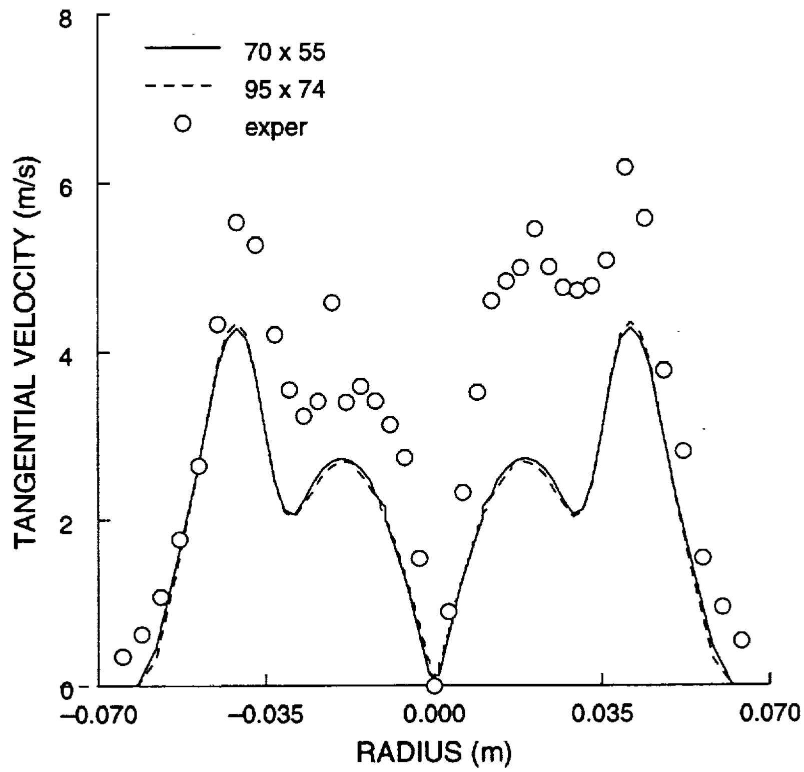

Figure 5.47 Tangential Velocity at 20.0 mm

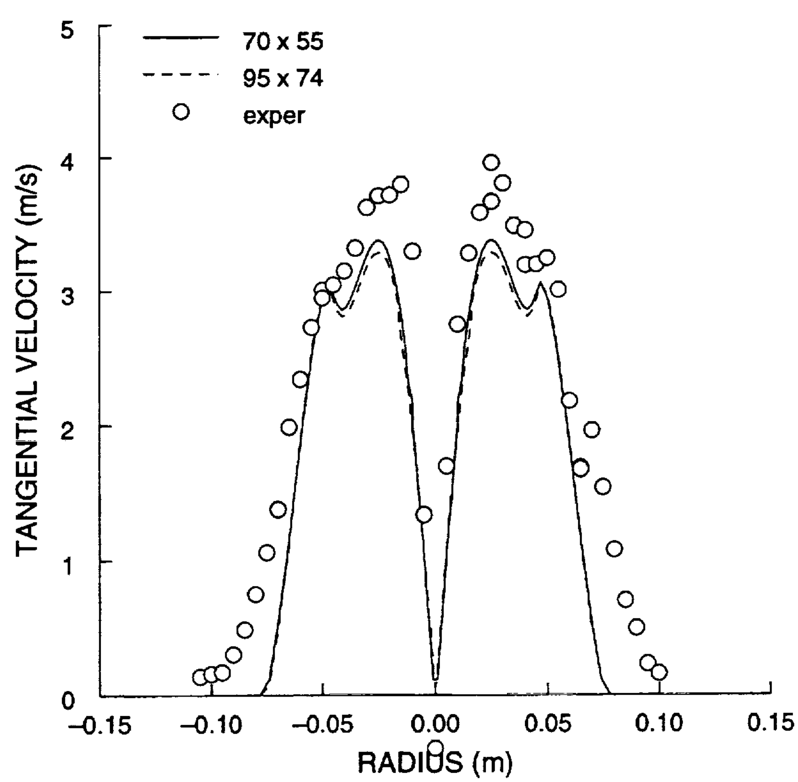

Figure 5.48 Tangential Velocity at 50.0 mm

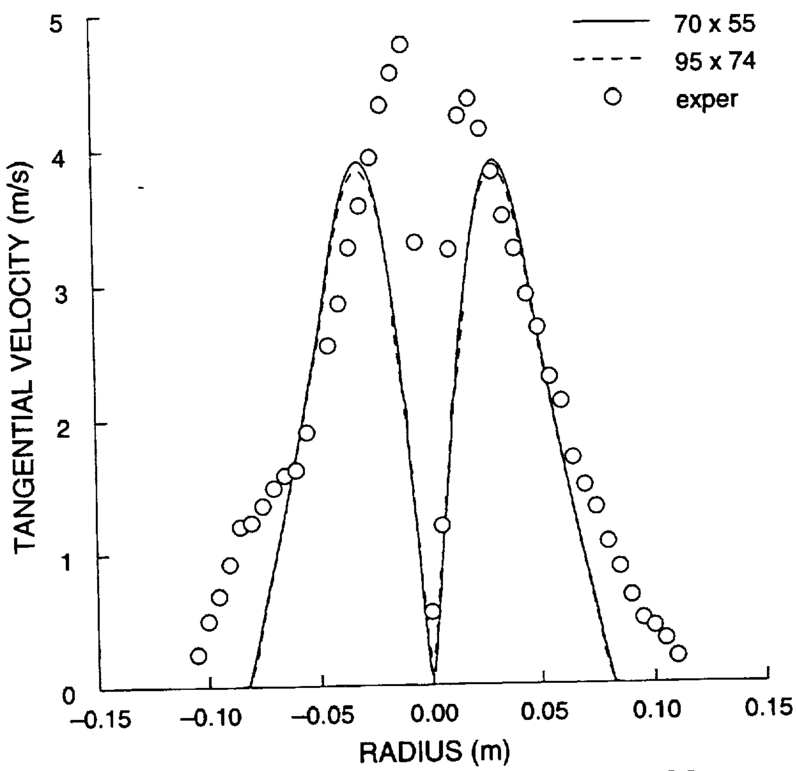

Figure 5.49 Tangential Velocity at 100 mm

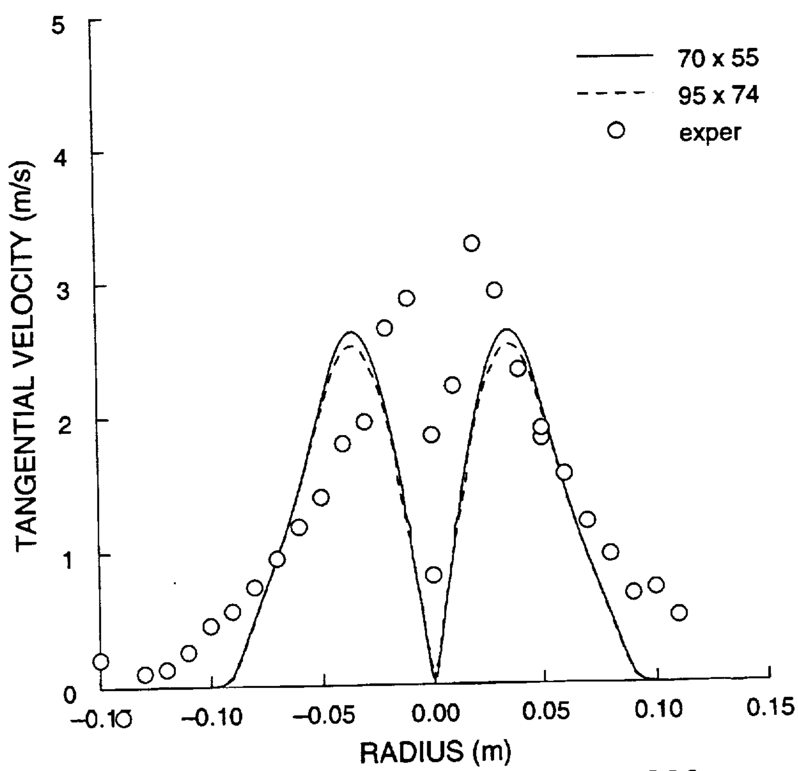

Figure 5.50 Tangential Velocity at 200 mm

profile is off, but predictions significantly improve! At 50.0, 100.0, and 200.0 mm the prediction of tangential velocity is good. The velocity peaks are only slightly under-predicted. The width of the profile are underpredicted, caused by a sharper drop in tangential velocity than is measured. The inner profile is underpredicted at the 100.0 and 200.0 locations. This was also seen for the axial velocity profile. The experimental data indicates stronger radial inflow near the centerline. Viscous effects are acting on the on the strong velocity gradient near the combustor centerline. The measured turbulence is quite high at this location. At 350.0 mm, the experimental axial velocity profile only shows a slight deficit along the centerline.

Plots of temperature profiles are shown in figure 5.51-56. The agreement on the left side of figure 5.51 is good. The left side agreement is noticeably better for the 5.0 through 20.0 mm stations. It appears that initial combustion is better on the left side for these stations. This is the side that the flow seems to shift or expand away from. The predicted profiles have rather sharp ridges at the outer edges of the high temperature region that are probably non-physical. The depressed temperatures due to fuel droplet impingement on the thermocouple probe are evident. The model predicts lower temperature in the fuel spray zone. Both experimental and predicted temperature profiles show

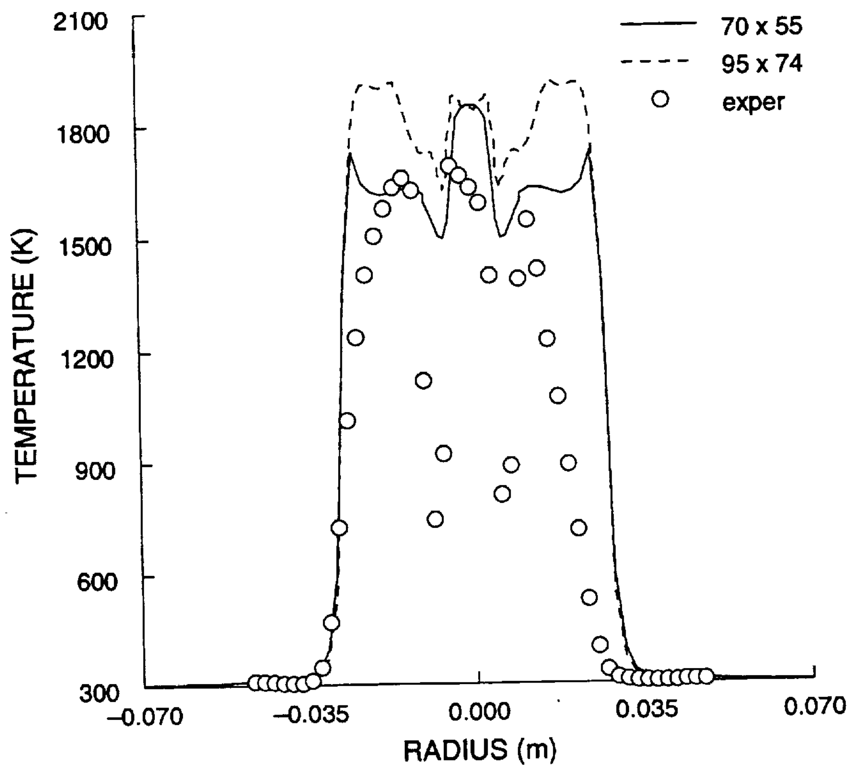

Figure 5.51 Temperature at 5.0 mm

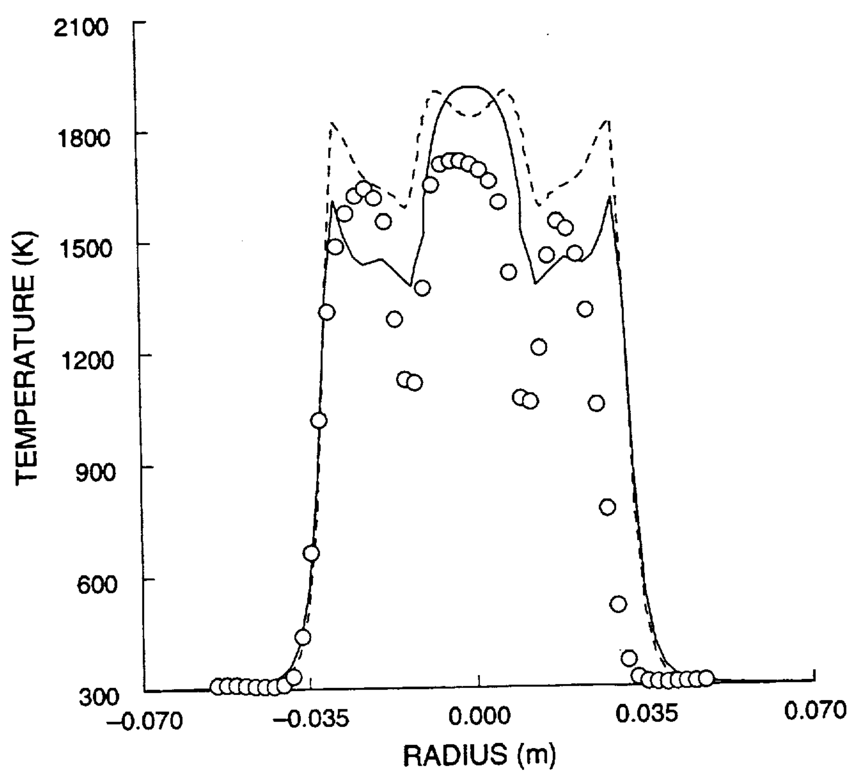

Figure 5.52 Temperature at 10.0 mm

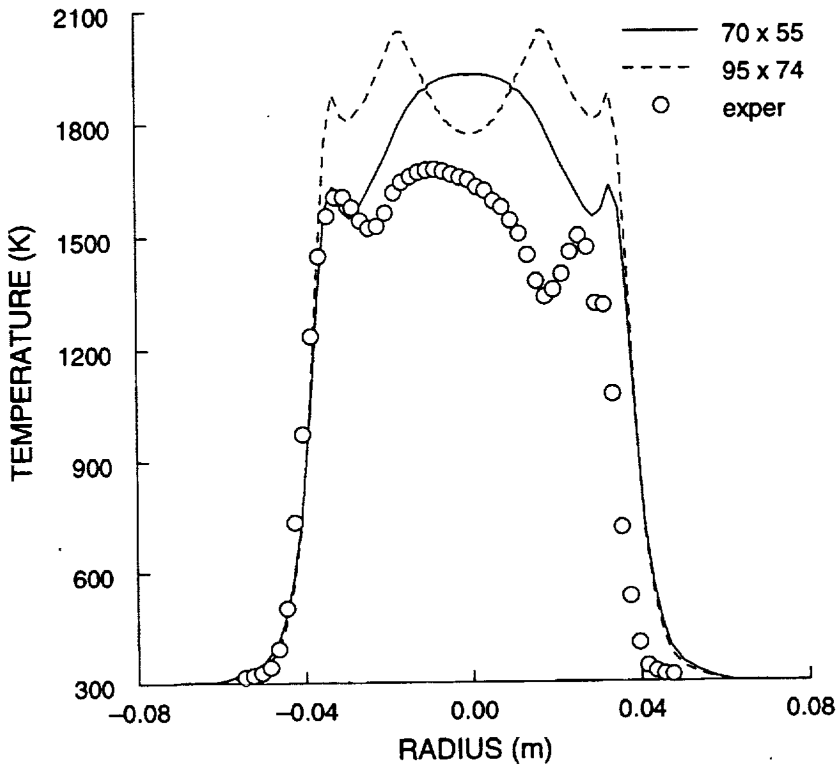

Figure 5.53 Temperature at 20.0 mm

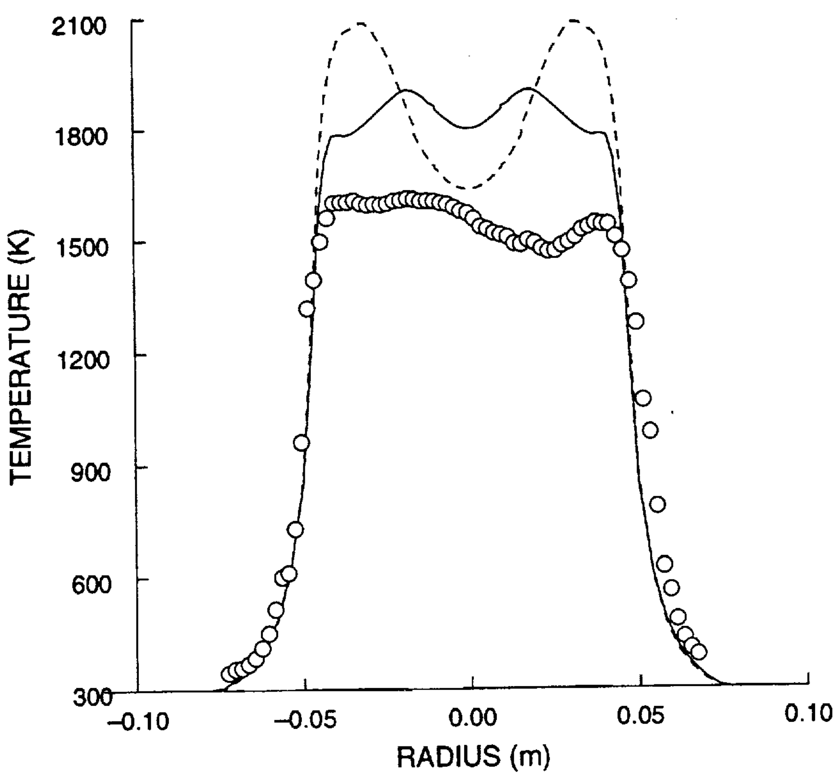

Figure 5.54 Temperature at 50.0 mm

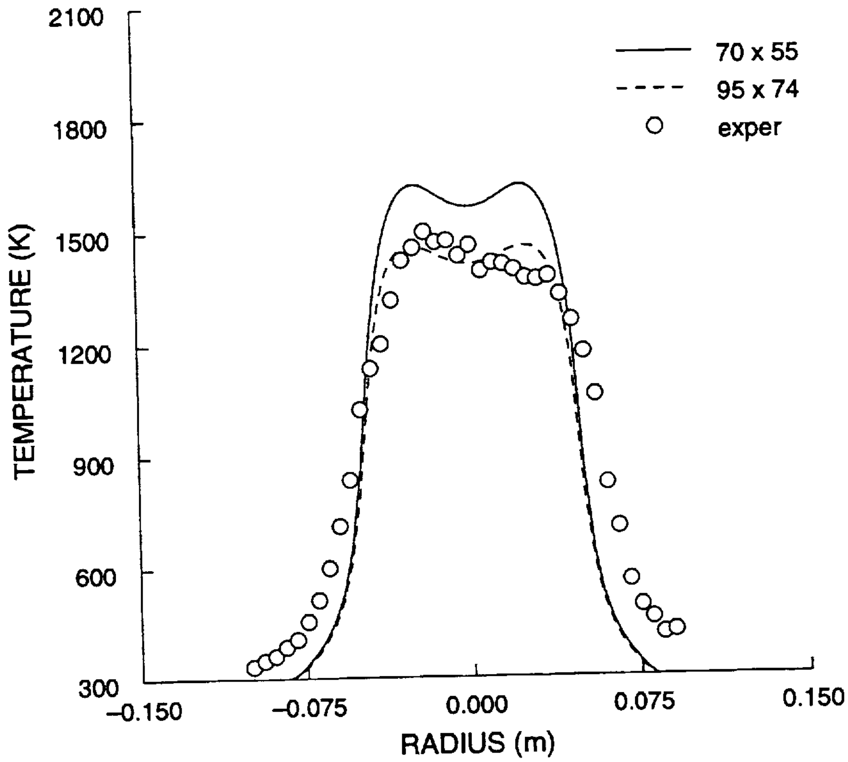

Figure 5.55 Temperature at 100.0 mm

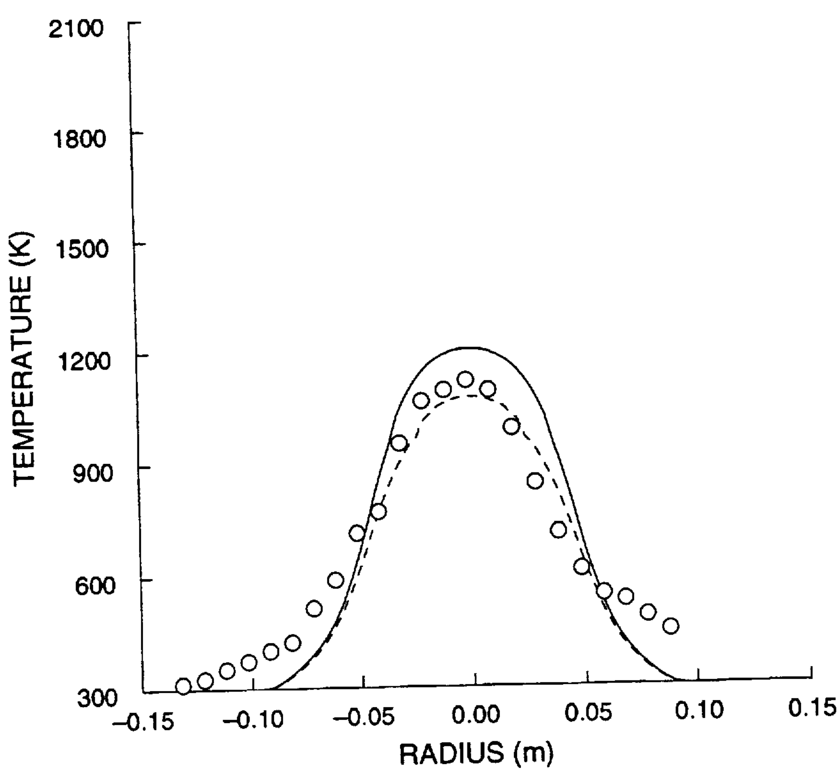

Figure 5.56 Temperature at 200.0 mm

very large gradients at the edges where combustion is not occurring. The finer-grid calculation predicts higher temperatures than the coarse grid. At 50.0 mm, the experimental temperature profile is fairly flat across the combustion zone. The coarser grid exhibits two small humps, while the fine grid has very prominent peaks. The peaks are much smaller at the 100 mm station. The width of the temperature profile is slightly underpredicted at the 100.0 mm station. The gradient at the edge of the high temperature profile is overpredicted. This is probably due to the underprediction in radial velocity. At 200 mm, the experimental and predicted profiles show a rather bell shaped curve. The experimental profile shows a little more spreading, again probably due to the radial velocity.

Fuel Droplet Comparisons

The droplet axial velocity comparisons are shown in figures 5.57-60. Droplets were not measured past the 50 mm station. The experimental data are shown for negative radii in the figure, and the fine grid numerical predictions are shown for positive radii. The solid line is the gas phase velocity shown for comparison purposes, as the droplets will eventually relax to the gas phase velocity due to drag. The experimental gas phase velocity plots were not smoothed. The different symbols denote the different size droplet groups. Only 6 of the 10 droplet sizes are plotted. At 5.0 mm, the numerical calculation of spray droplet axial

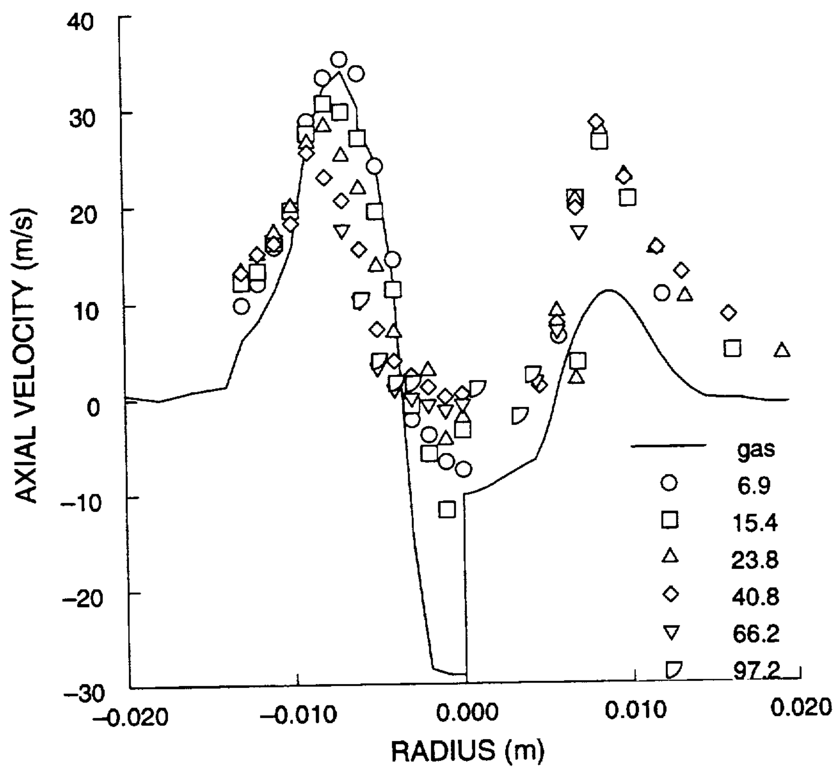

Figure 5.57 Droplet Axial Velocity at 5 mm

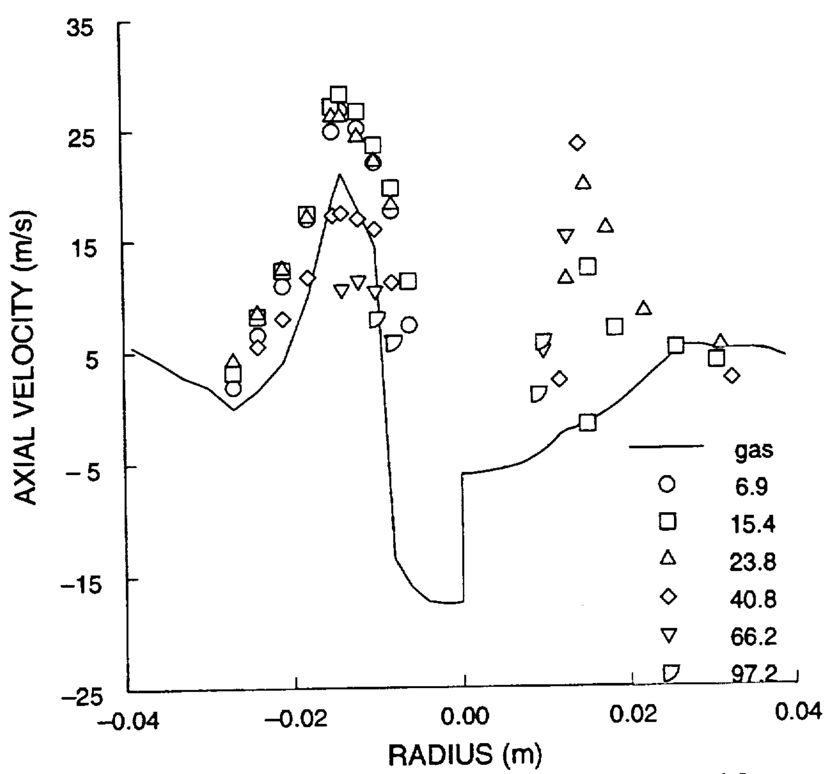

Figure 5.58 Droplet Axial Velocity at 10 mm

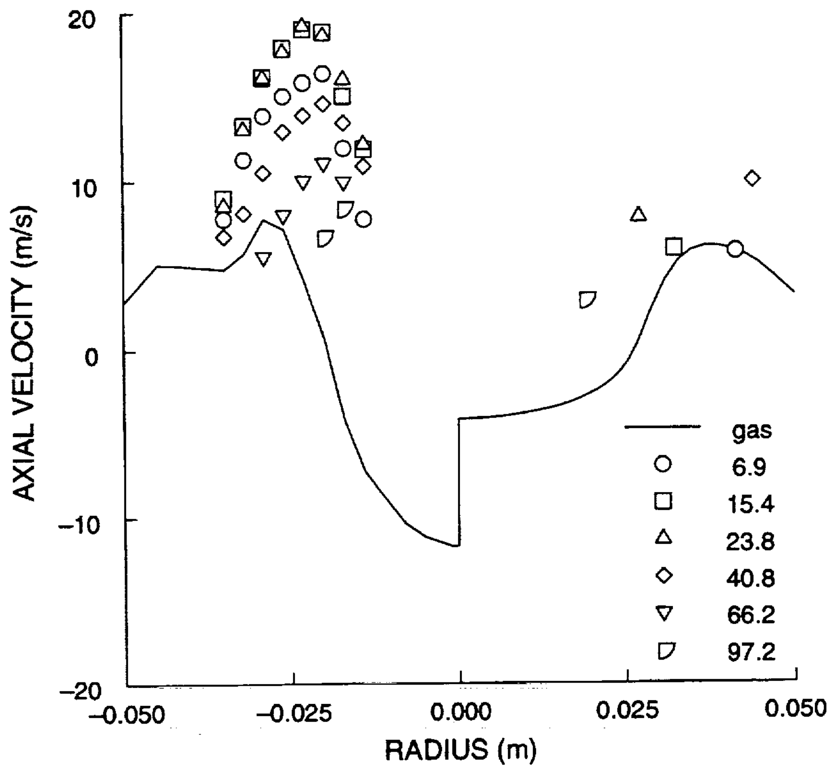

Figure 5.59 Droplet Axial Velocity at 20 mm

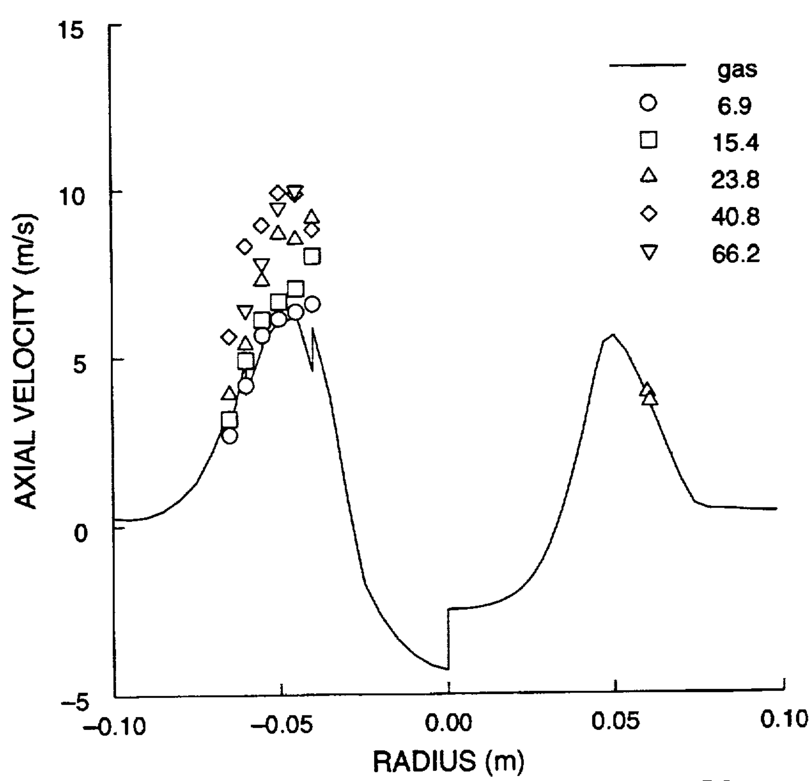

Figure 5.60 Droplet Axial Velocity at 50 mm

velocity is slightly underpredicted. This is caused by the under prediction of the gas phase axial velocity near the vicinity of the fuel injector. The larger difference between the predicted gas phase and droplet velocities results in higher drag forces, and a quicker reduction in droplet velocities. The smaller droplets generally track the gas phase velocity better. The shape of the droplet velocity profile is good, except, the droplet groups show greater radial spreading than experimentally measured. The experimental data at 5.0 mm indicates many particles near the combustor centerline. Many of these particles show negative axial velocities! The predictions do not show the same patterns. There are few predicted droplet groups near the centerline, and only one with negative axial velocity. Gaseous fuel is provided by evaporating droplets. The combustion of this fuel results in expansion and possible increase in reverse flow velocity. The experimental data shows an increase in negative axial velocity at this location, while the predictions show a decrease. The spray model is not picking up on possible phenomena to explain this effect. In setting up the droplet group input data, droplet groups with negative axial velocities were ignored. It would be useless to input this data. The spray flowing towards the injector significantly contributes to gaseous fuel mass fractions, but without doing some species measurements, it is unknown.

At 10.0 mm, The droplet axial velocities have decreased further. The predicted gas phase velocity does not even show a peak corresponding to the air-assist stream from the nozzle. The difference in predicted velocity for the two phases is much higher than the experimentally measured velocity difference. This will lead to further loss in droplet axial velocity. The predicted droplet velocities exhibit a much sharper peak than measured and show greater radial spreading. The experimental droplet data shows grouping of the data according to droplet size. Droplet groups having the same average diameter seem to plot along smooth curves. This isn't as obvious in the numerical predictions, especially, later in the flowfield, due to scarcity of particles.

The number of predicted droplet groups decreases as the droplets are burned. There are only 5 droplet groups plotted at the 20.0 location, and two at the 50.0 mm station. This is far too few show droplet size grouping. It is also questionable if this small number could cause any kind of local gas phase velocity peak. The experimental data shows good correlation between the injector gas velocity peak and the placement of the droplets. The simulations don't adequately predict the air-assist nozzle flow. To help validate the spray model, it would be better to have significantly more droplet groups. Unfortunately, the number of droplet groups was rather limited to begin with!

The current spray model significantly taxed computer time resources. The needed computer time would scale directly with the number of droplet groups. The experimentalist can widen the measuring probe volume to pick up more droplets where the spray is less dense. There isn't a numerical modeling counterpart to this. If one mentally averages the droplet axial velocities, the simulation seems about at third of the experimental average for both the 20.0 and 50.0 measurement stations. Intuitively, this should have a severe effect on the spray vaporization. Dr. Bulzan integrated his spray flux measurements across the flowfield. Correcting these measurements gives 21.3 % of the metered flow rate at 2.5 mm, 26.8 % at 5, 50.0 at 10, 23.1 at 20, and 2.6% at 50.0 mm downstream of the nozzle. It is obvious that much of the droplet data are not picked up at the 2.5 and 5.0 stations. The predictions presented here used 65% of the metered fuel flow for droplet input at 2.5 mm. The simulation predicted 51.7 % of the metered flow in the form of spray at 5, 24.0 % at 10, 6.3 % at 20, 0.13 % at 50.0 mm. Thus, the simulation does predict over-rapid fuel spray vaporization. However, as velocity predictions near the injector zone are overly diffusive, it would be inappropriate to blame the spray model. The droplet velocity is about 0.8 of what it should be for the 5.0 and 10.0 location. At the 20.0 location it is roughly a third and at the 50.0 location it is about a quarter. Assuming the amount of droplet vaporization is directly proportional to time, applying a correction for the time by factoring in how much the gas phase velocity differs from the data and compounding this correction at successive axial locations to the above percentages gives 57.4 % at 5, 33.3 % at 10, 15.5 at 20.0 and 1.1 % at the 50.0 location. These amounts are still too low. If one looks at the 20.0 location, this suggests that the spray is off by a third. This would then imply that all the nearly all the fuel should be in liquid form at the calculation start. This does not agree with the data, as inlet temperature is very high.

The droplet radial velocities are shown in figure 5.61-64. At the 5.0 mm station, there is surprising little velocity difference between the gas phase and spray droplets. This was also exhibited by the plots of axial velocity. The predicted gas phase radial velocity peak is only slightly less than the measured one. The axial velocity peak was a factor of three off. However, as previously noted, the profile is twice as wide as it should be, which causes additional nozzle flow dissipation. The numerical simulation predicts droplets at larger radii. The cause is a combination of the predicted axial and radial gas phase velocities. The calculated radial gas phase velocity profile is much broader than the experimental one, and the predicted axial velocities are much lower than measured. Thus, the predicted spray spreads out further than measured. At

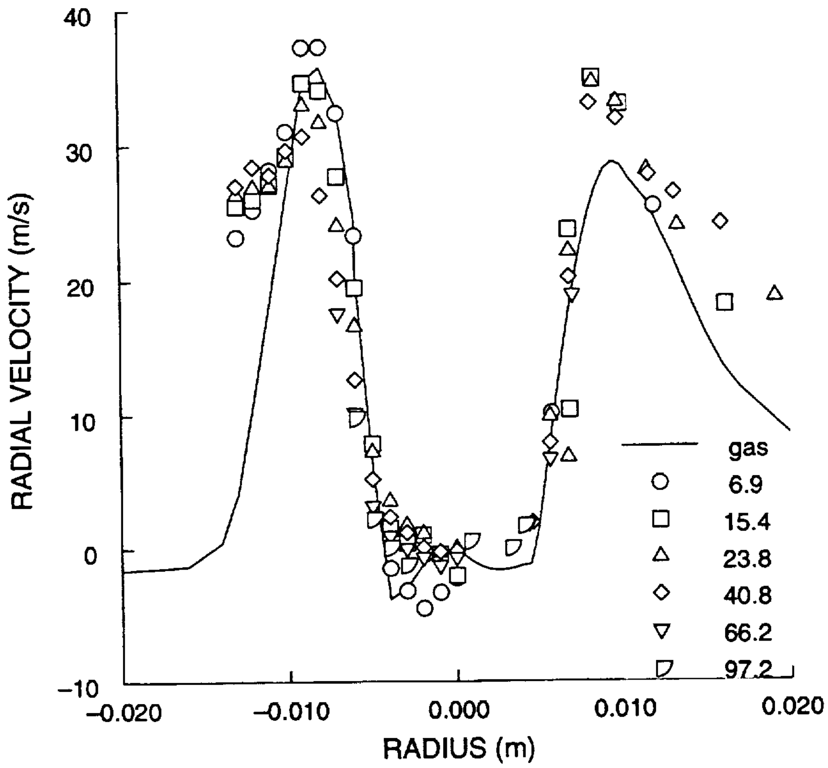

Figure 5.61 Droplet Radial Velocity at 5 mm

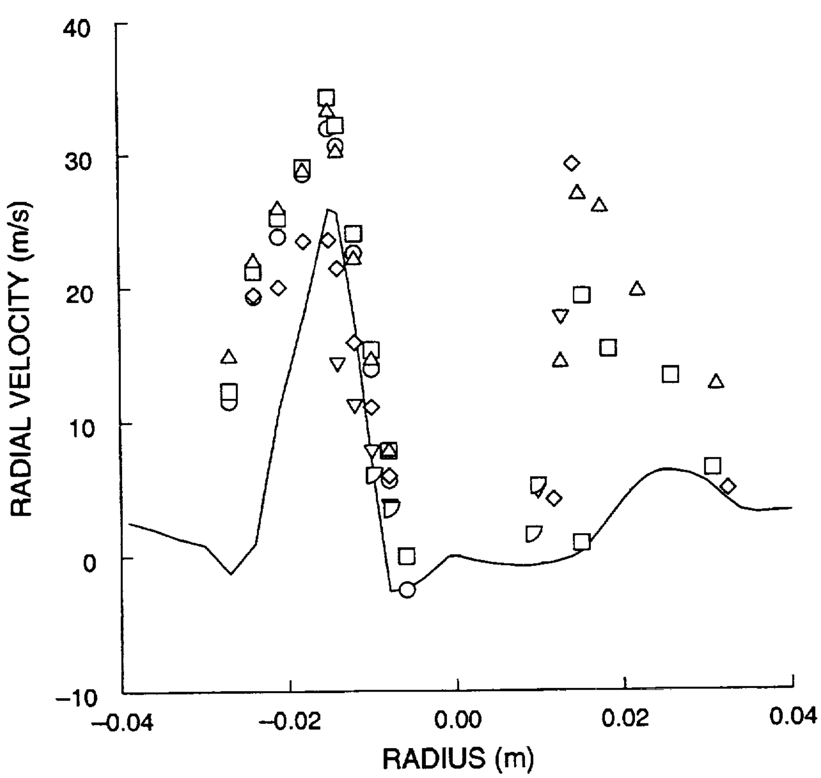

Figure 5.62 Droplet Radial Velocity at 10 mm

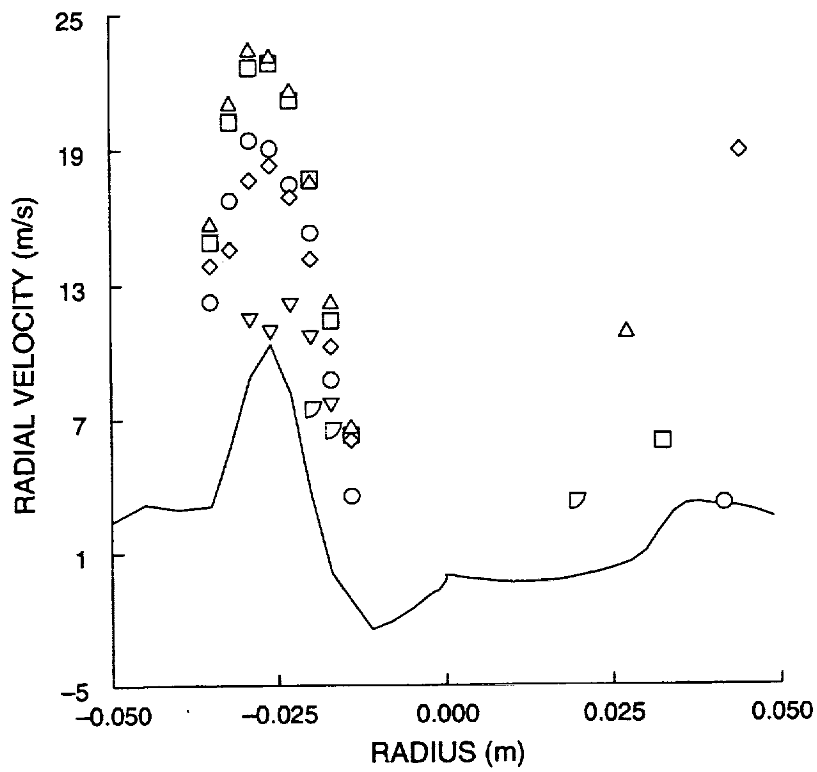

Figure 5.63 Droplet Radial Velocity at 20 mm

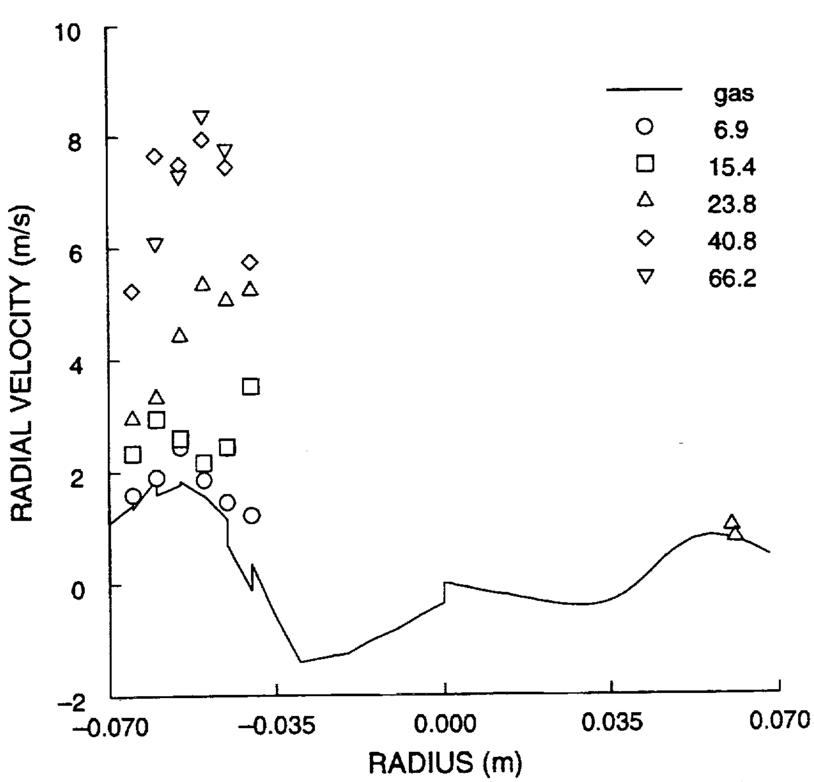

Figure 5.64 Droplet Radial Velocity at 50 mm

10.0 mm the predicted gas phase radial velocity peak for the injector flow is much lower than the measured one. The experimental data at this location only shows one group with negative radial velocity near the centerline. The average diameter of this group is small, which allows it to better track the local gas phase velocity. As mentioned previously, the reverse flow velocity at this point is decreasing. As previously discussed for droplet axial velocity, the predicted droplet groups display more radial dispersion than measured. At 20.0 mm, the predicted radial velocities are generally much smaller than the measured. There are 5 predicted droplet groups at this axial location. Some of the groups are in the high temperature flow. All of the measured groups are within the high temperature flow. At 50.0 mm there are only two predicted droplet groups and both of these are in the lower temperature flow. The measurements display many droplet groups at the 50.0 mm station. This suggests that the spray model is overpredicting evaporation. The experimental data at this location shows much higher radial velocities, both in gaseous and liquid phases. The spray is going to provide for gas phase source terms further downstream as the fuel evaporates and burns. The small number of predicted droplet groups means that most of the fuel is already gaseous and thus, already burning. From this information, it may be inferred that predictions should not noticeably improve with downstream distance. This was seen in previous figures of velocity and temperature.

Tangential droplet velocities are shown in fig. 5.65-68. These velocities are also under-predicted, at times, half the measured values. The calculated droplet velocities are nearly the same as the calculated gas phase velocity, while the experimental droplet velocities can be considerably lower than the measured gas velocities. The experimental droplet data shows noticeable stratification by droplet size. The smallest diameter droplets are closest in tangential velocity to the gas phase, while the largest diameter droplet groups differ the most. At the 20.0 mm station, the droplet groups plot nearly horizontally according to droplet size. The predicted droplet groups show slight pattern according to size at the 5.0 mm station. At later stations, the smaller number of predicted droplet groups does not allow a conclusion. The low number of predicted droplets suggests over-rapid vaporization and/or combustion. The numerical calculations do not adequately predict the fuel-air nozzle flow. Within a short distance, the injector flow has been seemingly dissipated.

The experimental data shows higher peak radial velocities than axial velocities for the 2.5 mm station to the 20 mm station. D. Bulzan [108] concluded that the flow was expanding more in the radial direction due to the strong central reverse flow caused by the recirculation zone. The poor velocity predictions for the injector nozzle flow are

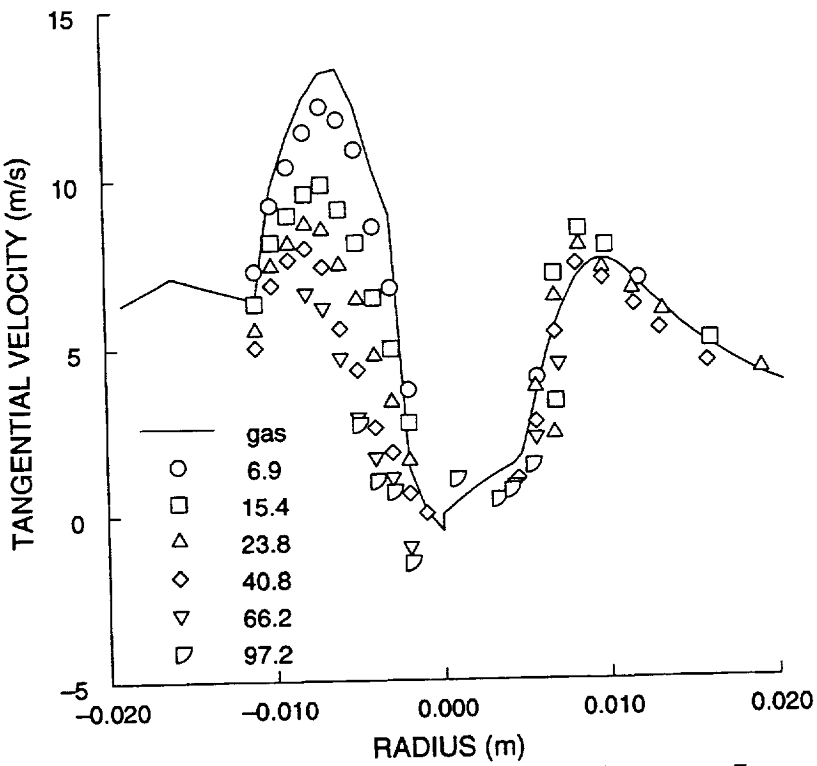

Fig. 5.65 Droplet Tangential Velocity at 5 mm

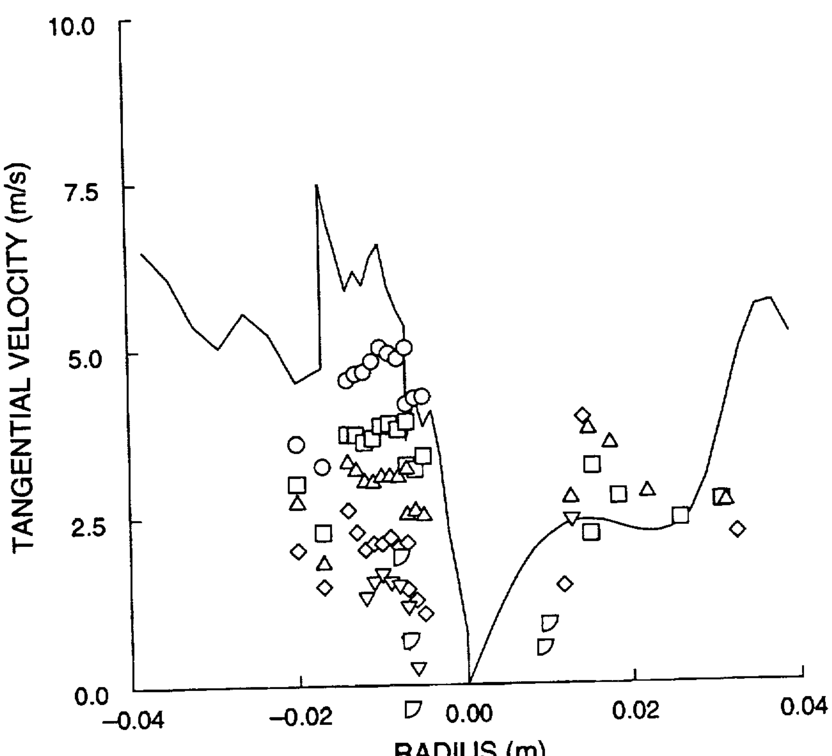

Fig. 5.66 Droplet Tangential Velocity at 10 mm

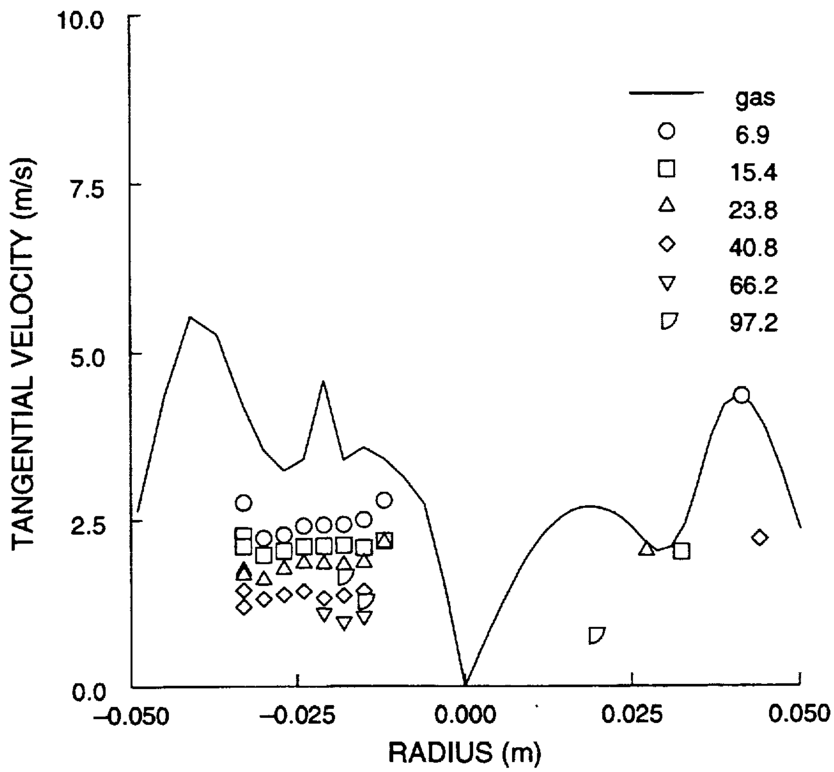

Fig. 5.67 Droplet Tangential Velocity at 20 mm

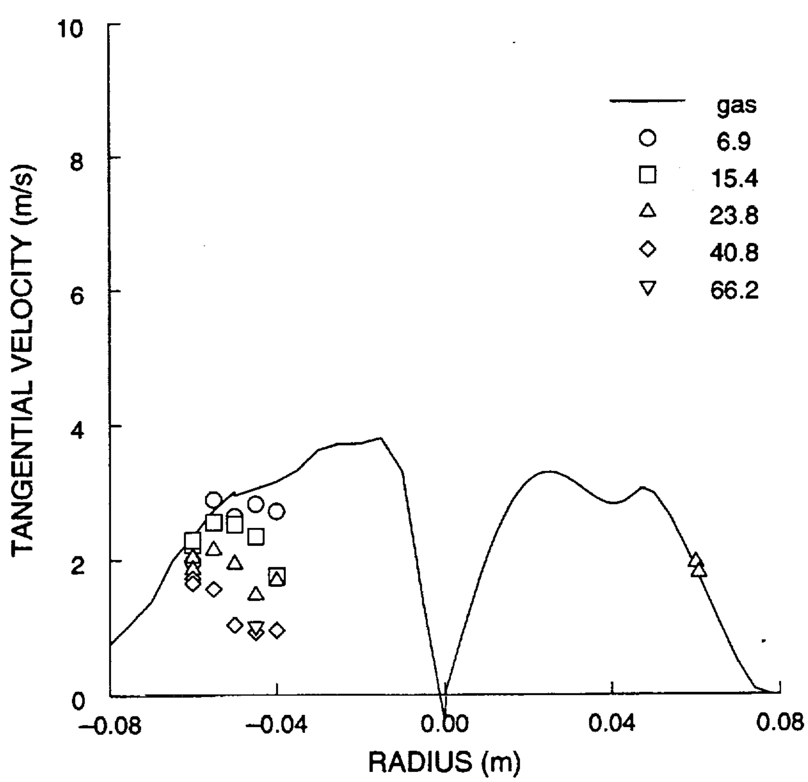

Fig. 5.68 Droplet Tangential Velocity at 50 mm

probably not the fault of the combustion model. The overly large radial dissipation of the injector flow must be investigated. This researcher feels the most probable modeling improvement would be an improved numerical differencing scheme to adequately calculate the high velocity nozzle flow which is severely skewed to the current cartesian grid. Modification of the spray or combustion models will probably provide little improvement. Indeed, a preliminary calculation was done using a pdf combustion model. While there are many differences in the modeling than used here, the gas phase velocities were very similar. The largest error was in calculating the injector flow, which is simply where the fuel spray is. If the fuel source terms to the gas phase are incorrectly calculated, a combustion model for the gas phase isn't the correct fix.

5.3 - Monte Carlo Pdf Model Predictions

Four cases are predicted using the hybrid pdf method. The stochastic part of the coding solves for enthalpy and species while velocity and pressure are solved using the SIMPLE algorithm of Patankar. The hybrid pdf predictions are compared with predictions made by a more traditional combustion model which is a combination global arrhenius reaction rate and eddy breakup or mixing model, which was also used in the previous spray combustion calculations. These predictions were generally optimized to obtain good comparisons between measurement and predictions.

The first case compares species concentration and temperature for an enclosed diffusion combustor. In this combustor, the fuel and air supply ducts are similar in size. The second case also involves a diffusion combustor, but the geometry is much closer to an actual gas turbine combustor. The fuel enters through a small conical duct which is at a large angle to the combustor axis. The third case involves premixed combustion. Premixed combustion is being studied as a way of lowering emissions and improving fuel efficiency. As simple combustion models may poorly predict premixed combustion, the ability of a combustion model to accurately predict both diffusion and premixed combustion is a desirable feature. The fourth case involves a swirling hydrogen jet diffusion flame. This combustor is extremely interesting as temperature pdfs were measured.

5.3.1 Non-Swirling Diffusion Combustion

The data of M. H. Lewis and L. D. Smoot[119] was chosen because of the simple geometry. Fuel and air are supplied by concentric tubes to a large insulated cylindrical combustion chamber. The combustion chamber is 152.4 cm long and 20.32 cm in diameter. The fuel inlet tube has an inside diameter of 1.6 cm and wall thickness of 0.32 cm. The fuel inlet tube has a blunt end. The outside radius of the air annulus is 2.86 cm. This type of research combustor is known as a dump combustor. The large increase in cross-sectional area is easy to model and causes a hot recirculating flow which provides a continuing ignition source for combustion. Lewis and Smoot did not measure velocities, although it appears that Smoot and another of his students, Philip Smith[120] used a CFD code to calculate flow properties.

The fuel is city-gas which is 88.53 % methane, 7.44 % ethane, 2.55 % nitrogen, 1.39 % carbon dioxide, and 0.09 % hydrogen. In this work, the fuel is modeled by assuming pure methane. The experimental inlet velocity and temperature of the fuel was reported as 21.3 m/s and 300 degrees Kelvin. 20.14 m/s was used in the numerical simulation so that the overall fuel to air ratio was stoichiometric. The inlet air velocity and temperature was 34.3 m/s and 589 degrees Kelvin. Temperature was measured at axial distances of 9.5 and 39.5 cm from the combustor inlet. Species were measured at axial distances of 9.5, 17.5, 24.6, 32.7,47.6, 63.2, 78.5, and 137.5 cm. The calculation modeled the combustor as being only 1.0 meter long, as initial pdf simulations exhibited numerical difficulty due to large aspect ratio grid cells. The grid was stretched in the axial and radial directions with the finest grid near the inlet.

The grid has 80 axial and 40 radial gridpoints. The fuel jet has 5 radial cells and the air has 11 radial cells. A recirculation zone is predicted. The length of the recirculation zone varies between the hybrid pdf and SIMPLE calculations. The SIMPLE simulation predicted a reattachment length of 46.5 cm while the pdf simulation predicted 57.8 cm.

Smith and Smoot used an assumed shape pdf model with an equilibrium combustion model. This model significantly over-predicted carbon dioxide, especially along the centerline. Oxygen was under-predicted in the same area. This implies that burning was not occurring as rapidly as predicted by Smith and Smoot's calculation. A finite rate single step combustion model is used in the simulations reported here. The model is:

$$CH_4 + 2O_2 \rightarrow CO_2 + 2\ H_2O$$

$$R_f = \min[A(\frac{\rho Y_f}{W_f})^a(\frac{\rho Y_o}{W_o})^b e^{-E/RT}, \frac{C_R}{W_f} g^{1/2}(\frac{\rho\epsilon}{k})] \qquad (5.6)$$

Where

$$A = 8.5 \times 10^{13} \qquad [\frac{Kg\text{-}mole}{m^3 \text{ sec}}]$$

The exponents used for the fuel and oxidant concentrations are 0.2 and 1.3 respectively. These are the third set recommended by Westbrook and Dryer [25] for Methane. The first two sets recommended a negative exponent on the fuel which resulted in some numerical difficulty with large reaction rates at very low fuel concentrations.

Comparisons of fuel, oxygen, water, and carbon dioxide mole fraction at an axial distance of 9.5 cm are made with experimental measurements in figure 5.69. There is little difference in the calculated species concentrations at this axial station. The simulations do a very good job of predicting the fuel concentration, except for over-predicting the peak fuel mole fraction. Up to a radius of 2 cm, the oxygen concentration is well predicted by both simulations. Beyond a radius of 2 cm, the oxygen concentration is over-predicted. The pdf simulation gives slightly lower oxygen concentrations at large radii.

The concentration of CO_2 was found from the concentration of fuel, oxygen, and atom balances. Using a finite rate reaction model for the prediction of CO_2 resulted in

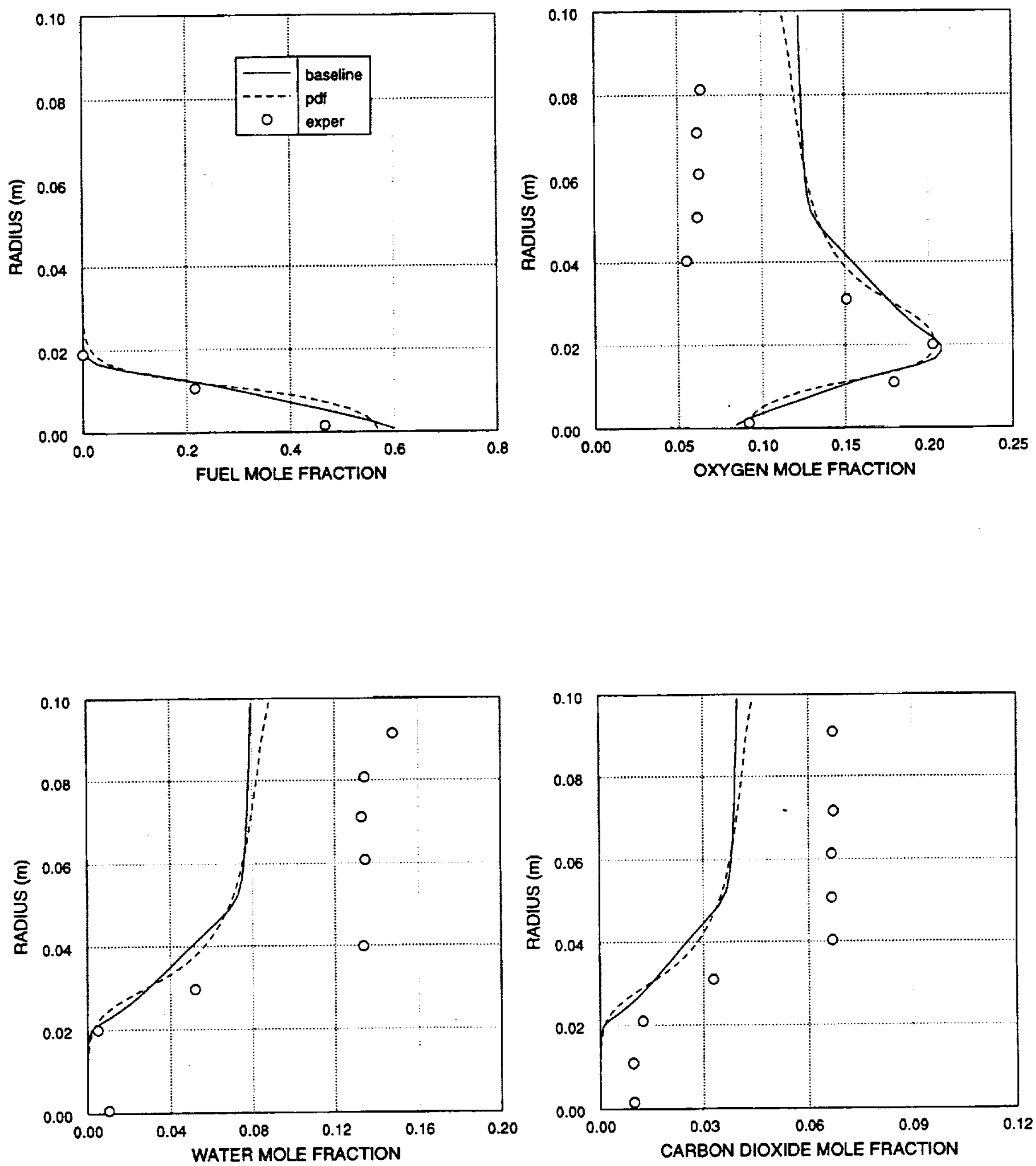

Figure 5.69 Species Mole Fractions at 9.5 cm

superfluous product concentrations at high temperatures. While the predicted concentration of fuel and oxygen can go to nearly zero, the rest of the arrhenius rate term is very large at high temperature. Initial computation product concentrations were 30 per cent above the theoretical maximum concentration. This has serious consequences for multiple reaction step models.

Beyond a radius of 2 cm, product concentrations are underpredicted by about 50%. This is about the level oxygen was overpredicted. The simulations underpredict combustion in the outer recirculation zone. There is some disparity in product concentration near the combustor axis. The predictions show zero product concentration at this location. Measurements show significant CO_2 concentration, but near zero water concentration. The temperature profiles for this axial location are shown in figure 5.70. The temperature is lowest near the combustor axis. The simulations predict temperatures about 200 degrees cooler along the combustor axis. Predicted temperatures off the combustor axis are very good, despite the error in predicted species concentrations. Temperature increases with radius up to 5 cm. Beyond a radius of 5 cm, temperature is fairly constant. The pdf simulation which shows a slight increase in temperature towards the combustor wall. The outer wall was modeled as adiabatic since the combustor wall was insulated. The experimental profile shows temperature slightly dropping

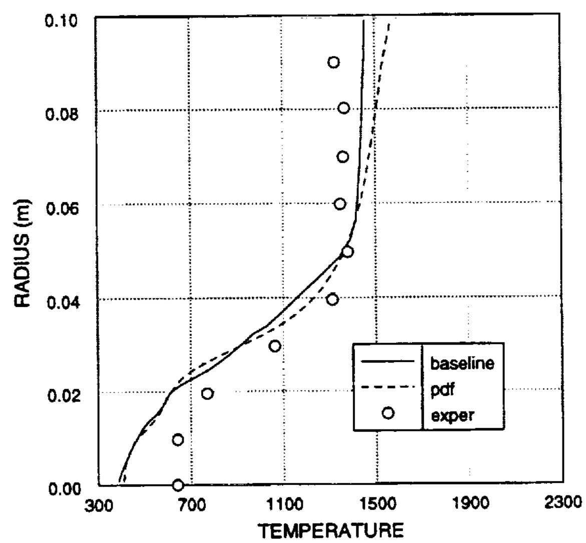

Figure 5.70 Temperature at 9.5 cm

near the wall.

M. Nikjooy and R. So [28] did some calculations for this same combustor. They used a two-step finite rate combustion and an equilibrium combustion model. The use of an equilibrium combustion model implies that infinite time exists for combustion or that combustion is extremely fast. The finite rate constant was higher than that employed in this work and very rapid combustion was predicted. Their calculations predicted peak temperatures above 2000 degrees close to the air and fuel inlet ducts, which is not in agreement with the experimental data.

Comparisons of species at an axial distance of 17.5 cm for the present simulations are shown in figure 5.71. The SIMPLE simulation best predicts the fuel concentration. The pdf simulation slightly over-predicts the centerline peak fuel mole fraction and the fraction at a radius of 2 cm.

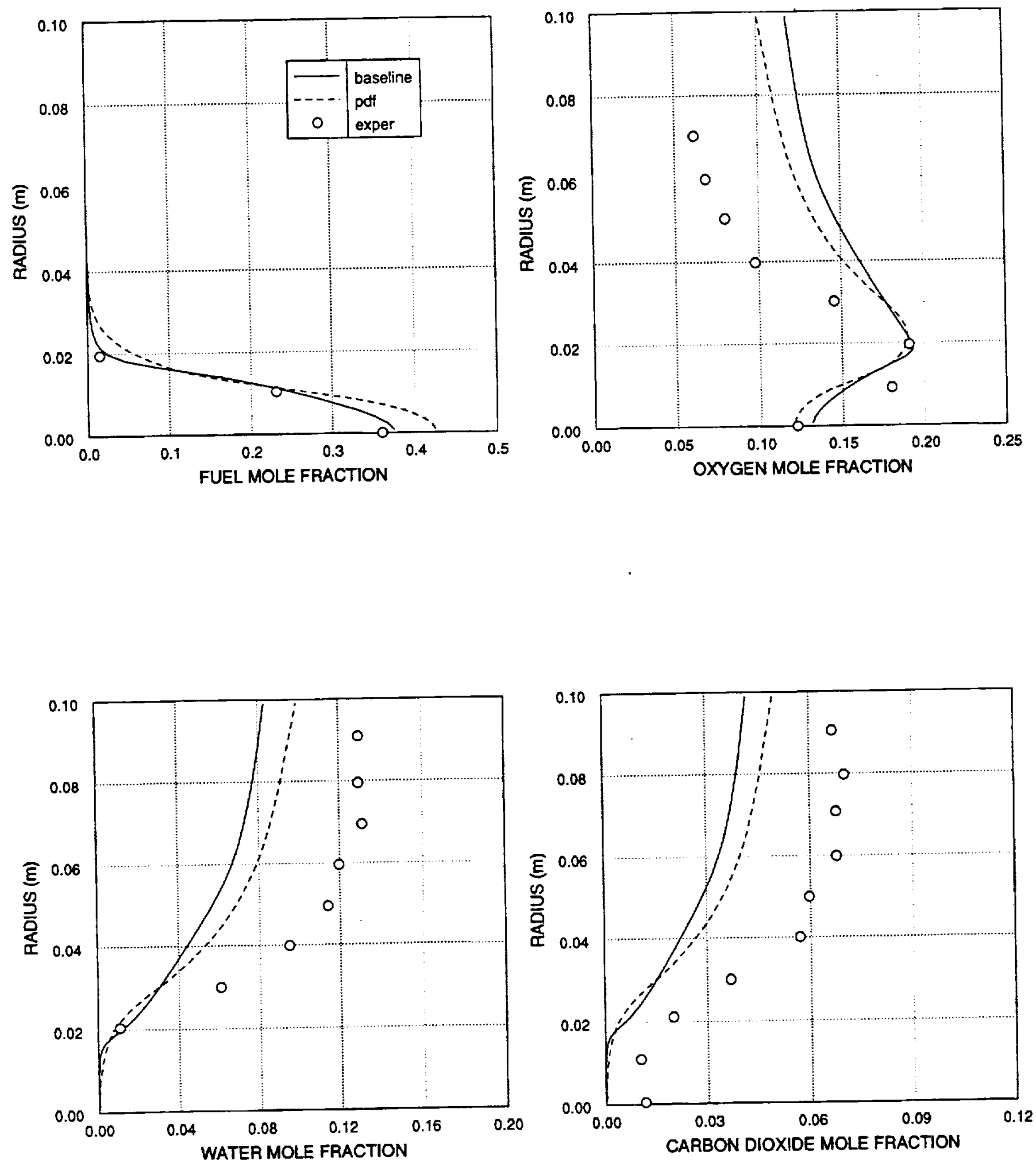

Figure 5.71 Species Mile Fractions at 17.5 cm

The hybrid pdf simulation better predicts oxygen mole fraction. Oxygen concentration is well predicted up to the peak oxygen concentration at a radius of 2 cm. Beyond the peak, both simulations overpredict oxygen concentration. The largest error is at the combustor wall. Product concentrations are underpredicted by the simulations as they were at 9.5 cm, although the hybrid pdf simulation is improving compared to the SIMPLE simulation. The anomaly in product concentrations near the combustor axis still exists.

The species mole fractions at 24.6 cm are shown in figure 5.72. The peak fuel mole fraction is significantly overpredicted. At larger radii, the fuel predictions are excellent. The pdf simulation again predicts higher fuel concentrations. Paradoxically, the pdf simulation also predicts lower oxygen concentration than the other simulation. Peak oxygen concentration is well predicted. Oxygen concentration is slightly underpredicted by both simulations near the combustor axis. Oxygen concentration beyond a radius of 2 cm are overpredicted, but are improving compared to previous comparisons. Both simulations underpredict product species concentration, with the exception of water near the combustor axis. The hybrid pdf simulation better predicts oxygen and product concentration. Carbon dioxide is detected near the combustor axis, but not predicted. The H_2O concentration near the combustor axis is very low for the predictions and measurements. Predictions and measurements of H_2O

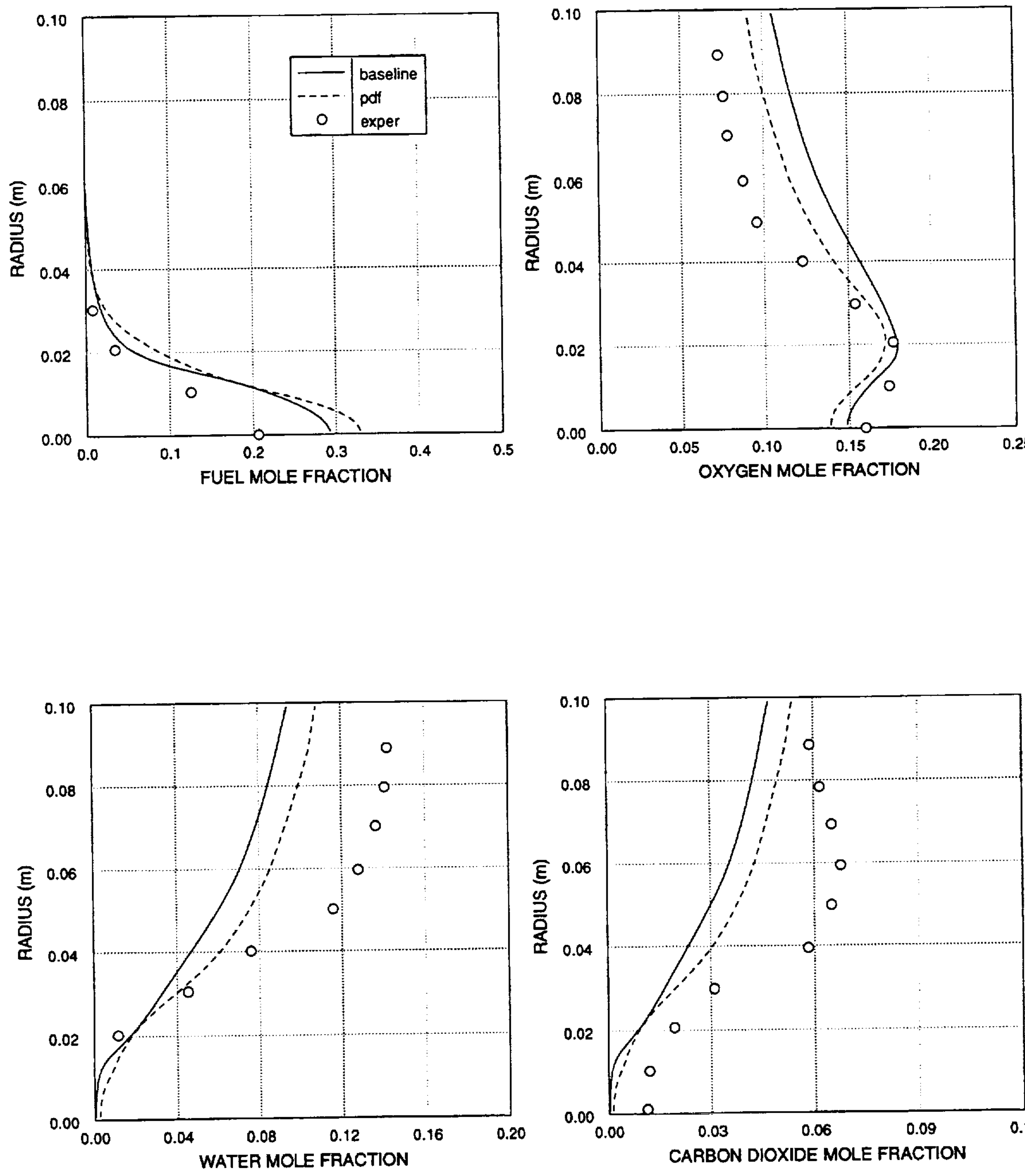

Figure 5.72 Species Mole Fractions at 24.6 cm

of H_2O concentration increase towards the combustor wall. A peak in CO_2 concentration is measured at a radius of 6 cm, while the simulations show CO_2 concentration increasing towards the combustor wall.

Predictions of fuel concentration along the combustor axis worsen at the next axial station. At 32.7 cm, both simulations over-predict peak fuel concentration by thirty per-cent. Paradoxically, predictions for oxygen are excellent, much improved from previous axial comparisons. Under a radius of 4 cm, the pdf simulation only slightly under-predicts oxygen. Much improvement is also seen in product species predictions. The carbon dioxide concentration is slightly underpredicted. Near the combustor axis, H_2O concentration is overpredicted by the hybrid pdf simulation, but the pdf simulation best predicts carbon dioxide. As a single step reaction is being employed in the combustion models, predicted product concentrations are related. The experimental data does not show this dependence between product concentrations near the combustor axis. Thus, evaluating only one product species at this location could lead to incorrect conclusions about the predictive capability of combustion models.

Figure 5.74 gives the predicted and corrected temperature profiles at 39.5 cm. The hybrid pdf simulation best predicts temperature near the combustor axis at this location. However, temperature is significantly overpredicted

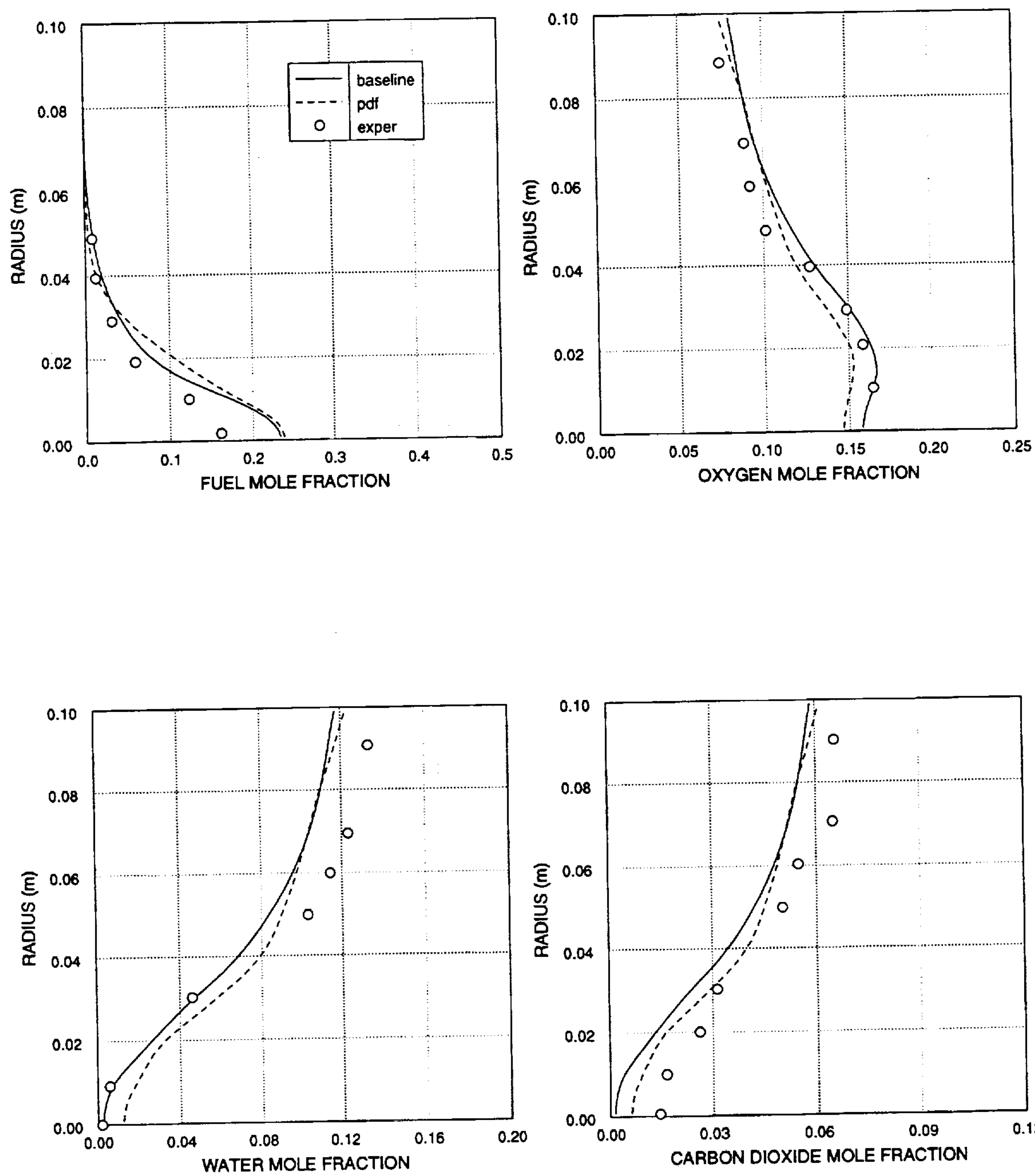

Figure 5.73 Species Mole Fractions at 32.7 cm

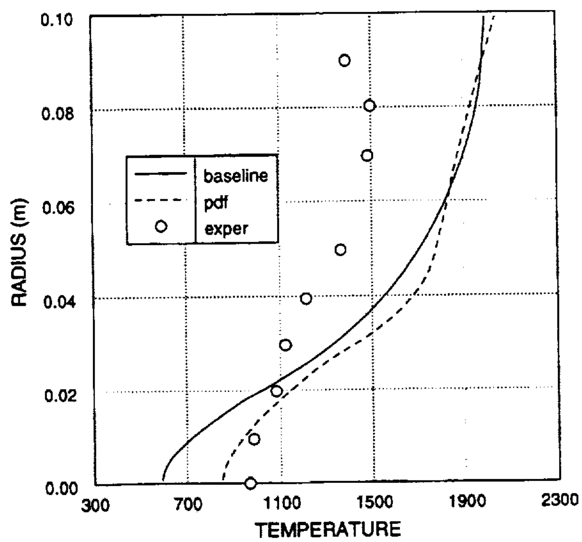

Figure 5.74 Temperature at 39.5 cm

beyond a radius of 2 cm. At a radius of 8 cm, the error in predicted temperatures is 400 degrees. Experimental temperatures near the combustor wall suggest some heat transfer is taking place. Measurements of species concentration were not reported at this axial location.

Species mole fractions at an axial distance of 47.6 cm are shown in figure 5.75. Fuel mole fraction is overpredicted by over 50%. Comparing fuel profiles for previous axial stations, this is the station with the largest relative error. The peak fuel concentrations have dropped by about a factor of two from the previous axial station. The fuel concentration profile is also spreading. Oxygen concentration is overpredicted near the combustor axis. Predicted oxygen concentration is lower than at the previous station. There is significant combustion near the combustor axis. Significant H_2O and CO_2 concentrations are measured

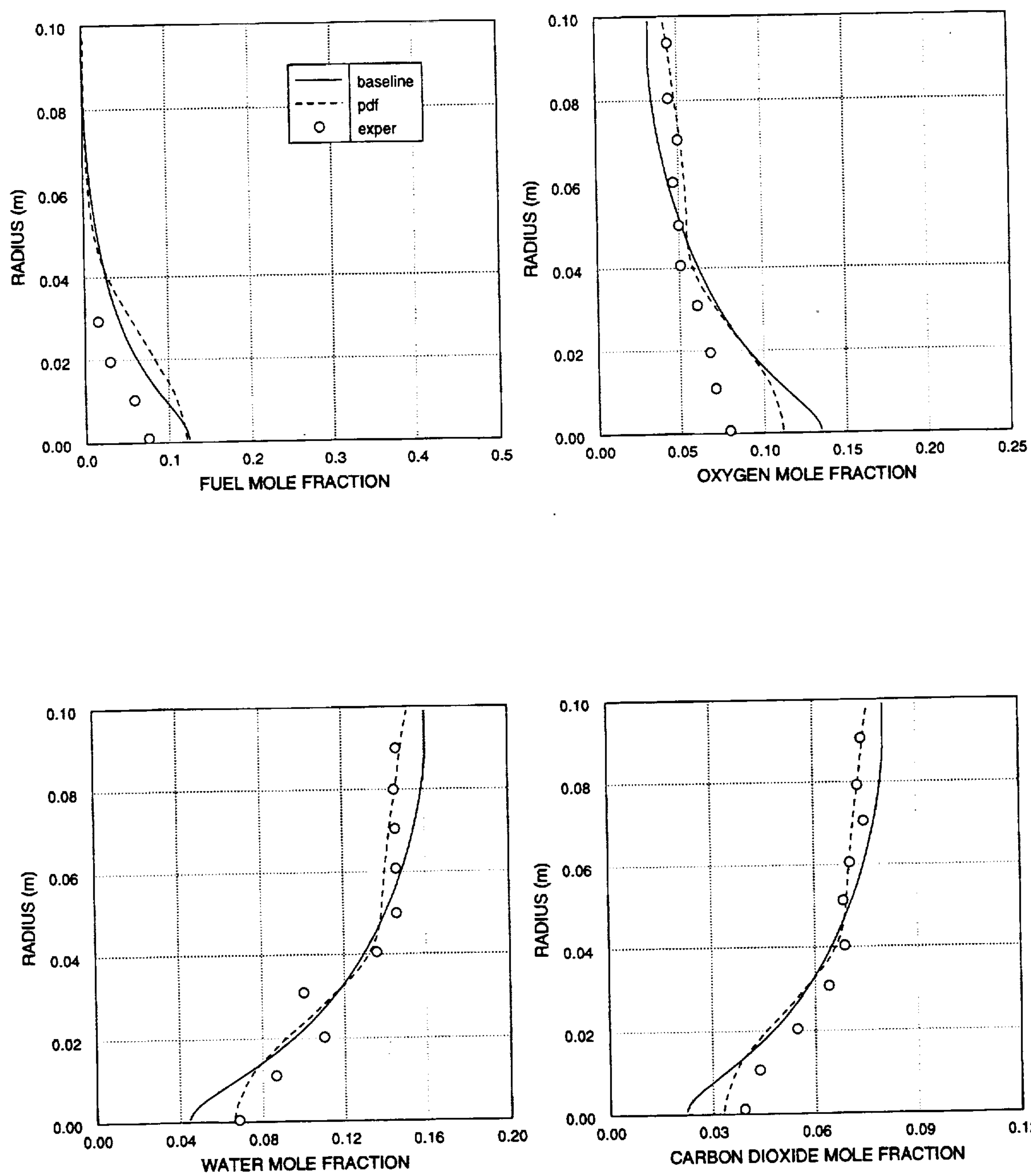

Figure 5.75 Species Mole Fractions at 47.6 cm

and predicted near the combustor axis. The pdf simulation of product concentrations are very close to the experimental values. As the pdf simulation overpredicts reactant concentration near the combustor axis, this shows some error possibly due to the one-step reaction mechanism. By not allowing intermediate chemical species, product species can be over-predicted. The conventional combustion simulation underpredicts product concentration near the combustor axis where fuel and oxidant are overpredicted.

Reactant concentrations at an axial distance of 63.2 cm, shown in figure 5.76, continue to rapidly decrease. Both simulations under-predict oxygen near the combustor wall. The pdf simulation predicts higher reactant concentration and lower product concentration than the conventional simulation. Predicted product concentrations are much more uniform than the measurements. Both simulations overpredict product concentrations. Product concentration predictions are worst near the combustor axis and the combustor wall. Except for fuel prediction, hybrid pdf predictions are closer to the experimental data, especially at larger radii.

At the 78.5 cm station, measurements show some oxidant and fuel concentration. This is despite the high temperatures that must exist. The pdf simulation overpredicts oxygen and fuel. The conventional simulation predicts a very slight amount of fuel near the combustor axis and some

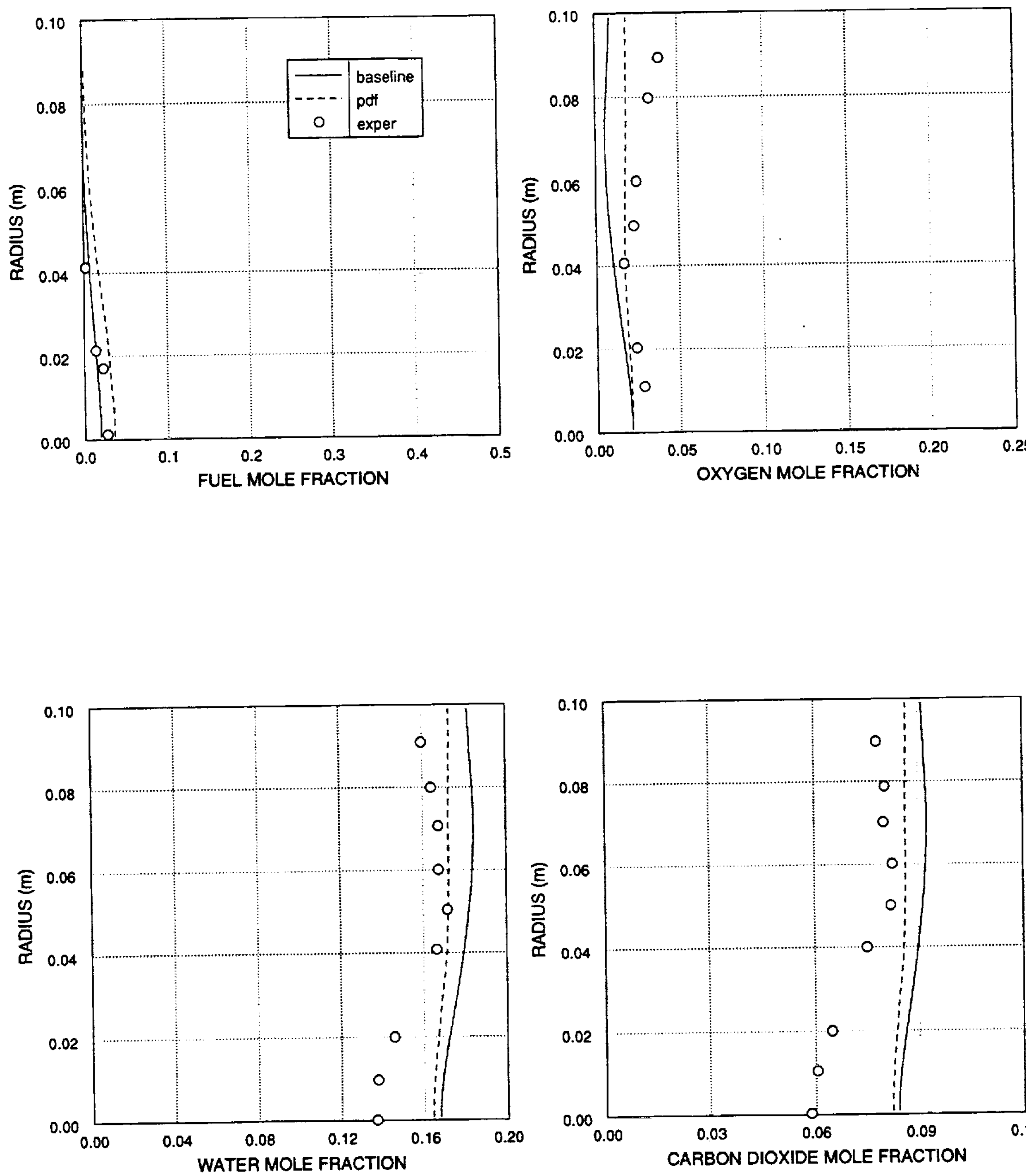

Figure 5.76 Species Mole Fractions at 63.2 cm

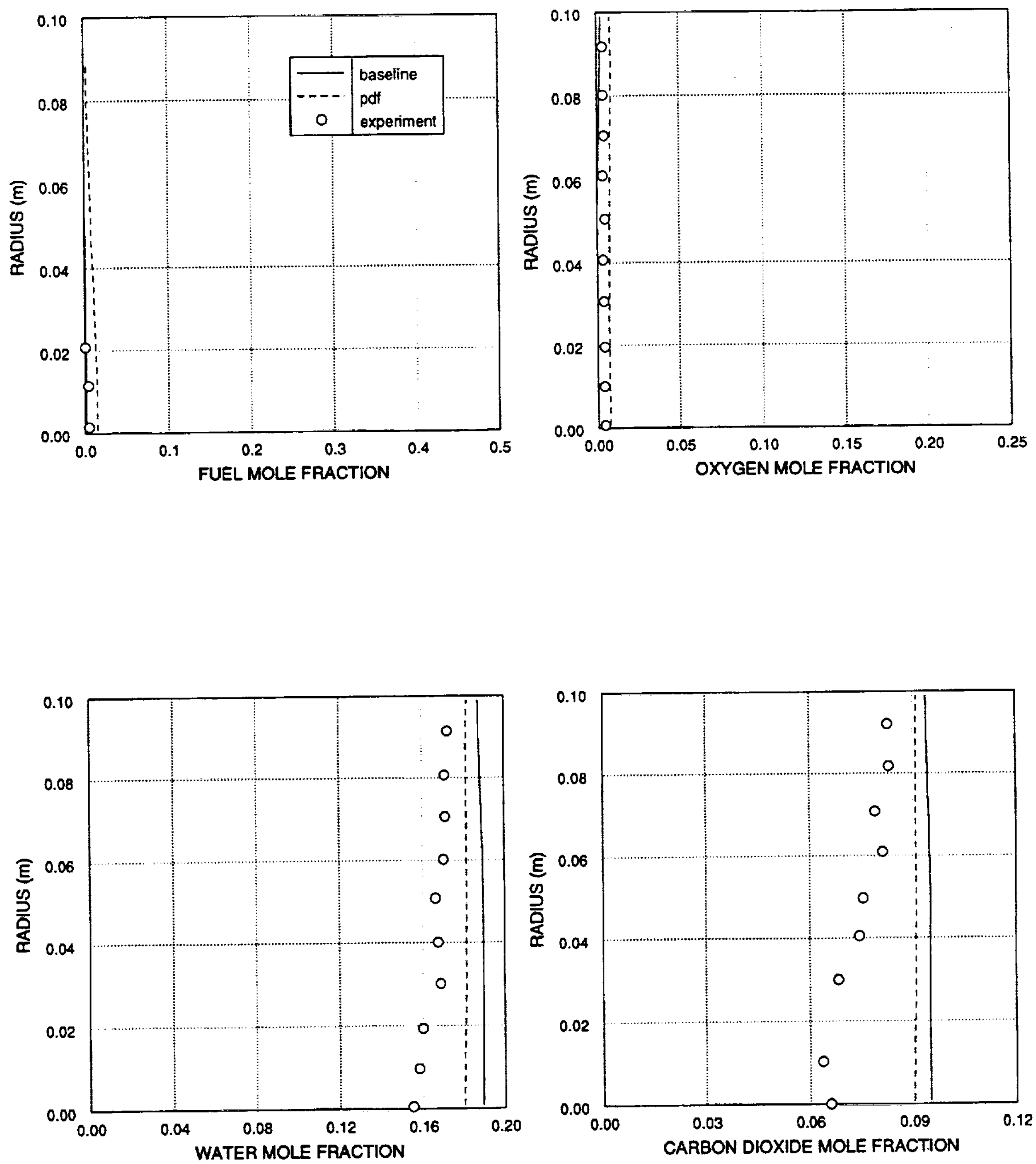

Figure 5.77 Species Mole Fractions at 78.5 cm

oxygen towards the combustor wall. Predicted product concentrations are nearly uniform across the combustor at this axial location. The experimental data shows considerable variability. Carbon dioxide concentrations vary more than the water. Product concentrations are overpredicted. The hybrid pdf simulation best predicts product concentration.

Experimental data showed nearly complete reaction at an axial distance of 137.5 cm. The complete length of the combustor was not simulated. The actual combustor was about 50% longer than simulated. In the pdf simulations, the much smaller distances in the radial direction cause the number of particles exchanged in the radial direction to vastly outnumber the number of particles exchanged in the axial direction. This hampers information transfer in the axial direction. Increasing the number of particles increases the number of particles exchanged axially, but is more computationally expensive. The number of particles used in this calculation was 250 particles per cell. Using low numbers of particles resulted in a gradual prediction of flame or combustor blow-off. Using fewer particles caused larger temperature oscillations in the iteration process.

Particles from three different computational cells for an axial distance of 9.18 cm from the combustor step are shown in figure 5.78. The particles are plotted as a function of mixture fraction and temperature, where mixture fraction is the sum of the mass fraction of fuel in all

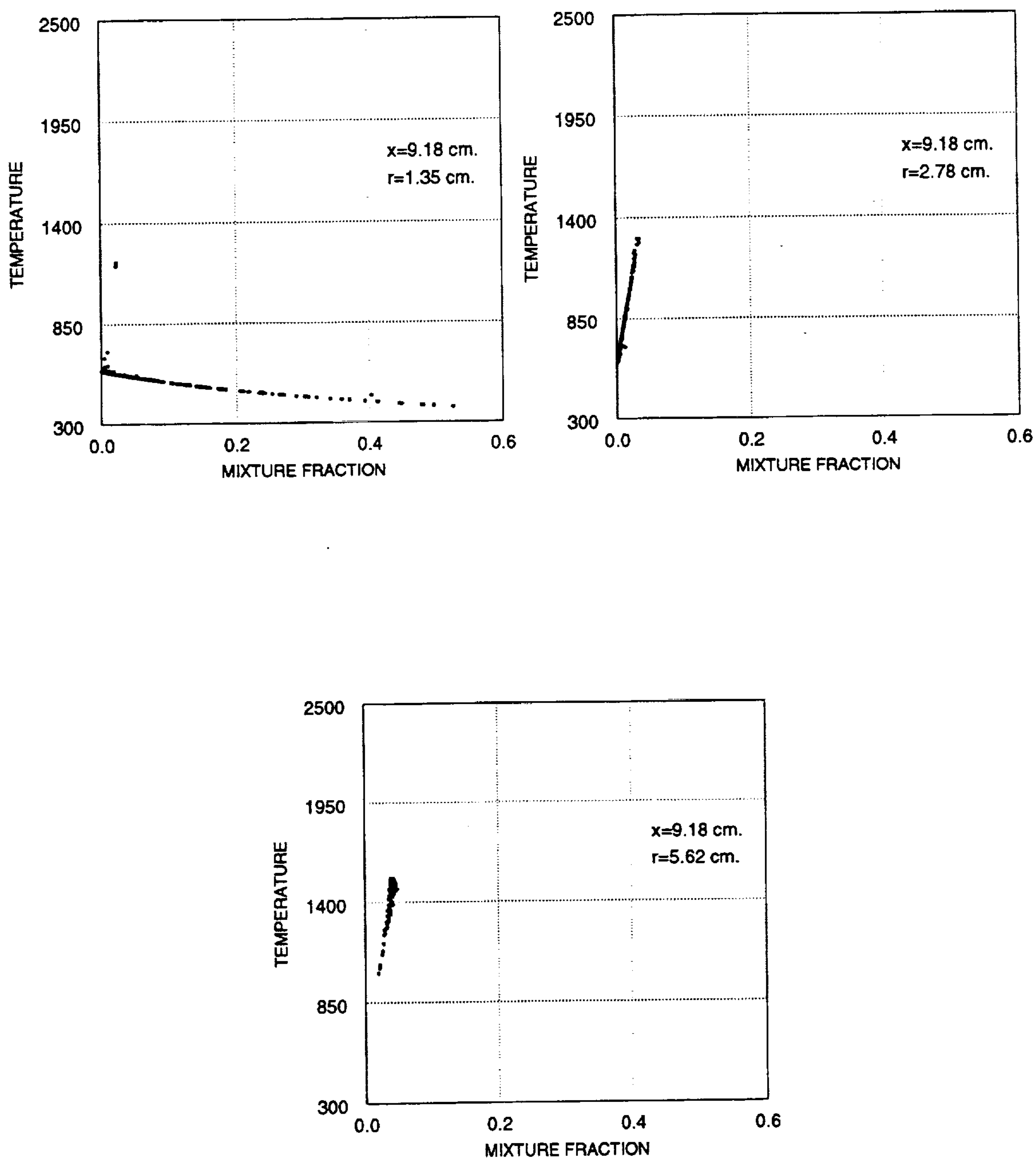

Figure 5.78 Particle plots at an axial distance of 9.18 cm.

species. Pure mixing with no combustion is represented by a line between mixture fraction of zero and temperature of 589 K (air) to a mixture fraction of 1.0 at a temperature of 300 K, which is pure fuel. The line would have some slight curvature due to variable C_p. Combustion is represented by an elevation off this line. Complete combustion is represented by a line from a mixture fraction of zero and temperature of 589 K (pure air) to a stoichiometric mixture fraction of 0.055 at 2500 K and hence to a mixture fraction of 1.0 at a temperature of 300 K.

The particle plots show that a range of mixtures is being simulated in various cells. The particle plot for the cell closest to the fuel inlet (r=1.35) shows various combinations of air and fuel with very little combustion. The maximum mixture fraction in this cell is 0.55. No pure fuel particles are shown. The plot for a radial location of 2.78 cm shows very lean, but complete combustion. The particle plot for a radial distance of 5.62 cm shows slightly richer combustion and higher temperatures.

Particle plots for an axial distance of 39.6 cm are shown in figure 5.79. These particle plots show much higher temperatures. As before, the level of combustion increases with distance from the combustor axis. The cell with a radial distance of 1.35 cm displays the largest number of unburned and partially burned particles. The cell at a radial distance of 5.62 cm displays only a few partially

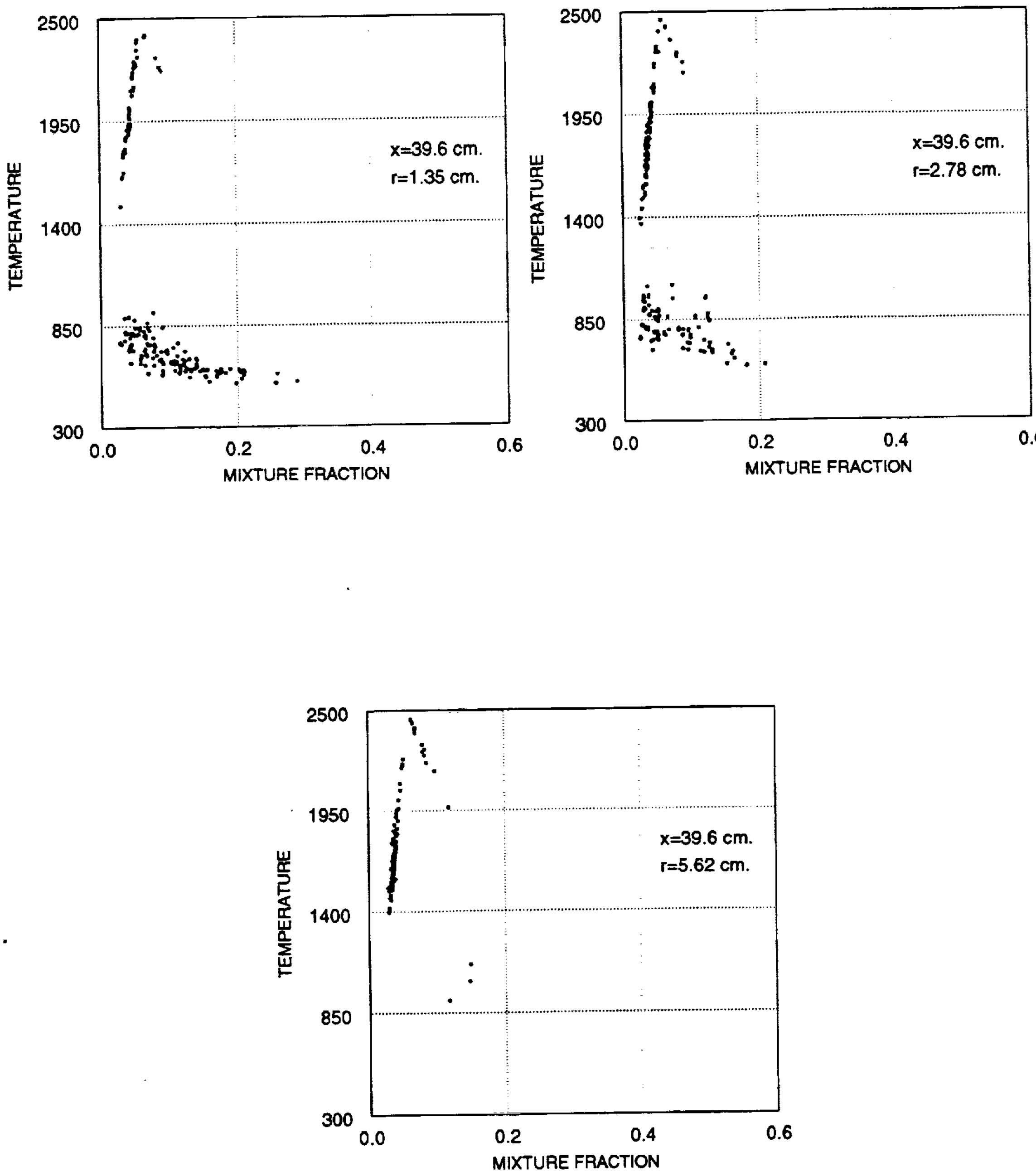

Figure 5.79 Particle plots at an axial distance of 39.6 cm.

burned particles. The reaction model implemented in the hybrid pdf model gives partially combusted particles for low temperatures, but most high temperature particles are almost fully burnt.

The use of a finite-rate reaction scheme here has allowed significant overlap of fuel and oxidant concentrations. The assumed shape pdf, equilibrium chemistry model used by Smith and Smoot predicted little overlap of oxygen and fuel concentration profiles. The finite-rate combustion models used here underpredicted the carbon dioxide concentrations in the recirculation zone, but the temperature predictions were much improved from their calculation. The hybrid pdf initially overpredicted fuel concentration, but predictions using the hybrid pdf were better than the baseline predictions at successive axial stations. Hybrid pdf predictions of oxygen, carbon dioxide and water were almost always superior to the baseline simulation.

5.3.2 SWIRLING DIFFUSION FLAME

Attempts were made to simulate the combustor of Jones and Wilhelmi[121]. This is a newer set of experimental data with LDA measurements of axial, radial, and tangential velocity, temperature and species data at numerous axial stations including data very close to the injector face. This combustor flow had a 45 degree gas turbine type swirler, was 100 mm in diameter and was 300 mm long. The fuel was gaseous propane introduced by a central conical annular injector. The axial velocity profile was completely positive by 100 mm, but the large centerline defect was still apparent at 289 mm, near the combustor exit. All SIMPLE calculations showed a nearly uniform axial velocity at this position. This axial velocity defect may be caused by unsteady effects. Also, there was some ambiguity in the initial axial velocity measurements. The first measurements showed two axial velocity peaks with a single radial velocity peak. This implied that the secondary peak was from the recirculating flow. This recirculating flow was stronger than any calculated. The second velocity peak may have something to do with a quarl at the top of the inlet swirler. The simulations did not model the quarl. At the second measurement station, the axial velocity exhibited strong reverse flow next to the fuel and air inlet flow, tapering off towards the centerline. All simulations attempted calculated the largest negative axial velocity along the centerline. The experimental flow along the combustor centerline was quiescent. The high reverse flow next to the inlet flow and adjacent quiescent flow seems more characteristic of flow being entrained into a jet.

It was decided to study a similar combustor with weaker swirl, as it is known that the k-ε turbulence model poorly predicts areas of high swirl. A similar combustor is that of Jones and Tober[122]. This combustor has a thirty degree swirler, with no quarl. The fuel is propane which enters through a conical annular nozzle with a cone angle of 90 degrees just inside of the air swirler. The internal diameter and length of the combustor are 196 mm and 700 mm, respectively. The inner and outer diameters of the swirler are 23.5 mm and 42 mm. The combustor was run at two air to fuel ratios. The case studied in this work had an air flow of 26.7 g/s and fuel flow of 1.37 g/s.

A 70 by 55 grid rectilinear grid system was used. Grid stretching was used to concentrate grid points near the inlet fuel injector. The axial inlet velocity was calculated by projecting back the velocity data from the x/D=.1 data using the flow angle from the peak axial and radial velocities, and then scaling the profile to give the correct mass flow. The radial velocity inlet data was found by doing numerous runs until a good match was obtained for the experimental data at the first couple of measurement stations. The hybrid pdf simulation used a stronger inlet radial velocity.

The flowfield is characterized by two hot recirculating flows. One recirculating flow is a toroidal vortex adjacent to the combustor walls. This recirculation zone extends to about x/D=0.5. The second recirculating flow occurs along the combustor axis and is referred to as a Central Recirculating Zone or CRZ. This recirculation zone is characteristically caused by high inlet swirl. Based on a contour plot in Jones and Tober, the CRZ appears to extend to x/D=1.6, and takes up half the diameter of the combustor at x/D=0.8. The combustor was simulated out to x/D=2.5. The two recirculation zones are separated by higher velocity flow which is at an angle of about 30 degrees to the combustor axis. Initially, this jet-like flow is largely composed of air and fuel from the combustor inlet. This flow is typically fuel rich at smaller radii and oxygen rich at larger radii.

Predictions and measurements of velocity and temperature at the x/D=.1 location are shown in figure 5.80. The calculated axial velocity peak for the flow separating the two recirculation zones is well predicted. This was one of the criteria for selecting inlet conditions. The width of the peak is overpredicted. The pdf simulation better predicts the lower portion of the velocity peak. The experimental data exhibits nearly constant, low velocity flow across the CRZ. Both calculations show the magnitude of the reverse-flow velocity increasing towards the combustor axis. The predicted maximum reverse flow velocity in the CRZ is

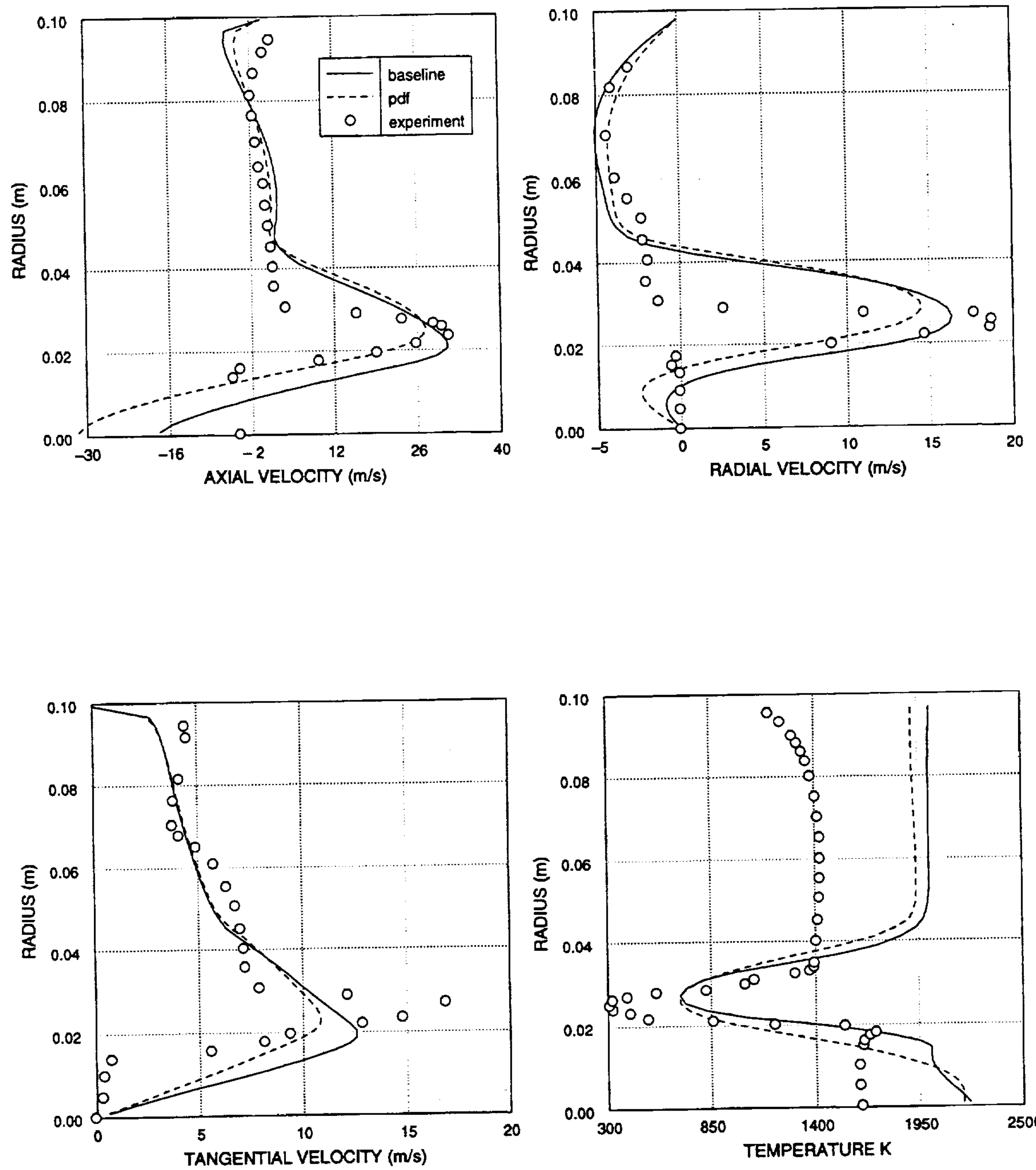

Figure 5.80 Velocity and Temperature at x/D = 0.1

much higher than measured, which was characteristic of trial calculations of Jones and Wilhelmi's combustor. The outer recirculation zone has rather low velocity which is well predicted by the simulations. Near the outer combustor wall, calculations exhibited slightly larger negative axial velocity than measured.

Radial velocity predictions for the outer recirculation zone are very good for both simulations. Both simulations underpredict the radial velocity peak and overpredict the width of the higher velocity jet-like flow by almost a factor of two. Measurements of radial velocity across the CRZ are nearly zero. The simulations predict slightly higher radial velocity flow. The radial velocity profiles near the combustor axis are parabolic, and scale on the cross-sectional size of the CRZ. The hybrid pdf radial velocity profile for the jet-like inlet flow is slightly shifted outward due to a larger inlet radial velocity profile. In this and other simulations of this flowfield, the pdf simulations exhibited lower radial displacement of the inlet flow with axial distance.

The predicted tangential velocity peaks are under-predicted and are highly diffusive. The experimental measurements show very low tangential velocity in the CRZ. The simulations show nearly constant angular rotation across the CRZ and up to the location of peak tangential velocity. Tangential velocity in the outer recirculation zone is well predicted by both simulations. The simulations do not predict an experimentally measured depression in tangential velocity at a radius of 7 cm.

The numerical simulations correctly predict high temperatures in both of the recirculating zones. However, these temperatures are over-predicted by hundreds of degrees. The high temperature predictions are the result of assuming 100 % combustion efficiency. Temperature predictions would improve if a lower heat release were used. The pdf module used here uses thermodynamic data of Gordon and McBride and assumes 100 % efficiency. This model is more difficult to manipulate to predict lower heat of reaction. The experimental data shows depressed temperatures near the outer wall. The combustor wall was treated as adiabatic in the both of the simulations as the pdf module does not have a wall heat transfer model in it. Thus, the predictions do not exhibit a drop in temperature near the wall. The large drop in temperature between the two recirculation zones is predicted, but the minimum temperature predicted is hundreds of degrees too high. Both simulations predict the same minimum temperature.

Fuel, oxygen, carbon dioxide, and mixture fraction concentrations at x/D=.2 are shown in figure 5.81. The mixture fraction is a combination of the mass fractions of hydrogen and carbon in all of the species. Other concentrations are in mole fractions. Mixture fraction, Carbon

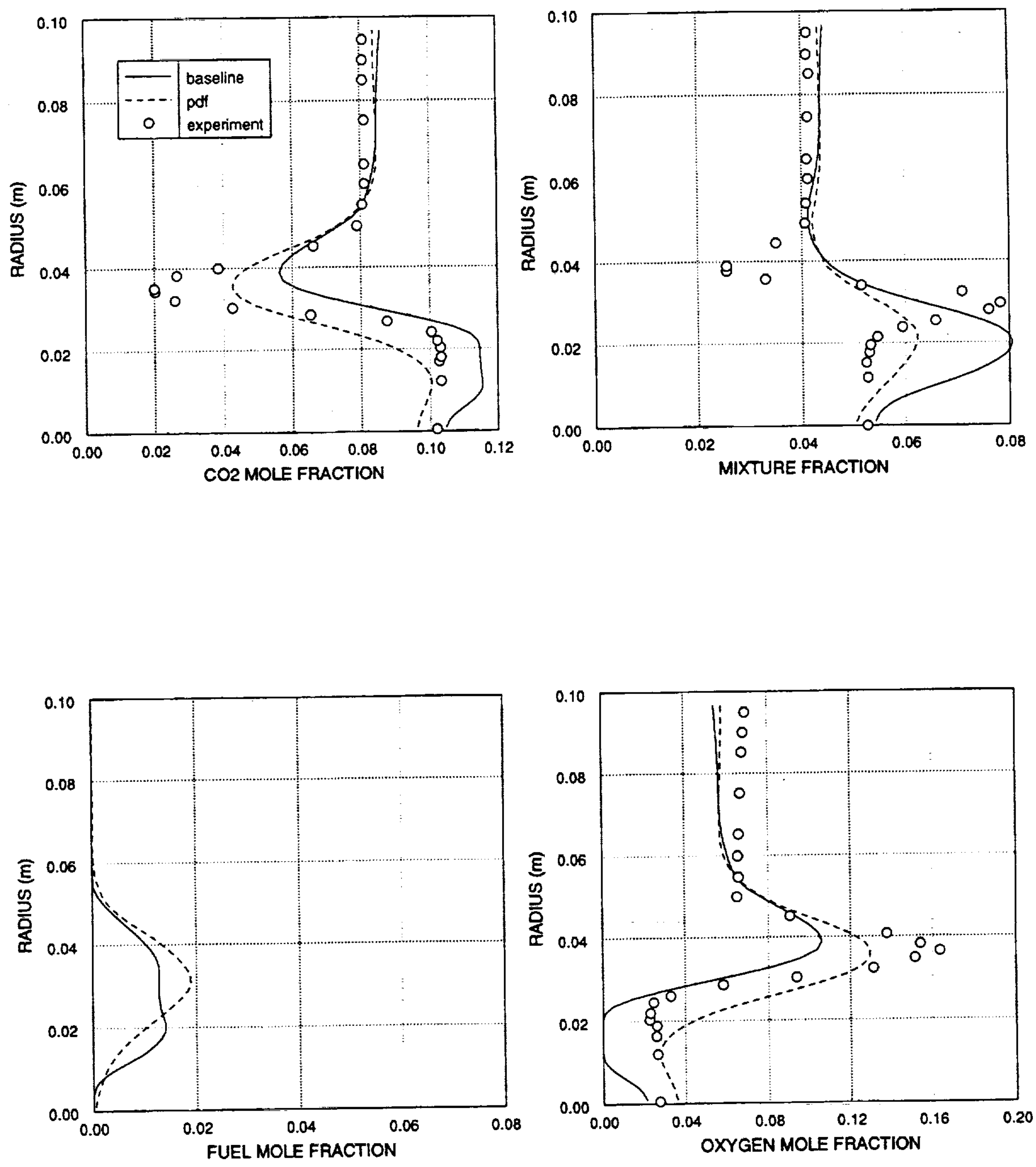

Figure 5.81 Species concentrations at x/D=0.2

dioxide predictions and measurements agree in the outer recirculation zone. The traditional type simulation over-predicts carbon dioxide concentration at other locations. The conventional simulation overpredicts the minimum carbon dioxide concentration by a factor of almost three. The hybrid pdf simulation does a better job of predicting carbon dioxide concentration. Both simulations show carbon dioxide initially increasing with radial distance from centerline. The experimental concentrations are constant in this area. The mixture fraction and carbon dioxide profiles match in the outer recirculation zone as the fuel is fully burned in this region. The drop in mixture fraction at a radius of 4 cm isn't shown in the simulations. This is due to the overprediction of carbon dioxide at this radial location. The peak experimental mixture fraction occurs at a larger radius than the peak for carbon dioxide. Thus, there must be significant fuel at a radius of 3 cm. The simulations predict significant fuel at this location. Unfortunately, the predicted fuel concentration is not large enough to predict the mixture fraction peak at the correct radial location. Instead, the simulations predict mixture fraction peaks at a lower radius where the fuel and carbon dioxide concentrations overlap. The conventional simulation predicts the magnitude of peak mixture fraction. Unfortunately, this is caused by an over prediction of carbon dioxide. Curiously, the conventional simulation predicts peak fuel concentration in the same region as peak carbon dioxide. The oxygen concentration predictions show the same trends as the experimental data. The predicted concentration of oxygen in the outer recirculation zone is excellent, as was other concentrations. At a radius of 4 cm, a peak is shown due to oxygen from the inlet flow. At 2.5 cm, the oxygen concentration is at a minimum due to large concentrations of carbon dioxide and fuel. The conventional simulation underpredicts oxygen, especially across the inlet flow. The pdf simulation best predicts the oxygen concentration. The radial location of peak oxygen concentration is well predicted. The hybrid pdf predicted peak lies midway between the experimentally measured peak and conventionally predicted peak. The low oxygen concentration inside the CRZ is best predicted by the pdf simulation, but the width of this part of the profile is predicted by the conventional simulation.

Temperatures corresponding to the above concentrations, are shown in figure 5.82. Temperature predictions in the recirculation zones are high. The temperature predictions across the outer recirculation zone are nearly constant, as were the species concentrations. The minimum temperature predicted by the pdf simulation is midway between the experimental minimum and conventionally predicted minimum. At the previous axial location, the simulations predicted the same minimum temperatures. The radial location of minimum

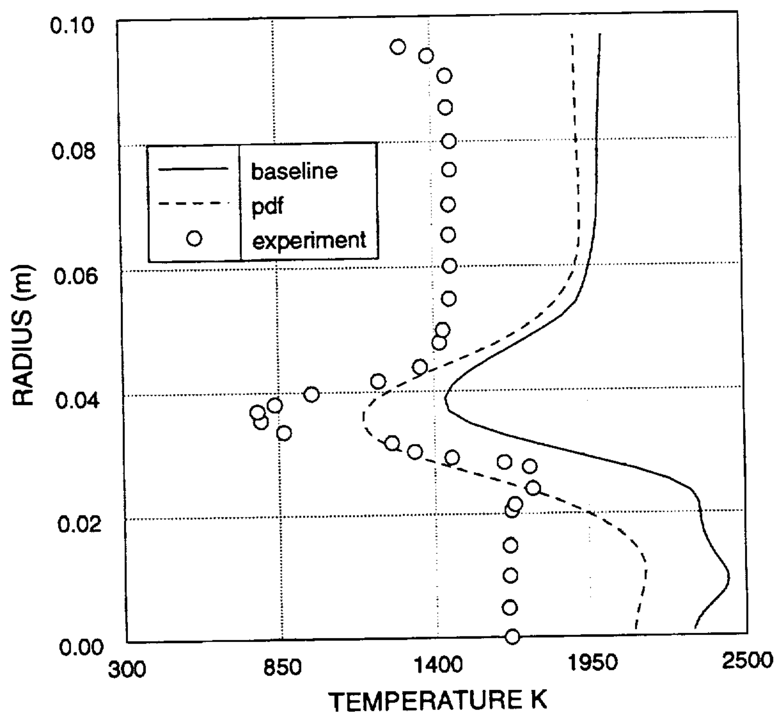

Figure 5.82 Temperature at x/D = .2

temperature is the same as that for minimum carbon dioxide and maximum oxygen concentration. The hybrid pdf simulation best predicts temperature in the CRZ.

Velocity and temperature at x/D=.3 are shown in figure 5.83. Both simulations predicted nearly identical axial velocity profiles. Predicted positive axial velocity profiles are much wider than the experimental profile. Peak axial velocity is underpredicted, although slightly beyond the peak, the predictions are excellent. The size of the CRZ is underpredicted. The maximum reverse velocity is over-predicted in the CRZ, although it is much improved from the x/D=.1 location. Again, the experimental measurements

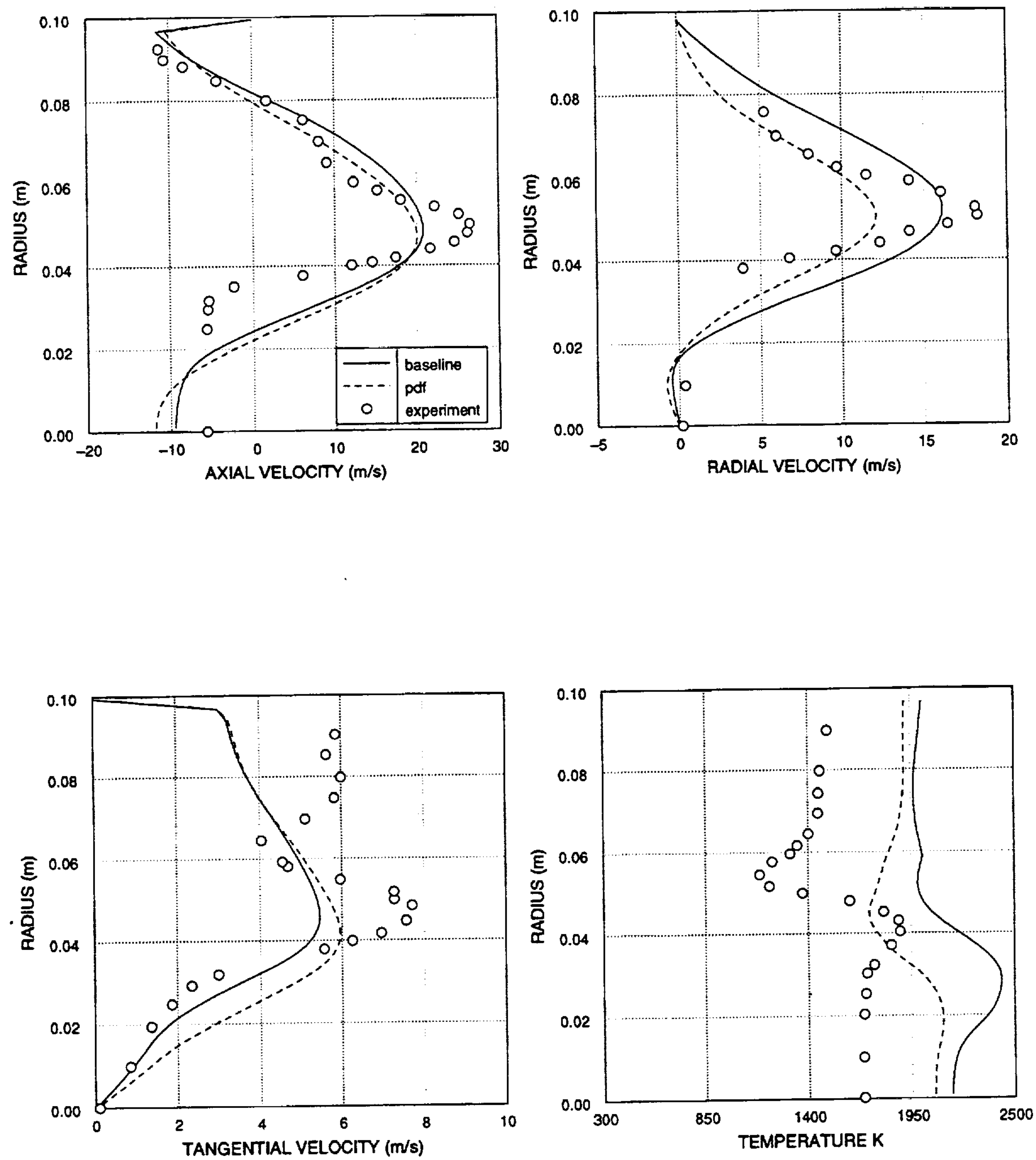

Figure 5.83 Velocity and Temperature at x/D=0.3

show nearly constant, low axial velocity across the CRZ. The experimental radial velocity profile shows a narrow high velocity peak. Predicted peak profiles are blunter and wider. The general shape of the predicted profiles is very similar, only differing in magnitude. The hybrid pdf simulation predict a velocity profile about 30 % lower than the conventional simulation.

The experimental tangential velocity profile shows two peaks. The first peak is due to the swirling inlet swirling flow. The second velocity peak is adjacent to the outside combustor wall. Tangential velocities in this region are 4-6 m/s. At x/D=0.1, tangential velocities were less than 5 m/s near the outer wall. The increase in tangential velocity at larger radii is due to spreading of the peak tangential velocity which has decreased by about a factor of two from the x/D=0.1 location. The numerical simulations only predict the first velocity peak. Examination of the axial and radial velocity profiles does not give an apparent reason for the second outer tangential velocity peak or a tangential velocity defect in the profile.

The shape of the predicted temperature profiles is qualitatively correct. Predicted temperatures are too high. The conventional simulation predicts the minimum temperature at about the correct radial location. The hybrid pdf profile shows the radial location of minimum temperature about one cm less than was measured. Both simulations significantly underpredict the radial position of peak temperature. The pdf simulation predicts lower temperatures than the conventional simulation. Experimental temperature gradients are much larger than predicted.

Velocity and temperature results at x/D=.4 are shown in figure 5.84. The agreement between the simulations is better than the agreement between the predictions and measurements. The simulations predict the same magnitude of peak axial velocity, but the hybrid pdf simulation predicts a smaller radial displacement of the velocity profiles. Predicted profile peaks are again wider and blunter than the experimental peaks. Predicted radial velocities are almost identical out to a radius of 4 cm. Beyond 4 cm, the hybrid pdf simulation predicts lower radial velocities. The velocity predictions within the CRZ are closer to the experimental measurements than at previous stations. The width of the CRZ is again underpredicted. The maximum reverse flow velocity in the CRZ is decreasing. The experimental velocity gradient between the reverse flow in the CRZ and adjoining flow is greater than predicted. Predicted velocity profiles show diffusive, gradual changes. The comparison between predicted and measured tangential velocities is very good out to a radius of 3 cm. Beyond 4 cm the hybrid pdf simulation predicts higher tangential velocity at a lower radii, which agrees with the data. This is due to the reduced radial expansion predicted in the hybrid pdf simulation.

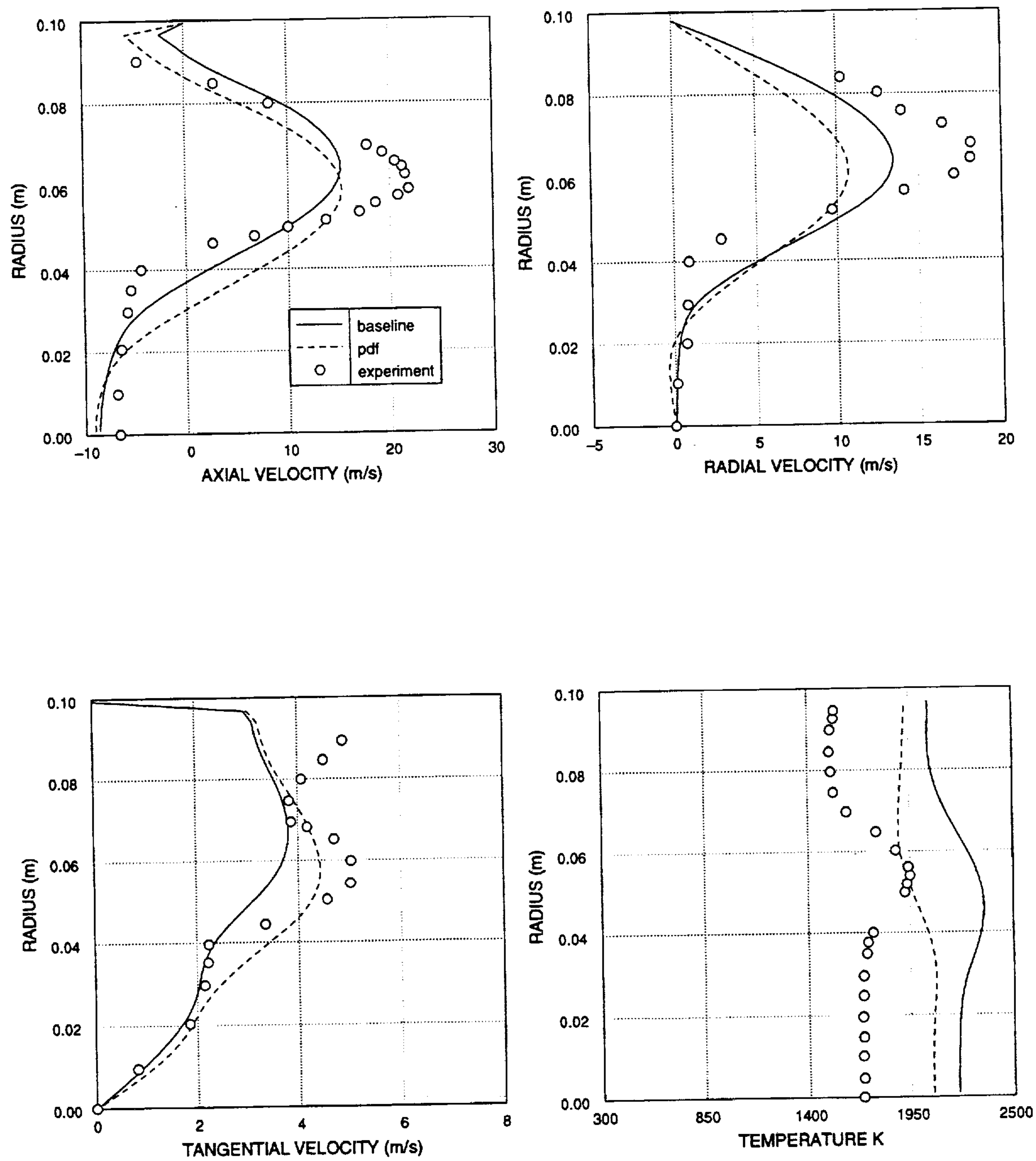

Figure 5.84 Velocity and Temperature at x/D=0.4

Again, experimental data shows a second tangential velocity peak, which isn't predicted by the calculations. Temperature predictions are high. Temperatures continue to become more uniform with axial distance. The pdf simulation predicts lower temperatures than the conventional simulation, but the conventional simulation better predicts the radial location of peak temperature.

Concentrations for x/D=.4 are shown in figure 5.85. The simulations predict relatively constant carbon dioxide concentration across the combustor. The experimental measurements predict a 30 % drop in concentration at a radius of 7 cm. The conventional simulation predicts peak carbon dioxide at 5 cm. Carbon dioxide is underpredicted at smaller diameters and overpredicted at larger diameters. The experimental mixture fraction shows only a slight dip at 7 cm, unlike the carbon dioxide profile. Also, the mixture fraction shows a significant peak at 5.5 cm while the peak carbon dioxide is at 3 cm. This implies that there is significant fuel or partially burned fuel between these points. The fuel mole fraction should be on the order of 0.01. The conventional simulation predicts almost no fuel at this axial station. The pdf simulation shows a maximum mole fraction of 0.0025 around 5 cm.

The conventional simulation does a good job of predicting oxygen concentration out to 6 cm. The peak experimental oxygen concentration at 7 cm isn't predicted in the

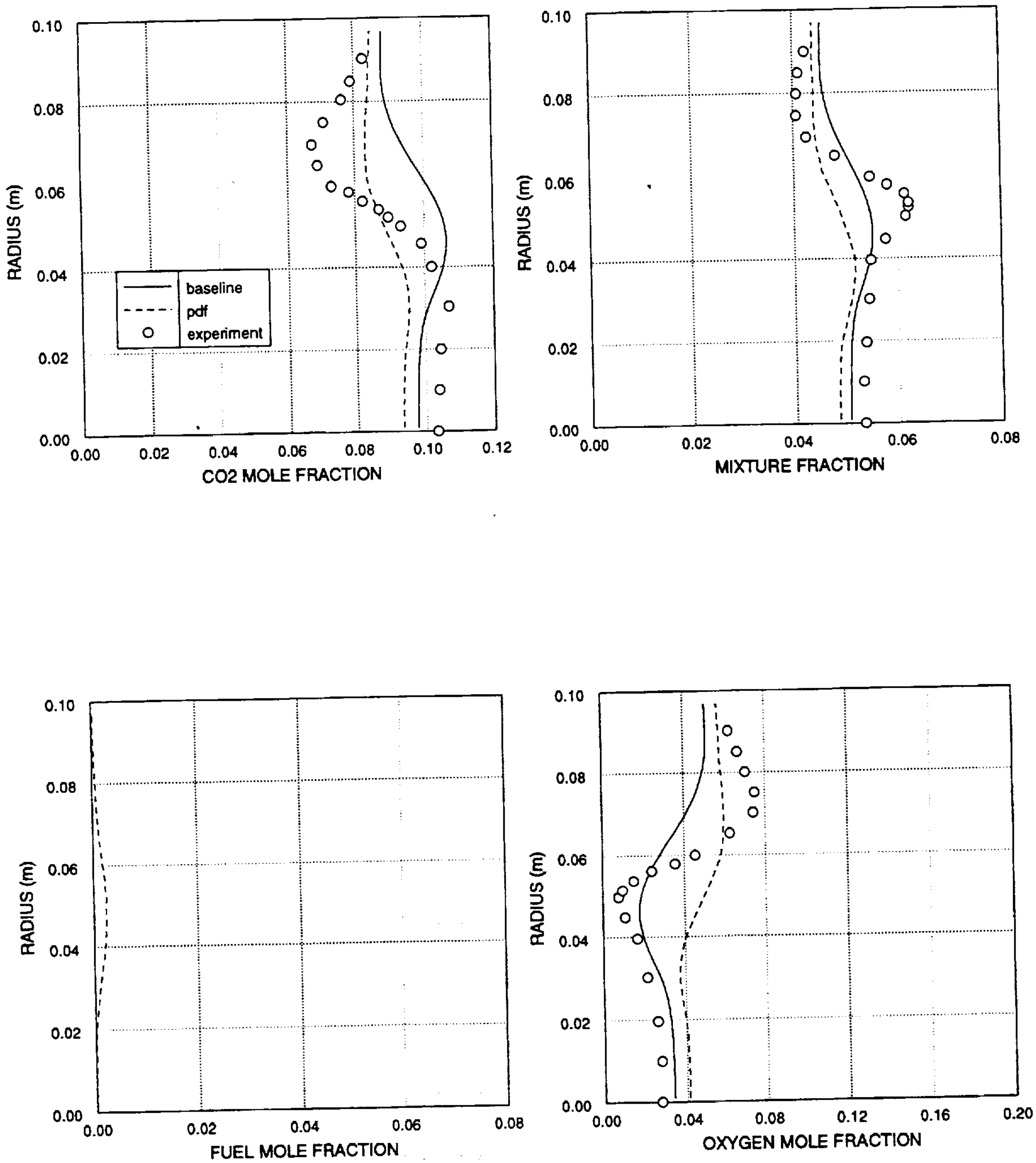

Figure 5.85 Species concentrations at x/D=0.4

simulations. The pdf simulation predicts the highest oxygen concentration at this station. Neither simulation is superior in the prediction of oxygen. Both simulations overpredict combustion. This results in more expansion at smaller axial and radial displacement from the combustor inlet.

Velocities at x/D=.6 are shown in figure 5.86. Negative axial velocity is measured over 60 % of the combustor inner diameter at this station. The simulations underpredict the size of this flow. Thus, the experimental velocity profiles show higher positive axial flow at greater radii. The back-flow velocity along the combustor axis is well predicted. The hybrid pdf simulation shows lower reverse velocity near the combustor axis, which may be due to increased combustion at smaller radii. The conventional simulation best predicts the axial velocity profile at this location. Experimental radial velocities are all positive. Simulations predict negative radial velocity for at least half of the inner diameter. The pdf simulation shows higher radial velocity at larger radii, unlike previous stations. Both simulations predict very similar tangential velocity profiles at this station. Predicted tangential velocities are nearly constant from 3 cm to 9 cm. The experimental data shows a tangential velocity peak at 5 cm, which is significantly underpredicted in the simulations.

Species concentration and temperature at x/d=.6 are shown in figure 5.87. The experimental carbon dioxide

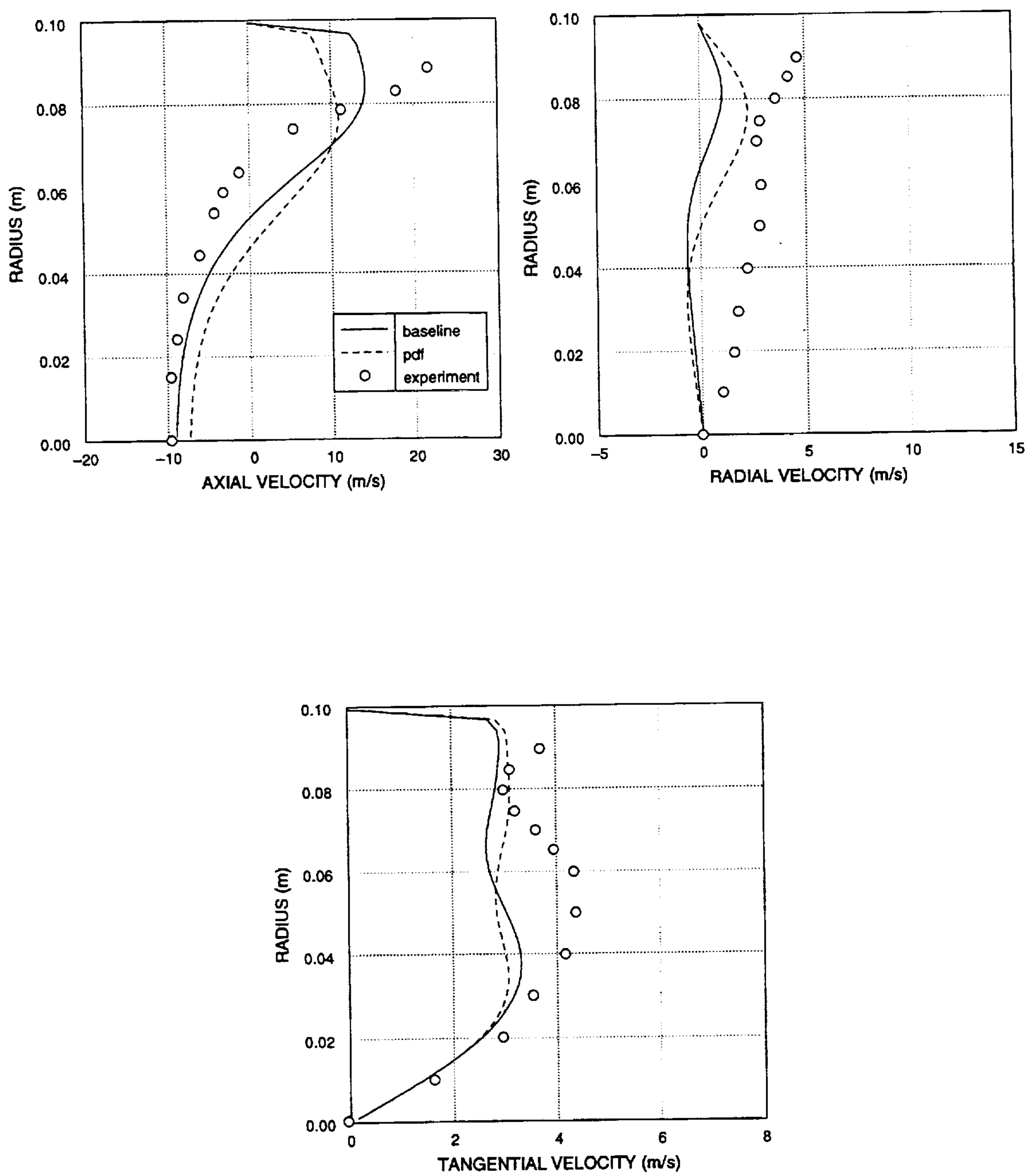

Figure 5.86 Velocities at x/D=0.6

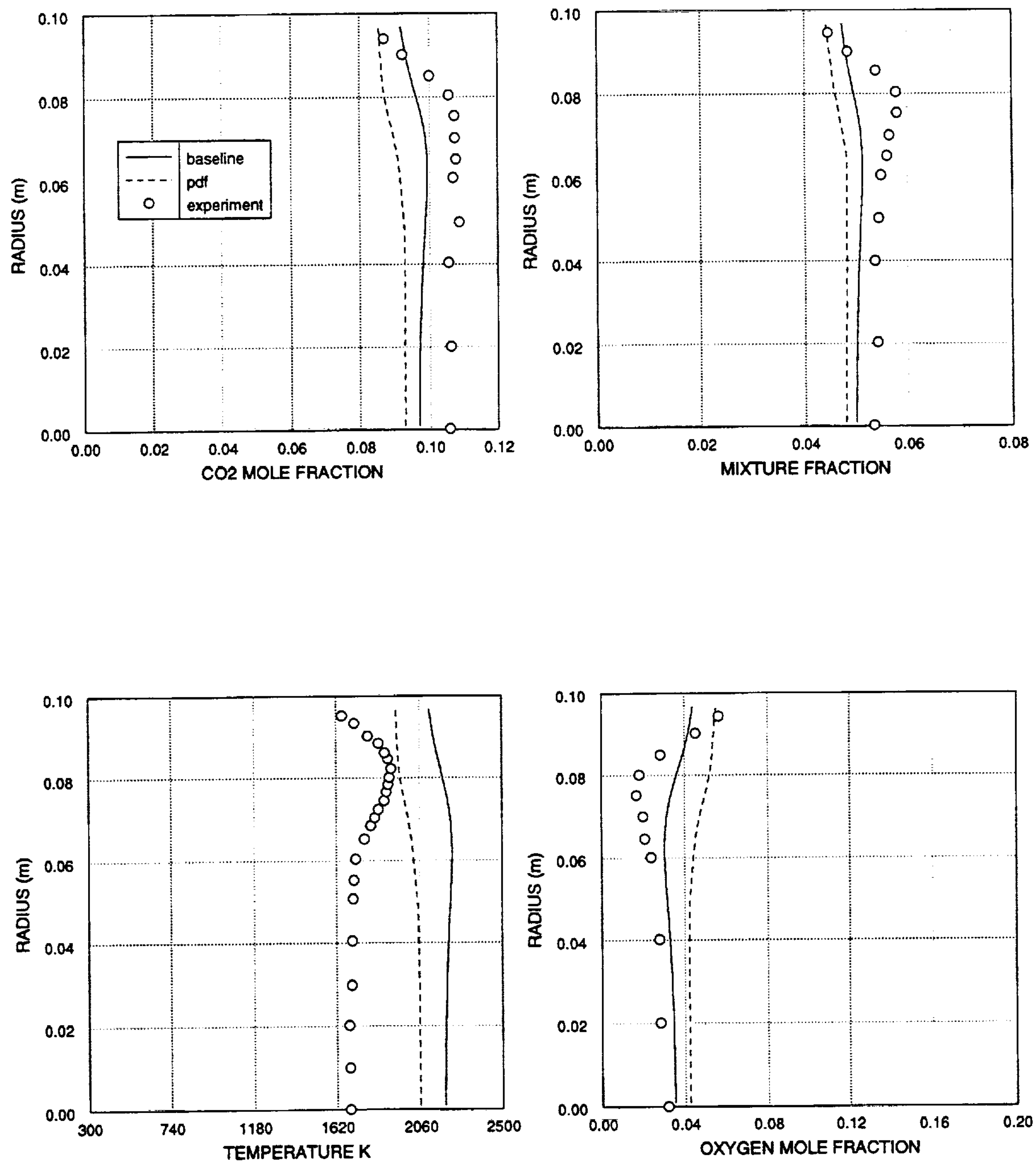

Figure 5.87 Species Concentration and Temperature at x/D=0.6

concentration is constant out to a radius of 8 cm. The mixture fraction shows a slight peak at 8 cm, which implies that there is still unreacted or partially reacted fuel at this location. Insufficient fuel is predicted at this axial station. The shape of the predicted mixture fraction profile is the same as the carbon dioxide profile. Measurements show a temperature peak and a drop in oxygen concentration at 8 cm, which suggests ongoing combustion at that location. The simulations show increased oxygen concentration past 6 cm.

Velocity and temperature at x/D=0.8 are shown in figure 5.88. The experimental data show the CRZ is about the same diameter as the previous station, but the reverse flow velocity has slightly increased. The simulations show a smaller diameter CRZ and reduced reverse flow velocity from the previous station. Predicted radial velocities are all negative at this station. The experimental data for radial velocity is rather sparse, but suggest a different flow pattern. The discrepancy in prediction of peak tangential velocity grows to 50 %. The second tangential velocity peak isn't seen at this location. Measured tangential velocities at this station are greater than at the previous axial location at all radii. This implies there is some error in tangential velocity. Predicted temperatures across the combustor are nearly constant. The experimental data shows a slight temperature peak at 9 cm. The pdf simulation shows

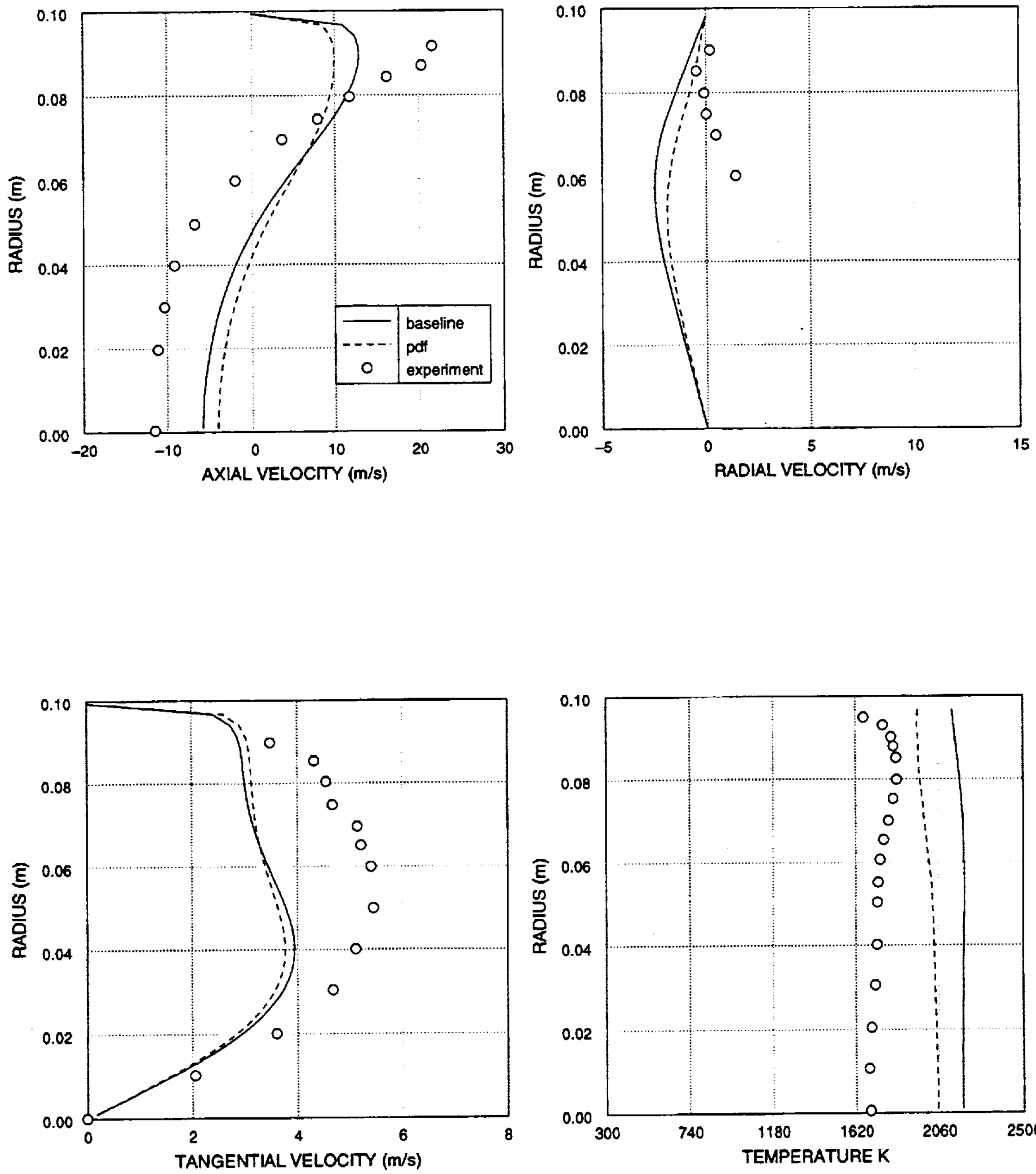

Figure 5.88 Velocity and Temperature at x/D=0.8

lowest temperature, closer to experimental data.

Mixture fraction isn't perfectly conserved in these calculations. If everything were perfectly conserved in the calculations, the predicted temperatures would be closer at this location. Summing the conventional mixture fraction flow across the combustor shows a slight increase in total mixture fraction at this location. Summing the hybrid pdf predictions of mixture fraction flow shows a slight decrease. Thus, some of the improvement seen between the calculations should be attributed to error, not better modeling.

Some cells on which to perform particle plots were chosen for examination. Particle plots of mixture fraction versus temperature for x/D of 0.0034 are shown in figure 5.89. The particle plot for r/D of 0.054 displays a wide variety in mixture fraction and temperature. This cell is within the CRZ. Most particles that appear in this cell are fully reacted. The particle plot for r/D of 0.74 displays three distinct particle groupings. One grouping is air with a slight amount of unburned fuel. The second group is a single particle at 1914 K and a mixture fraction of 0.14. The third particle grouping is almost pure unburned fuel. This particle plot is of a cell between the two recirculation cells. The particle plot for r/D of 0.198 is actually of 250 particles clustered around 1940 K and a mixture fraction of 0.044. The fluid from this cell is within the outer

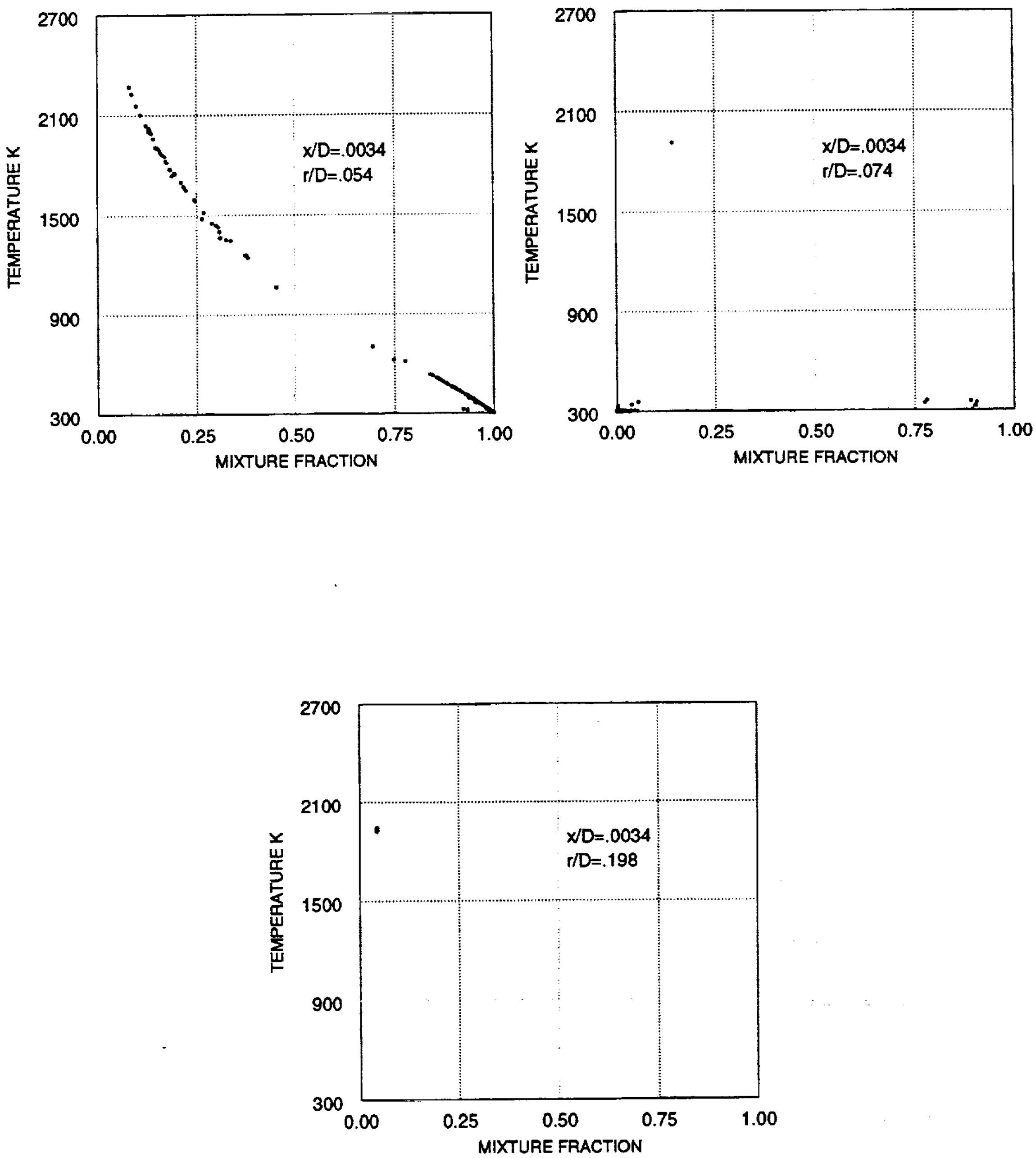

Figure 5.89 Particle plots at x/D=0.0034

recirculation zone, next to the combustor wall. The fluid is almost completely mixed. The fluid velocity in this cell is very low. Information transfer in this zone of the combustor is very slow in the hybrid pdf calculation.

A second set of particle plots for x/D of 0.136 is shown in figure 5.90. All of these plots show considerable variability. No particularly fuel rich particles are shown. The plot for r/D=0.054 is within the CRZ. Most particles are fully burned except for a smaller number centered around 900 K. The plot for r/D=0.074 is closer to the fuel stream. The number of partially burned particles centered near 900 K is larger than for the r/D=0.054 plot. There are also a few more particles with higher mixture fraction. The plot for r/D=.198 has the greatest number of particles with moderate temperature and mixture fraction. These particle plots are used to show variability within the fluid cells. Particles can be plotted over one another. Some sort of statistical analysis would probably help in interpreting this data. However, much of the easier statistical analysis assumes normal or Gaussian type distributions. The distributions are obviously bimodal at low temperature in and near the low temperature fuel-air stream.

Neither simulation captures the experimentally measured low fluid velocity of the CRZ near the combustor inlet. The pdf simulation predicts slower combustion and generally less radial displacement. The inlet radial

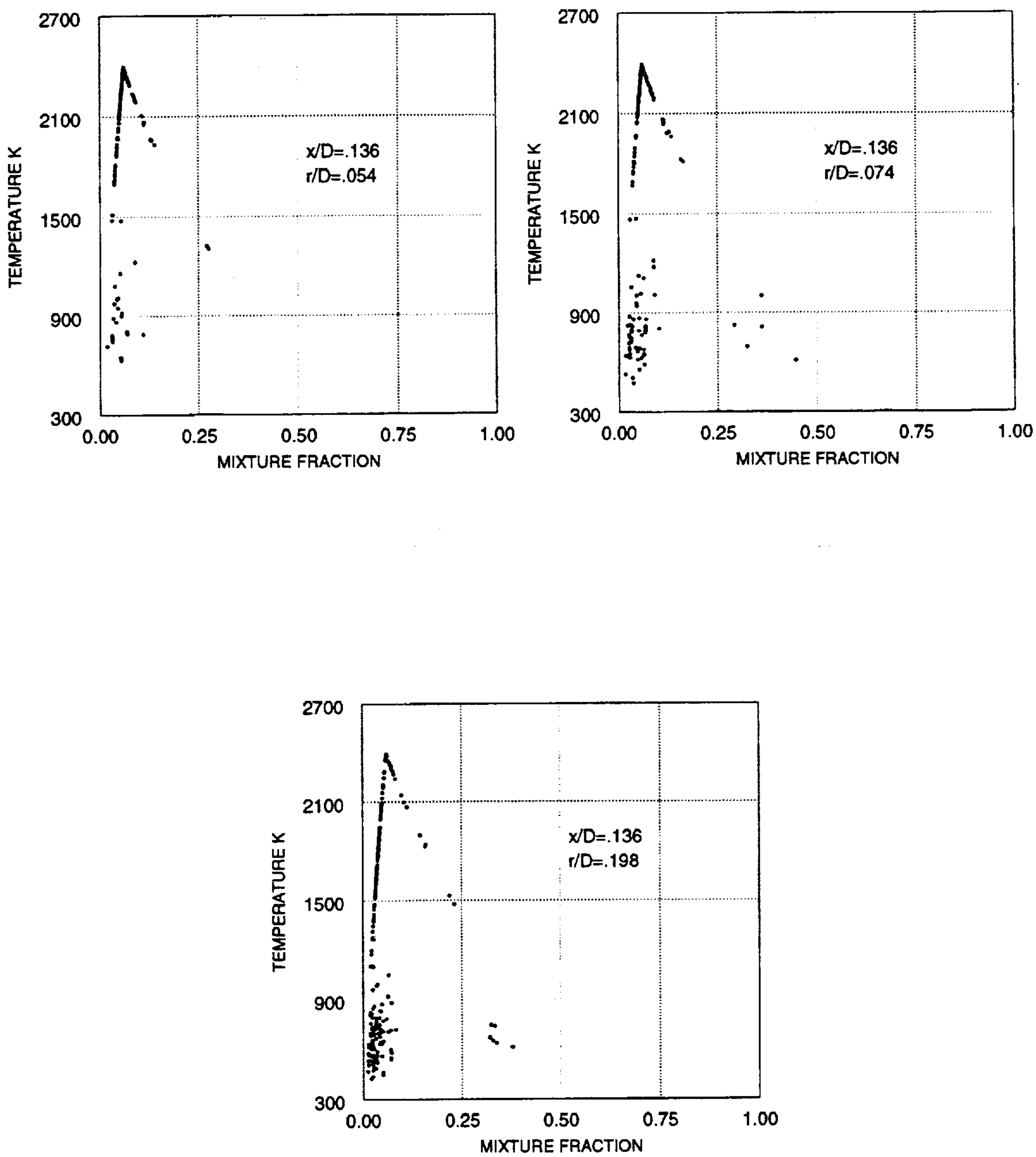

Figure 5.90 Particle plots at x/D=0.136

velocities had to be increased so that the hybrid pdf results would compare to the conventional simulation. While the lower rate of combustion predicted by the pdf simulation predicted temperatures closer to the experimental data, the larger radial displacement of fuel and its products by the conventional simulation produces profiles that were closer to the data in regards to shape. Both simulations use hybrid differencing for calculation of coefficients. As the flow is about 30 degrees to the grid (initially 45 degrees for fuel), hybrid differencing can be expected to give larger errors due to numerical diffusion, compared to higher order schemes. The pdf scheme should be tested with higher order schemes. Unfortunately these schemes will to have all positive coefficients, if the same differencing scheme is used to calculate the pdf particle number exchanges as transporting a negative number of particles does not have a physical meaning. A quick fix for this may be to use lower order differencing for the transport of particles.

5.3.3 PREMIXED COMBUSTION CASE

To explore the further applicability of the hybrid pdf model, a lean premixed combustor case is considered. In a premixed combustor, fuel and oxidant are mixed upstream of the actual combustor. This results in uniform air to fuel ratios. In normal combustors, there is a wide variation in air to fuel mixture. Some areas are lean, some are rich, and some are near stoichiometric. Burning near stoichiometric results in high temperature which markedly increases nitrous oxide emissions. Lean premixed combustors do not have this problem. Thus, lean premixed combustion is one way in which to lower nitrous oxide emissions. Nitrous oxides are one component of smog. Currently, some European countries are proposing taxes based on nitrous oxide emissions of the aircraft flying through their airspace. Since the combustor inlet mixture is premixed and is combustible, the location where combustion occurs must be fixed or anchored. Combustion can flash back into the inlet duct or can be blown downstream. This is deleterious to performance and safety, particularly in aircraft. Combustion is anchored by forming hot recirculation zones. One way to form a recirculation zone is to put an obstruction, or flame holder, in the combustor. Some examples of flame holders are disks, disks with holes, v-gutters, and conical bluff bodies. In the combustor studied here, a large increase in flow area is used to form a recirculation zone. This configuration is also known as a step or dump combustor. The basic flow configuration is the familiar flow over a step. The combustor studied here is that of Gould, Stevenson, and Thompson[123] at Purdue University. Premixed fuel and air goes through a converging nozzle, with an exit diameter of 76.2 mm, into the combustor chamber of 152.4 mm outer diameter. The inlet nozzle was contoured to provide a nearly uniform velocity flow across the combustion chamber inlet plane. There is a slight velocity defect due to the boundary layer. The inlet mixture is gaseous propane and air at an equivalence ratio of 0.5. Velocities were measured using Laser Doppler Velocimetry. Temperature was measured using high speed thermometry. Various turbulent correlations were also measured. A corrective lens was used to take optical measurements. This lens degraded due to combustion, limiting the number of axial stations where data was taken.

Gould performed computational combustion simulations as part of his dissertation study. A pressure based solver with the eddy-breakup combustion model of Magnussen and Hertajer[124] was used. In this combustion model, combustion is proportional to turbulent eddy lifetime, and minimum species concentration of fuel, oxygen or combustion product. Combustion is initiated in this model by temporarily introducing product species at specified cells in the simulation. Recently Magnussen[125] proposed an improved combustion model called the Eddy Dissipation Concept combustion model. This model was used in a calculation of Brum and Samuelson's combustor[126], which was then compared to the predictions of Nikjooy [28].

An inlet axial velocity of 22 m/s was specified in the combustor calculations, except for the boundary layer. Zero radial velocity was specified. There was no swirl component. The measured inlet turbulent kinetic energy was very low, $0.0006{*}U^2$, except for the boundary layer, which was measured at 10.0 m^2/s^2. Combustion simulations did not satisfactorily converge using such low inlet turbulence. Values of $0.0054{*}U^2$ were used, except for the boundary layer. This allowed the simulations to converge much further. High inlet temperature was initially specified to initiate combustion simulations. The simulations were then restarted using the correct inlet temperature of 300 K. The pdf simulation started from a converged SIMPLE calculation restart file. As the current pdf model does not allow heat transfer to the wall, adiabatic wall treatment was also used in the conventional simulation. The heat of reaction term used in the conventional simulation was adjusted to give the same final temperature as the thermodynamic model used in the pdf module for a single cell calculation.

Experimental values of velocity, temperature, and various double and triple correlations of these quantities were measured. The experimental data taken near the combustor axis shows radial velocities around -2.0 m/s. This is physically unrealistic. Evidently, the thermometry apparatus affected radial velocity measurements. Radial velocities measured without the thermometry apparatus for the isothermal case were reasonable. Predicted radial velocity profiles do not agree with the measured profiles for the burning case. There was significant anisotrophy in the turbulent Reynold's stresses. Axial velocity and temperature at a location of one step height past the combustor inlet are shown in figure 5.91. The axial velocity is well predicted by the two different combustion model simulations. The axial velocity in the main flow is slightly over-predicted. The experimental data shows a slightly sharper velocity gradient between the cold core flow and the hot recirculation zone. Temperature measurements in the recirculation zone are hundreds of degrees lower than predicted temperatures. Low temperatures are measured near the combustor wall. The predictions assumed no heat transfer to the walls. Both the conventional simulation and hybrid pdf simulation predict complete combustion for much of the recirculation zone. As velocity is lowest next to the combustor wall, this portion of the flow has the longest time for combustion to occur. With the high temperatures measured at other axial stations, much of the recirculation zone should be fully reacted. This researcher feels that the peak experimental temperature at this axial location should closely match the peak temperatures found at other

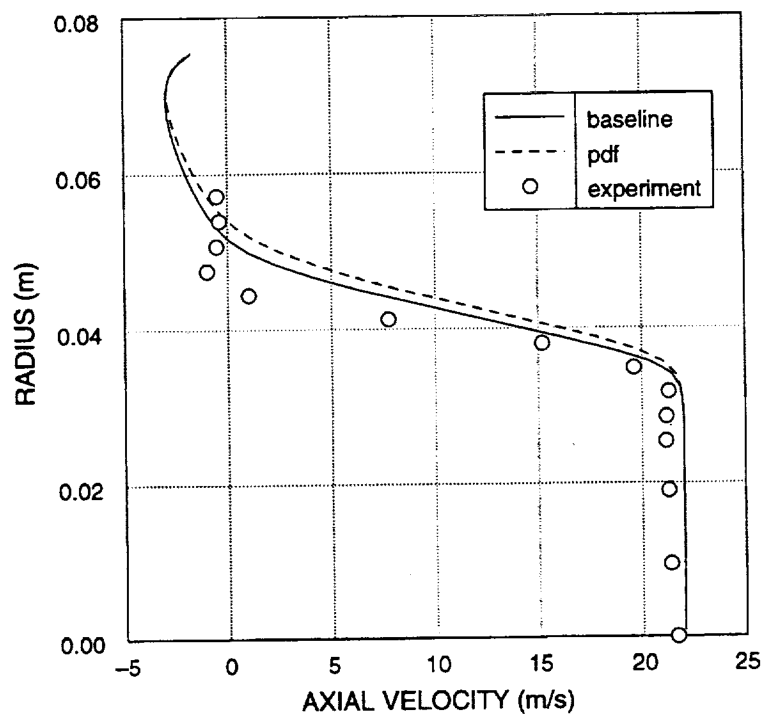

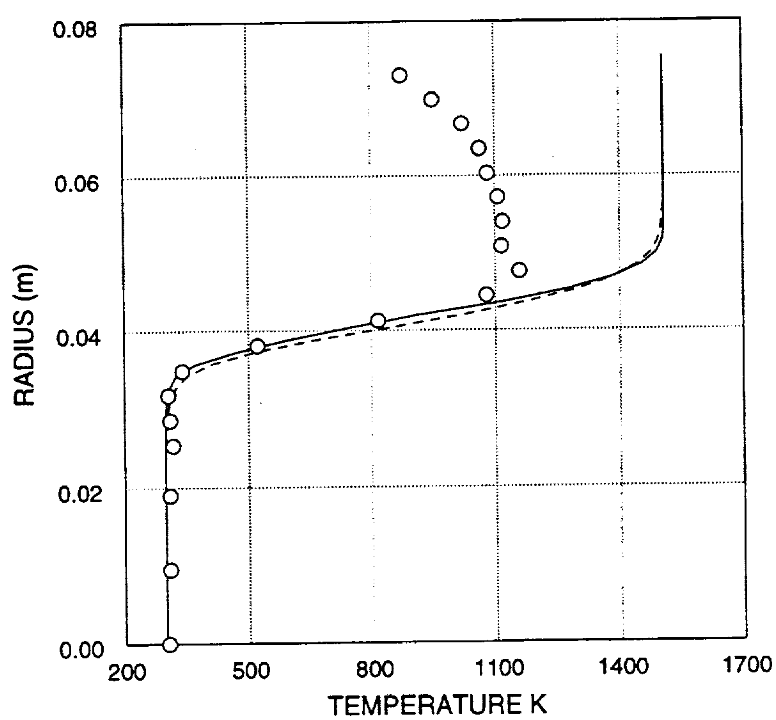

Figure 5.91 Axial Velocity and Temperature at x/H=1.0

axial stations. Allowing some heat transfer in the calculations would improve the temperature predictions along the wall, but shouldn't produce a 400 degree drop in temperature across the whole recirculation zone. Experimental velocity data was only taken out to 80 % of the combustor diameter. Predictions of axial velocity in the recirculation zone appear quite good, despite the large temperature discrepancy in the recirculation zone. This implies that temperature measurement in the recirculation zone at this station is in error or, velocity is not as strongly coupled to density as it is in the core flow.

The results at an axial location of 3 step heights are shown in figure 5.92. The axial velocity predictions and measurements are very close. The pdf predictions show a slightly higher axial velocity outside of the cold central core. The hybrid pdf simulation shows a slightly faster combustion progress into the core flow. High temperature is predicted at slightly lower radii in the pdf simulation. The pdf simulation predicts a wider blunter temperature peak than the conventional simulation. The conventional simulation predicts slightly higher temperature than measured in the hot recirculation zone.

At 5 steps heights past the inlet, the axial velocity predictions, shown in figure 5.93, are very similar. The conventional simulation comes closest to the measurements in the outer recirculation zone, but axial velocity is

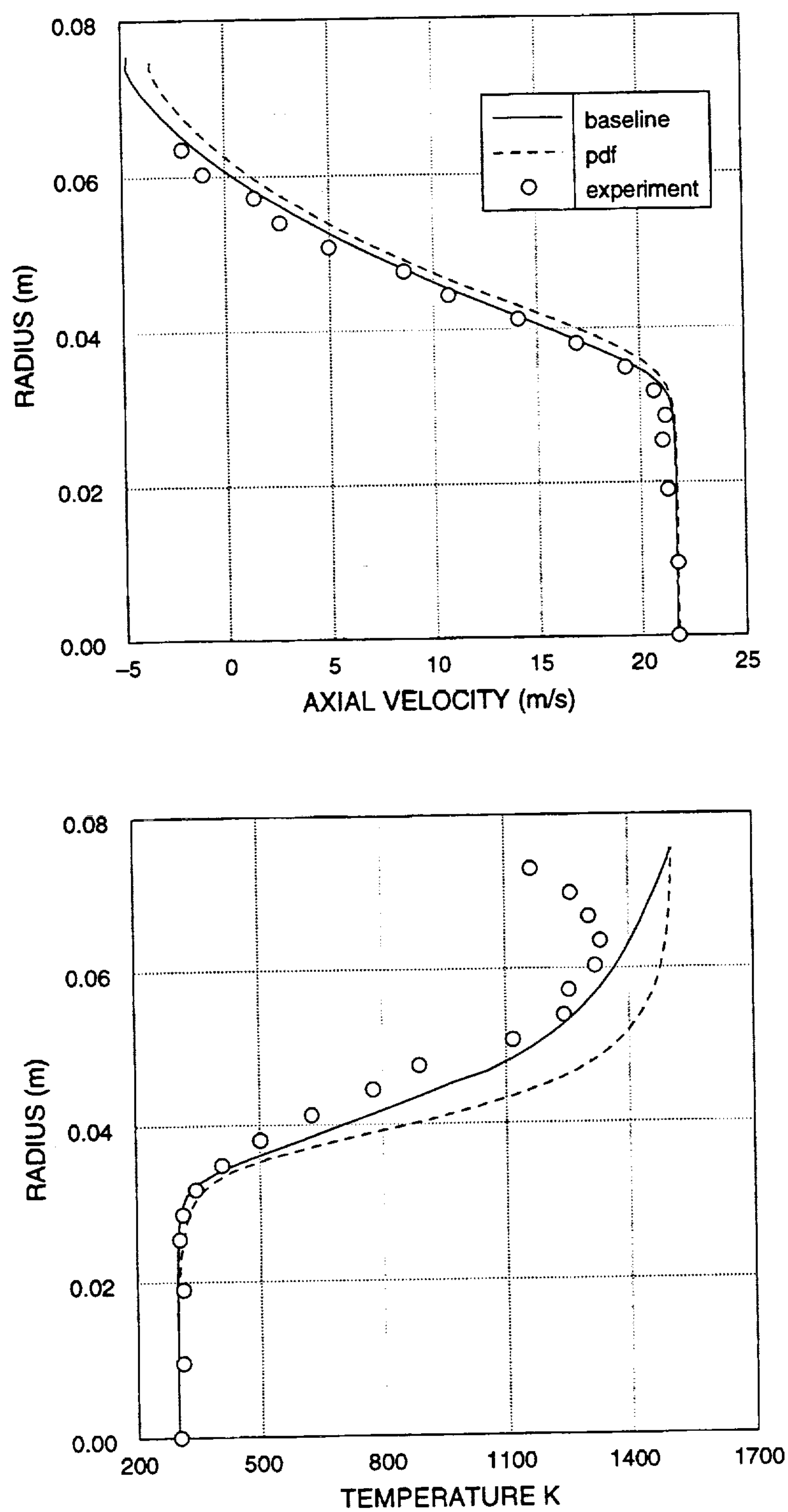

Figure 5.92 Axial Velocity and Temperature at x/H=3.0

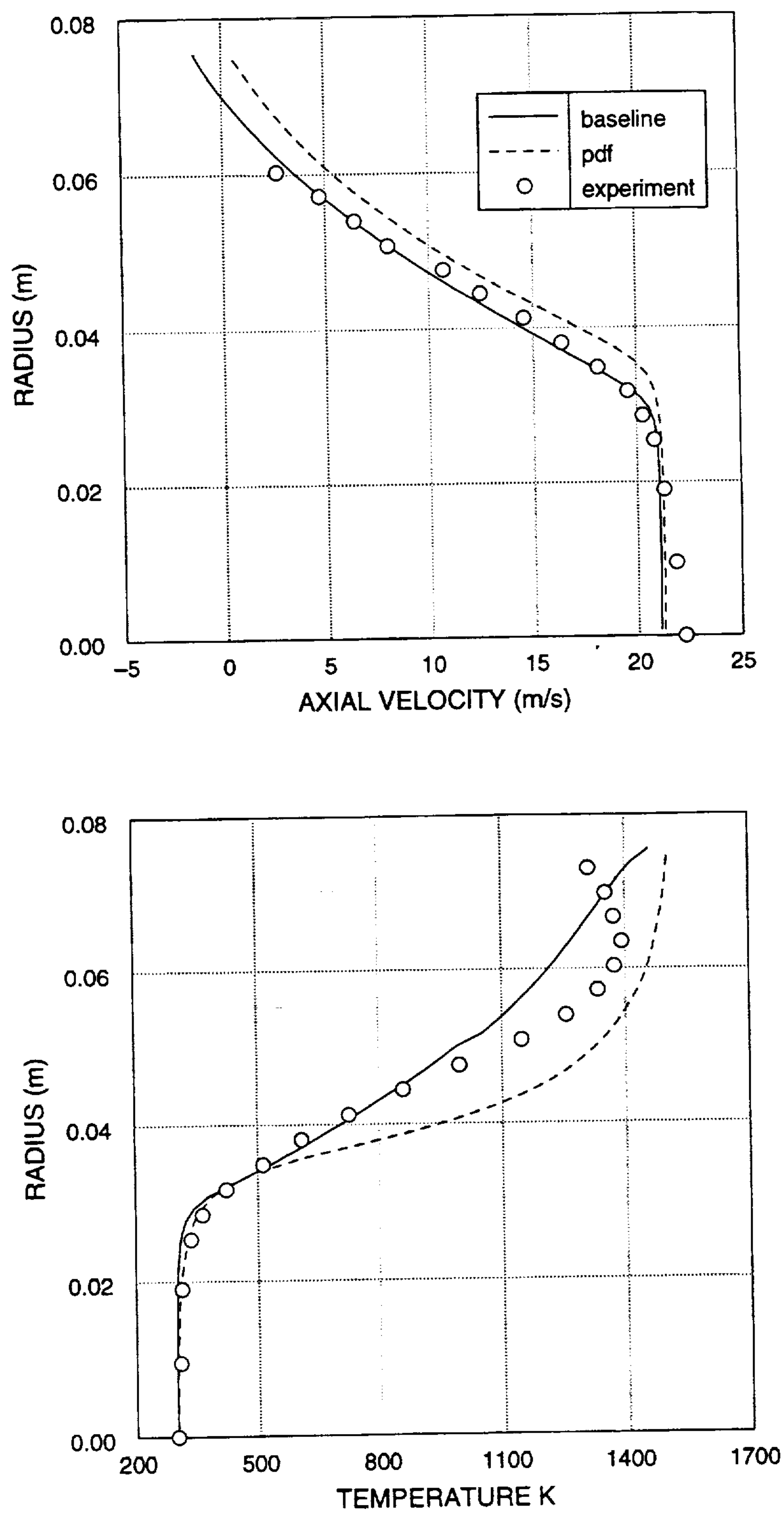

Figure 5.93 Axial Velocity and Temperature at x/H=5.0

bracketed by the predictions in the inner recirculation zone. The small negative axial velocities shown near the wall in the conventional simulation mean that the recirculation bubble is almost closed for that simulation. The pdf simulation shows slightly positive axial velocity near the wall. The axial velocity near the combustor axis is underpredicted by both the simulations. Previously velocity was slightly overpredicted. In this same area, predictions and measured data for temperature are very close. Beyond the cold core flow, the hybrid pdf simulation noticeably predicts higher velocity and temperature than the both the conventional simulation and experimental measurements. Up to a radius of 4.5 cm, the conventional simulation predicts temperature almost perfectly. At the previous station, temperature was slightly overpredicted. Beyond a radius of 4.5 cm, temperature measurements are bracketed on the low side by the conventional simulation and on the high side by the hybrid pdf simulation, except near the wall. Qualitatively, the shape of the pdf simulation temperature profile is closest to the measured temperature profile at this axial location.

At the last measurement station of 12 step heights past the inlet, both numerical simulations deteriorate, as shown in figure 5.94. The difference between the simulations and experimental data is largest at this station. In most experimental combustors the last measurement station is

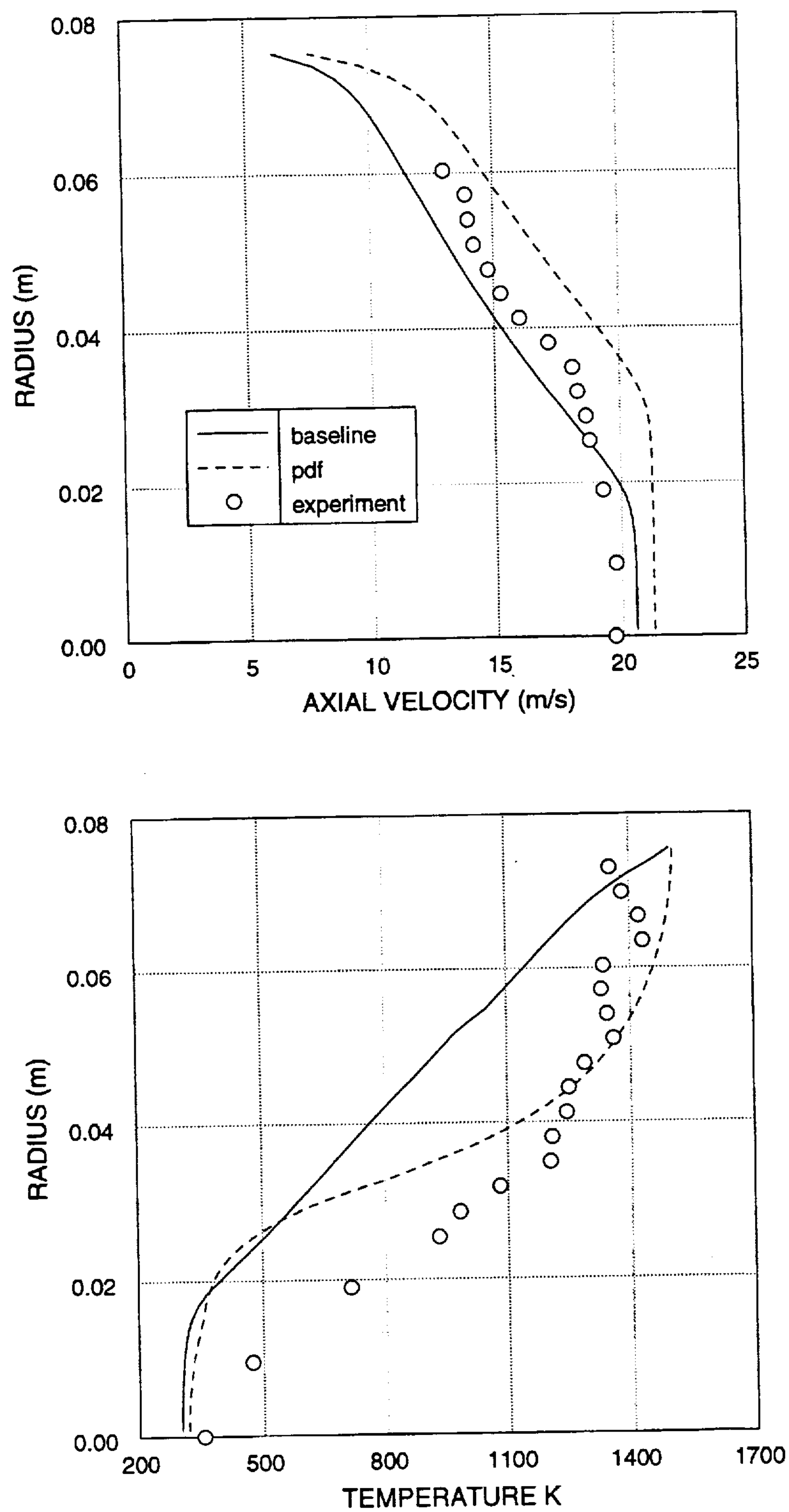

Figure 5.94 Axial Velocity and Temperature at x/H=12.0

usually at the completion of combustion and mixing, and exit profiles are fairly uniform. In this experiment, a large fraction of the cold inner flow is still unreacted. Thus, there are significant gradients in combustor profiles. Both predictions show a higher axial velocity along the centerline than measured, while temperature is underpredicted. This is somewhat of an anomaly. Beyond a radius of 2 cm, the conventional simulation underpredicts axial velocity, while the pdf simulation continues to overpredict it. The experimental measurements show an almost linear increase in temperature off the combustor axis. At a radius of two centimeters, both temperature predictions are off by 300 degrees K. The hybrid pdf simulation best predicts the high temperature zone at this temperature. Gould noted similar deficiencies in his predictions and theorized that it was the fault of turbulence model. At previous stations, the predictions in and near the low turbulence level cold core flow were excellent. At this last station, the cold flow is hotter and more turbulent. The results at this station could be more closely predicted by increasing inlet turbulence. Unfortunately, this would work at the detriment of previous predictions. With the extremely low inlet turbulence, turbulence modeling may be more in the realm of turbulent transition. The turbulence model used in these simulations assumes high levels of turbulence, that is, it is a high-Reynolds number turbulence model. It would be interesting to try a low Reynold's number turbulence model in another simulation.

The hybrid pdf temperature simulation exhibited sharper temperature gradients between the cold inner flow and hot outer flow, and higher temperature, particularly at the last station. At the last station, the pdf simulation best predicts temperature.

5.3.4 SWIRLING HYDROGEN DIFFUSION FLAME

Recently, a group of researchers at the University of Dayton, Research Institute, have taken benchmark data for model validation. This includes non-swirling and swirling air jet flows[127], methane jet flames[128], and hydrogen jet diffusion flames[129]. The combustion data for the burning hydrogen is the most complete. Three components of velocity were measured along with many turbulence quantities using LDV equipment. Temperature was measured using Coherent Anti-Stokes Raman Spectroscopy (CARS). Typically 500 temperature measurements were taken at each location. These measurements were processed to get rms temperature fluctuations and temperature pdfs. The CARS method is still being developed and the data is ideal for validating the composition pdf method employed here.

The experimental system consists of a central fuel tube of 9.45 inner diameter, a concentric annular air tube of 26.92 inner diameter, and external non-swirling air supplied to a vertical 150 by 150 mm semi-rectangular test section which is 486 mm long. Various combinations of velocity and swirl were tested. The case studied here is case no. 3 which had a fuel jet bulk velocity of 100 m/s, annulus air bulk velocity of 20 m/s with thirty degree swirl, and external air bulk velocity of 4 m/s. Radial data was taken at 1.5, 10, 25, 50, 150, 250 mm from the inlet. Additional combustor centerline data were also taken. Data at the first measurement plane were used for inlet data in the simulations. The mass fraction of species were inferred from the geometry and temperature measurements. The high temperature combustion interface between the fuel and air jets provided an ignition source. A one step chemistry submodel was employed. This mechanism was inferred from several larger reaction mechanisms for heavier fuels which included a hydrogen-oxygen to water reaction step. The activation energy used was 40 Kcal/mole. The exponent used for the fuel concentration was 0.25, and the oxygen exponent was 1.5. The frequency number had to be increased to 2.7×10^{13} to simulate continuing combustion in the calculations.

Baseline calculations were done with a coarse grid of 40 by 30 and a fine grid of 70 by 60. These simulations predicted nearly identical axial velocity and temperature profiles. The pdf calculations were performed using the same grids. An adiabatic wall boundary condition was imposed at a radius of 75 mm.

Temperature, turbulent kinetic energy, axial and tangential velocity at an axial distance of 25 mm from the inlet plane are shown in figure 5.95. Temperature at this plane is best predicted by the baseline coarse grid simulation. The coarse grid temperature profiles are largely the same as the fine grid profiles except the coarser grids truncate the temperature peaks. The peak temperature is

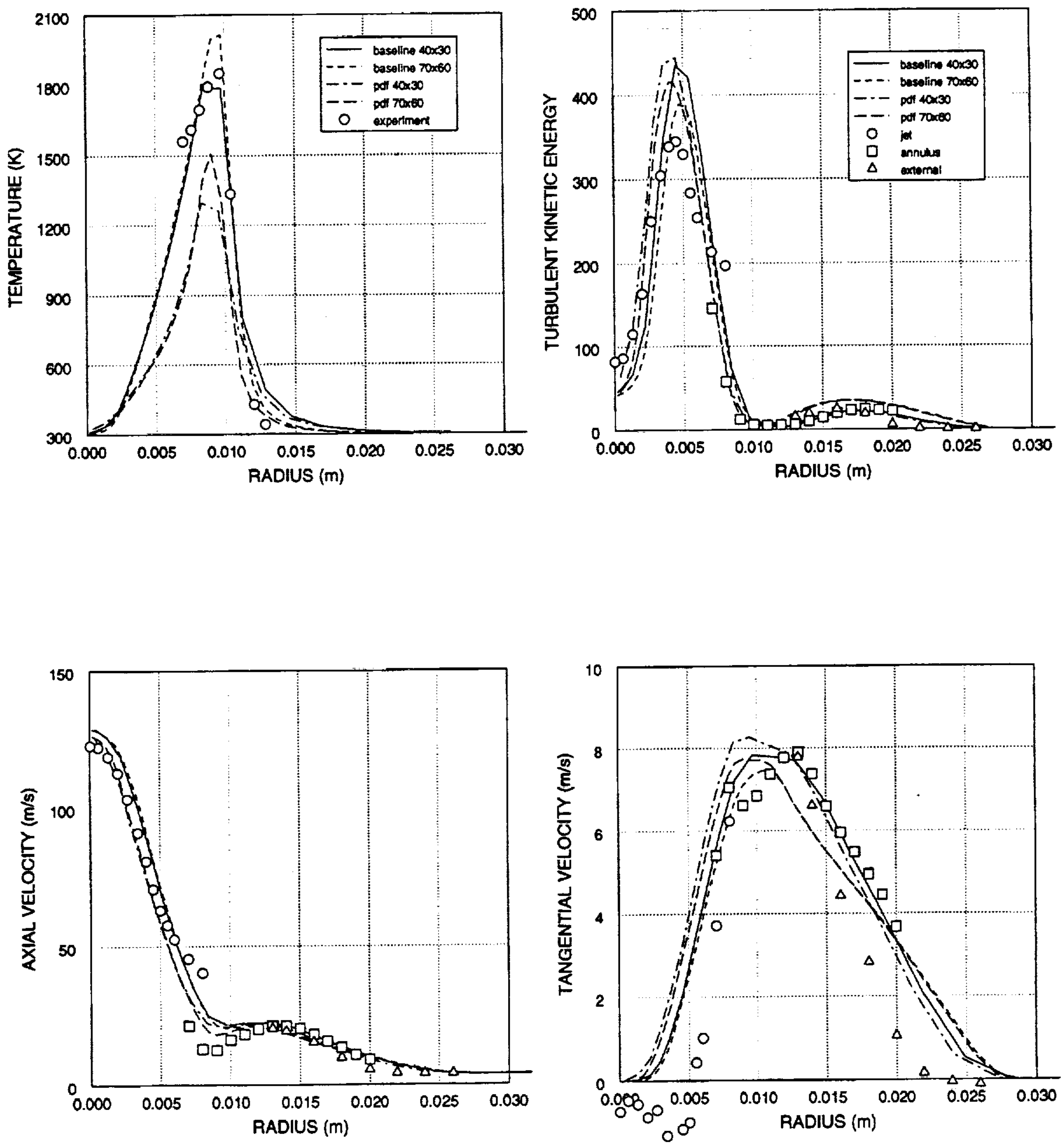

Figure 5.95 Temperature, turbulent kinetic energy, axial and tangential velocity at x = 25 mm.

slightly overpredicted by the baseline fine grid calculation. The pdf simulations underpredict temperature. Efforts to increase the coarse grid peak temperature by increasing reaction rate and maximum inlet temperature at this axial location were largely unsuccessful.

There are three sets of experimental measurements. Measurements of velocity and turbulence quantities are conditional. That is, the fuel jet, annular jet, and external air were seeded in successive runs. Calculated turbulence kinetic energy and velocities are not conditional. An average, unconditional velocity is calculated. To calculate conditional velocities a joint velocity-scalar pdf would have to be developed.

Predictions of turbulent kinetic energy are very good. The baseline fine grid calculation best predicts the peak turbulent kinetic energy. The fine grid pdf simulation predicts slightly higher peak turbulent kinetic energy. The two coarse grid solutions predict the highest peaks. The pdf simulations best predict centerline and near centerline turbulence kinetic energy. At larger radii, the fine grid calculations slightly overpredict the turbulence kinetic energy.

Axial velocity predictions tightly bracket the experimental measurements out to a radius of 5 mm. The baseline simulations predict higher axial velocity due to the higher predicted temperatures. The fine grid pdf simulation best predicts the axial velocity deficit between the fuel jet and annular air flow. At larger radii, predicted axial velocities converge. The pdf simulations predict slightly higher tangential velocity out to a radius of 12 mm due to lower temperature predictions and reduced expansion of the flow. The tangential velocity predictions are quite good. The coarse grid calculations predict higher tangential velocity beyond the tangential velocity peak more in agreement with the data. Overall, the baseline coarse grid calculation best matches tangential velocity data.

Some plots of temperature versus mixture fraction (total fuel component) at an axial distance of 26 mm are shown in figure 5.96 for the coarse grid solution. There are 250 particles in each cell plot. Each computational grid cell in this region is of the order of one mm in the radial direction and 3 mm in the axial direction. The cells are in the mixing layer region where the combustion rate is highest. The pdf simulation predicts a wide variation of temperature and mixture fraction in the mixing layer. Each particle generally falls close to a state function composed of a straight line connecting mixture fraction of zero, temperature 300 degrees (pure air) with mixture fraction 0.029, temperature 2550 (stoichiometric or complete burning of both reactants) and thence a curved line ending at mixture fraction of 1.0, temperature of 300.0 (pure fuel).

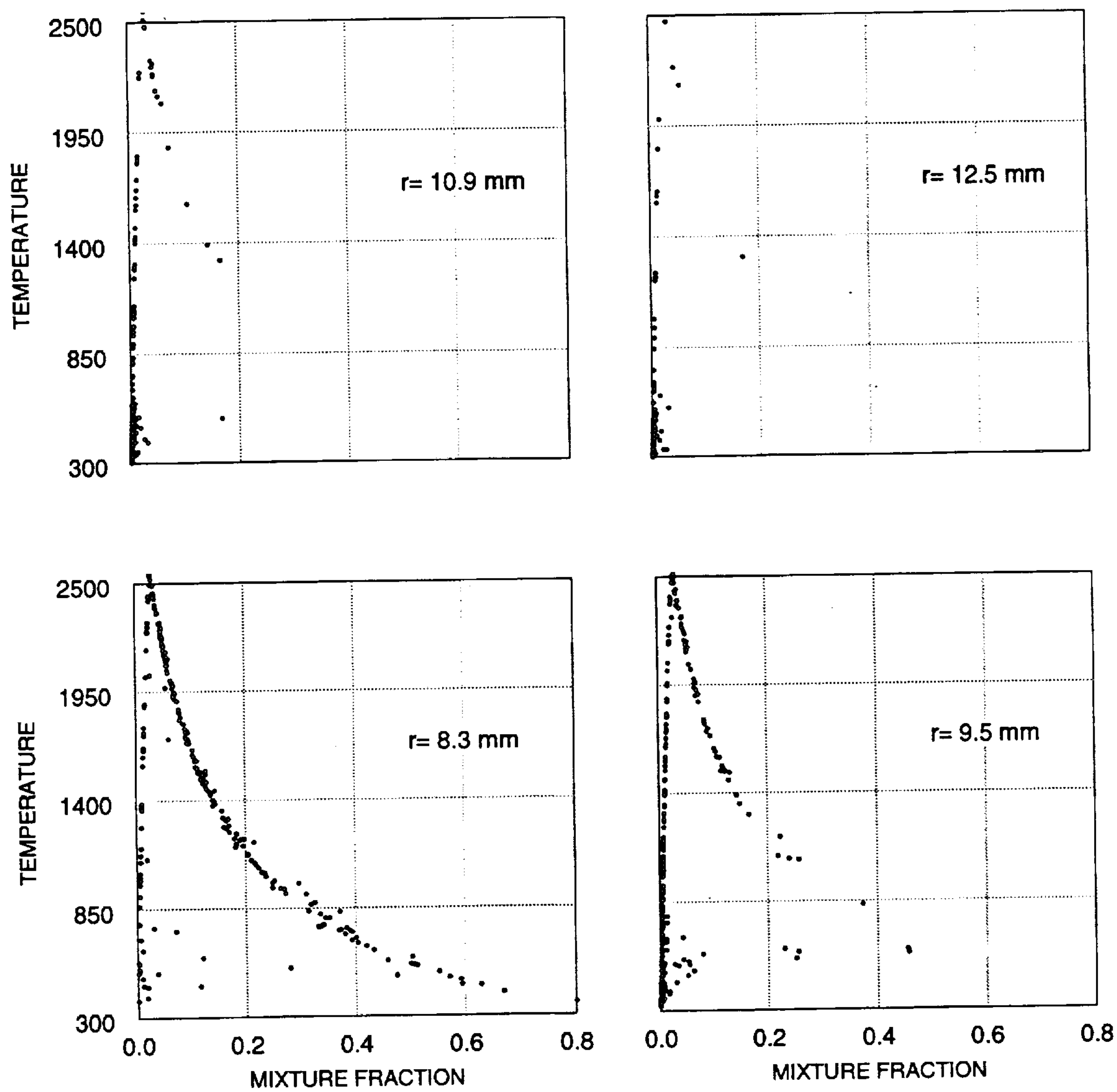

Figure 5.96 Coarse grid temperature vs mixture fraction at x = 26 mm.

This composite line represents complete burning of fuel for lean mixtures and complete consumption of oxidant for rich mixtures, effects of variable C_p, and a fixed ratio of nitrogen to oxygen. Temperature is highly nonlinear with mixture fraction. Temperature increases most rapidly near stoichiometric. This thermodynamic behavior causes very large temperature gradients in the mixing layer.

The cell plots show that the total fuel component decreases with increasing radius. Only a few particles are richer than stoichiometric at a radius of 12.5 mm. There are at least a dozen partially reacted particles. These partially reacted particles have temperatures less than 850 degrees. Most particles above 850 degrees are either fully reacted or very close to being fully reacted. As the majority of particles in these plots are fully reacted, this explains why efforts to increase reaction rate didn't increase peak temperature predictions. The mixing of fuel and oxidant species would have to be increased to increase temperature predictions in the pdf simulation.

Initial coarse grid pdf simulations were done using 100 and 250 particles per cell. Predictions of velocity and temperature were largely unaffected by varying the particle numbers. What did seem to affect initial calculations was the method of treating residual or partial particle transfers. The results shown here were obtained by keeping track of residual particle transfers and actually exchanging particles when the residual was greater or equal to one, rather than randomly adding in particles as was done previously. This improved temperature predictions at larger radii.

Four cell plots of temperature vs mixture fraction for the fine grid pdf simulation are shown in figure 5.97. There are only 100 particles in these cells. Most of the particles in these cells plots are fully reacted.

Five coarse grid pdfs of temperature at an axial distance of 26 mm are shown compared to experimental measurements at 25 mm in figure 5.98. The simulated pdf is taken from the final iteration. The temperatures passed to the velocity solver are averaged over hundreds of iterations. Thus, calculated pdfs should be also averaged over hundreds of iterations. This would require more memory than is currently needed for the complete calculation, unless a weighted running average is employed. Temperature measurements or particle temperature predictions are partitioned into bins which are multiples of one hundred degrees. The experimental measurements don't show any temperatures beyond 2500 degrees while the simulations show a few particles just beyond 2500 degrees. The simulations assume 100 percent combustion efficiency. The experimental pdfs seem to be composed of one or two gaussian pdfs. At the largest radial location the predicted and measured temperature pdf are very similar, a single peak near 300 degrees. The pdfs taken at

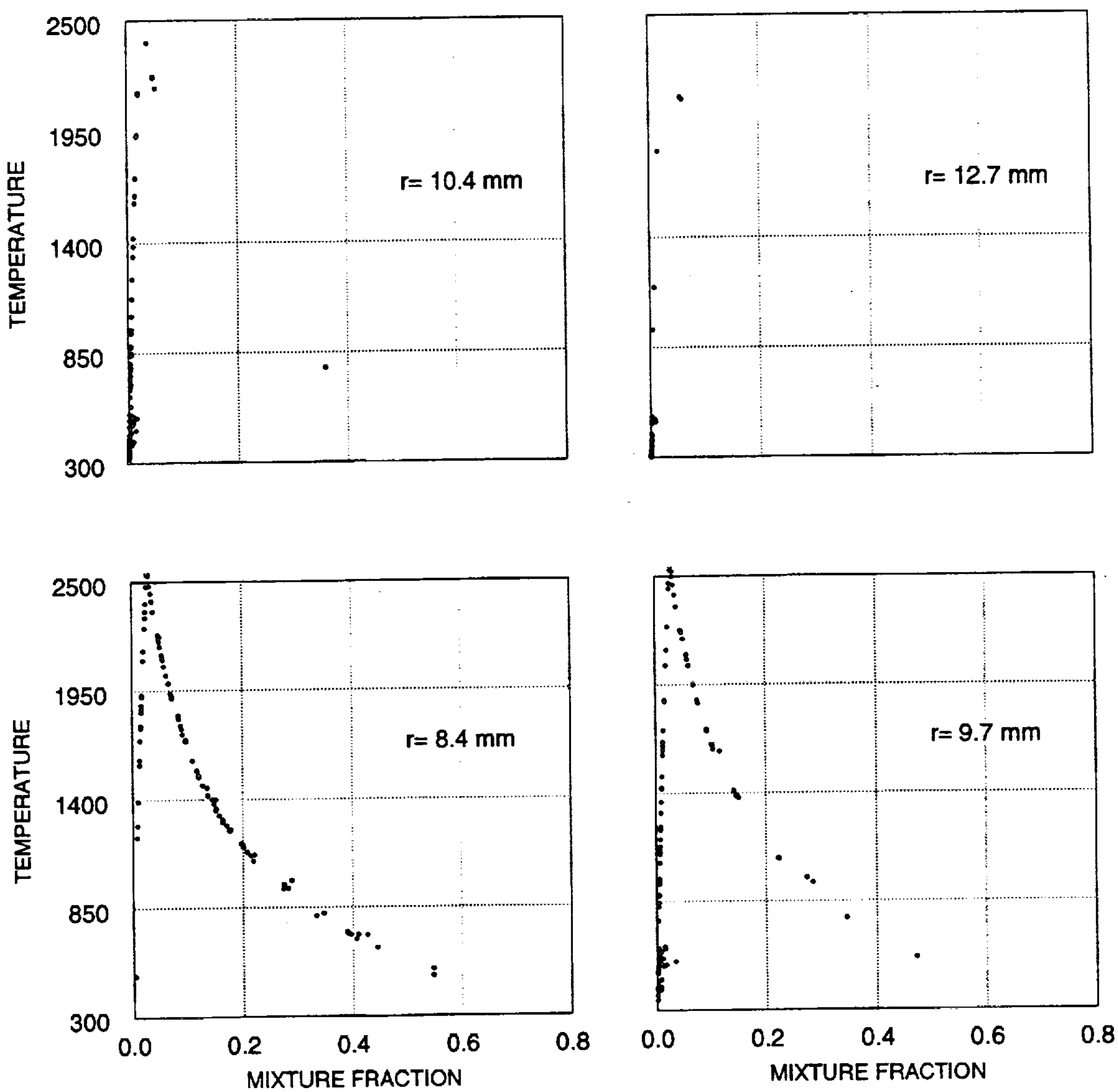

Figure 5.97 Fine grid predictions of temperature vs mixture fraction at x = 26 mm.

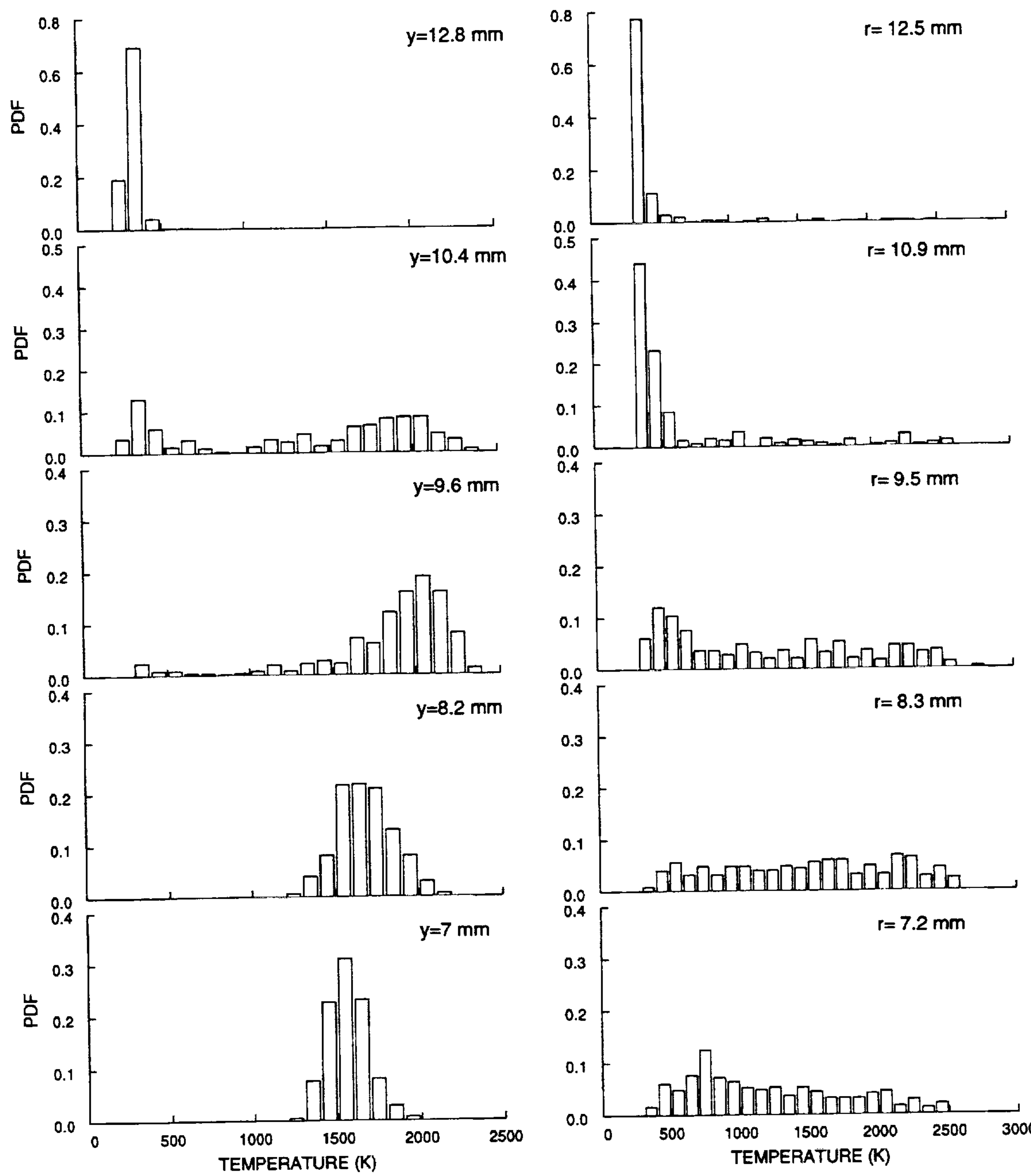

Figure 5.98 Measured temperature pdfs at x = 25 mm, and predicted coarse grid temperature pdfs at 26 mm.

the next smaller radial distance still show a pdf peak near 300 degrees, but differ largely in the number of particles at higher temperatures. The simulation correctly predicts a wide variation in temperature at this location. At the 9.5-9.6 mm radial cell location, the experimental peak pdf occurs at higher temperature, while the simulation shows a pdf peak at much lower temperature. The average temperature plot showed an experimental peak temperature at 9.6 mm, while the coarse grid pdf simulation predicted a peak temperature at 8.3 mm. This agrees with the pdf plots shown here. The pdf coarse grid simulation shows the largest number of high temperature particles at 8.3 mm. The pdf is fairly uniform at this radius and this is one of the reasons why a fine grid pdf solution was done.

A comparison of fine grid pdfs versus the same experimental pdfs is shown in figure 5.99. The fine grid pdf simulation predicts a peak temperature at 9 mm. This cell isn't shown here, but the plot for 8.4 mm shows more particles at higher temperature than does the coarse grid pdf at 8.3 mm.

Profiles of temperature, turbulent kinetic energy, axial and tangential velocity at 50 mm are shown in figure 5.100. Peak temperature is best predicted in the coarse grid pdf simulation. At this station, the fine grid pdf simulation underpredicts peak temperature. The baseline simulations overpredict peak temperature by over 300

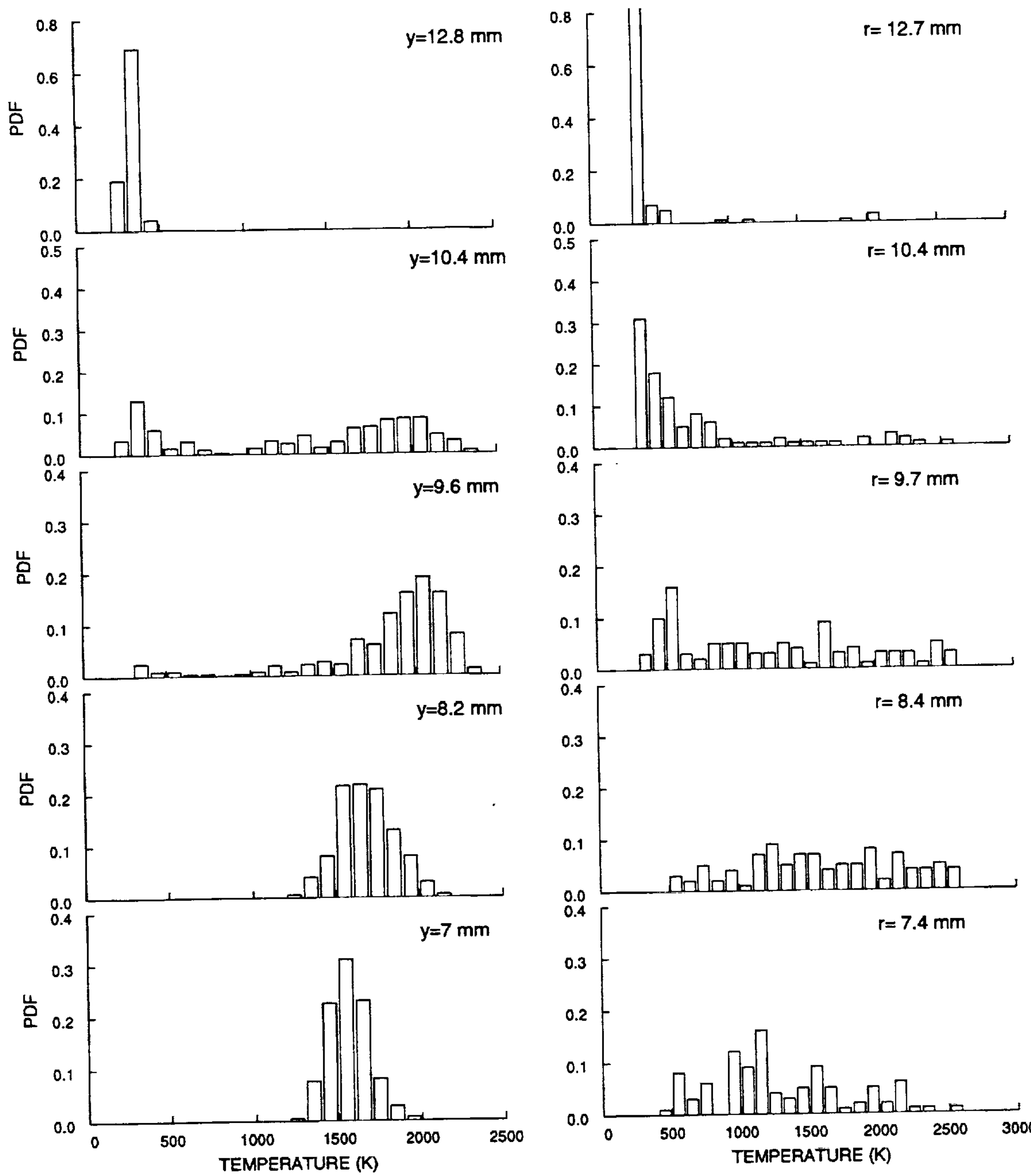

Figure 5.99 Measured temperature pdfs at x = 25 mm and predicted fine grid temperature pdfs at x =26 mm.

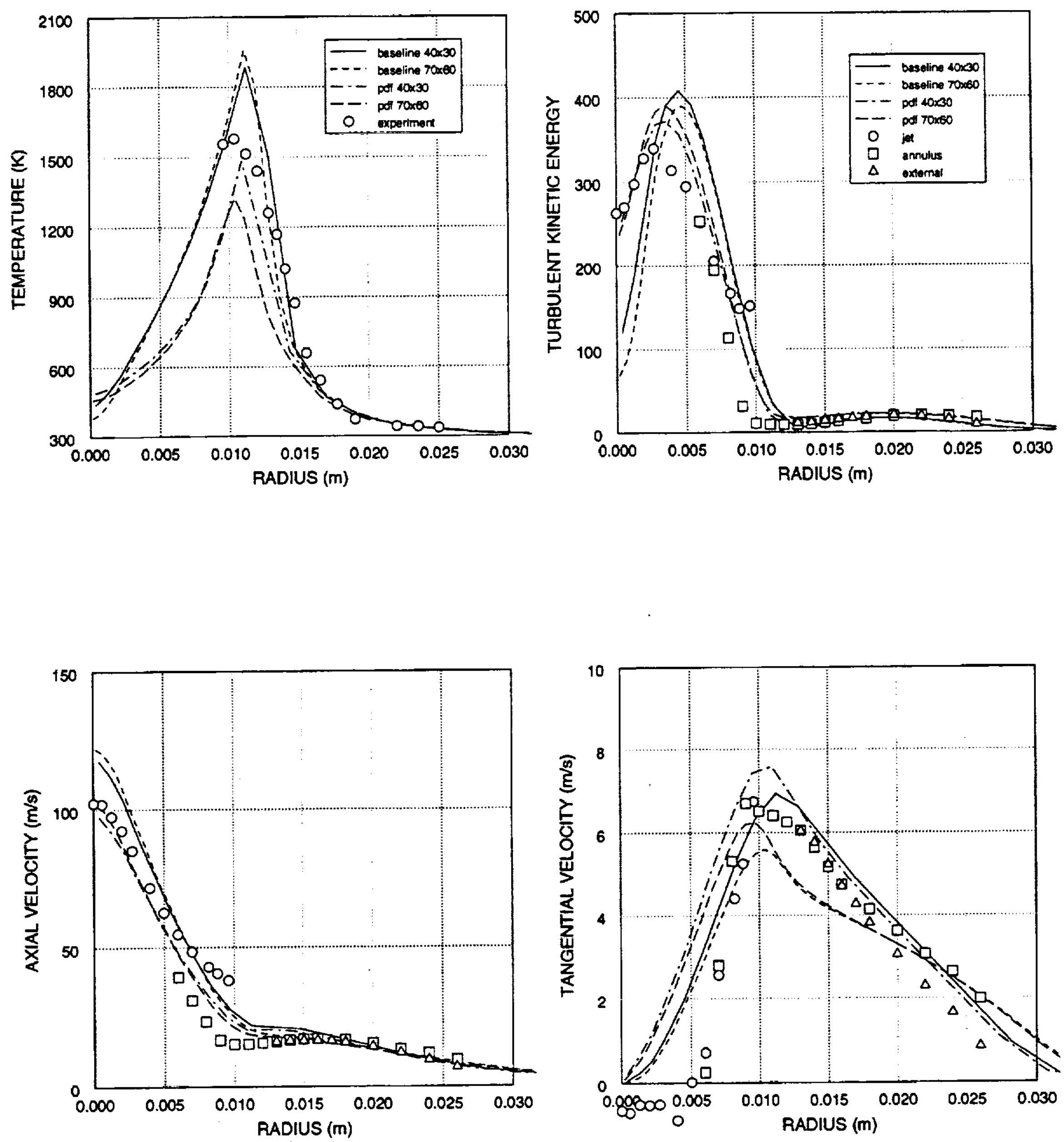

Figure 5.100 Temperature, turbulent kinetic energy, axial and tangential velocity at x = 50 mm.

simulations overpredict peak temperature by over 300 degrees. All numerical simulations predict very sharp temperature peaks while temperature measurements show more rounded peaks. The pdf simulations best predict turbulent kinetic energy. The baseline simulations predict larger radial displacement of the turbulent kinetic energy peak, overpredict the peak, and underpredict turbulence kinetic energy at and near the combustor axis. Axial velocity is best predicted by the pdf simulations. Baseline simulations overpredict centerline axial velocity by about 20 %. The axial velocity predictions between the simulations converge with increasing radius. The baseline coarse grid simulation best predicts the tangential velocity profile. The coarse grid simulations are almost identical beyond a radius of 13 mm. The fine grid tangential velocity predictions are almost identical beyond a radius of 12 mm. The tangential velocity predictions are affected by predicted heat release (radial flow expansion) and also show grid dependence.

Comparisons at an axial distance of 75 mm from the inlet are shown in figure 5.101. The pdf simulations underpredict the peak temperature by about 100 degrees, while the baseline simulations overpredict temperature by 300-400 degrees. Predicted temperature peaks are quite sharp, while the temperature measurements are starting to show a plateau like area of high temperature just inside the peak temperature. The fine grid pdf simulation shows the bluntest

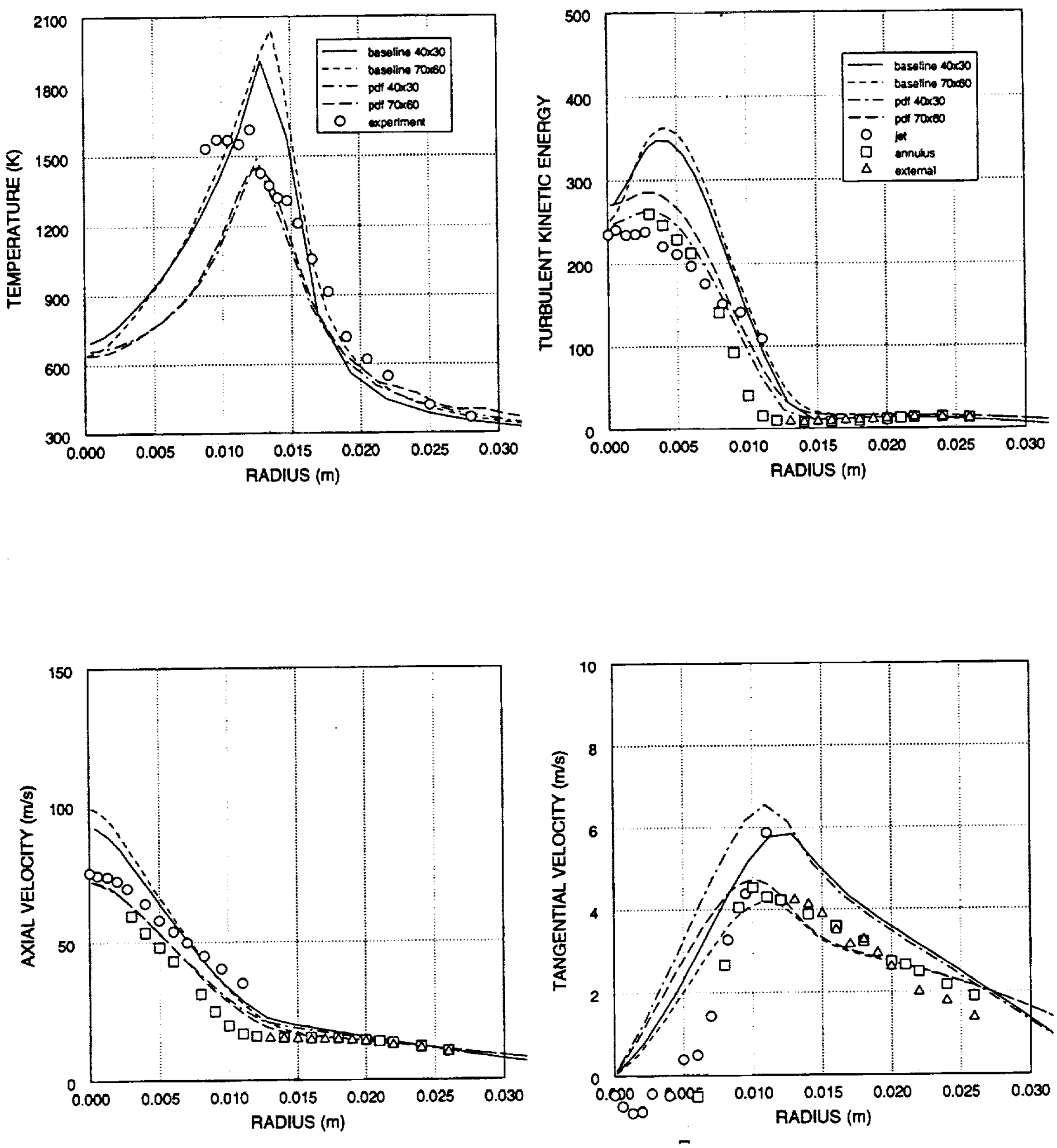

Figure 5.101 Temperature, turbulent kinetic energy, axial and tangential velocity at x = 75 mm.

temperature peak. The pdf simulations excellently predict turbulent kinetic energy and axial velocity, while the baseline simulations overpredict both quantities out to a radius of 15 mm. From a radius of 9 to 15 mm, the predictions of axial velocity are surprisingly close to each other, despite the large difference in temperature predictions at this axial station. The largest difference in axial velocity predictions occurs along the flame centerline. The fine grid simulations predict the lowest tangential velocity which is also closest to the experimental measurements. The coarse grid pdf simulation predicts highest tangential velocity, in part due to lower predicted heat release. At the previous axial station, the coarse grid simulations best predicted tangential velocity beyond the peak. Under a radius of 8 mm at this station, the shape of the tangential velocity appears to be poorly predicted. Predicted tangential velocity profiles show almost linear increases with radial distance out to 10 mm. The experimental data shows near zero, or even negative tangential velocity out to a radius of 5 mm and then a fairly linear profile to the tangential velocity peak. This predictive behavior is also shown in previous plots.

The comparisons at an axial distance of 150 mm are shown in figure 5.102. Baseline simulations overpredict the peak by almost 500 degrees. Pdf simulations slightly overpredict the temperature peak. All simulations show a

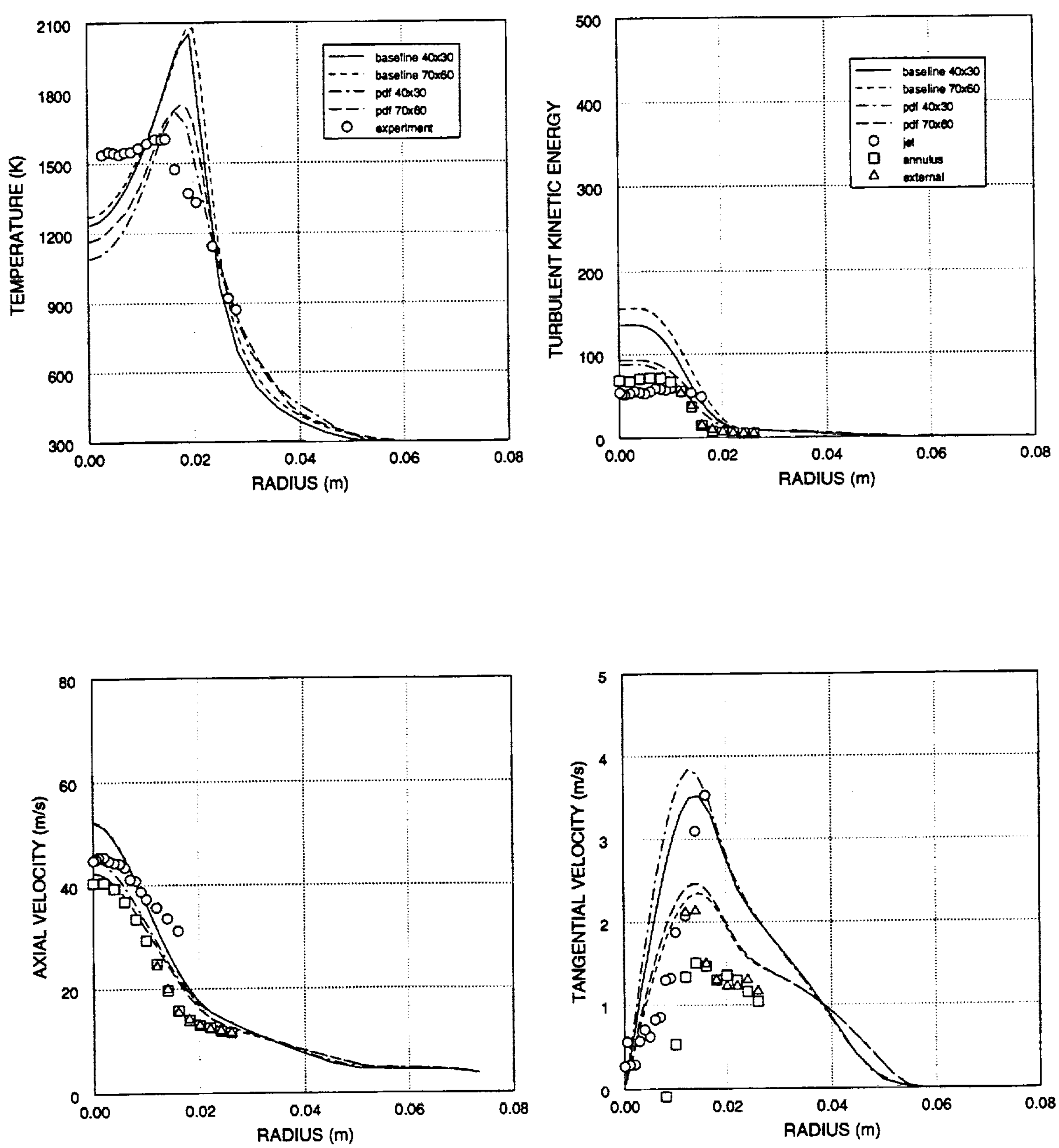

Figure 5.102 Temperature, turbulent kinetic energy, axial and tangential velocity at x = 150 mm.

strong drop in temperature towards the combustor axis, while temperature measurements show a nearly constant profile. Turbulent kinetic energy is best predicted in the pdf simulations. The baseline simulations overpredict centerline turbulent kinetic energy and axial velocity. The jet seeded axial velocity measurements are larger than the annulus seeded velocity measurements at the same radii. The pdf simulations predict axial velocity profiles lying between the sets of conditional measurements. Fine grid predictions of tangential velocity are very similar to each other, as are the two coarse grid simulations. The fine grid simulations best predict tangential velocity, while the coarse grid simulations overpredict tangential velocity by 50 percent.

The largest disagreement in the sets of conditional velocity measurements occurs for radial velocity, which is shown in figure 5.103. The experimental data does not benchmark or validate the predictions. Instead, the data largely bounds the various velocity predictions. Measurements of fuel seeded flow show peaks at least twice as high as all predictions. Radial velocity measurements taken at the 75 and 150 mm axial locations by seeding the fuel jet are much higher than measurements found by seeding the annulus and external air flows. To best compare traditionally calculated velocities, velocity measurements should be unconditional or averaged. All inlet flows should be

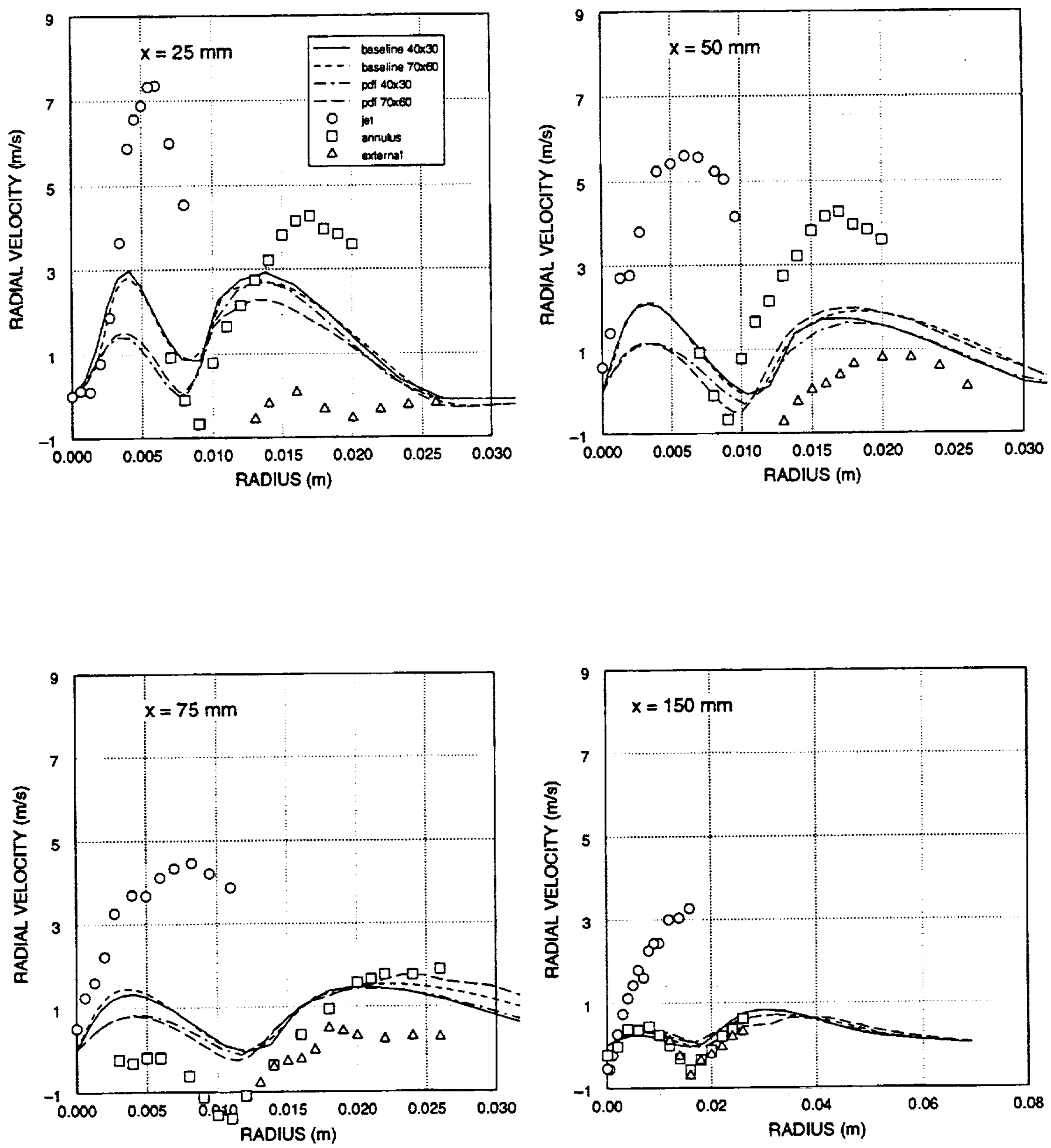

Figure 5.103 Radial velocity at x = 25, 50, 75, and 150 mm.

simultaneously seeded.

Chapter 6

CONCLUDING REMARKS

A joint pdf solver for species and temperature was incorporated and further developed. Velocity, pressure, turbulent kinetic energy and dissipation are solved for using the SIMPLE algorithm of Patankar. The pdf model uses Monte Carlo solution technique to solve for the evolution of the pdf. The effects of transport between fluid cells, mixing and combustion within fluid cells are treated sequentially. The composition pdf handles the turbulence combustion interaction due to varying species and temperature. This eliminates the need to correct reaction rate terms due to turbulence effects, as is typically done in current combustion models. Turbulence causes large local variation in species and temperature. As reaction rates are non-linear functions of species and temperature, reaction rates determined from mean species and temperature are physically incorrect. Pdf modeling allows the proper incorporation of reaction rates without corrections.

The pdf method used in this work employs a constant number of particles in each fluid cell. An Eulerian framework is to solve for the evolution of the pdf. The solution of particle transfers, mixing and combustion gives a finite number representation of the true pdf. This corresponds nicely to measurement techniques which also use a finite number of data points to ascertain pdfs.

Various improvements were made to the pdf model. First, variable C_p and proper treatment of thermodynamic properties was incorporated into the model. The original model assumed a single specific heat for all species and temperatures. Temperature rather than enthalpy was used to keep track of energy. The improved thermodynamic model uses data in the form of a two temperature range fifth order polynomial to calculate specific heat and enthalpy. This way of handling thermodynamic data has been widely used in equilibrium and finite rate single cell or one dimensional combustion calculations. The method is accurate over a wide temperature range and is very highly regarded in the thermodynamic field. An improved Newton-Raphson species solver was incorporated into the composite pdf for solving finite chemical reaction rates.

The validation of the improved hybrid pdf model involves the comparison of pdf simulations, baseline calculations, and experimental data. The baseline combustion model uses the SIMPLE algorithm to solve for velocity, pressure, species and enthalpy. The baseline model also includes the effect of variable specific heat. Originally it was desired to calculate spray combustion, so the baseline combustion model was evaluated for these flows. The liquid phase fuel spray was solved in an Lagrangian framework. The interaction between the liquid phase and gaseous phase was handled by including drag effects on liquid drops and source terms in the gas phase for the evaporating spray. The baseline spray predictions for an evaporating methanol case were very good. Acceptable results were also obtained for the isothermal swirling air in a spray combustor by including some turbulence modeling changes. The baseline model also gave qualitatively good results for the same combustor with heptane spray combustion. Turbulence model changes did not need to be done for the combusting case, as turbulence levels generated by combustion were higher. The region containing spray was not particularly well calculated despite various changes. The largest source of error in the spray calculation was caused by an overly quick dissipation of the gaseous velocity components surrounding the spray. The spray occurs in a high shear region where the gaseous flow is severely skewed to the computational grid. Velocity predictions further from the spray atomizer were much better. As this deficiency in calculating spray combustion would not be improved by turbulence combustion models, further testing was confined to single phase flows. It was decided not to pursue pdf modeling of combusting sprays.

There are a few misconceptions about pdf modeling in the CFD community. Pdf modeling does not predict emissions if they are not included in the reaction mechanisms. Also, pdf modeling will not make up for deficientcies in turbulence modeling. The hybrid pdf model which was used here used the k-ε turbulence model to predict mixing. The k-ε model is known to be deficient for high swirl and turbulence transition.

The hybrid pdf was first tested for an enclosed diffusion combustor. A set of co-annular jets supplied methane and air to a dump combustor. Simulations predicted an outer recirculation zone. The pdf simulation predicted a recirculation zone length almost 25% longer. As the recirculation zone was hot, and the central fuel core was cool, this provided an continuing combustion source. Both simulations predicted substantial overlap of fuel and oxygen concentration profiles in agreement with measurements. Hybrid pdf predictions were most often superior to results obtained with the baseline method, especially along the combustor centerline. The hybrid pdf produced superior predictions of oxygen, carbon dioxide and water concentration. Fuel was significantly overpredicted by both hybrid and baseline simulations at three axial stations. Both simulations did an excellent job of predicting the first temperature profile. Temperatures on and near the combustor axis were much better predicted by the hybrid pdf simulation for the second and final temperature profile. The methane combustion simulations were beginning to show larger temperature differences with axial distance. More temperature measurements would have helped to better evaluate the combustion models. Also, measured velocities were not available to validate the calculations. Temperature plots of the pdf particles at selected cells showed substantial numbers of partially reacted particles co-existing with very hot, fully reacted particles.

The second case involved a swirling combustor flow characteristic of an actual gas turbine combustor. The high swirl component causes a central recirculation zone. Inlet fuel and air flows were at fairly high velocity at a severe angle to the computational grid for this combustor. This is where the baseline method was identified as being deficient for spray calculations. The fuel jet was very coarsely modeled. Combustor predictions of velocity and species were more diffuse than measurements. The hybrid pdf results for the second case did not display as much radial displacement of fuel as was measured. Thus, the pdf modeling did not make up for the deficiency identified in the baseline combustor spray calculations. It is likely that a pdf calculation done in a Lagrangian framework would prove to be less diffusive, and improve flow predictions. Substantial grid modification to better model the fuel jet would also help modeling this flow. Velocity and turbulence predictions for this type of flow would probably be improved with the implementation of higher-order numerical scheme. However, such fixes are not known for their robustness. The hybrid pdf simulation did predict a slower rate of combustion more in agreement with experimental temperature and species data.

The third case involved premixed combustion in a simple dump type combustor. This tested whether pdf modeling could be used in cases were the fuel and oxidant are intimately mixed. The hybrid pdf results were generally superior to the baseline simulation. The baseline calculation best predicted velocity and temperature profiles for the first two axial stations. The baseline calculation predicted lower temperatures than measured for substantial portions of the flow at succeeding axial stations. The baseline simulation of combustion seemed overly limited by the eddy-breakup reaction rate for latter portions of the flowfield. Efforts to improve the baseline prediction by increasing the reaction rates resulted in significant change in the flowfield and overall solution degradation. The pdf simulation predicted higher temperature gradients than the baseline simulation. This particularly improved predictions for the latter portion of the combustor flowfield. A test was done to evaluate the molecular mixing submodel in the pdf model. A second simpler relax-to mean mixing submodel was incorporated. This change didn't significantly affect the pdf predictions. The simpler model is more economical to use.

Very low levels of turbulence were measured in the experimental apparatus. A slight deficientcy in the turbulence model is suggested. While the pdf model produced improved temperature profiles, it should not be implied that the pdf model make up for deficientcies in turbulence model.

The fourth case involved a swirling hydrogen-air jet flame. The swirl mass flow component was small enough that recirculation was not involved. The hybrid pdf solver produced superior predictions of temperature, axial velocity, and turbulent kinetic energy. The pdf simulation and baseline coarse grid simulation both predicted higher tangential velocity than measured later in the flowfield. A fine grid pdf calculation better predicted tangential velocity decay. The baseline fine grid calculation better predicted tangential velocity decay.

The pdf simulations correctly predict turbulent phenomena, specifically, large variation in local species concentration and temperature. This represents an improvement in turbulent-combustion modeling where turbulent combustion has been either ignored or various ad-hoc corrections have been applied to chemical reaction rates. Current multi-dimensional CFD modeling generally produces predict too large temperatures and superfluous product species concentrations. The inclusion of multiple species concentrations and temperatures ala pdf modeling helps correct this deficiency. The pdf method usually improves combustor flowfield predictions. These cases prove that the pdf method can be used for both diffusion flames and premixed flames provided a proper reaction model is used.

All simulations here used a single reaction step. Including multiple reaction rates is known to improve predictions of species and temperature for zero or one dimensional flows, and allows the calculation of additional species, specifically, pollutants. The inclusion of multiple finite-rate reaction steps in current models, while possible, involves increasing numerical inaccuracy. Multiple reaction steps can involve the introduction of highly reactive intermediate species. The solution of reaction rates at higher temperatures in current models is only accurate for very small time steps. Errors generated by using too high of reaction rates can produce physically impossible predictions of temperature and product species concentrations. Use of finite reaction rate models in current multidimensional models involves overwriting negative species concentration. Such corrections depend a lot on the experience of the CFD modeler. The pdf method can easily incorporate chemical kinetic rate solvers which have been developed to overcome these problems. These solvers can handle the largest chemical kinetic reaction schemes that have been proposed. The drawback to this is a rather large amount of computer resources and time to perform calculations. Pdf modeling may be used to improve the solution accuracy of combustor predictions done with simpler combustion models.

References

forest

1. Patankar, S.V., "Numerical Heat Transfer and Fluid Flow", Hemisphere Publishing Corp., New York, 1980.

2. Chen, K-H, Duncan, B., Fricker, D., Lee, J., and Quealy, A., "ALLSPD-3D, Version 1.0", NASA Lewis Research Center, Nov., 1995.

3. Joshi, D.S., and Vanka, S.P., "A Multigrid Calculation Procedure for Internal Flows in Complex Geometries", AIAA 90-0442, 1990.

4. Tafti, D.K., and Vanka, S.P., "Hot Gas Environment Around STOVL Aircraft in Ground Proximity: Part 2: Numerical Study", AIAA 90-2270, 1990.

5. Vanka, S.P., and Krazinski, J.L., "Efficient Computational Tool for Ramjet Combustor Research", J. Propulsion, Vol. 5, pp. 431-437, 1989.

6. Radhakrishnan, K., and Bittker, D., "LSENS, A General Chemical Kinetics and Sensitivity Analysis Code for Homogeneous Gas-Phase Reactions", NASA RP-1328, 1329, and 1330, 1994.

7. Jones, W.P, and Launder, B.E., "The Prediction of Laminarization with a two-equation model of turbulence", Int. J. Heat Mass Transfer, Vol 15, pp. 301-314, 1972.

8. Correa, S.M., and Shyy, W., "Computational Models and Methods for Continuous Gaseous Turbulent Combustion", Prog. Energy Combust. Sci., Vol. 13, pp. 249-292, 1987.

9. Leonard, B.P., "A Stable and Accurate Convective Modeling Procedure Based on Quadratic Upstream Interpolation", Comput. Meth. Appl. Mech. Engng., Vol. 19, pp. 59-98, 1979.

10. Faeth, G.M., "Current Status of Droplet and Liquid Combustion", Prog. Energy Combust. Sci., Vol. 3, pp. 191-224, 1977.

11. Law, C.K., "Recent advances in Droplet Vaporization and Combustion", Prog. Energy Combust. Sci., Vol. 8, pp. 171-201, 1982.

12. Faeth, G.M., "Vaporization and Combustion of Sprays", Prog. Energy Combust. Sci., Vol. 9, pp. 1-76, 1983.

13. Sirignano, W.A., "Fuel Droplet Vaporization and Spray Combustion Theory", Prog. Energy Combust. Sci., Vol. 9, pp. 291-322, 1983.

14. Onuma, Y., and Ogasawara, M., "Studies on the Structure of a Spray Combustion Flame", Fifteenth Symposium (International) on Combustion, The Combustion Institute, Pittsburgh, pp. 453-465,

1975.

15. Spaulding, D.B., "The Combustion of Liquid Fuels", Fourth Symposium (International) on Combustion, The Combustion Institute, Pittsburgh, pp. 847-864, 1953.

16. Faeth, G.M., "Mixing, Transport and Combustion in Sprays", Prog. Energy Combust. Sci., Vol. 13, pp. 293-345, 1987.

17. Tsai, J.S., and Sterling, A.M., "The Combustion of Linear Droplet Arrays", Twenty-Third Symposium (International) on Combustion, The Combustion Institute, Pittsburgh, pp. 1405-1411, 1990.

18. Odgers, J., Kretschmer, D., Norster, E.R., Lefebvre, A.H., and Fletcher, R.S., "The Design and Development of Gas Turbine Combustors", Northern Research and Engineering Corp., Woburn, Massachusetts, 1980.

19. Tong, A.Y., and Sirignano, W.A., "Multicomponent Transient Droplet Vaporization with internal Recirculation: Integral Formulation and Approximate Solution", Numerical Heat Transfer, Vol. 10, pp. 253-278, 1986.

20. Raju, M.S., and Sirignano, W.A., "Multicomponent Spray Computations in a Modified Centerbody Combustor", J. of Propulsion, Vol. 6, pp. 97-105, 1990.

21. Reid, R.C., Prausnitz, J.M., and Sherwood, T.K., "Properties of Liquids and Gases", McGraw-Hill, 1977.

22. Kumar, R. K., "Ignition of Hydrogen_Oxygen_Diluent Mixtures Adjacent to a Hot, Nonreactive Surface," Combustion and Flame, Vol. 75, pp. 197-215, 1989.

23. Kim, S.-W., "Numerical Investigation of Chemical Reaction-turbulence Interaction in Compressible Shear Layers," Combustion and Flame, Vol. 101, pp. 197-208, 1995.

24. Dryer, F.L., and Glassman, I., "High Temperature Oxidation of Co and CH_4", Fourteenth Symposium (International) on Combustion, The Combustion Institute, Pittsburgh, pp. 987-1003, 1972.

25. Westbrook, C. K., and Dryer, F. L. "Simplified Reaction Mechanisms for the Oxidation of Hydrocarbon Fuels in Flames", Combustion Science and Technology, Vol. 27, pp.31-43, 1981.

26. Coffee, T. P., "On Simplified Reaction Mechanisms by Oxidation of Hydrocarbon Fuels in Flames by C. K. Westbrook and F. T. Dryer", Combust. Sci. and Tech., Vol. 43, pp. 333-339, 1985.

27.Coffee, T. P., Kotlar, A. J., Miller, M. S., "The Overall Reaction Concept in Premixed, Laminar, Steady-State Flames. I. Stoichiometries",Combustion and Flame, Vol. 54, pp. 155-169, 1983.

28. Nikjooy, M., So, R.M.C., "On the Modelling of Non-Reactive and Reactive Combustor Flows", NASA CR 4041, 1987.

29.Srivatsa, S. K., "Computations of Soot and Nox Emissions from Gas Turbine Combustors", NASA CR-167930, 1982.

30. Hautman, D.J., Dryer, F.L., Schug, K.P., and Glassman, I., "A Multi-step Overall Kinetic Mechanism for the Oxidation of Hydrocarbons", Combust. Sci. and Tech., Vol. 25, pp. 219-235, 1981.

31. Abdalla, A.Y., Bradley, D., Chin, S.B., and Lam, C., "Global Reaction Schemes for Hydrocarbon Oxidation", Oxidation Communications, Vol. 4, pp. 113-130, 1983.

32. Duterque, J., Borghi, R., and Tichtinsky, H., "Study of Quasi-Global Schemes for Hydrocarbon Combustion", Comb. Sci. and Tech., Vol. 26, pp. 1-15, 1981.

33. Westbrook , C.K., and Dryer, F.L., "Chemical Kinetic Modeling of Hydrocarbon Combustion", Prog. Energy Combust. Sci., Vol. 10, pp. 1-57, 1984

34. Paczko, G., Lefdal, P.M., and Peters, N., "Reduced Reaction Schemes for Methane, Methanol, and Propane Flames", Twenty-first Symposium (International) on Combustion, The Combustion Institute, Pittsburgh, pp. 739-748, 1986.

35. Seshadri, K., Peters, N., "Asymptotic Structure and Extinction of Methane-Air Diffusion Flames", Combustion and Flame, Vol. 73, pp. 23-44, 1988.

36. Kiehne, T.M., Matthews, R.D., and Wilson, D.E., "An Eight-Step Kinetics Mechanism for High Temperature Propane Flames", Combust. Sci. and Tech., Vol. 54, pp. 1-23, 1987.

37. Jones, W.P., and Lindstedt, R.P., "Global Reaction Schemes for Hydrocarbon Combustion", Combustion and Flame, Vol. 73, pp. 233-249, 1988.

38. Bilger, R.W., and Starner, S.H., "On Reduced Mechanisms for Methane-Air Combustion in Nonpremixed Flames", Combustion and Flame, Vol. 80, pp. 135-149, 1990.

39. D. B. Spaulding, "Mixing and Chemical Reaction in Steady, Confined Turbulent Flames", Thirteenth Symposium (International) on Combustion, The Combustion Institute, Pittsburgh, pp. 649-657, 1970.

40. D. B. Spaulding, "Concentration Fluctuations in a Round Turbulent Free Jet," Chem. Eng. Sci, vol 26, pp. 95-107, 1971.

41. Mason, H. B., and Spaulding, D. B., "Prediction of reaction rates in turbulent pre-mixed boundary layer flows", Combustion Institute European Symposium, pp. 601-606, 1973.

42. Spaulding, D. B., "Mathematical Models of Turbulent Flames; A Review," Comb. Sci. and Tech., Vol 13, pp. 3-25, 1976.

43. Magnussen, B. F., and Hjertager, B. H., "On Mathematical Modeling of Turbulent Combustion With Special Emphasis On Soot Formation and Combustion," Sixteenth Symposium (International) on Combustion, The Combustion Institute, Pittsburgh, pp. 719-729, 1976.

44. Srinivasan, R., et. al., "Aerothermal Modeling Program Phase I Final Report," NASA CR-168243, GARRETT 21-4742-1, 1983.

45. Libby, P. A., and Williams, F. A., " Turbulent Reacting Flows," Springer-Verlag, 1980.

46. Richardson, J.M., Howard, H.C., and Smith, R.W., "The Relation Between Sampling Tube Measurements and Concentration Fluctuations in a Turbulent Gas Jet", Fourth Symposium (International) on Combustion, The Combustion Institute, Pittsburgh, pp. 814-817, 1953.

47. Jones, W. P., "Models for Turbulent Flows with Variable Density and Combustion," in Prediction Methods for Turbulent Flows (Edited by Kollman, W.), pp. 379-422, Hemisphere Publishing Corp., 1980.

48. Tsuji, H. and Yamoka, L. "Structure Analysis of Counterflow Diffusion Flames in the Forward Stagnation Region of a Porous Cylinder, " Thirteenth Symposium (International) on Combustion, The Combustion Institute, Pittsburgh, pp. 723-731, 1971.

49. Bilger, R. W., "Reaction Rates in Diffusion Flames", Combustion and Flame, Vol. 30, pp. 277-284, 1977.

50. Jeng, S.-M., "An Investigation of Structure and Radiation Properties of Turbulent Buoyant Diffusion Flames, Ph.D. Thesis, Pennsylvania State University, 1984.

51. Spaulding, D. B., "GENMIX: A General Computer Program for Two-dimensional Parabolic Phenomena", Pergamon Press, 1977.

52. Liew, S. K., Bray, K. N. C., and Moss, J. B., "A flamelet model of Turbulent Non-premixed Combustion", Comb. Sci. and Tech., Vol. 27, pp. 69-73, 1981.

53. Liew, S.k., and Bray, K.N.C., "A Stretched Laminar Flamelet Model of Turbulent Nonpremixed Combustion", Combustion and Flame, Vol. 56, pp. 199-213, 1984.

54. Drake, M.C., and Blint, R.J., "Structure of Laminar Opposed-flow Diffusion Flames With $CO/H_2/N_2$ Fuel", Combust. Sci. and Tech., Vol. 61, pp. 187-224, 1988.

55. Borghi, R., "Turbulent Combustion Modelling", Prog. Energy Combust. Sci., Vol. 14, pp. 245-292, 1988.

56. Peters, N., "Laminar diffusion flamelet models in nonpremixed turbulent combustion", Prog. Energy Combust. Sci., Vol. 10, pp. 319-339, 1984.

57. Janika, J., and Kollman, W., "A two-variable formalism for the treatment of chemical reactions in turbulent H_2-air diffusion flames, Seventeenth Symposium (International) on Combustion, The Combustion Institute, Pittsburgh, pp. 421-431, 1979.

58. Dixon-Lewis, G., Goldsworthy, F. A., and Greenburgh, J.B., "Flame structure and flame reaction kinetics. IX. Calculation of properties of multi-radical premixed flames", Proc. R. Soc. Lond., Vol. 346, 261-278, 1975.

59. Janika, J., and Kollman, W., "The Calculation of Mean Radical Concentrations in Turbulent Diffusion Flames", Combustion and Flame, Vol. 44, pp. 319-336, 1982.

60. Kent, J.H., and Bilger, R.W., "Turbulent Diffusion Flames", Fourteenth Symposium (International) on Combustion, The Combustion Institute, Pittsburgh, pp. 615-625, 1974.

61. Correa, S.M., Drake, M.C., Pitz, R.W., and Shyy, W., "Prediction and Measurement of a non-equilibrium turbulent diffusion flame", Twentieth Symposium (International) on Combustion, The Combustion Institute, Pittsburgh, pp. 337-343, 1984.

62. Correa,S.M., "A model for non-premixed turbulent combustion of CO/H_2 jets", Archvm. Combust., Vol. 5, 223-242, 1985.

63. Pope, S.B., and Correa, S.M., "Joint PDF Calculations of a Non-equilibrium Turbulent Diffusion Flame", Twenty-first Symposium (International) on Combustion, The Combustion Institute, Pittsburgh, pp. 1341-1348, 1986.

64. Mongia, H.C., "Combustion Modeling in Design Process: Applications and Future Direction", AIAA 94-0466, 1994.

65. Kuo, K.K., "Principles of Combustion", John Wiley & Sons, New York, 1986.

66. Williams, F.A., "Combustion Theory", Benjamin/Cummings Publishing Company, Inc., Menlo Park, 1985.

67. Bartok, W., and Sarofim, A.F., "Fossil Fuel Combustion, A Source Book", John Wiley & Sons, New York, 1991.

68. Chigier, N., "Energy, Combustion and Environment", McGraw-Hill, New York, 1981.

69. Oran, E.S., and Boris, J.P, "Numerical Simulation of Reactive Flow", Elsevier, New York, 1987.

70. Anand, M.S., Pope, S.B., and Mongia, H.C., "A PDF Method for Turbulent Recirculating Flows", in Turbulent Reactive Flows, Lecture Notes in Engineering, Springer-Verlag, Vol. 40, pp. 672-693, 1989.

71. Curl, R.L., "Dispersed Phase Mixing, I, Theory and Effects of Simple Reactors", A.I.Ch.E.J., vol. 9, p. 175-181, 1963.

72. Janika, J., Kolbe, W., and Kollman, W. "Closure of the Transport Equation for the Probability Density Function of Turbulent Scalar Fields," J. Non-Equilib. Thermodyn., Vol. 4, pp. 47-66, 1979.

73. Dopazo, C., "Pdf approach for a turbulent axisymmetric heated jet: Centerline evolution", Physics of Fluids, Vol. 18, 397-404, 1975.

74. Pope, S. B., "Pdf Methods for Turbulent Reactive Flows", Prog. Energy Combust. Sci., Vol. 11, pp. 119-192, 1985.

75. Hsu, A. T., and Chen, J. Y., "A Continuous Mixing Model for Pdf Simulations and its Application to Combusting Shear Flows", Eighth Symposium on Turbulent Shear Flows, Technical University of Munich, p. 22-4, Sept. 9-11, 1991.

76. Chen, J.Y., and Kollman, W., "Segregation Parameters and Pair-Exchange Mixing Models for Turbulent Nonpremixed Flames", Twenty-Third Symposium (International) on Combustion, The Combustion Institute, Pittsburgh, pp. 751-757, 1990.

77. Pope, S. B., "An Improved Turbulent Mixing Model", Comb. Sci. Tech., Vol. 28, pp. 131-135, 1982.

78. Norris, A. T., and Hsu, A., "Comparison of PDF and Moment Closure Methods in the Modeling of Turbulent Reacting Flows", NASA TM 106614, 1994.

79. Masri, A. R., Dibble, R. W., and Barlow, R. S., "The Structure of turbulent, pilot stabilized Flames of $CH_4/CO/H_2/N_2$ fuel mixtures", Combustion and Flame, Vol. 88, pp. 239-264, 1992.

80. Villermaux, J., "Micromixing phenomena in stirred reactors", Encyclopedia of Fluid Mechanics, pp. 707-768, Gulf Pub. Co., West Orange, NJ, 1986.

81. Yamazaki, and Ichigawa, A., Intl. Chem. Eng., Vol. 10, pp. 471-478, 1970.

82. Correa, S.M., and Braaten, M.E., "Parallel Simulations of Partially Stirred Methane Combustion", Combustion and Flame, Vol. 94, pp. 469-486, 1993.

83. Correa, S.M., "A Direct Comparison of Pair-Exchange and IEM Models in Premixed Combustion", Combustion and Flame, Vol. 103, pp. 194-206, 1995.

84. J.Y. Chen, and Kollman, W., "Mixing Models for Turbulent Flows with Exothermic Reactions", Turbulent Shear Flows 7, Springer-Verlag, Berlin Heidelberg, pp. 277-292, 1991.

85. Chen, J. Y., Kollman, W., and Dibble, R. W., "Pdf modeling of Turbulent Nonpremixed Methane Jet Flames," Combust. Sci. and Tech., Vol. 64, pp. 315-346, 1989.

86. Maas, U.A., and Pope, S. B., "Simplifying chemical kinetics: Intrinsic Low-Dimensional Manifolds in Composition Space", Combustion and Flame, Vol. 88, pp 239-264, 1992.

87. Chen, J.Y., and Kollman, W., "Chemical Models for Pdf Modeling of Hydrogen-Air Nonpremixed Turbulent Flames", Combustion and Flame, Vol. 79, pp 75-99, 1990.

88. Hsieh, K.-C., Shuen, J.-S., Tsai, Y.-L. Peter, and Yu, S.-T., "RPLUS2D/3D USER'S MANUAL," Sverdrup Technology, Inc., NASA Lewis Research Center, Oct. 22, 1990.

89. Yoon, S., and Jameson, A. "An LU-SSOR Scheme for the Euler and Navier-Stokes Equations," AIAA Paper 87-0600, 1987.

90. Burros, M. C., and Kurkov, A. P., "Analytical and Experimental Study of Supersonic Combustion of Hydrogen in a Vitiated Air Stream," TMX-2828, NASA, 1973.

91. Rogers, R. C., and Chinitz, W., "Using a Global Hydrogen-Air Combustion Model in Turbulent Reacting Flow Calculations", AIAA J., Vol. 21, pp. 586-592, 1983.

92. Strahle, W.C., and Lekoudis, S.G., "Evaluation of Data on Simple Turbulent Reacting Flows", AFSOR-TR-85-0880, 1985.

93. Kline, S.J., Morkovin, M.J., and Moffat, "Computation of Turbulent Boundary Layers", 1968 AFSOR-IFP-Stanford Conference, 1969.

94. Baker, R.J., Hutchinson, P., Khalil, E.E., and Whitelaw, J.H., "Measurements of Three Velocity Components in a Model Furnace With and Without Combustion", Fifteenth Symposium (International) on Combustion, The Combustion Institute, Pittsburgh, pp. 553-559, 1974.

95. Lockwood, F.C., El-Mahallawy, F.M., and Spaulding, D.B., "An Experimental and Theoretical Investigation of Turbulent Mixing in a Cylindrical Furnace", Combustion and Flame, Vol. 23, pp. 283-293, 1974.

96. McDannel, M.D., Peterson, P.R., and Samuelson, G.S., "Species concentration and Temperature Measurements in a Lean, Premixed Flow Stabilized by a Reverse Jet", Combust. Sci. and Tech., Vol. 28, pp. 211-224, 1982.

97. El Banhawy, Y., Sivasegaram, S., and Whitelaw, J.H., "Premixed, Turbulent Combustion of a Sudden-Expansion Flow", Combustion and Flame, Vol. 50, pp. 153-165, 1977.

98. Smith, G.D., Giel, T.V., and Catalano, C.G., "Measurements of Reactive Recirculating Jet Mixing in a Combustor", AIAA J., Vol.21, pp. 270-276, 1983.

99. Lightman, A.J., Richmond, R.D., Krishnamurthy, L., Magill, P.D., Roquemore, W.M., Bradley, R.P., Stutrud, J.S., and Reeves, C.M., "Velocity Measurements in a Bluff-Body Diffusion Flame", AIAA-80-1544, 1980.

100. Magill, P.D., Lightman, A.J., Orr, C.E., Bradley, R.P., and Roquemore, W.M., "Simultaneous Velocity and Emission Measurements in a Bluff-Body Combustor", AIAA-82-0833, 1982.

101. Schefer, R.W., Namazian, M., and Kelly, J., "Velocity Measurements in a Turbulent Nonpremixed Bluff-Body Stabilized Flame", AIAA-87-1349, 1987.

102. Sivasegaram, S. and Whitelaw, J.H., "Oscillations in Axisymmetric Dump Combustors", Combust. Sci. and Tech., Vol. 52, pp. 413-426, 1987.

103. Sivasegaram, S., Thompson, B.E., and Whitelaw, J.H., "Acoustic Characterization Relevant to Gas Turbine Augmentors", J. Propulsion, Vol. 5, pp. 109-115, 1989.

104. Charles, R., "Detailed Data Set: Velocity and Temperature Measurements in the Axisymmetric Can Combustor for a Parametric Variation in Inlet Conditions", University of California, Irvine, UCI-ARTR-87-6, 1988.

105. Pan, J.C., "Laser-Diagnostic Studies of Confined Turbulent Premixed Flames Stabilized by Conical Bluff Bodies", Ph.D. Thesis, University of Dayton, 1991.

106. Heitor, M.V., and Whitelaw, J.H., "Velocity, Temperature, and Species Characteristics of the Flow in a Gas-Turbine Combustor", Combustion and Flame, Vol. 64, pp. 1-32, 1986.

107. Bicen, A.F., Tse, D.G.N, and Whitelaw, J.H., "Combustion Characteristics of a Model Can-Type Combustor", Combustion and Flame, Vol. 80, pp. 111-125, 1990.

108. Bulzan, D.L. "Structure of a Swirl-Stabilized Combusting Spray", Journal of Propulsion and Power, Vol. 11, pp. 1093-1102, 1995.

109. Srivasan, R.,"Aerothermal modeling program Phase I final report", NASA CR-168243, 1983.

110. Sloan, D.G., Smith, P.J., and Smoot, L.D.,"Modeling of swirl in turbulent flow systems", Prog. Energy Combust. Sci., Vol. 12, 163-250, 1986.

111. Shih, T-H, Zhu, J., and Lumley, J.L., "Modeling of wall-bounded complex flows and free shear flows," NASA TM 106513, 1994.

112. McDonell, V.G., Adachi, M., and Samuelsen, G.S., "Structure of Reacting and Non-Reacting Swirling Air-Assisted Sprays", Combust. Sci. and Tech., Vol. 82, pp. 225-248, 1992.

113. El Banhawy, Y., and Whitelaw, J.H., "Calculation of the Flow Properties of a Confined Kerosene-Spray Flame", AIAA. J., Vol. 18, pp. 1503-1510, 1980.

114. Edwards, C.F., and Rudoff, R.C., "Structure of a Swirl-Stabilized Spray Flame by Imaging, Laser Doppler Velocimetry, and Phase Doppler Anemometry", Twenty-Third Symposium (International) on Combustion, The Combustion Institute, Pittsburgh, pp.1353-1359, 1990.

115. Bachelo, W.D., Brena de la Rosa, A., and Rudoff, R.C., " Diagnostics Development for Spray Characterization in Complex Turbulent Flows", AIAA 88-0236, 1988.

116. Zhu, J.Y., Rudoff, R.C., Bachalo, E.J. and Bachalo, W.D., "Number Density and Mass Flux Measurements Using the Phase Doppler Particle Analyzer in Reacting and Non-Reacting Flows", AIAA 93-0361, 1993.

117. Presser, C., Gupta, A.K., and Semerjian, H.G.,"Aerodynamic Characteristics of Swirling Spray Flames: Pressure-Jet Atomizer", Combust. and Flame, Vol. 92, pp. 25-44, 1993.

118. Ghaffarpour, M., and Chehroudi, B., "Experiments on Spray Combustion in a Gas Turbine Model Combustor", Combust. Sci. and Tech., Vol., 92, pp. 173-200, 1993.

119. Lewis, M. H., and Smoot, L. D. "Turbulent Gaseous Combustion Part I: Local Species Concentration Measurements", Combustion and Flame, Vol. 42, pp. 183-196, 1981.

120. Smith, P. J., and Smoot, L. D. "Turbulent Gaseous Combustion Part II: Theory and Evaluation for Local Properties", Combustion and Flame, Vol. 42, pp. 277-285, 1981.

121. Jones, W. P., and Wilhelmi, J., "Velocity, Temperature and Composition Measurements in a Confined Swirl Driven Recirculating Flow", Combust. Sci. and Tech., Vol. 63, pp. 13-31, 1989.

122. Jones, W. P., Tober, A., "Velocity, Composition and Temperature Fields in an Axisymmetric Model Combustor", International Symposium on Applications of Laser Anemometry to Fluid Mechanics, Lisbon, Portugal, p. 3.9, 1988.

123. Gould, R. D., Stevenson, W. H., and Thompson, H. D., "Turbulence Characteristics of an Axisymmetric Reacting Flow", NASA CR 4110, Feb., 1988.

124. Magnussen, B.F., and Hjertager, B.H., "On Mathematical Modeling of Turbulent Combustion with Special Emphasis on Soot Formation and Combustion", Sixteenth Symposium (International) on Combustion, The Combustion Institute, Pittsburgh, pp. 719-729, 1978.

125. Magnussen, B.F., "The Eddy Dissipation Concept for Turbulent Combustion Modelling. Its Physical and Practical Implications", Division of Thermodynamics, University of Trondheim, Norway, 1990.

126. Gran, I. R., Melaaen, M. C., and Magnussen, F., "Numerical Simulation of Fluid Flow and Combustion in Gas Turbine Combustors", ASME 93-GT-166, International Gas Turbine and Aeroengine Congress and Exposition, 1993.

127. Takahashi, F., Vangsness, M.D., Belovich, V.M., "Conditional LDV Measurements in Swirling and Non-Swirling Coaxial Turbulent Air Jets for Model Validation," AIAA 92-0580, 1992.

128. Durbin, M.D., Vangsness, M.D., Ballal, D.R., and Katta, "Study of Flame Stability in a Step Swirl Combustor," ASME 95-GT-111, 1995.

129. Takahashi, F., Vangsness, M.D., Durbin, M.D., and Schmoll, W.J., "Structure of Turbulent Hydrogen Jet Diffusion Flames," ASME HTD-Vol. 317-2, Proceedings of the ASME Heat Transfer Division, pp. 183-193, 1995.

Appendix 1

GAS PHASE SOURCE TERMS

Equation	$S_{\phi,g}$
Axial momentum	$-\frac{\partial P}{\partial x}+\frac{\partial}{\partial x}\left(\mu_{eff}\frac{\partial U}{\partial x}\right)+\frac{1}{y}\frac{\partial}{\partial y}\left(y\mu_{eff}\frac{\partial V}{\partial x}\right)$
Radial momentum	$-\frac{\partial P}{\partial y}-\frac{2\mu_{eff}V}{y^2}+\frac{\partial}{\partial x}\left(\mu_{eff}\frac{\partial U}{\partial y}\right)+\frac{1}{y}\frac{\partial}{\partial y}\left(y\mu_{eff}\frac{\partial V}{\partial y}\right)+\frac{\rho W^2}{y}$
Tangential momentum	$-\left(\frac{\mu_{eff}}{y}+\rho V+\frac{\partial \mu_{eff}}{\partial y}\right)\frac{W}{y}$
Fuel mass fraction	$-W_f R_f$
Oxygen mass fraction	$-W_O R_f$
Energy	$W_f Q_f R_f$
Turbulent kinetic energy	$\mu_t G-\rho\varepsilon$
Dissipation	$C_1 C_\mu G k\rho - C_2\rho\varepsilon^2/k$
Concentration fluctuation	$C_{g1}\mu_{eff}\left[\left(\frac{\partial Y_f}{\partial x}\right)^2+\left(\frac{\partial Y_f}{\partial y}\right)^2\right]-C_{g2}\rho g\frac{\varepsilon}{k}$

$$G = 2\left[\left(\frac{\partial U}{\partial x}\right)^2+\left(\frac{\partial V}{\partial y}\right)^2+\left(\frac{V}{y}\right)^2\right]+\left(\frac{\partial W}{\partial x}\right)^2+\left[y\frac{\partial}{\partial y}\left(\frac{W}{y}\right)\right]^2+\left(\frac{\partial U}{\partial y}+\frac{\partial V}{\partial x}\right)^2$$

Turbulent parameters				
C_1=1.44	C_2=1.92	C_μ=0.09	C_{g1}=2.8	C_{g2}=2.0

Appendix 2

SPRAY SOURCE TERMS FOR GRIDCELLS

Equation	$S_{\phi,1} d(Vol)$
Continuity	$\sum n_k m_k$
Axial momentum	$\sum \left(n_k m_k U_k - \frac{4\pi}{3} \rho k r_k^3 n_k \frac{dU_k}{dt} \right)$
Radial momentum	$\sum \left(n_k m_k V_k - \frac{4\pi}{3} \rho_k r_k^3 n_k \frac{dV_k}{dt} \right)$
Tangential momentum	$\sum \left(n_k m_k W_k - \frac{4\pi}{3} \rho_k r_k^3 n_k \frac{dW_k}{dt} \right)$
Fuel mass fraction	$\sum n_k m_k$
Energy	$\sum n_k m_k (h_s - l_{k,eff})$

REPORT DOCUMENTATION PAGE

Form Approved
OMB No. 0704-0188

1. AGENCY USE ONLY (*Leave blank*)	2. REPORT DATE	3. REPORT TYPE AND DATES COVERED
	November 1998	Technical Memorandum

4. TITLE AND SUBTITLE

Improved Modeling of Finite–Rate Turbulent Combustion Processes in Research Combustors

5. FUNDING NUMBERS

WU–523–26–33–00

6. AUTHOR(S)

Thomas J. VanOverbeke

7. PERFORMING ORGANIZATION NAME(S) AND ADDRESS(ES)

National Aeronautics and Space Administration
Lewis Research Center
Cleveland, Ohio 44135–3191

8. PERFORMING ORGANIZATION REPORT NUMBER

E–11430

9. SPONSORING/MONITORING AGENCY NAME(S) AND ADDRESS(ES)

National Aeronautics and Space Administration
Washington, DC 20546–0001

10. SPONSORING/MONITORING AGENCY REPORT NUMBER

NASA TM—1998-208823

11. SUPPLEMENTARY NOTES

Responsible person, Thomas J. VanOverbeke, organization code 5830, (216) 433–5867.

12a. DISTRIBUTION/AVAILABILITY STATEMENT

Unclassified - Unlimited
Subject Category: 07 Distribution: Nonstandard

This publication is available from the NASA Center for AeroSpace Information, (301) 621–0390.

12b. DISTRIBUTION CODE

13. ABSTRACT *(Maximum 200 words)*

The objective of this thesis is to further develop and test a stochastic model of turbulent combustion in recirculating flows. There is a requirement to increase the accuracy of multi–dimensional combustion predictions. As turbulence affects reaction rates, this interaction must be more accurately evaluated. In this work a more physically correct way of handling the interaction of turbulence on combustion is further developed and tested. As turbulence involves randomness, stochastic modeling is used. Averaged values such as temperature and species concentration are found by integrating the probability density function (pdf) over the range of the scalar. The model in this work does not assume the pdf type, but solves for the evolution of the pdf using the Monte Carlo solution technique. The model is further developed by including a more robust reaction solver, by using accurate thermodynamics and by more accurate transport elements. The stochastic method is used with Semi–Implicit Method for Pressure–Linked Equations. The SIMPLE method is used to solve for velocity, pressure, turbulent kinetic energy and dissipation. The pdf solver solves for temperature and species concentration. Thus, the method is partially familiar to combustor engineers. The method is compared to benchmark experimental data and baseline calculations. The baseline method was tested on isothermal flows, evaporating sprays and combusting sprays. Pdf and baseline predictions were performed for three diffusion flames and one premixed flame. The pdf method predicted lower combustion rates than the baseline method in agreement with the data, except for the premixed flame. The baseline and stochastic predictions bounded the experimental data for the premixed flame. The use of a continuous mixing model or relax to mean mixing model had little effect on the prediction of average temperature. Two grids were used in a hydrogen diffusion flame simulation. Grid density didn't effect the predictions except for peak temperature and tangential velocity. The hybrid pdf method did take longer and required more memory, but has a theoretical basis to extend to many reaction steps which cannot be said of current turbulent combustion models.

14. SUBJECT TERMS

Combustion; Modeling; Stochastic; Numerical

15. NUMBER OF PAGES 281

16. PRICE CODE A13

17. SECURITY CLASSIFICATION OF REPORT	18. SECURITY CLASSIFICATION OF THIS PAGE	19. SECURITY CLASSIFICATION OF ABSTRACT	20. LIMITATION OF ABSTRACT
Unclassified	Unclassified	Unclassified	